INFORMATION TO USERS

This manuscript has been reproduced from the microfilm master. UMI films the text directly from the original or copy submitted. Thus, some thesis and dissertation copies are in typewriter face, while others may be from any type of computer printer.

The quality of this reproduction is dependent upon the quality of the copy submitted. Broken or indistinct print, colored or poor quality illustrations and photographs, print bleedthrough, substandard margins, and improper alignment can adversely affect reproduction.

In the unlikely event that the author did not send UMI a complete manuscript and there are missing pages, these will be noted. Also, if unauthorized copyright material had to be removed, a note will indicate the deletion.

Oversize materials (e.g., maps, drawings, charts) are reproduced by sectioning the original, beginning at the upper left-hand corner and continuing from left to right in equal sections with small overlaps.

ProQuest Information and Learning
300 North Zeeb Road, Ann Arbor, MI 48106-1346 USA
800-521-0600

Theory and Simulation of Flow-Induced Microstructure and Rheology of Discotic Mesophases

By

Arvinder Pal Singh

Department of Chemical Engineering
McGill University, Montreal, Canada

November 2000

A Thesis submitted to the Faculty of Graduate Studies and Research
In partial fulfillment of the requirements for the degree of
Doctor of Philosophy

© Arvinder Pal Singh, 2000

National Library of Canada
Acquisitions and Bibliographic Services
395 Wellington Street
Ottawa ON K1A 0N4
Canada

Bibliothèque nationale du Canada
Acquisitions et services bibliographiques
395, rue Wellington
Ottawa ON K1A 0N4
Canada

Your file Votre référence

Our file Notre référence

The author has granted a non-exclusive licence allowing the National Library of Canada to reproduce, loan, distribute or sell copies of this thesis in microform, paper or electronic formats.

L'auteur a accordé une licence non exclusive permettant à la Bibliothèque nationale du Canada de reproduire, prêter, distribuer ou vendre des copies de cette thèse sous la forme de microfiche/film, de reproduction sur papier ou sur format électronique.

The author retains ownership of the copyright in this thesis. Neither the thesis nor substantial extracts from it may be printed or otherwise reproduced without the author's permission.

L'auteur conserve la propriété du droit d'auteur qui protège cette thèse. Ni la thèse ni des extraits substantiels de celle-ci ne doivent être imprimés ou autrement reproduits sans son autorisation.

0-612-70054-2

Canada

FOR MY PARENTS

ਅਸੀਂ ਜਿਨ੍ਹਾਂ ਨੇ ਯੁੱਧ ਨਹੀਂ ਕੀਤਾ
ਤੇਰੇ ਸਾਊ ਪੁੱਤ ਨਹੀਂ ਹਾਂ ਜ਼ਿੰਦਗੀ
... *ਪਾਸ਼*

FOREWORD

The author, Arvinder Pal Singh, of this dissertation chooses the manuscript-based thesis option according to the following thesis preparation guideline given by the Faculty of Graduate Studies and Research:

Candidates have the option of including, as a part of the thesis, the text of a paper(s) submitted or to be submitted for publication, or the clearly duplicated text of a published paper(s). These texts must be bound as an integral part of the thesis.

If this option is chosen, connecting texts that provide logical bridges between the different papers are mandatory. The thesis must be written in such a way that it is more than mere collection of manuscripts; in other words, results of a series of papers must be integrated.

The thesis must still conform to all other requirements of the "Guidelines for Thesis Preparation". The thesis must include: A table of Contents, an abstract in English and French, an introduction which clearly states the rationale and objectives of the study, a comprehensive review of the literature, a final conclusion and a summary, and a thorough bibliography or reference list.

Additional material must be provided where appropriate (e.g. in appendices) and in sufficient detail to allow a clear and precise judgement to be made of the importance and originality of the research reported in the thesis.

In case of manuscripts co-authored by the candidate and the others, the candidate is required to make an explicit statement in the thesis as to who contributed to such work and to what extent. Supervisors must attest to the accuracy of such statements at the doctoral oral defense. Since the task of the examiner is made more difficult in these cases, it is in the candidate's interests to make perfectly clear responsibilities of all the authors of co-authored papers. Under no circumstances can a co-author of any component of such a thesis serve as an examiner for that thesis.

Contents of chapters 2 to 7 of the present thesis are adopted from the published papers in scientific journals under the normal supervision of thesis research supervisor, Professor Alejandro D. Rey, who is also a co-author.

I, Alejandro D. Rey, hereby give copyright clearance of the following manuscripts of which I am a co-author. The *extent of my contribution* to following manuscripts is that of a research director. I provided the research directions, technical consultation on the subject, and general supervision throughout the duration of this Ph.D. thesis.

Chapter 2

A.P. Singh and A.D. Rey, "Microstructure constitutive equation for discotic nematic liquid crystalline materials. Part I: Selection procedure and shear flow predictions", *Rheologica Acta* **37**(1) p30-45 (1998).

Chapter 3

A.P. Singh and A.D. Rey, "Microstructure constitutive equation for discotic nematic liquid crystalline materials. Part II: Rheological predictions", *Rheologica Acta* **37**(4) p374-386 (1998).

Chapter 4

A.P. Singh and A.D. Rey, "Consistency of predicted shear-induced orientation modes with observed mesophase pitch-based carbon fiber textures", *Carbon* **36**(12) p1855-1859 (1998).

Chapter 5

A.P. Singh and A.D. Rey, "Theoretical analysis of microstructure dependent extensional viscosity of mesophase pitches", *Liquid Crystals* **26**(7) p999-1005 (1999).

Chapter 6

A.P. Singh and A.D. Rey, "Effect of long range elasticity and boundary conditions on microstructural response of sheared discotic mesophases", *Journal of Non-Newtonian Fluid Mechanics* **94**(2-3) p87-111 (2000).

Chapter 7:

A.P. Singh and A.D. Rey, "Modeling shear-induced microstructure in mesophase pitches", *XIIIth Congress of Rheology "Rheology 2000"* Cambridge, U.K. Volume 2, p117-119 (2000).

Alejandro D. Rey
Professor
Department of Chemical Engineering
McGill University, Montreal, Canada

ABSTRACT

Carbonaceous mesophase are naturally occurring discotic nematic liquid crystals that are used as precursor materials to manufacture high performance mesophase carbon fibers, which are increasingly being employed in next generation composite materials in chemical, electronics, and aerospace industries. The superior set of product property profile of these fibers is due to the preferred microstructure development, during the fiber spinning process, which is facilitated by anisotropic nature of the carbonaceous mesophase. The development of microstructure during the fiber formation process is critical to optimize their properties. However, the flow behavior of carbonaceous mesophases under such complex external fields is largely unknown. Several experimental studies have been performed worldwide to explore the flow behavior of precursor materials. Mathematical modeling, on the other hand, has not only complemented the experiments but has also emerged as a more economical alternative, and forms the basis of this study.

In this thesis we developed a constitutive equation (CE) for carbonaceous mesophases by taking into account full microstructure characteristics. The microstructural and rheological predictions of the constitutive equation are computed by subjecting it to shear and extensional flows. The steady and dynamical microstructure features of the various orientation regimes are thoroughly characterized and analyzed. The predicted relations among the rheological properties (simple shear and uniaxial extensional), flow-induced microstructure, processing conditions, and material properties are discussed. The effect of surface anchorings and the long-range elasticity on the bulk shear-induced microstructure of discotic mesophases is analyzed. The numerical results are used to put forth the fundamental principles that govern mesophase carbon fiber texture generation under shear. The simulations reproduce and explain a significant number of experimental facts and trends. The excellent performance of selected CE strongly suggests that it is a reliable contribution towards formulation of a process model for carbonaceous mesophase spinning.

RÉSUMÉ

Les mésophases carboniques, qui apparaissent naturellement dans les cristaux liquides nématiques distiques, sont utilisées comme matériaux précurseurs pour la préparation de fibres de carbones mésophasiques à hautes performances. Ces fibres seront de plus en plus employées dans la nouvelle génération de matériaux composites destiné à l'industrie chimique, électronique et aérospatiale. La supériorité de l'ensemble des propriétés de ce produit est due au développement préférentiel de la microstructure, durant le processus de filage, qui est facilité par la nature anisotropique des mésophases carboniques. Le développement de la microstructure durant le procédé de formation des fibres est critique pour l'optimisation des propriétés. Cependant, le comportement de l'écoulement des mésophases carboniques dans de si complexes conditions est très largement inconnue. Plusieurs études expérimentales ont été réalisées à dans le monde sur l'écoulement de ces matériaux précurseurs. La modélisation mathématique, d'un autre coté, n'a pas seulement été un complément des expériences mais s'est aussi avéré une alternative plus économique, et elle forme les bases de cette étude.

Dans cette thèse, nous développons une équation constitutive (EC) pour les mésophases carboniques en prenant en compte l'ensemble des caractéristiques de la microstructure. Les prédictions micro-structurelles et rhéologiques de l'équation constitutive sont calculées sujet aux écoulements de cisaillement et extensionnel. Les caractéristiques de la microstructure statique et dynamique des différents régimes d'orientations sont complètement caractérisés et analysés. Les relations prédites parmi les propriétés rhéologiques (cisaillement simple et écoulement uni-axiaux extensionnels), les microstructures induites par l'écoulement, les conditions de déroulement, et les propriétés des matériaux sont discutées. Les effets de la surface fixée et de l'élasticité de longue porté sur la microstructure du volume intérieur induit par cisaillement des mésophases discotiques est analysée. Les résultats numériques sont utilisés pour mettre en avant les principes fondamentaux qui gouvernent la génération de texture de mésophases de fibres de carbone sous cisaillement. Les simulations reproduisent et expliquent un nombre signifiant de faits expérimentaux et de tendances. Les excellentes performances de l'équation constitutive sélectionnée suggèrent fortement que ce soit une contribution fiable vis à vis de la formulation d'un modèle du procédé d'extrusion de mésophases carboniques.

ACKNOWLEDGEMENTS

It is with great pleasure that I express my gratitude to my research supervisor, Professor Alejandro D. Rey, for his sincere research guidance, continuous support and encouragement throughout the course of this thesis and my graduate studies. I will always be indebted regarding what I learnt from him about dedication, perseverance and hard work. His continuous strive to teach me "by example" on how to be a good researcher, and kindness are highly appreciated.

I would like to extend my appreciation to the followings:

All the fellow slogging researchers at "6th Floor" of Wong Building, especially my lab mates Professor Philip Chan, Professor Tomohiro Tsuji, Dr. Tao Huang, Dinesh Sharma, Ae-Gyeong Cheong for their help, lively discussions, and most of all making theoretical research an enjoyable experience.

Dr. Dana Radu and Gino DeLuca for their kind help with translating the thesis abstract into French.

Mrs. Edie, Professor Edie and his research group for making my visit at Clemson University a 'memorable' one.

The Donors of Petroleum Research Fund (PRF), administered by the American Chemical Society, for support of this research.

My 'extended' family, especially my parents for their love, support, encouragement and most of all believing in me.

CONTENTS

LIST OF TABLES

LIST OF FIGURES

NOMENCLATURE

Alphabets

$\mathbf{A}$	Rate of deformation tensor
c	Concentration of molecules per unit volume
De	Deborah number
D_r	Rotary diffusivity
Er	Ericksen number, ratio of viscous flow effects to long-range order elasticity
H	Characteristic distance between two plates of shear cell
K_{11}, K_{22}, K_{33}	Frank elastic constants
$\mathbf{l}$	Biaxial director, biaxial orientation
L_1, L_2	Landau coefficients
$\mathbf{m}$	Biaxial director, biaxial orientation
$\mathbf{n}$	Uniaxial director, uniaxial orientation
$\mathbf{N}$	Jaunmann/corotational derivative of director $\mathbf{n}$
N_1	First normal stress difference
N_2	Second normal stress difference
N_D	Discotic nematics
p	Aspect ratio of molecules
P	Biaxial scalar order parameter, biaxial alignment
Pe	Peclet number, ratio of viscous flow effects to short–range order elasticity
$\mathbf{Q}$	Tensor order parameter
$\hat{\mathbf{Q}}$	Jaunmann/corotational derivative of $\mathbf{Q}$
$r_\perp$	Length of longest semi axis of oblate spheroid
$r_\parallel$	Length of shortest semi axis of oblate spheroid

R	Ratio of short-range order to long-range order elasticity
S	Uniaxial scalar order parameter, uniaxial alignment
S_{eq}	Equilibrium uniaxial scalar order parameter
t	Time
$\mathbf{t}^t$	Extra stress tensor
$\mathbf{t}^s$	Symmetric contribution to extra stress tensor $\mathbf{t}^t$
$\mathbf{t}^a$	Anti-symmetric contribution to extra stress tensor $\mathbf{t}^t$
$\mathbf{t}^v$	Viscous stress contribution to symmetric stress tensor $\mathbf{t}^s$
$\mathbf{t}^e$	Elastic stress contribution to symmetric stress tensor $\mathbf{t}^s$
T	Temperature
T_{NI}	Nematic-isotropic phase transition temperature
T_p	Dimensionless time period
U	Nematic potential
$\mathbf{v}$	Velocity
$\mathbf{W}$	Vorticity tensor

Symbols

$\alpha_1, \alpha_2, \alpha_3, \alpha_4, \alpha_5$	Leslie coefficients
β	Shape factor
$\dot{\varepsilon}$	Extension rate
$\dot{\gamma}$	Shear rate
γ_1	Rotational viscosity
γ_2	Irrotational torque coefficient
δ	Dimensionless boundary layer thickness
$\nabla\mathbf{v}$	Velocity gradient tensor
λ	Uniaxial tumbling (reactive) parameter
$\lambda_\mathbf{n}, \lambda_\mathbf{m}, \lambda_\mathbf{l}$	Eigenvalues corresponding to eigenvectors (directors) **n**, **m**, and **l** respectively

$\theta_{\mathbf{a}}, \theta_{\mathbf{n}}, \theta_{\mathbf{m}}, \theta_{\mathbf{l}}$	Azimuthal angle of vector **a**, **n**, **m**, **l** respectively
$\phi_{\mathbf{a}}, \phi_{\mathbf{n}}, \phi_{\mathbf{m}}, \phi_{\mathbf{l}}$	Polar angle of vector **a**, **n**; **m**, **l** respectively
ω	Tilt angle between molecules in smectic C phase and the normal to the smectic plane
μ	Viscosity
η_E	Elongational/tensile viscosity
σ_E	Tensile modulus
ξ_v	Ratio of viscous to elastic stress contributions
ζ	Intrinsic length scale

CHAPTER 1

Introduction

1.1 Thesis Motivation

One of the most important components in the recent revolution towards new and more efficient materials has been development and use of polymer-based precursors. Successful use of polymers for new materials applications involves two essential steps: first is synthesis of novel materials, and second processing of the polymer into useful products. Both steps play a critical role in determining the underlying properties of the material - the first because of changes in chemical structure, and the second because the physical structure of the precursors can be altered dramatically by thermomechanical forces. Manipulation of molecular orientation and micro-phase structure in the processing steps often plays a dominant role in current applications. For example, the excellent product property profiles of some liquid crystal polymer (LCP)-based fibers like Kevlar and mesophase carbon fibers is due mainly to high degree of alignment imposed at the molecular level in the processing steps. Although during the past decade some important advances have been made in understanding polymer melt viscoelasticity, relatively less is known if the material systems include more complex processing materials such as miscible polymers, block copolymers, and liquid crystalline materials. The present molecular theories of polymer melt rheology need to be extended to include

liquid crystals to further our understanding of the underlying principles governing microstructure-viscoelasticity responses, and thus to ultimately improve product-property-profiles. Modeling and simulation provides economical alternatives to more expensive time consuming experimentation, and has been employed in this thesis to understand the microstructural behavior of carbonaceous mesophase, a liquid crystalline phase currently being employed to manufacture high performance carbon fibers.

The high performance carbon fibers posses exceptional mechanical and thermal transport properties (McHugh, 1994); they exhibit ultra high Young's modulus, low density, extremely large thermal conductivity, and negative coefficient of expansion; and are increasingly being employed in the next generation composite materials for aerospace, the electronics and automotive industries. The superior set of product property profile of mesophase carbon fibers depends on their microstructure that evolves during spinning process (McHugh, 1994; Fleurot, 1998), and is a strong function of the operating conditions, geometry, and material properties. There has been a great interest in understanding the texture evolution during the fiber formation melt spinning process, in which the carbonaceous mesophases are subjected to non-homogeneous mixed shear and extensional flows, to control and optimize their product property profile. Figure 1.1 shows thermal conductivity and electrical resistivity for a number of metals and Amoco series of mesophase pitch-based (suffix 'P') and PAN-based (polyacrylonitrile) carbon fibers (Kowalsky, 1987). The thermal conductivity of mesophase carbon fibers is considerably higher than that of Copper and PAN carbon fibers. These high values of thermal conductivity are due to the inherent graphitic crystallinity in the well ordered textures of the mesophase carbon fibers. PAN carbon fibers can not exhibit these higher values due to their fibrillar microstructure. The thermal conductivity of mesophase carbon fibers is due to phonon conduction as opposed to electronic conduction (Kelly, 1967), and is influenced by several factors such as: high degree of crystallinity, large size of crystallites etc. (Endo, 1988). Moreover, PAN-based carbon fibers, due to the fibrillar nature, are unable to develop any extended graphitic structure, hence their modulus is considerably less than the theoretical value, a limit which is nearly achieved by mesophase carbon fibers, as shown in Figure 1.2 (Bacon, 1989).

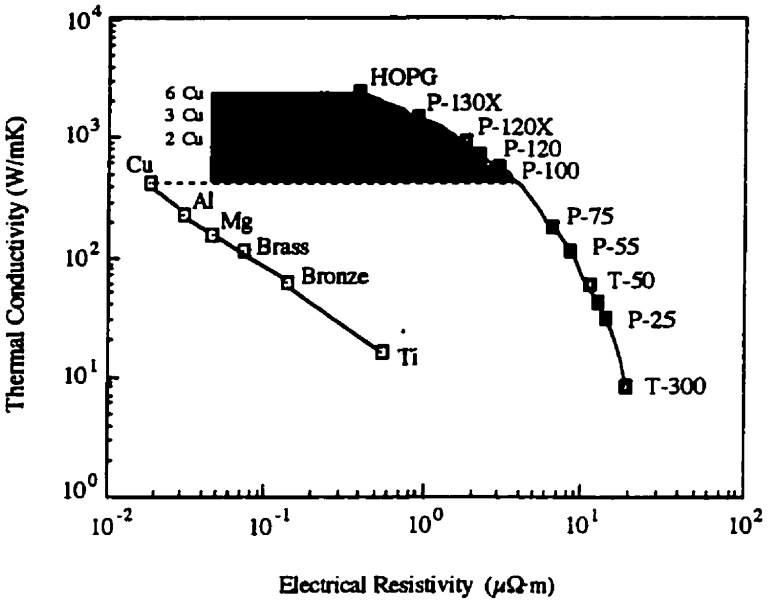

Figure 1.1: Thermal conductivity versus electrical resistivity product property phase plane for various metals and carbon fibers. The thermal conductivity of mesophase carbon, P-130X, P-120X etc., is considerably higher than that of the most conductive metals like Copper. Adapted from Kowalsky (1987).

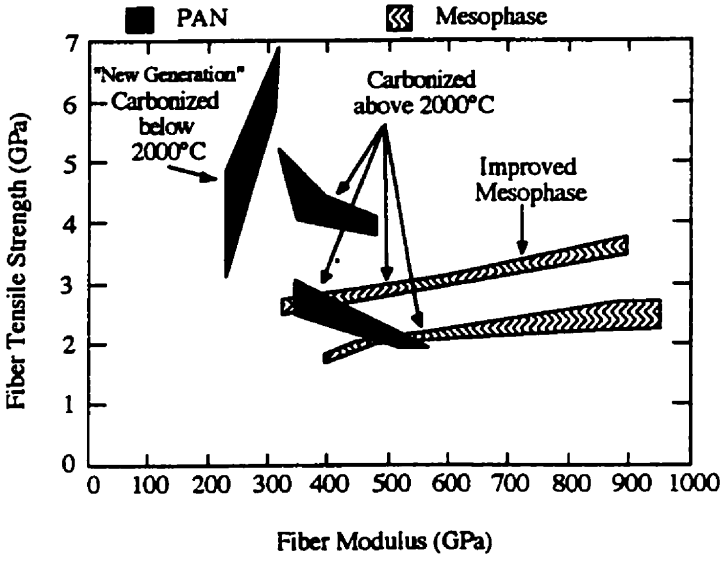

Figure 1.2: Tensile strength versus modulus of elasticity (stiffness) product property phase plane of various carbon fibers. The PAN-based carbon fibers have considerably higher strength than the mesophase carbon fibers, however the former lack considerably in terms of stiffness. The stiffness of mesophase carbon fibers reaches the theoretical limits of pure graphite. Adapted from Bacon (1989).

1.2 General Background

Many organic compounds do not undergo a single-phase transition from a solid to a liquid phase, but assume one or more intermediate states called mesophases, which possess both liquid-like fluidity and solid-like molecular order (Priestley et al., 1975; Vertogen and de Jeu, 1988; Chandrasekhar, 1992; deGennes and Proust, 1993). The centers of masses of molecules constituting solids crystals are located in a three dimensional periodic lattice, thereby having both positional as well orientational order. On the other hand in isotropic liquids only short-range order prevails among the constituent molecules. The extent of ordering in mesophases (mesomorphic or anisotropic liquids) lies between that of a solid crystal and an isotropic liquid, as shown in Figure 1.3. Based on this partial ordering two fundamentally different types of mesophases have been observed. (Priestley et al., 1975; Vertogen and de Jeu, 1988). Mesophases which possess the positional order but lack any significant orientational order, are called disordered crystal mesophases or plastic crystals (Priestley et al., 1975; Vertogen and de Jeu, 1988). On the other hand mesophases in which the positional order has been reduced or completely disappeared but still exhibit long-range orientational order (in addition to the isotropic liquid like short-range order), are called ordered fluid mesophases or liquid crystals, see Figure 1.3 for example. A particular type of liquid crystal, termed as discotic liquid crystal, composed of polyaromatic disc-like molecules, is investigated in this thesis.

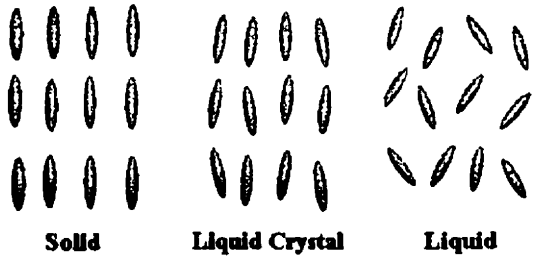

Figure 1.3: Schematic representation of molecular alignment in a crystalline solid, a liquid crystal, and an isotropic liquid. It is sometimes difficult to distinguish weather the material is in a crystalline or liquid crystal state. Crystalline materials demonstrate long-range periodic order, whereas isotropic liquids have no orientational order. Liquid crystals are not as ordered as crystalline solids, yet have some degree of alignment. Adapted from PLC, CWRU (2000).

The shape of the molecule is an important criterion for mesomorphism to occur. Since early investigations of liquid crystalline behavior the accepted fact, until recently, was that for thermotropic mesomorphism to occur the molecules must posses rod-like shape. It was discovered in the last two decades that compounds, naturally occurring or synthetic, consisting of disc-like (poly-aromatic) molecules can also exhibit thermotropic mesomorphism and are termed as discotic liquid crystals, discotic nematics or discotic mesophases. The first discotic liquid crystal was synthesis and identified in 1977 (Chandrasekhar et al., 1977). A number of synthetic (Dubois, 1978; Destrade et al., 1979; Levelut, 1983) and naturally occurring (Brooks and Taylor, 1965; Destrade et al, 1981; Otani, 1981; Singer, 1985) discotic liquid crystals have since been discovered. Naturally occurring carbonaceous mesophases display discotic liquid crystalline behavior and are derived from pyrolysis of low cost coal and petroleum pitches (Otani, 1981; Singer, 1981, 1985). This low cost mesophase is used as precursor materials to manufacture high performance mesophase carbon fibers with superior product-property profile.

1.3 Types of Liquid Crystals

1.3.1 Thermotropic Liquid Crystals

Single component systems, which show mesomorphic behavior in a definite temperature range, are called thermotropic liquid crystals. Every molecule in the thermotropic liquid crystalline phase participates in the long-range order. Figure 1.4 shows phase diagram of a typical thermotropic nematic liquid crystal (explained below). The material exhibits nematic liquid crystalline behavior below transition temperature T_{NI}. The liquid phase is isotropic above the transition temperature.

1.3.2 Lyotropic Liquid Crystals

These exhibit the mesomorphic behavior in solution, and are usually the solutions of rigid molecules in strong solvents (Priestley et al., 1975; Vertogen and de Jeu, 1988). The anisotropic behavior is shown above a particular concentration. Moreover, the

temperature range in which lyotropic liquid crystals are stable depends mainly on the phase concentration. The long-order is mainly controlled by the rigid rod-like (solute) molecules. A renowned example of lyotropic liquid crystals is Kevlar, which is a solution of Poly(p-phenylene terephthalamide) in sulfuric acid. In general, the lyotropic liquid crystals are of great interest in biological systems, and appear to play an important role in living systems.

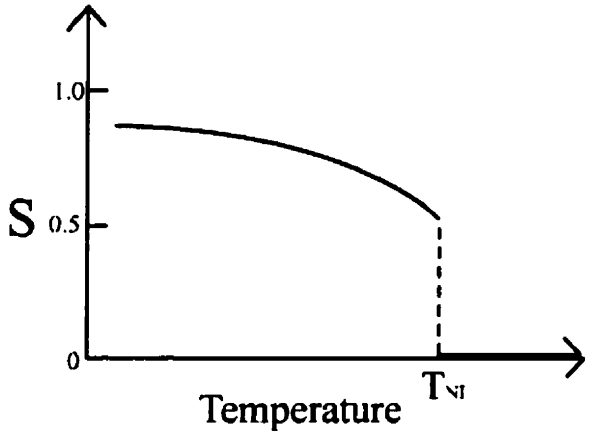

Figure 1.4: Schematic representation of phase change brought about by temperature in liquid crystalline materials. At lower temperatures $T < T_{NI}$ the material exhibits liquid crystallinity (the degree of molecular alignment, $S > 0.3$). However, for $T \geq T_{NI}$ the same material is an isotropic fluid. Adapted from PLC, CWRU (2000).

1.4 Classification of Liquid Crystals based on Molecular Order

According to the nomenclature proposed originally by Friedel in 1922, the liquid crystals are classified based on their molecular or orientational order into three major classes: nematic, cholesteric, and smectic liquid crystals.

1.4.1 Nematic Liquid Crystals

The schematics given in Figure 1.5 represent nematic order in liquid crystalline materials. The molecules tend to align parallel to each other and along some common axis called director **n**, a unit vector (Figure 1.5a). The centers of gravity of the constituent molecules are distributed randomly in space. Hence, nematic liquid crystals

posses orientational order like that of crystals but positional disorder like that of isotropic fluids. Long-range orientational order and cylindrical symmetry are exhibited by nematic order.

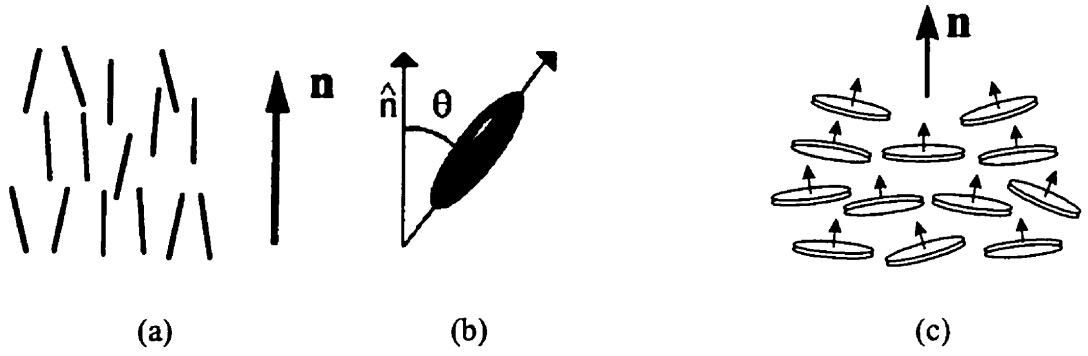

Figure 1.5: Schematic representation of (a) rod-like nematic liquid crystals, and (c) discotic nematic liquid crystals. The director **n** represents the average preferred orientation of the molecules for (b) rod-like nematics, whereas in discotic nematics **n** is the average preferred orientation of the unit normals to the disc-like molecules. The molecular degree of alignment is given by scalar order parameter *S*, which is a measure of alignment of individual molecule along the director **n**. See text for more details.

In rod-like nematics, the director **n** represents the average preferred direction of the molecules, as shown in Figure 1.5a. Whereas in case of disk-like nematics, the director **n** represents the preferred direction of the unit normal to the disk-like constituting molecules as shown in Figure 1.5c. This thesis is geared towards developing a fundamental understanding of the microstructure features of the discotic nematics. Based on the different molecular geometries disk-like (rod-like) molecules are represented by oblate (prolate) ellipsoids.

The degree of alignment of the individual molecules along the director **n** is given by a scalar known as scalar order parameter *S*:

$$S = \left\langle \frac{3}{2}\cos^2\theta - \frac{1}{2} \right\rangle \tag{1.1}$$

where θ is the angle between the director **n** and the long axis of each rod-like molecule in rod-like nematics (see Figure 1.5b), and that between the director **n** and unit normal of each disc-like molecule in discotic nematics. The brackets denote an average over all of the molecules in the sample. In an isotropic liquid, the average of the cosine terms is

zero, and therefore the order parameter $S \rightarrow 0$, whereas for a perfect crystal $S \rightarrow 1$. Typical values for the order parameter of a liquid crystal range between 0.3 and 0.9, with the exact value a function of temperature, as a result of kinetic molecular motion.

1.4.2 Cholesteric Liquid Crystals

The cholesteric liquid crystals are typically composed of nematic mesogenic molecules containing a chiral center, which produces intermolecular forces that favor alignment between molecules at a slight angle to one another. This results in formation of a structure, which can be visualized as a stack of very thin 2-D nematic-like layers with the director in each layer twisted with respect to those above and below. In this structure, the directors actually form a continuous helical pattern about the layer normal as illustrated by the black arrows in Figure 1.6. The molecules shown are merely representations of the many chiral nematic mesogens lying in the slabs of infinitesimal thickness with a distribution of orientation around the director. An important characteristic of the cholesteric mesophase is the pitch, the distance that the cholesteric director in cholesteric traverses to rotate one full turn (360 degrees) in the helix.

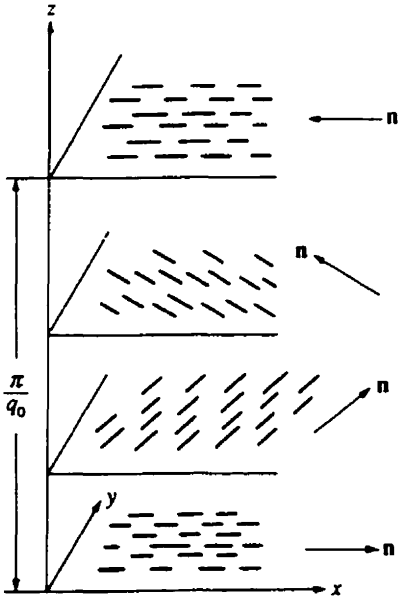

Figure 1.6: Schematic arrangement of rod-like molecules in a cholesteric liquid crystalline phase. The localized director **n** follows a helical trajectory along the z-axis. Please note that the successive planes are drawn for convenience, and do not have any physical meaning. Adapted from de Gennes and Proust (1993).

1.4.3 Smectic Liquid Crystals

A smectic phase has, in addition to the orientational order of nematics and cholesterics, a single degree of translational order (limited preferred arrangement in space) that results in a layered structure. In the smectic state, the molecules maintain the general orientational order of nematics, but also tend to align themselves in layers or planes. Motion is restricted to within these planes, and the separate planes are observed to flow past each other. The increased order means that the smectic state is more "solid-like" than the nematic. Since smectic phases are more ordered they always occur at temperatures below the nematic range. Many compounds are observed to form more than one type of smectic phase. As many as 12 of these variations have been identified, however only the most distinct phases are discussed here briefly. Figure 1.7a shows a schematic of smectic-A mesophase, the director is perpendicular to the smectic plane, and there is no particular positional order within the layer. Similarly, the smectic-B mesophase orients with the director perpendicular to the smectic plane, but the molecules are arranged into a network of hexagons within the layer. In the smectic-C mesophase, Figure 1.7b, molecules are arranged as in the smectic-A mesophase, but the director is at a constant tilt angle ω measured normally to the smectic plane.

1.5 Discotic Phases

The general consensus before the discovery of discotic nematics in 1977 (Chandrasekhar et al., 1977), was that for thermotropic mesomorphism to occur the constituting molecules have to be rod-like in shape. However, early studies (Brooks and Taylor, 1965; Dubois, 1978; Destrade et al., 1979, 1981) have established that many compounds composed of disc-shaped molecules also exhibit stable thermotropic liquid crystalline phases. Theoretically the possibility of existence of an assembly of plate-like particles in the transition from isotropic to nematic phase was established (Alben, 1973) well before the experimental discovery of discotics. Some typical molecules, which display the discotic mesomorphism, are given in Figure 1.8 (Chandrasekhar, 1992). A typical molecule that exhibits discotic liquid crystallinity has flat (or nearly flat) cores with six to eight long chain substituents, which are essential for formation of discotic

liquid crystals. Structurally, discotic liquid crystals fall into two categories: columnar phase (see Figure 1.8a,c,d,f,g,h); and nematic phase (see Figure 1.8b,e). The columnar phase is observed more often in compounds exhibiting discotic nematic behavior. In its simplest form the columnar phase consists of discs stacked one on top of each other aperiodically to form liquid like columns, the different columns constitute a two dimensional lattice. However, a number of variants of this structure have been found (Levelut, 1983). Figures 1.9a,b,c,d,e show, schematically, various two dimensional columnar lattices found in columnar discotic crystals (Levelut, 1983; Chandrasekhar, 1992). The various ellipses represent discs, which are tilted with respect to the column axis. To summarize, the columnar phase has long-range translational periodicity in two dimensions and liquid-like disorder in the third dimension. The columnar phase of discotic liquid crystals is not considered in this thesis, and therefore will not be discussed further.

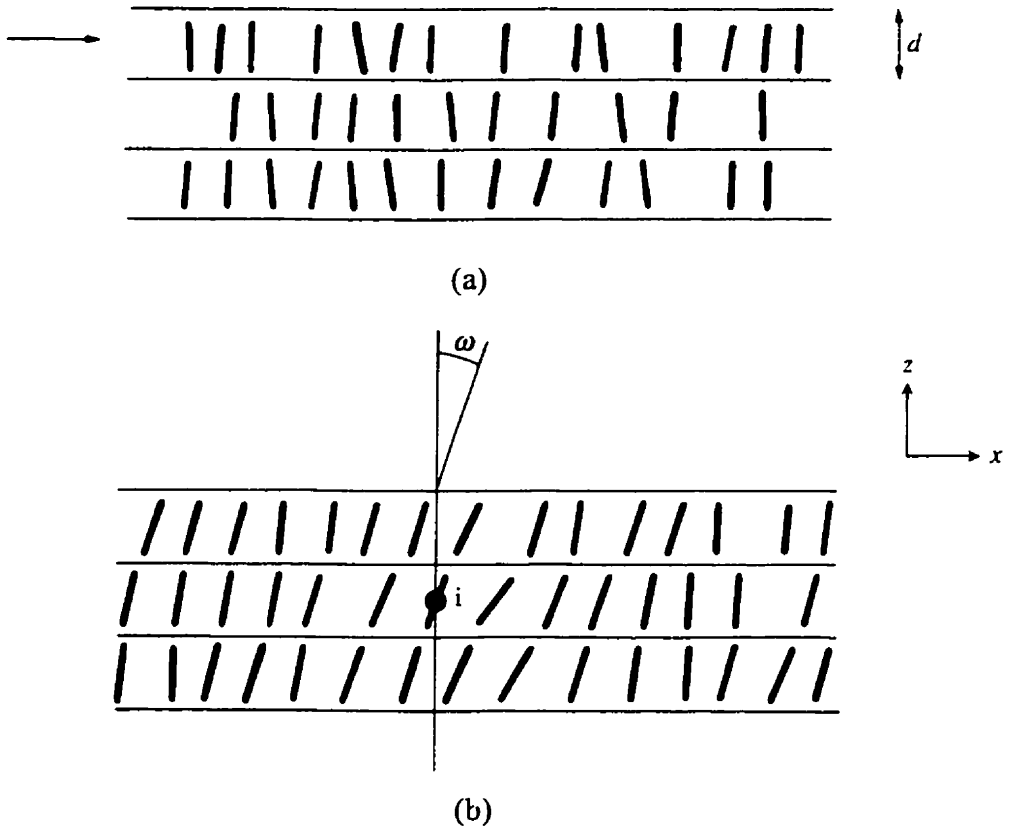

Figure 1.7 Schematic arrangement of rod-like molecules in (a) Smectic A, and (b) Smectic C liquid crystalline phases. The shown smectic phases have 2-dimensional layered structure. In smectic C phase the constituting molecules are tilted at an angle ω normal to the smectic plane. Adapted from de Gennes and Proust (1993).

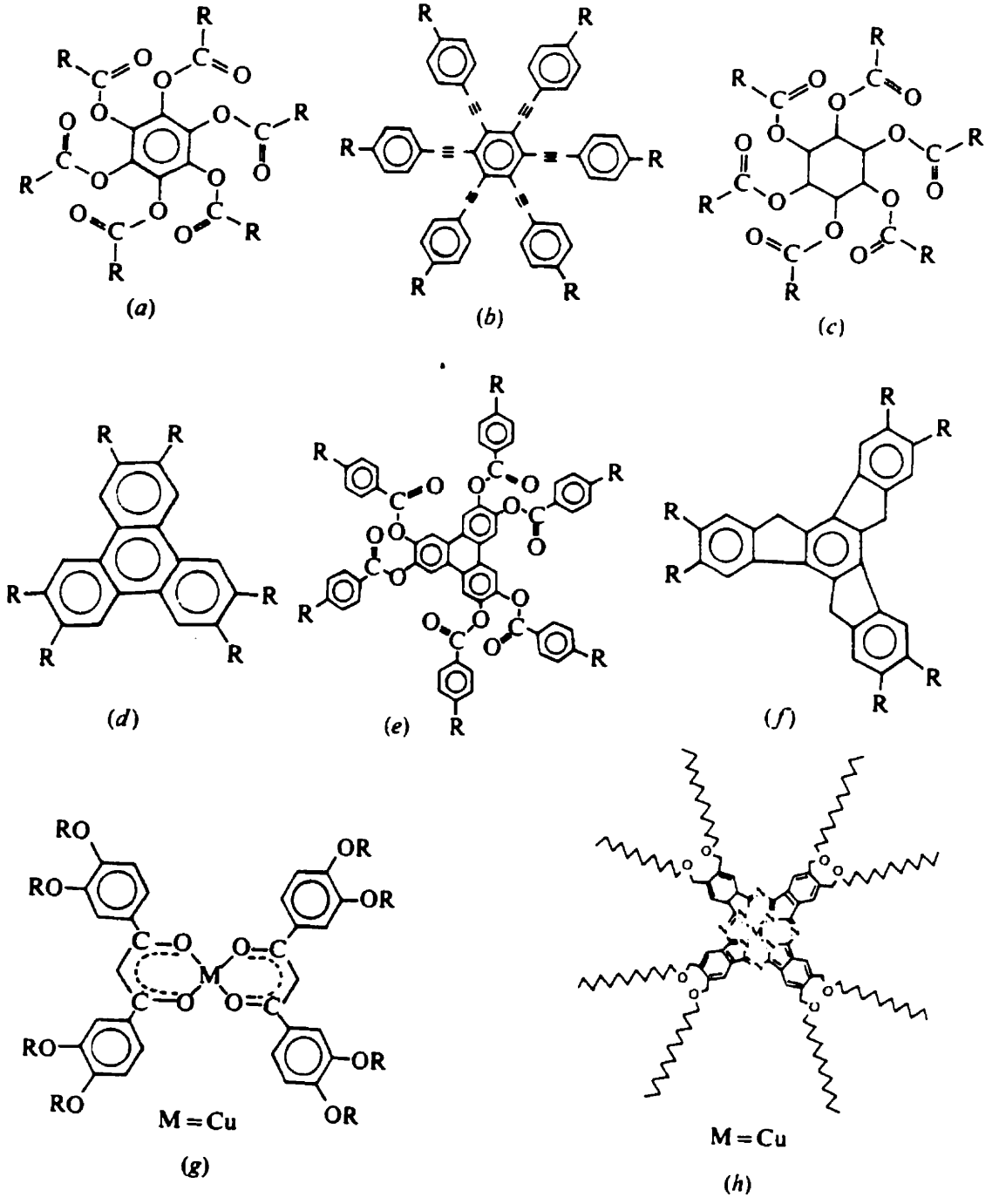

Figure 1.8: Examples of disc-like molecules that display discotic mesomorphism: (a) hexa-n-alkanoates of benzene, (b) hexakis((4-octylphenyl)ethynyl)benzene, (c) hexa-n-alkanoates of scylloinositol, (d) hexa-n-alkanoates of triphenylene and hexa-n-alkoxytriphenylene, (e) hexa-n-alkyl and alkoxybenzonates of triphenylene, (f) hexa-n-alkanoates of truxene, (g) bis(3,4-nonyloxybenzoyl)methanato copper(II), and (h) octasubstituted metallophthalocyanine. Adapted from Chandrasekhar (1992).

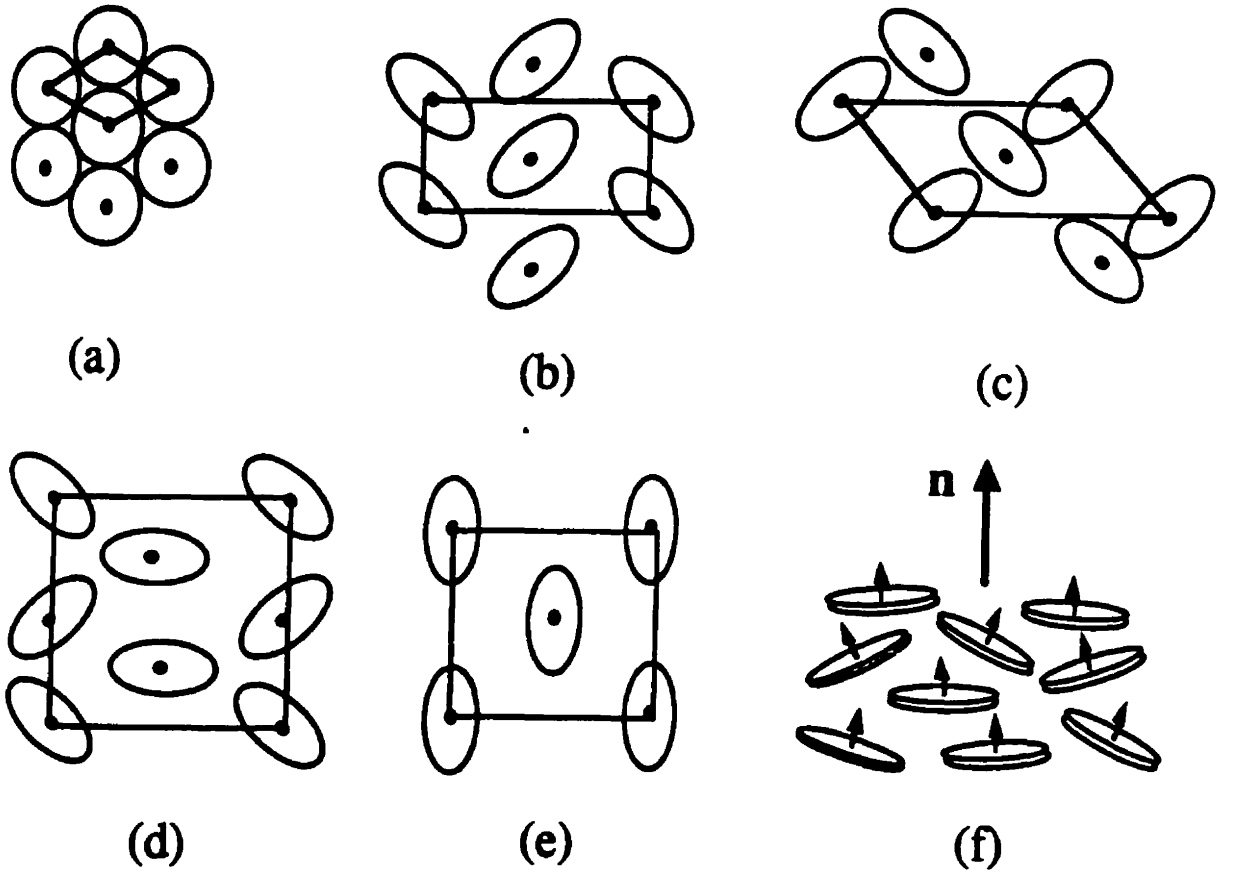

Figure 1.9: (a-e) Schematic top view of columnar phases of disc-like molecules. The column axis points out of plane of the paper towards the reader. The ellipses represent the disc-like molecules, which are tilted with respect to the column axis. (f) Schematic side view the molecular ordering of the disc-like molecules in a typical discotic nematic liquid crystalline material.

Figure 1.9f, shows a schematic of discotic nematic phase (N_D). Nematic order is found to be exhibited by relatively lesser number of disc-shaped molecules. The nematic phase of discotics possess orientational order without any long-range translational order. (Chandrasekhar, 1992). Discotic nematics in contrast to the conventional rod-like nematics, are optically negative and the director **n** represents the preferred orientation of the short molecular axis (or the normal to the disc-like molecules). Only discotic nematics of the type shown in Figure 1.9f are investigated in this thesis.

1.6 Carbonaceous Mesophases (Mesophase Pitches)

The carbonaceous mesophase (CM) or mesophase pitch (MP) is a uniaxial discotic nematic liquid crystalline thermodynamic phase composed of large polynuclear aromatic hydrocarbon molecules with molecular weights approximately near 2000 (White et al., 1967; Singer, 1976; Lewis 1978; Hamagushi and Nishizawa 1992; FitzGerald 1994). The CMs or MPs are employed as low cost precursor materials in the manufacture of high performance mesophase carbon fibers (Zimmer and White, 1982). There are currently three main processes that are used to produce spinnable MPs. The classical way is the liquid phase pyrolysis of coal tar or petroleum pitches. The second more recent process is the catalytical polymerization of pure aromatic hydrocarbons, such as Naphthalene. The third technique, developed recently by Hutchenson et al. (1991), uses a solvent in its supercritical state to extract mesophase fractions from isotropic pitches.

Figure 1.10, shows the thermodynamic and structural changes brought about during the pyrolysis of isotropic pitches. As the temperature rises above 350°C, optically anisotropic spheres, known as spherules, appear in the isotropic matrix (Singer, 1977, 1985; Gasparoux, 1981; Zimmer and White, 1982). As the hydrogenative polymerization reactions continue the poly-aromatic molecules get larger, and the anisotropic phase grows and becomes more viscous. When the molecules reach an average molecular weight of approximately 2000, they are apparently, sufficiently large and flat to favor the formation of a liquid crystalline discotic nematic phase called carbonaceous mesophase or simply mesophase pitch. The formation of carbonaceous mesophase follows a nucleation and growth process, typical of meta-stable thermodynamic systems. The spherules, droplets of anisotropic phase (see Figure 1.11), are easily observed due to their optical anisotropy. Attractive forces among the spherules give rise to droplet coalescence and overall growth of the mesophase. The structure of the spherules and the molecular organization of the disc-like poly-aromatic molecules within the spherules have been described by Brooks and Taylor (1965). The characteristic mechanisms that are involved in establishing the mesophase morphology are spherule precipitation, spherule coalescence to form a continuous anisotropic phase, and deformation of mesophase by external fields. Lewis and Chwastiak (1978) modified the above simplistic heat soaking

process of isotropic pitches by propelling an inert gas into the reaction vessel. Riggs and Dienfendorf (1980) developed an alternate heat soaking mechanism, which used solvents like Benzene and Toluene to extract the high molecular components from the isotropic pitch. The extracted portion was then polymerized for only 10 minutes at relatively lower temperatures, 230°C to 400°C to yield a 75% to 100% anisotropic phase. The primary advantage of heat soaking and solvent extraction of natural petroleum pitches is the inexpensive nature of the feedstock, however, there are inherent disadvantages as well. First, natural pitch contains heavy impurities that accumulate in the high-density mesophase, which in turn have detrimental effects on the final properties of carbon fibers. Moreover, the composition of a natural isotropic petroleum pitch varies depending on crude oil composition, therefore the properties of the resulting MP also tend to be highly variable. Thirdly, the MPs exhibit broad molecular weight distribution, which hinders spinning. Due to these problems, alternate methods of production of MPs with fewer impurities were sought. A typical molecule of a heat-soaked mesophase pitch is illustrated in Figure 1.12.

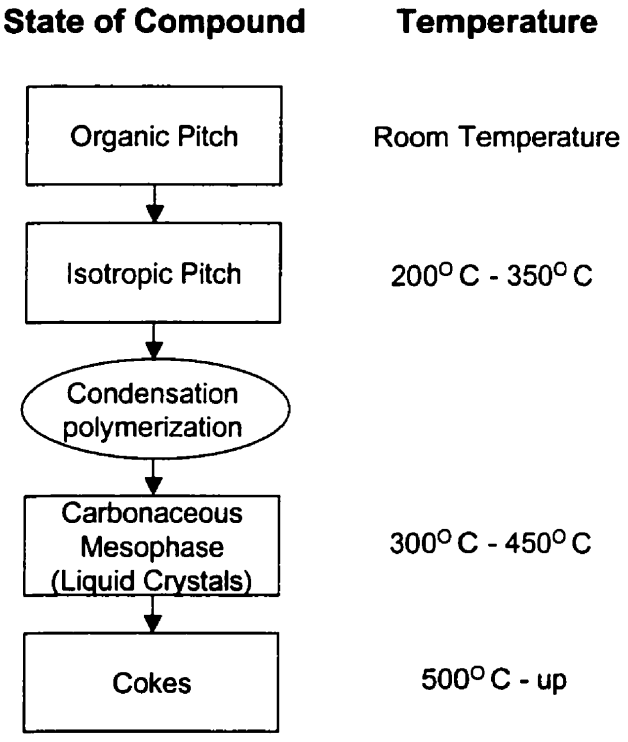

Figure 1.10: Changes in the non-volatile organic compounds like coal or petroleum pitches brought about by heating in the absence of air. Adapted from Otani (1991).

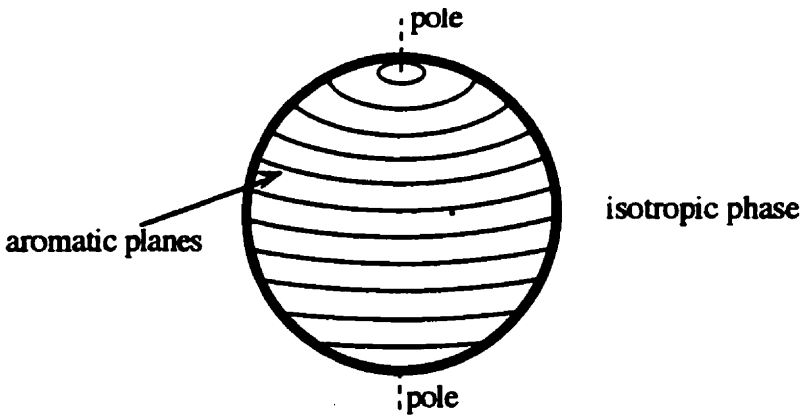

Figure 1.11: Lamellar structure of mesophase spherule before coalescence. The aromatic planes are normal to the spherule surface. The spherule grows as the aromatic molecule fuse together due to hydrogenative polymerization. Adapted from Brooks and Taylor (1965).

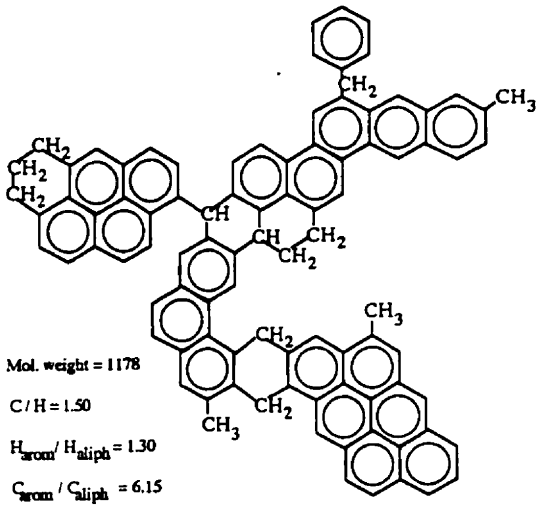

Figure 1.12: Typical molecule of a heat soaked mesophase pitch. Adapted from Fitzer et al. (1986).

Hutchenson et al. (1991) have reported that supercritical fluid extraction, using supercritical Toluene, can be employed to fractionate pitches. By continuously varying pressure and/or temperature, thereby changing the solvent strength, selective pitch fractions of relatively narrow molecular weight distribution can be isolated in a cascading process. Such a process offers the potential of producing a uniform product from an ever-changing raw material. Moreover, the heaviest fraction is not the only one that yields a

bulk mesophase; it may be possible to produce a mesophase fraction largely free of inherent impurities.

Another way to alleviate the problems associated with the natural petroleum pitches is to catalytically convert well-controlled synthetic precursors, such as Anthracene, Phenanthrene and Naphthalene, to produce mesophase pitches (Mochida et al. 1988, 1990; Fujiura 1992). For example, Naphthalene can be polymerized in an autoclave with the aid of "super catalyst" HF/BF_3, at temperatures ranging from 260°C to 300°C and under pressures from 2.1 MPa to 3.1 MPa for approximately 4 hours (Korai et al., 1991). The contents of the autoclave are heated to 340°C and purged with Nitrogen to distill off the catalyst, the unreacted monomer, and other volatile components (HF and BF_3 have boiling points of 19.9°C and 101°C, respectively), thereby leaving 100% anisotropic pitch in the autoclave.

1.7 Order in Carbonaceous Mesophases (Mesophase Pitches)

As stated above the carbonaceous mesophase consists of disc-like molecules that display long-range order, such that the molecules lie approximately parallel to each other without any point-to-point registry among themselves. The orientation of each molecule is defined by its unit normal. The symmetry elements in mesophase pitches are:

- any translation,
- any rotation about the unit normal to the disc-like molecule, and
- a rotation of π radians about any axis parallel to the plane of the molecules.

Although the degree of symmetry is the same for a discotic nematic and a conventional rod-like nematic, yet the molecular geometrical differences, for the discotic (rod-like) nematics the axis of symmetry is normal (along) to the long dimension, have important consequences on optical properties, response to external fields such as mechanical stresses, electrical and magnetic fields etc. In this dissertation we focus on the distinguishing features of flow-induced molecular orientation and rheology of discotic mesophases. Figure 1.13 presents a schematic of molecular stacking of molecules in

discotic nematics. The model suggests that the stacking, size, and the possible shape of disc-like molecules which may be quite irregular and have vacant sites.

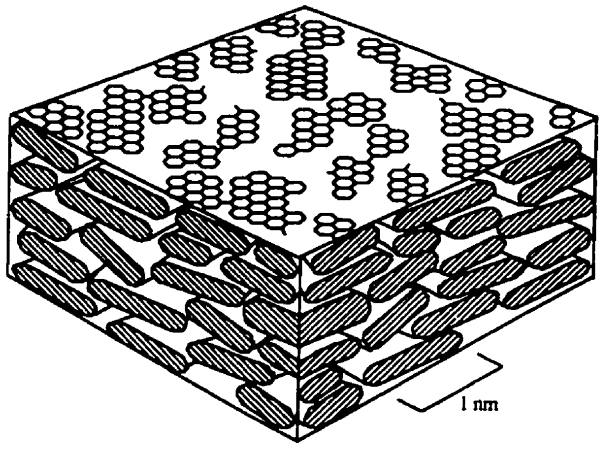

Figure 1.13: Schematic model representing stacking arrangement of polyaromatic molecules in carbonaceous mesophases or mesophase pitches. The disc-shaped molecules lie more or less parallel to each other. Adapted from Zimmer and White (1982).

As mentioned before, the main microstructural features of CMs, the uniaxial discotic nematic liquid crystals, are captured by a (uniaxial) director **n**, and by (uniaxial) scalar orientation order S. The director **n** is a unit vector that describes the direction of the average molecular alignment of unit normals of the disks, and S is a measure of average molecular alignment along **n**. The dispersion of the molecular orientation along **n** is captured by the magnitude of S ($-\frac{1}{2} \leq S \leq 1$): when $S \approx 0$ the phase is isotropic, and when $S \approx 1$ all the molecular normals are perfectly align along **n**. For normal discotic nematics the order parameter S is restricted to the range $0 \leq S \leq 1$ (Brooks and Taylor, 1965; Destrade et al., 1981; Singer, 1985). The basic microstructural and rheological phenomena have to at least include the description of spatial-temporal changes of (S, **n**).

1.8 Rheology of Mesophase Pitches

Numerous experimental studies are reported in the literature to characterize the rheological features of the mesophase pitches. However, most of the them are either concerned with changes in viscosity during thermal treatment (Fitzer et al., 1987; Collet and Rand, 1987a; Yamada et al., 1987), or have performed classical viscometric studies

(Turpin et al., 1994; Daji and Rand, 1997). Figure 1.14 shows the extreme temperature dependency of three different mesophase pitches (prepared from three different processes) relative to that of Nylon-6 (Fleurot and Edie, 1998). The temperature dependent viscosity of the mesophase pitches follows Arrhenius-type law. Figure 1.14 illustrates that activation energy of the mesophase pitches is significantly higher than that of a typical polymer (Nylon-6).

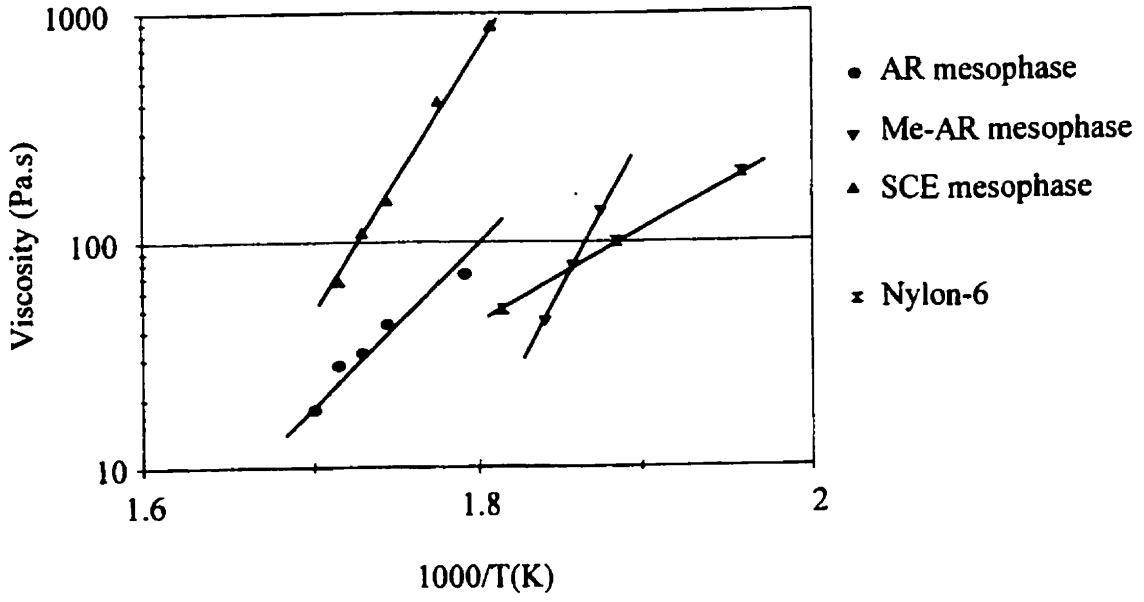

Figure 1.14: Temperature dependent viscosity of three mesophase pitches and Nylon-6 as a function of decreasing temperature. The mesophase pitches are prepared from three different processes. AR mesophase and Me-AR mesophase are synthetic mesophase pitches, and are obtained by catalytic polymerization of naphthalene (AR mesophase), and methyl naphthalene (Me-AR mesophase), respectively. SCE mesophase pitch is derived through supercritical fluid extraction process from a petroleum pitch. The viscosity of mesophase pitches is extremely dependent on temperature. Adapted from Fleurot and Edie (1998).

A few experimental studies have focused on origin and control of the microstructure in mesophase carbon fibers (Nazem, 1983; Matsumoto, 1985; Edie et al., 1986, 1993; Hamada et al., 1987, 1988; Mochida et al., 1993). These investigations showed that the transverse fiber textures are strongly dependent on the spinning conditions, precursor properties, and geometry. The theoretical predictions by using theories for monodomain, uniaxial discotic nematics (Singh and Rey, 1995; Rey 1995; McHugh and Edie, 1995; Wang and Rey, 1997) match some of the textures observed in

the mesophase carbon fibers. Fleurot (1998) studied the viscoelastic behavior of a series of pitches obtained from different sources, and through various processes. Figure 1.15 shows the apparent shear viscosity of a mesophase pitch obtained from catalytic polymerization of naphthalene, and is typical of the mesophase pitches (Fleurot, 1998). The apparent shear viscosity shows two regions, shear thinning at low shear rates and Newtonian plateau at higher shear rates. The apparent shear viscosity increases with decreasing temperature. Both regions persist at low and high temperatures. The results clearly suggested that the rheological behavior of pitches with high mesophase content is qualitatively similar to that of liquid crystalline polymers (LCPs). It has also been reported that mesophase pitch can exhibit thixotropic behavior (Collect and Rand, 1987b).

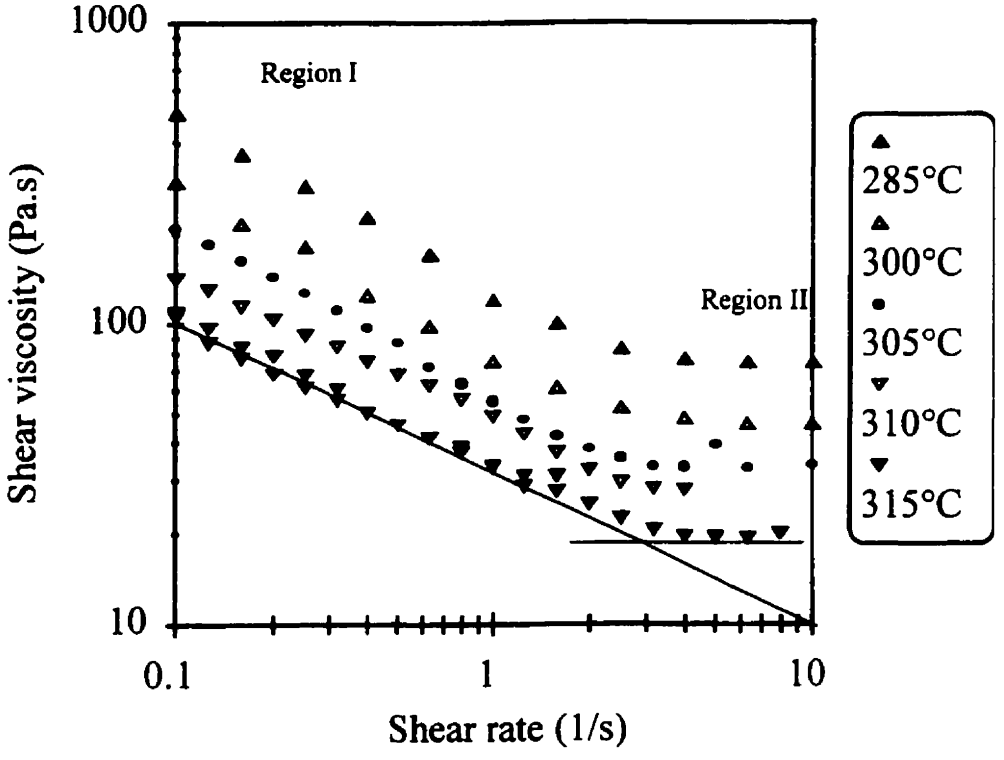

Figure 1.15: Apparent shear viscosity of a mesophase pitch at various temperatures obtained from catalytic polymerization of naphthalene. The apparent shear viscosity shows two regions, shear thinning at low shear rates and Newtonian plateau at higher shear rates. The viscosity increases with decreasing temperature. Both regions persist at higher temperatures. Adapted from Fleurot and Edie, 1998.

1.9 Mesophase Pitch-Based Carbon Fiber Processing

Three different processing steps are employed during the manufacturing of mesophase pitch-based carbon fibers: (1) melt spinning; (2) oxidative stability; and (3) carbonization. The high cost of the fibers is due to the peculiar difficulties encountered in melt spinning and subsequent heat treatment process (Edie et al., 1990). Figure 1.16 presents the processing sequence of the 3 involved steps.

1.9.1 Melt Spinning of Mesophase Pitch

Conventional high-speed melt spinning process used for many thermoplastic polymers is employed to convert palletized mesophase pitch into fibers (McHugh, 1994). Normally, an extruder melts and pressurizes the pitch, and pumps it through the spin pack. The molten pitch is filtered before being extruded through a multi-holed spinneret. The pitch is subjected to high extensional and shear stresses as it approaches and flows through the spinneret capillaries. The associated flow-induced torques tend to align the liquid crystalline pitch in a particular fashion. The average orientation of the disc-like molecules depends on the processing conditions, the flow geometry, and the material properties of the pitch, and has an enormous impact on final properties of the mesophase carbon fibers. Upon emerging from the spinneret capillaries, the mesophase fibers, called as-spun or green fibers, are drawn to improve the axial orientation, and are collected on a windup device.

1.9.2 Mesophase Pitch Fiber Heat Treatment

The as-spun mesophase fibers are extremely weak, and must be heat-treated to develop their ultimate mechanical and thermal properties. The first step in the heat treatment involves oxidation or stabilization. The purpose of oxidation is to prevent the fiber from melting during the subsequent carbonization step, and to lock-in the microstructure developed earlier during the melt spinning process. Most typically, the stabilization is achieved by exposing the fibers to flowing air at a temperature near 300°C for a duration of time ranging from a few minutes to a few hours, depending on the precursor, the fiber size, and the oxidation temperature (McHugh, 1994).

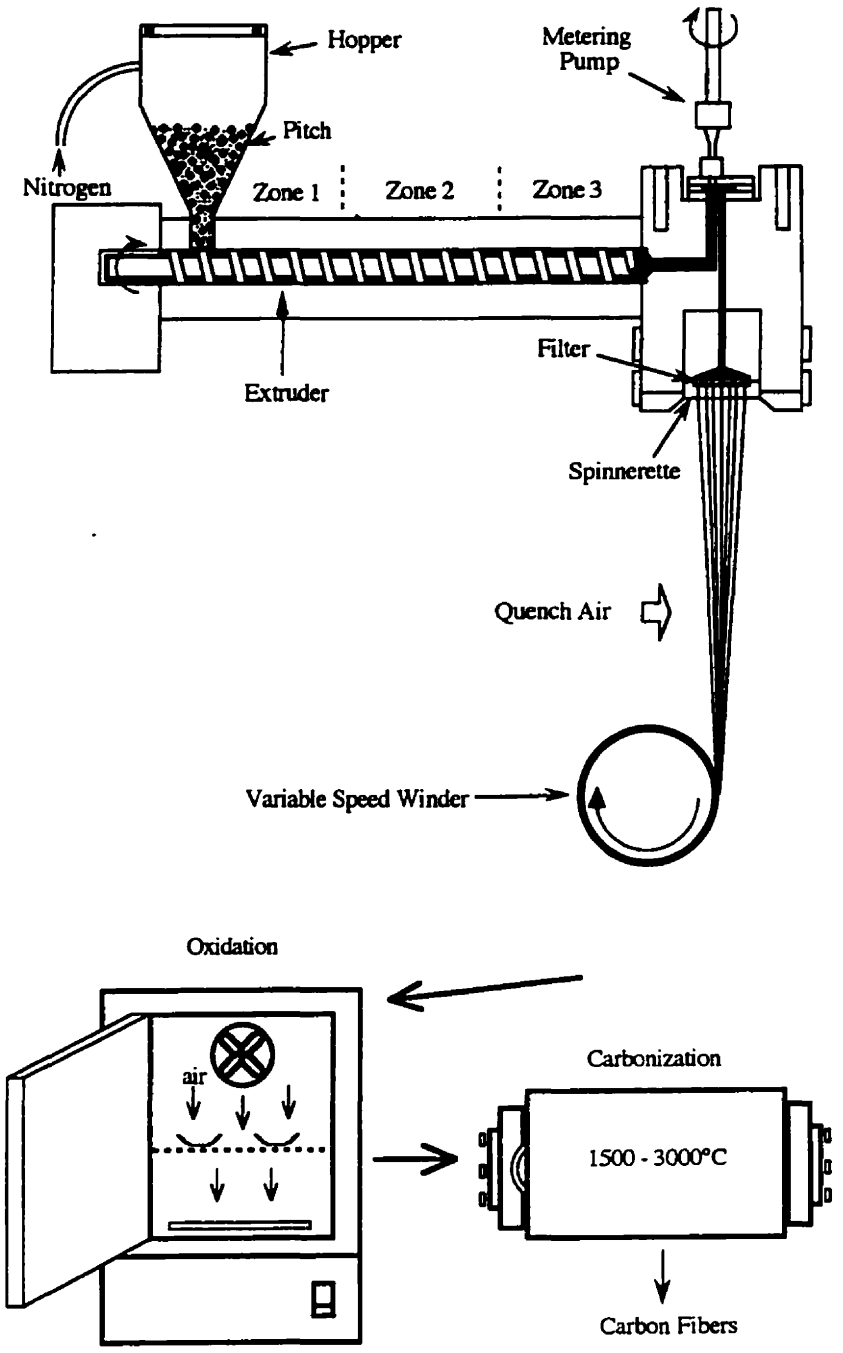

Figure 1.16: Processing sequence of mesophase carbon fibers, showing continuous conventional melt spinning of mesophase pitch, and subsequent batch processes: oxidization stabilization, and carbonization. See text for details. Adapted from McHugh (1994).

Once the fibers have been sufficiently stabilized, they can be carbonized or graphitized. During the carbonization the stabilized fibers are heated in an inert environment to temperatures up to 3000°C, to drive off all non-carbon elements thereby

leaving behind only cross-linked carbon. During carbonization, dislocations in the initial disordered carbon stacks are annealed out, eventually resulting in the formation of a three-dimensional graphite lattice. The graphitization process primarily involves atomic diffusion and crystallite growth (Fischbach, 1971).

1.10 Mesophase Pitch based-Carbon Fiber Textures

It turns out that the mesophase carbon fibers exhibit a spectrum of transverse textures that are associated with various thermal and mechanical transport properties. The morphological features of the textures are defined by the spatial arrangement of the constituting flat disc-like polyaromatic molecules in the fibers of different cross sectional shapes. Some most typical examples, reported in literature (Singer, 1971, 1981, 1981a; Honda, 1983; Edie, 1990; McHugh, 1994) are presented schematically in Figure 1.17. The lines represent loci of side view of the disk like molecules. In a radial texture, the discotic molecules orient with their unit normals describing circles concentric with the fiber axis, while in an onion-like texture, the discotic molecules themselves follow a circular paths concentric with the fiber axis. The scanning electron micrographs (SEM) of radial, random, onion, and radial-folded textures are shown in Figure 1.18. In addition to this, the fiber cores may be isotropic or anisotropic, the latter would give rise to singular lines running along the fiber core. Although the stiffness and thermal conductivity of mesophase carbon fibers are generally high, however, these properties can vary significantly with fiber textures. For radial textures, the presence of a singular line along the fiber axis introduces a potential fast failure mode by longitudinal crack propagation (Singer, 1981a), such failure modes are absent in the onion like outer layer textures. Commonly, the textures are not perfect and some degree of folding of the crystallites is observed. This appears to improve the resistance of the fiber to crack propagation, and thereby increasing its tensile strength (McHugh, 1994). Folding may be an artifact of the disclinations in the mesophase pitch, which are not annihilated by the strong deformations. (Buechler, 1983; Hamada 1987). Creation of a random texture, no clearly defined morphology, may be due to complete disruption of the flow fields inside the spinneret (Nazem, 1983), and such fibers also offer the potential of improved compressive strengths.

The fiber texture morphology can be controlled by the pretreatment of mesophase pitches, the constitution and spinnability of pitches, the spinning conditions, the spinneret geometry, the processing conditions, the fiber size and shape, and numerous other factors (Nazem 1984; Matsumoto 1985; Otani and Oya 1986; Rey, 1990; Mochida et al 1993; Wang and Rey 1997). Otani and Oya (1986) and Mochida et al. (1993) produced fibers at various spinning temperatures, and showed that radial transverse texture prevails at low temperatures, whereas onion-skin textures is generated at higher temperatures. Wang and Rey (1997) also proved theoretically, by minimizing the Frank long-range elasticity of discotic mesophases, that radial and onion textures could be controlled via a judicious selection of processing temperature. Many researchers focused on controlling the transverse structure of the fibers by disturbing the flow of mesophase pitches during processing (Nazem, 1984; Hamada et al., 1988), or designing spinnerets with peculiar geometries (Stoner et al., 1990; Yoon et al., 1993). Hamada et al. (1988) controlled the fiber texture by placing the micro-stirrers just above the spinneret capillaries, and showed that the resulting texture is highly sensitive to the micro stirring. Nazeem (1984) employed porous media just above the spinneret capillaries to disrupt the flow of mesophase, thereby controlling the transverse fiber textures. Matsumoto (1985) managed to control the transverse texture by extruding the precursors through capillaries of different diameters. It was reported that larger diameter capillaries yielded onion-skin texture, whereas the capillaries with smaller cross section produced radial textures.

1.11 Thesis Objectives

The main objective of this thesis is to develop a fundamental understanding of the microstructural and rheological response of discotic mesophases under shear and extensional flows, and to use this knowledge to put forth fundamental principles that govern mesophase carbon fiber texture generation under various flows. At the beginning of this thesis no theories were available for discotic mesophase. Therefore, as a first step in a systematic scientific study, this thesis was geared towards proposing, analyzing and selecting a most appropriate set of constitutive equations, CEs, (microstructure and hydrodynamic) for discotic mesophase in general and that for mesophase pitches in general. Based on this, the particular objective of this thesis can be itemized as follows:

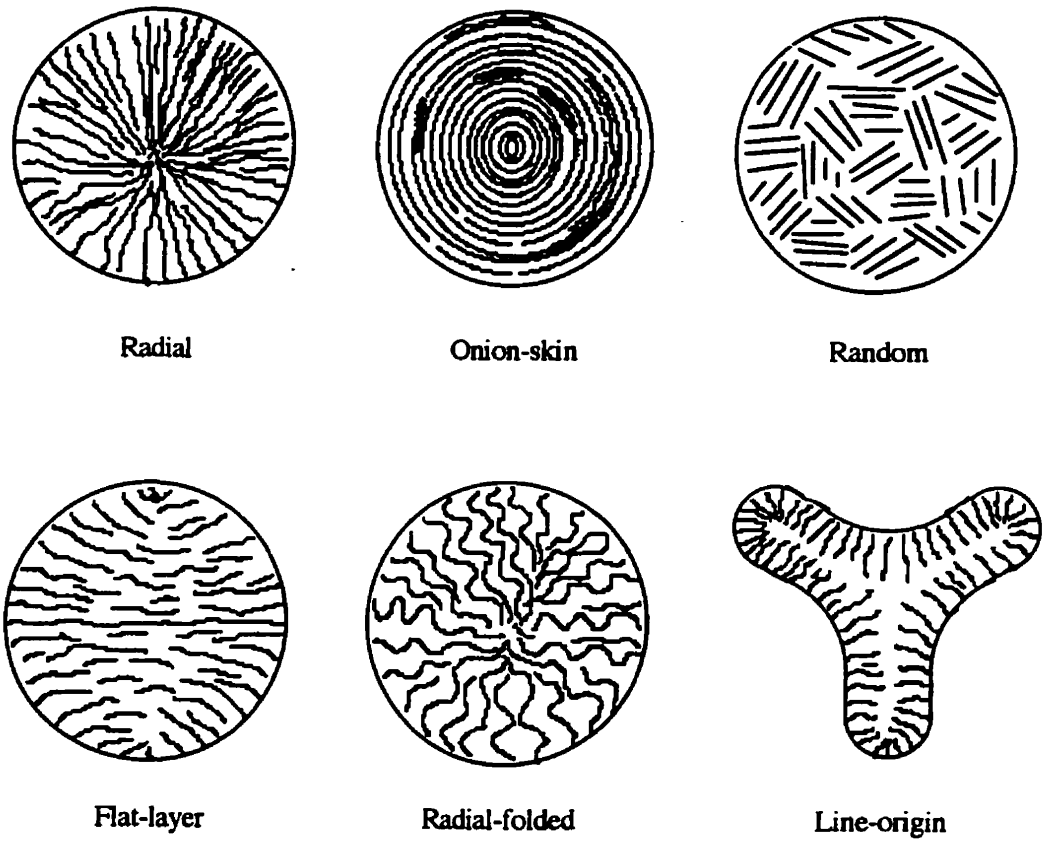

Figure 1.17: Schematics of the observed mesophase carbon fiber textures. The lines represent the locus of the side view of the disc-like molecules, such that in a radial texture, the discs orient with their unit normals describing circles concentric with the fiber axis, while in an onion-like texture, the discotic molecules themselves follow a circular paths concentric with the fiber axis. Adapted from Edie (1990).

Figure 1.18: SEM images of mesophase pitch-based carbon fibers with (a) radial texture, (b) random texture, (c) onion texture, and (d) radial-folded-texture. The fiber diameter range is 5-15 microns. Adapted from Otani and Oya (1986), and Peebles (1994).

1. To develop, from a set of generic CEs, the most suitable CE for discotic mesophases based on the computed microstructure behavior that reproduces with sufficient accuracy the experimentally observed behavior of representative discotics, and which is consistent with thermodynamic restrictions.
2. To apply the developed CE to isothermal, incompressible shear and extensional flows and characterize the dynamic and steady state microstructure response of discotic mesophases.
3. To analyze and characterize the shear and extensional rheological properties predicted by the formulated theory, and put forth the relations among rheology, microstructure modes, processing conditions, and material parameters.
4. Based on the fundamental understandings obtained above, provide guidelines and theoretical feedback to ongoing experimental work being performed in this field, and to elucidate the general principles which govern mesophase carbon fiber texture generation during spinning of carbonaceous mesophases.

1.12 Thesis Organization

This thesis presents a detailed investigation, using theory and simulation, of shear and extensional microstructure phenomena in discotic mesophases. The numerical results are used to put forth general principles governing complex mesophase carbon fiber textures. The structure of this thesis covers three facets of this scientific study:

1. Formulation of material constitutive equation for discotic mesophases by taking into account full microstructure characteristics.
2. Analysis and characterization of shear and extensional microstructural and rheological phenomena of discotic mesophase.
3. Understanding of fundamental principles, which govern main mesophase carbon fiber textures.

The detailed organization of this thesis is as follows:

Chapter 2 focuses on formulation of microstructure constitutive equation (CE) of discotic mesophases by taking into account full microstructure characteristics. Well-established theories for rod-like nematics are adopted and modified for discotic mesophases. An iterative selection procedure is employed to select the proposed microstructure constitutive equations by performing an exhaustive bifurcation analysis.

In Chapter 3, the hydrodynamic constitutive equation or stress tensor equation complimenting the microstructure governing equation for discotic mesophases was formulated from first principles. The predicted relations among shear-induced microstructure, shear rheological properties, processing conditions, and material parameters are characterized and discussed. The predicted numerical results provide essential theoretical feedback to on-going experimental work being undertaken elsewhere to unravel the couplings between microstructure and rheological properties of these complex fluids.

In chapter 4 the consistency of the numerical results presented in chapters 2 and 3 is established with the observed mesophase pitch-based carbon fibers. The present theoretical model is able to predict the fiber texture transition, radial to onion, with increasing temperature.

Chapter 5 is solely geared towards analyzing and characterizing the uniaxial extensional rheological predictions of the selected CE. It is shown that two distinct uniaxial extensional viscosity parameters are needed to fully characterize extensional rheological functions of discotic mesophases. The rheological analysis is used to put forth the relations between extensional viscosities, and the classical mesophase fiber textures.

Chapter 6 presents comprehensive analysis of microstructure response of sheared discotic mesophases in the presence of curvature elasticity in different planar surface anchorings. Four different microstructure modes, steady state and periodic, are shown to be stable. It is shown that the bulk molecular orientation is along the velocity gradient direction irrespective of the surface anchorings. Novel scaling laws relating the microstructure mode domains with the Frank elasticity are presented. This chapter puts forth a systematic study of flow induced microstructural behavior of discotic mesophases,

and provides a useful fundamental understanding of the flow of discotic mesophases of use in the processing of carbonaceous mesophases.

In chapter 7 the microstructural response of sheared discotics subjected to mixed boundary conditions, equivalent of that in a hybrid aligned nematic (HAN) cell, is computed. The strong surface anchorings at the bottom and the top plate corresponds to the stable orientation configuration. A novel model of continuous generation of defect-like structures in the bulk is discovered, and is due to asynchronous rotational kinematics. The simulation results are used to put forth the generation of more complex fiber textures, such as mixed texture (radial core with onion exterior), and skin-core textures observed during processing of a carbonaceous mesophase.

Chapter 8 presents the thesis conclusions and original contributions to knowledge.

Bibliography

R. Alben, *Phys Rev Lett* **30** 778 (1973).

R. Bacon, L.C. Nelson, L.S. Singer, D.A. Schulz, G. Wagoner, I.C. Lewis, R.T. Lewis, S.L. Strong, B.W. Rosen, and B.J. Sullivan, "Spacecraft applications for carbon-carbon—Basic research effort", Naval Surface Warfare Center Transcript 89-168, Silver Spring, MD (1989).

J.D. Brooks, and G.H. Taylor, *Carbon* **3**(2) p185 (1965); *Nature* **206** 697 (1965).

M. Buechler, C.B. Ng, and J.L. White, Extended Abstractof the 16th Biennial Conference on Carbon, San Diego, CA (1983).

S. Chandrasekhar, "Liquid Crystals", 2nd edition, *Cambridge University Press*, Cambridge (1992).

S. Chandrasekhar, B.K. Sadashiva, and K.A. Suresh, *Pramana* **9** 471 (1977).

S. Chwastiak and I.C. Lewis, "Solubility of mesophase pitch", *Carbon* **16**(2) 156 (1978).

G.W. Collet and B. Rand, "Rheological investigation of coal tar pitch during its transformation to mesophase", *Fuel* **57** 162 (1978a).

G.W. Collet and B. Rand, "Thixotropic changes occuring on reheating a coal tar pitch containing mesophase", *Carbon* **16** 477 (1978b).

J. Daji and B. Rand, *23rd Bienniel conference on Carbon*, p184 (1997)

C. Destrade, M.C. Mondon, and J. Malthete, *J Physique France* **40** 3 (1979).

C. Destrade, M.C. Mondon, and J. Malthete, *Mol Cryst Liq Crys* **71** 111 (1981).

R.J. Diefendorf and D.M. Riggs, "Forming optically anisotropic pitches", U.S. Patent 4,208,267 (1980).

J.C. Dubois, *Ann Phys* **3** 131 (1978).

D.D. Edie and M.G. Dunham, "Melt-spinning pitch based carbon fibers", *Carbon* **24**(4) 477 (1986).

D.D. Edie, N.K. Fox, B.C. Barnett, and C.C. Fain, "Melt spun non circular carbon fibers", *Carbon* **24** 477 (1986).

D.D. Edie and E.G. Stoner, "The effect of microstructure on shape and carbon fiber properties", in *carbon-carbon materials and composites*, Editors: J.D. Buckley and D. D. Edie, Noyes, Park Ridge, NJ p41 (1993).

M. Endo, "Structure of mesophase pitch-based carbon fibers", *J Mat Sci* **23**(2) 598 (1988).

D.B. Fischbach, "The kinetics and Mechanism of Graphitization", Chemistry and Physics of carbon, Volume **7**, Editor: P.L. Walker, Marcel Dekker Inc., New York, p1 (1971).

J.D. Fitz Gerald, G.H. Taylor, and G.M. Pennock, "Microstructure of hydrogenated coal tar pitches", *Carbon '94*: Proceedings of International Carbon Conference, Granada, Spain, p16 (1994).

E. Fitzer, D. Kompalik, and B. Mayer, "Influence of additives on pyrolysis of mesophase pitch", *Carbon '86*: Proceedings of International Carbon Conference, Baden-Baden, Germany, p842 (1986).

E. Fitzer, D. Kompalik, and K. Yudate, "Rheological characteristics of coal tar pitches", *Fuel* **66** 1504 (1987).

O. Fleurot, "The viscoelastic flow behavior of pitches", Ph.D. dissertation, Clemson University, Clemson, SC, USA (1998).

O. Fleurot and D.D. Edie, "Steady and transient rheological behavior of mesophase pitches", *J Rheo* **42**(4) 781 (1998).

R. Fujiura, T. Kojima, Y. Korai, and I. Mochida, *Carbon '92*: Proceedings of International Carbon Conference, Essen, Germany (1992).

H. Gasparoux, *Mol Cryst Liq Cryst* **63** 647 (1981).

T. Hamada, T. Nishida, Y. Sajiki, and M. Matsumoto, "Structure and physical properties of carbon fibers from coal tar mesophase pitch" *J Mat Res* **2**(6) 850 (1987).

T. Hamada, T. Nishida, M. Furuyama, and T. Tomioka, "Transverse structure of pitch fiber from coal tar mesophase pitch" *Carbon* **26**(6) 837 (1988).

M. Hamaguchi and T, Nishizawa, "Fused state ^{13}C NMR study on carbonaceous mesophase: orientational order and molecular motions of several aromatic compounds dissolved in carbonaceous mesophase", *Carbon '92*: Proceedings of International Carbon Conference, Essen, Germany, p45 (1992).

H. Honda, *Mol Cryst Liq Cryst* **94** 97 (1983).

K.W. Hutchenson, J.R. Roebers, and M.C. Thies, "Fractionation of petroleum pitch by supercritical fluid extraction", *Carbon* **29**(2) 215 (1991).

B.T. Kelly, "The effect of defects on the Basal Plane thermal conductivity of a graphite crystal", *Carbon* **5**(3) 247 (1967).

Y. Korai, M. Nakamura, and I. Mochida, "mesophase pitch prepared from methylnaphthalene by the aid of HF/BF_3", *Carbon* **29**(5) 561 (1991).

I.M. Kowalsky, "New high performance domestically produced carbon fibers", Advanced Materials Technology '87: Volume 32 of the International SAMPE Symposium, Editors: R. Calrson *et al.*, Anaheim, p953 (1987).

A.M. Levelut, *J Chem Phys* **88** p149 (1983).

I.C. Lewis, "Thermotropic mesophase pitch", *Carbon* **16**(6) p503 (1978).

M. Matsumoto, "Mesophase pitch and its carbon fibers", *Pure and Appl Chem* **57**(11) p1553 (1985).

J.J. McHugh and Edie, "Orientation of mesophase pitch in capillary and channel flows", *Liq Cryst* **18** p327 (1995).

J.J. McHugh, "The development of orientation in Mesophase pitch during fiber formation", Ph.D. dissertation, Clemson university, Clemson, SC, USA (1994).

I. Mochida, S. Shimizu, Y. Korai, Y. Otsuke, H. Sakai, and S. Fujiyama, "Structure and carbonization properties of pitches produced catalytically from aromatic hydrocarbons with HF/BF_3", *Carbon* **26**(6) 843 (1988).

I. Mochida, S. Shimizu, Y. Korai, Y. Otsuke, H. Sakai, and S. Fujiyama, "Preparation of mesophase pitch from aromatic hydrocarbons by the aid of HF/BF_3", *Carbon* **28**(2) 311 (1990).

I. Mochida, S.H. Yoon, and Y. Korai, "Control of transverse texture in circular mesophase pitch based carbon fiber using non-circular spinning nozzle", *J Mat Sci* **28** 2331 (1993).

F.F. Nazeem, "Flow of molten mesophase pitch", *Carbon* **20**(4) 345 (1982).

F.F. Nazeem "Process for controlling the cross-sectional structure of mesophase pitch derived fibers" U.S. Patent 4,376,747 (1983).

F.F. Nazeem "Apparatus for controlling the cross-sectional structure of mesophase pitch derived fibers" U.S. Patent 4,480,977 (1984).

S. Otani and A. Oya, "Process of pitch-based carbon fibers in Japan", *ACS Symp Ser* **303**(22) 323 (1986).

S. Otani, *Mol Cryst Liq Cryst* **63** 249 (1981).

L.H. Peebles, "Carbon fibers: formation, structures and properties", *CRC Press*, Boca Raton, USA (1994).

E.B. Priestley, P.J. Wojtowicz, and P. Sheng, "Introduction to Liquid Crystals", *Plenum Press*, New York (1975).

A.D. Rey, 62nd Annual Meeting of Society of Rheology, New Mexico (1990).

A.D. Rey, ""Elasticity driven texture selection mechanism in mesophase carbon fibers", *Phys Rev E* **51** 6278 (1995).

L.S. Singer, *Carbon* **16** 413 (1971).

L.S. Singer, "Process of producing orientation in mesophase pitch by rotational motion relative to a magnetic field and carbonization of the oriented mesophase" U.S. Patent 3,991,170 (1976).

L.S. Singer, "High modulus high strength fibers produced from mesophase pitch" U.S. Patent 4,005,183 (1977).

L.S. Singer, "Ind. Conv.of Coal and Carbon to Gas, Liquid, and Solid Products" London, (1981).

L.S. Singer, *Fuel* **60** 839 (1981a).

L.S. Singer, *Faraday Discuss* **79** 265 (1985).

A.P. Singh and A.D. Rey, "Computer simulation of dynamics and morphology of discotic mesophases in extensional flows", *Liq Cryst* **18** 219 (1995).

E.G. Stoner, D.D. Edie, and J.M. Kennedy, "Mechanical properties of non circular pitch based carbon fibers", *High Temp High Press* **22** 299 (1990).

M. Turpin, B. Rand, and T. Cheung, "Rheological characterization of mesophase pitch precursors for carbon fibers" *Carbon'92*: Proceedings of International Carbon Conference, Essen, Germany, p825 (1992).

G. Vertogen, and W.H. deJeu, "Thermotropic Liquid Crystals", *Springer-Verlag*, Berlin, Heidelberg, (1988).

L. Wang and A.D. Rey, "Pattern selection mechanism in mesophase carbon fibers", *Modelling Simul Sci Eng* **5** 67 (1997).

J.L. White, G.L. Guthrie, and J.O. Gardner, "Mesophase microstructures in carbonized coal-tar pitch" *Carbon* **5**(5) 517 (1967).

Y. Yamada, H. Fujii, and M. Takayanagi, "The relationship between structure and viscosity of petroleum pitch in the process of mesophase formation", *J mat Sci* **21** 4067 (1987).

S.-H. Yoon, Y. Korai, and I. Mochida, "Spinning characteristics of mesophase pitches derived from naphthalene and methylnaphthalene with HF/BF_3", *Carbon* **31**(6) 849 (1993).

J.E. Zimmer and J.L. White, "Advances in liquid crystals", Volume **5**, Editor: H.G. Brown, Academic Press, New York, 157 (1982).

PLC, CWRU (2000), Polymer and Liquid Crystals Website, Case Western Reserve University, http://abalone.cwru.edu/tutorial/enhanced/main.htm.

[1]CHAPTER 2

Microstructure Constitutive Equation for Discotic Nematic Liquid Crystalline Materials

Part I: Selection Procedure and Shear Flow Predictions

This chapter focuses on formulation and selection of microstructure constitutive equation (CE) of discotic mesophases. Well-established theories for rod-like nematics are adopted and modified for model discotic mesophases. The CEs are subjected to homogeneous simple shear flows, and their steady state, and dynamical microstructural response are computed. An iterative selection criterion is employed to select the most appropriate CE for discotic mesophases by performing exhaustive bifurcation analysis and dynamic simulations. Bifurcation methods are employed to analyze the complex interactions among various orientation regimes (stable and unstable) as predicted by each CE. The dynamic simulations are performed to characterize the stable microstructure features of the CEs. The selected CE is able to capture all the experimental features and is consistent with the theoretical results, and will be used to develop the fundamental understanding of rheology of discotic mesophases in general and that of carbonaceous mesophase pitches in particular.

---

[1] This chapter appeared as an original article in *Rheological* Acta **37**(1) p30-45 (1998).

2.0 Abstract

Four different microstructure constitutive equations (CEs) for discotic nematic liquid crystals based on Doi's modified nematodynamics theory are formulated. Their dynamic and steady state responses under simple shear flows are computed and analyzed in terms of the tensor order parameter **Q**, the orientation director triad (**n**, **m**, **l**), and the uniaxial S and biaxial P alignments. A unit sphere description of the director triad is used to characterize and classify the various predicted stable orientation states, and to discuss and analyze their multi-stabilities as a function of dimensionless shear rate. Various attractors, steady and periodic, are also identified and their stability is discussed in detail for all the CEs. A validation procedure based on the predicted microstructural response along with bifurcation diagrams of the individual CE and representative experimental observations as well as theoretical results is implemented, and used to select the most appropriate CE. The selected CE predicts, under shear, the simultaneous presence of stable in-plane (steady and periodic) states and out-of-plane steady state, and the classical transition among the in-plane periodic and steady states with increasing shear rate. The excellent performance of the selected CE in shear flows strongly suggests that it is a reliable contribution towards the formulation of a process model for mesophase pitch spinning.

2.1 Introduction

Carbonaceous mesophases or mesophase pitches are obtained from natural (petroleum or coal tar pitches) or synthetic feed stock (naphthalene), and are used in the manufacture of high performance mesophase pitch-based carbon fibers (Zimmer and White, 1982; Singer, 1985; McHugh and Edie, 1996). The mesophase carbon fibers show outstanding stiffness and thermal transport properties due to their ability to develop extended graphitic structures. The physical properties of high performance fibers are mainly due to the molecular orientation developed during the spinning process (McHugh, 1994).

These precursor mesophase pitches consist of flat poly-aromatic molecules that adopt a uniaxial thermotropic discotic nematic liquid crystalline phase (Chandrasekhar 1981; Destrade et al., 1981). The flat disc-like molecules orient more or less along a common direction (see Figure 2.1), represented by the (uniaxial) director $\mathbf{n}$; in what follows we use $\mathbf{n}$ and uniaxial orientation interchangeably (deGennes, 1975). The average degree of alignment of unit normals to the discs along the director $\mathbf{n}$ is defined by the (uniaxial) scalar order parameter S; in what follows we use S and uniaxial alignment interchangeably. The inherent nature of liquid crystalline materials to acquire a preferred orientation in the presence of flow provides a natural advantage to these materials to be used as precursors for the manufacturing of high performance fibers (e.g. mesophase pitch-based carbon fibers, Kevlar). In the spinning of mesophase carbon fibers the preferred orientation is achieved as the precursor material passes through the spin-pack where it is subjected to non-homogeneous mixed shear and extensional flows. The extensional flows during fiber drawing only accentuates the already attained orientation in the spinneret in a plane normal to the fiber axis (McHugh, 1994).

The preferred orientation and degree of alignment of the disk-like molecules, and the average crystallite size are expected to have a predominant effect on all mechanical and thermal properties. The optimization and control of preferred orientation hence is of practical importance. Unfortunately, the fundamental understanding of the factors that affect the development of preferred orientation in mesophase carbon fibers is currently lacking, and is hindering their further development. One cost effective way to develop this understanding is through the use of modeling and simulation by adopting the well developed theories for liquid crystalline polymers (LCPs). The transfer of knowledge by adopting the theories for conventional rod-like nematics to discotic nematics is successfully demonstrated by Farhoudi and Rey (1993a), Rey (1995a), and Singh and Rey (1994, 1995a, 1995b).

The classical theories for describing the rheology of LCPs are the Leslie-Ericksen (L-E) continuum theory and Doi's molecular theory for mono-domain LCPs. Doi's theory has fewer parameters and is shown to predict satisfactorily the steady state shear and extensional rheology (Ooi and Sridhar, 1994). There exists a lot of theoretical work,

based on the above mentioned theories, on modeling the flows of conventional rod-like nematics (Doi and Edwards, 1986; Larson, 1988; Marrucci and Greco, 1993; Beris and Edwards, 1994). However, these theories have not been used in a significant way to model discotic nematic flows; and currently there is no appropriate constitutive equation that can describe the flow-induced microstructure of discotic nematics in general, and that of mesophase pitches in particular. In the present work we will adopt well established Doi's mesoscopic theory as a starting point and modify it to establish the most suitable constitutive equation for mesophase pitches. Next we present a summary of the theoretical work performed in modeling the microstructural response of discotics along with the essential features that are used to transfer the theoretical knowledge from rod-like nematics to discotic nematics.

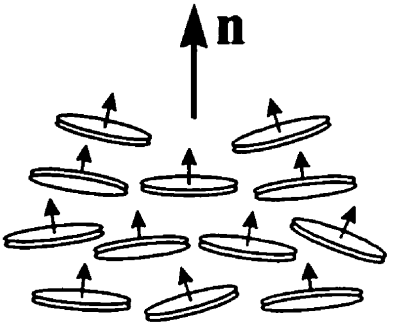

Figure 2.1: Definition of uniaxial director **n** orientation of a discotic nematic liquid crystalline material. The uniaxial director **n** is the average orientation of the unit normals to the disc-like molecules.

The previous work of Volovik (1980), Carlsson (1982, 1983), Baals and Hess (1988), and Ho and Rey (1991) on the rheology and flow-induced orientation of uniaxial discotic nematics (DNs) assumed that the scalar order parameter S remains unaffected by the induced flow. The validity of this assumption for low molecular weight materials justifies the use of Leslie-Ericksen (L-E) theory (Leslie, 1979; deGennes, 1975; Chandrasekhar, 1992) for uniaxial nematics with the proper values of the materials parameters. The important difference in sign and magnitude of the material parameters corresponding to the uniaxial rod-like and discotic nematics arises from the fact that the rod-like nematics orient their longest molecular dimension along the director whereas

discotic nematics orient their shortest dimension along the director. The orienting properties of the uniaxial nematics subjected to shear flows are governed by the sign and magnitude of the uniaxial tumbling (reactive) parameter λ such that for aligning (non-aligning) rods $\lambda > 1$ ($0 < \lambda < 1$), and for aligning (non-aligning) discs $\lambda < -1$ ($-1 < \lambda < 0$). The uniaxial tumbling parameter λ is given by the negative ratio of the irrotational torque coefficient (γ_2) and the rotational viscosity (γ_1), and represents the ratio of strain to the vorticity torques acting on the uniaxial director **n** (deGennes, 1975). Previous works by Carlsson (1982, 1983) focus on the orienting properties of the aligning uniaxial discotic nematics in shear, and that of Ho and Rey (1991) on Hamel flows. In these works, it was found that shear orients the director in the shear plane and at a steady angle θ_n, lying in the $90° \leq \theta_n \leq 135°$ sector with respect to the flow direction, while extension orients the director anywhere in a plane normal to the flow direction. Farhoudi and Rey (1993a) focused on the orienting properties of non-aligning uniaxial discotic nematics in steady simple shear flows in which they showed that the uniaxial director **n** tumbles, oscillates or aligns according to the strength of the applied shear; the existence and transition between the various regimes is shown to be similar to that predicted by molecular theories of the rod-like nematics. In steady uniaxial extensional flows, the orienting behavior of uniaxial nematics is again determined by the sign of λ: when $\lambda > 0$ the director aligns along the stretching direction, and when $\lambda < 0$ the director aligns somewhere in the compression plane, orthogonal to the stretching direction (Ho and Rey, 1991; Singh and Rey, 1994, 1995a, 1995b). In a previous work (Singh and Rey, 1994) the authors developed, from variational principles, a model for discotic nematics that takes into account variable alignment, and applied the model to a series of extensional flows such as uniaxial, equi-biaxial and planar extensional flows. It was found that the director aligns anywhere in a plane perpendicular to the extension direction (i.e., anywhere in the plane of uniform compression) under uniaxial extensional flows, along compression direction in biaxial, and planar extensional flows, and the director trajectories and steady states exhibit strong sensitivity with the initial director orientation (Singh and Rey, 1994, 1995a).

The main objective of this work is to develop a constitutive equation for the idealized uniaxial discotic nematics that is consistent with the existing predictions of molecular and macroscopic theories for the rod-like nematics, and that is in qualitative agreement with the experimental observations. The particular objectives of this paper are:

1. To formulate a set of generic constitutive equations (CEs) for discotic nematics,
2. To characterize the main microstructure features predicted by the various proposed CEs in terms of uniaxial orientation dynamics,
3. To identify the various multi-stabilities of uniaxial orientation dynamics predicted by various CEs under shear flows,
4. To select the most suitable CE based on the computed microstructure behavior that reproduces with sufficient accuracy the experimentally observed behavior of representative discotics, and that is consistent with previous theoretical predictions.

The organization of this paper is as follows. In the following section we present the selection criteria for establishing the most suitable CE for mesophase pitches. Then we define the coordinate system, the state variables, the shear flow, and briefly present the elements of unit sphere description used to characterize the bifurcation and dynamic results. In the same section, we present representative schematics of the main microstructure phenomena in terms of uniaxial director **n** that are used to characterize the predicted bifurcational and dynamical phenomena, followed by the various proposed CEs and a brief description of the solution methods employed to solve them. Next, we present the computed bifurcation results for each CE and employ the validation and selection criteria to select the most appropriate microstructure CE. Subsequently, the main features of dynamic results of orientation and alignment (uniaxial and biaxial) are presented and summarized. Finally, the conclusions are given.

2.2 Selection Procedure

As mentioned before in the present study we adopt well established theories for rod-like nematics and modify them for discotic nematics. In this paper we propose and

select a CE using an iterative selection process that starts with a series of CEs and ends with the selection of the one that meets a set of criteria. The criteria are based on: (1) consistency with previous theoretical results; (2) consistency with experimental data; and (3) simplicity. In this iterative process we propose a CE, investigate the predicted orientation (microstructure) phenomena under simple shear flows, validate the computed results with the existing classical theoretical and experimental results available in the literature, and select the CE that best meets the criteria. If the simulated results of the proposed CE fail to satisfy the criteria it is then modified and tested again. In this iterative process we start with the simplest available CE for discotics which is derived from Doi's mesoscopic theory and was investigated by Rey (1995a) for extensional flows.

The theoretical results of classical molecular, and macroscopic theories for conventional rod-like nematics are employed to check the consistency of the CEs. The simulated results of modified macroscopic theories for DNs (Farhoudi and Rey, 1993a) are also used to check the validity of the simulated results of the proposed CEs. It is well established that the necessary uniaxial director $\mathbf{n}$ orientation features of the non-aligning nematics under shear are: rotation of $\mathbf{n}$ in the shear plane or in-plane tumbling (ITO), oscillation of $\mathbf{n}$ in the shear plane or in-plane wagging (IWO), and stationary orientation of $\mathbf{n}$ in the shear plane or in-plane steady states (ISS); along with the smooth transition ITO $\rightarrow$ IWS $\rightarrow$ ISS with increasing shear rate (Larson and Ottinger, 1991; Farhoudi and Rey, 1993a, b).

The experimental results for representative discotic nematics and mesophase pitches are used to test the predicted simulation results of CEs. Hammouda et al. (1995) showed that the disc-like molecules of discotic nematics, subjected to shear flows, orient their unit normals along the velocity gradient or the vorticity directions. In a recent study on the development of microstructure of mesophase pitches in narrow channels, McHugh and Edie (1996) reported that very close to the channel walls the preferred orientation of discotic mesophase pitches is along the vorticity axis (see Figure (4, 9) of McHugh and Edie, 1996).

The mesophase carbon fibers derived from the discotic mesophase pitches show a spectrum of textures as a function of materials properties, processing conditions, and/or

geometry which are consistent with the ISS, LRS (in which **n** aligns along the neutral/vorticity direction) and ITO orientation modes. The consistency between fiber textures and the predicted orientation modes will be explained thoroughly in chapter 4. Therefore the most suitable microstructure CE for discotic mesophase pitches should predict, when subjected to shear flows, all the essential orientation features (ITO, ISS, and LRS) over an appropriate range of parameters. Moreover, there exists multiplicity in textures of mesophase pitch-based carbon fibers for the same set of processing conditions (see Otani and Oya, 1986). Hence an essential requirement for a CE that can be used to describe the microstructure features in mesophase pitches is prediction of multi-stabilities. One way to capture and characterize the multi-stabilities of the simulated microstructures and their transitions is through bifurcation methods, as is explained and employed in nematic flows by Farhoudi and Rey (1993b), Rey (1995a, b) and Maffettone and Crescitelli (1995). Thus the most appropriate CE equation for mesophase pitches must show the bifurcation phenomena that are reported in the real spinning process that is used to manufacture mesophase-based carbon fibers.

2.3 Theory and Governing Equations

2.3.1 Definition of Coordinates, Kinematics, Orientation and Alignment

In this paper we study the spatially uniform microstructural response (dynamic and steady state) of model uniaxial discotic nematics (DNs) subjected to a steady simple shear flow, of known and constant shear rate $\dot{\gamma}$. The microstructure of the DNs is characterized by a second order tensor, known generally as tensor order parameter **Q**:

$$\mathbf{Q} = S\left(\mathbf{nn} - \tfrac{1}{3}\boldsymbol{\delta}\right) + \tfrac{1}{3}P(\mathbf{mm} - \mathbf{ll}) \tag{2.1a}$$

where the following restrictions apply:

$$\mathbf{Q} = \mathbf{Q}^{\mathrm{T}};\quad tr(\mathbf{Q}) = 0;\quad -\tfrac{1}{2} \le S \le 1;\quad -\tfrac{3}{2} \le P \le \tfrac{3}{2} \tag{2.1b,c,d,e}$$

$$\mathbf{n}\cdot\mathbf{n} = \mathbf{m}\cdot\mathbf{m} = \mathbf{l}\cdot\mathbf{l} = 1 \;; \quad \mathbf{nn} + \mathbf{mm} + \mathbf{ll} = \delta = \begin{bmatrix} 1 & 0 & 0 \\ 0 & 1 & 0 \\ 0 & 0 & 1 \end{bmatrix} \tag{2.1f,g}$$

The uniaxial director **n** corresponds to the maximum eigenvalue $\frac{2}{3}S$, the biaxial director **m** corresponds the second largest eigenvalue $-\frac{1}{3}(S-P)$, and the second biaxial director **l** ($=\mathbf{n}\times\mathbf{m}$) corresponds to the smallest eigenvalue $-\frac{1}{3}(S+P)$. The orientation is defined completely by the orthogonal director triad (**n**, **m**, **l**). The magnitude of the uniaxial scalar order parameter S is a measure of the molecular alignment along the uniaxial director **n**, and is given as $S=\frac{3}{2}(\mathbf{n}\cdot\mathbf{Q}\cdot\mathbf{n})$. The magnitude of the biaxial scalar order parameter P is a measure of the molecular alignment in a plane perpendicular to the direction of uniaxial director **n**, and is given by $P=\frac{3}{2}(\mathbf{m}\cdot\mathbf{Q}\cdot\mathbf{m}-\mathbf{l}\cdot\mathbf{Q}\cdot\mathbf{l})$. On the principal axes, the tensor order parameter **Q** is represented as:

$$\mathbf{Q} = \begin{bmatrix} -\frac{1}{3}(S-P) & 0 & 0 \\ 0 & -\frac{1}{3}(S+P) & 0 \\ 0 & 0 & \frac{2}{3}S \end{bmatrix} \tag{2.2}$$

Details on uniaxial and biaxial scalar order parameters and their interrelations are given in (Singh and Rey, 1995b). Both S and P are positive for normal disc-like uniaxial nematic liquid crystals, and this study is restricted to normal discotic nematics.

Figure 2.2(a) is the schematic representation of the steady shear flow. The flow direction is along the x-axis, the velocity gradient direction is along the y-axis, and the vorticity axis (neutral axis) is along the z-axis. To visualize and analyze the individual director (**n**, **m**, **l**) behavior, we parametrize them as follows (see Figure 2.2b):

$$\mathbf{a} = (a_x, a_y, a_z) = (\sin\phi_a\cos\theta_a, \sin\phi_a\sin\theta_a, \cos\phi_a) \tag{2.3a}$$

where **a** (= **n**, **m**, **l**) is a unit vector. We use this parametrization to present the results of uniaxial (**n**) and biaxial (**m**, **l**) directors in a simple and direct way. However, the directors (**n**, **m**, **l**) form a right hand triad, and equations (2.1f, g) hold. This parametrization is shown in Figure 2.2(b), where $\theta_a (0 \le \theta_a \le 2\pi)$ is the azimuthal angle

and $\phi_a (0 \le \phi_a \le \pi)$ is the polar angle defining the unit vector **a**. In terms of angles, the equator lies in the shear plane and is given as $(\theta_a, \phi_a) = \left([0, 2\pi], \pm \pi/2\right)$, and the north pole and the south pole are located on the vorticity axis and are given as $\phi_a = 0$ and $\phi_a = \pi$ respectively. In the unit sphere description the tip of each director lies on the surface of unit sphere, and defines a trajectory in the presence of flow. In what follows all angles are reported in degrees.

To characterize the various stable orientation states predicted by the various CEs (presented below), the dynamics of the uniaxial director **n** will be employed. Figure 2.3 shows the representative schematics of the stable dynamics (steady as well as periodic) of the uniaxial director **n**, under homogeneous simple shear flow, and gives a complete classification of all the relevant states to the four CEs, discussed below. Figure 2.3 consists of two column, the left one contains in-plane states (i. e., $n_z = 0$) and the right one the out-of-plane states (i. e., $n_z \neq 0$). The schematic at the top shows the representative shear plane and vorticity axis with regard to the unit sphere. The six stable orientation states are: (a) ITO(1) or in-plane tumbling orbit, (b) IWS(2) or in-plane wagging state, (c) ISS(2) or in-plane steady state, (d) LRS(2) or log rolling state, (e) KO(2) or kayaking orbit, and (f) PDO(4) or period doubling orbit. The representative schematics for the stable biaxial orientations, **m** and **l**, are not shown in Figure 2.3. The number in the parenthesis accompanying the stable state name represents the number of equivalent states that exist for a particular set of parameters due to the inherent equivalence of the uniaxial director in spatially homogeneous flows: $\mathbf{n} = -\mathbf{n}$.

The top-left schematic represents the in-plane tumbling orbits (ITO) in which the uniaxial director **n** tumbles (rotates) on the equator (shear plane). The middle-left schematic shows the in-plane wagging (oscillatory) states (IWS), in which **n** oscillates around a point near y-axis (velocity gradient direction). The uniaxial director **n** oscillates inside the regions ($-45° < \theta_n < -135°$) and ($45° < \theta_n < 135°$). There are two equivalent IWS for **n**, one near positive and the other near negative direction of y-axis (velocity gradient direction). The bottom-left schematic represents the in-plane steady state (ISS) in which the stable steady state of **n** is close to the y-axis (velocity gradient direction). A

detailed analysis of ITO, IWS and ISS, in terms of uniaxial director **n** and uniaxial scalar order parameter S, for discotic mesophases under shear flow is given by Farhoudi and Rey (1993). Biaxiality effects, in terms of (**m**, **l**) and P, are discussed briefly later on in this paper.

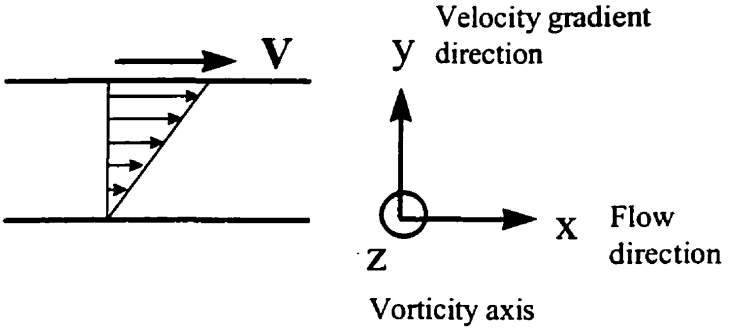

(a)

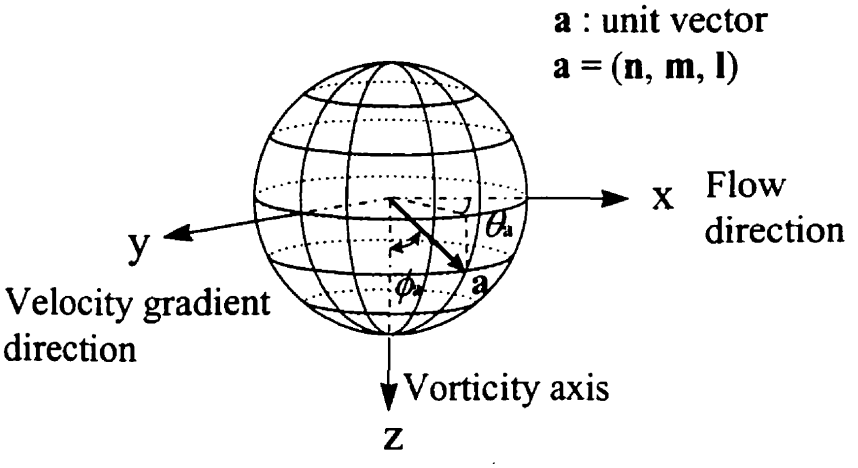

(b)

Figure 2.2: (a) Definition of rectilinear shear flow deformation, (b) coordinate system. (a) x-axis is the flow direction, y-axis is the velocity gradient direction, and z-axis (normal outwards to the plane of paper) is the neutral (vorticity) direction. (b) Unit vector angle and unit sphere description: unit vector **a** is completely defined by the azimuthal angle $\theta_a (0 \le \theta_a \le 2\pi)$ and polar angle $\phi_a (0 \le \phi_a \le \pi)$. In terms of unit vector angles, the equator lies in the shear plane and is given as $(\theta_a, \phi_a) = \left([0,2\pi] \ \pm \pi/2\right)$, and the north pole and the south pole are located on the vorticity axis and are given as $\phi_a = 0$ and $\phi_a = \pi$ respectively.

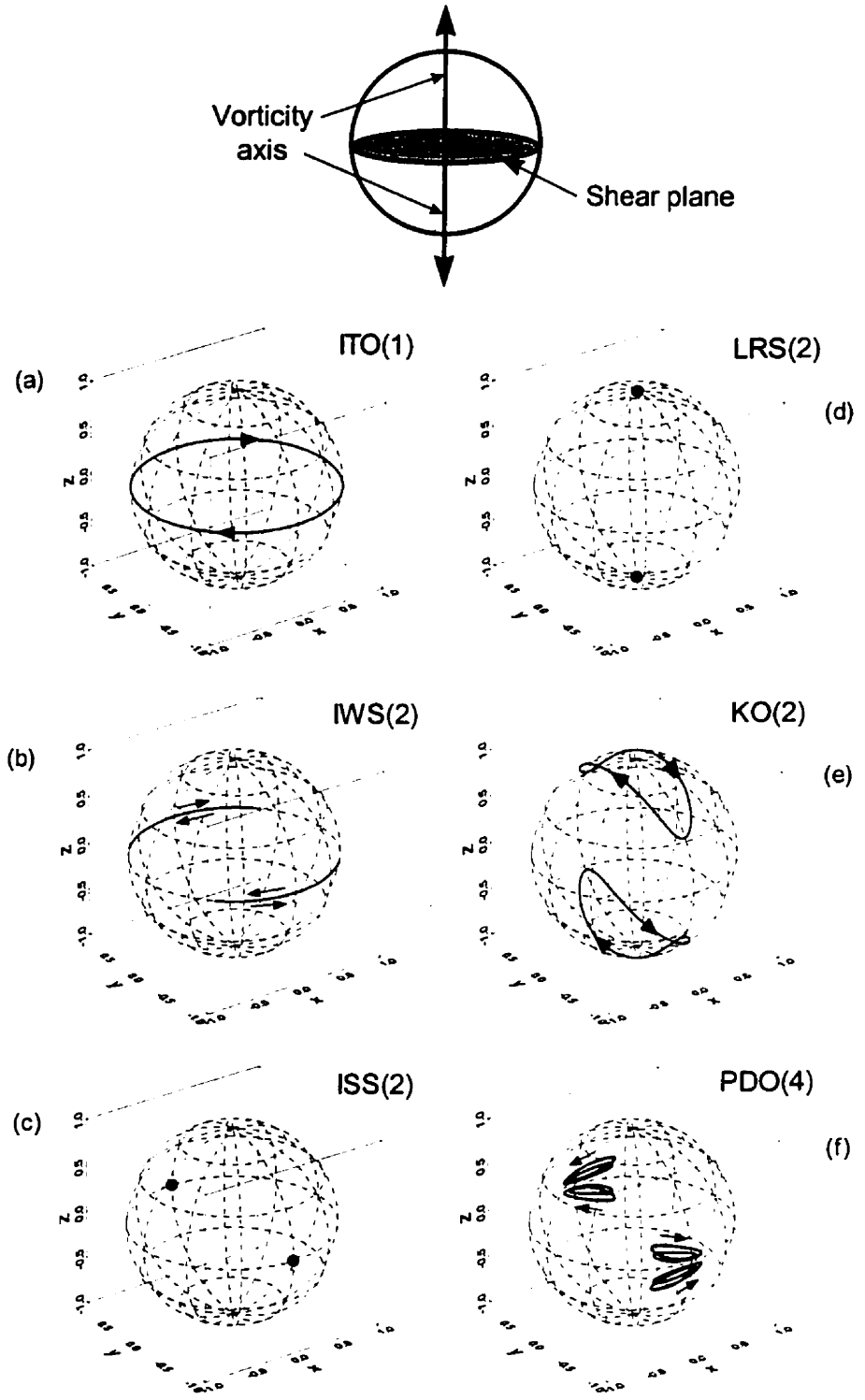

Figure 2.3: The representative schematics of the stable states of uniaxial orientation **n** of DNs under homogeneous simple shear flow predicted by the various CEs. The top schematic shows the representative shear plane and vorticity axis with regard to the unit sphere. The six stable orientation states are: (a) ITO(1) or in-plane tumbling orbit, (b) IWS(2) or in-plane wagging state, (c) ISS(2) or in-plane steady state, (d) LRS(2) or log rolling state, (e) KO(2) or kayaking orbit, and (f) PDO(4) or period doubling orbit. For details see text.

The top-right schematic shows the two LRS (Larson and Öttinger, 1991) in which the uniaxial director **n** is aligned along the vorticity axis. The middle-right schematic represents the out-of-plane tumbling orbits named Kayaking Orbits (KO) by Larson and Öttinger (1991). In this periodic state **n** rotates around the vorticity axis on the surface of the unit sphere in a close out-of-plane orbit such that the orbit stretches more towards the shear plane near the velocity gradient direction than along the flow direction (see Figure 2.3e). The bottom-right schematic represents the stable out-of-plane period doubling orbits (PDO), in which **n** traverses trajectories, which are eccentric to the vorticity axis. In one complete orbit the trajectory crosses itself. These stable PDOs emerge from the shear plane and move away from it with the increase of the flow strength. More details regarding the LRS, KO and PDO are presented in the section entitled dynamic simulations.

2.3.2 Governing Equations

The microstructure response of liquid crystalline polymers, as given by Doi's mesoscopic nematodynamic theory, is found to be (Doi and Edwards, 1986):

$$\hat{\mathbf{Q}} = \mathbf{F}(\mathbf{Q}, \nabla\mathbf{v}) + \mathbf{H}(\mathbf{Q}) \tag{2.4}$$

where $\nabla\mathbf{v}$ is the velocity gradient tensor and $\hat{\mathbf{Q}}$ is the Jaunmann/corotational derivative of $\mathbf{Q}$ and is defined as:

$$\hat{\mathbf{Q}} = \frac{\partial \mathbf{Q}}{\partial t} + (\mathbf{v}\cdot\nabla)\mathbf{Q} - \mathbf{W}\cdot\mathbf{Q} + \mathbf{Q}\cdot\mathbf{W} \tag{2.5}$$

$\mathbf{F}(\mathbf{Q}, \nabla\mathbf{v})$ and $\mathbf{H}(\mathbf{Q})$ represent the flow contribution (macroscopic flow field) and the thermodynamic contribution (Brownian motion) respectively. Comprehensive reviews of many aspects of this equation, and its modifications and generalizations are available (Larson, 1988; Marrucci and Greco, 1993; Beris and Edwards, 1994).

In this paper we investigate the following four CEs for DNs:

CE-1: In the first CE for DNs, used by Rey (1995), the rotary diffusivity is assumed to be independent of $\mathbf{Q}$. The flow term, $\mathbf{F}_1(\mathbf{Q}, \nabla\mathbf{v})$, in CE-1 contains only a partial

contribution from $\mathbf{Q}^2$ terms, and all the terms of higher order than $\mathbf{Q}^2$ are neglected. The CE-1 is given as follows:

$$\hat{\mathbf{Q}} = \mathbf{F}_1(\mathbf{Q}, \nabla\mathbf{v}) + \mathbf{H}(\mathbf{Q}) \tag{2.6}$$

where flow and thermodynamic contribution are given as:

$$\mathbf{F}_1(\mathbf{Q}, \nabla\mathbf{v}) = \tfrac{2}{3}\beta\mathbf{A} + \beta\left[\mathbf{A}\cdot\mathbf{Q} + \mathbf{Q}\cdot\mathbf{A} - \tfrac{2}{3}(\mathbf{A}:\mathbf{Q})\delta\right] - 2\beta(\mathbf{Q}:\mathbf{A})\mathbf{Q} \tag{2.7}$$

$$\mathbf{H}(\mathbf{Q}) = -6D_r\left[\left(1 - \tfrac{U}{3}\right)\mathbf{Q} - U\mathbf{Q}\cdot\mathbf{Q} + U\left\{(\mathbf{Q}:\mathbf{Q})\mathbf{Q} + \tfrac{1}{3}(\mathbf{Q}:\mathbf{Q})\delta\right\}\right] \tag{2.8}$$

where

$$\beta = \frac{p^2 - 1}{p^2 + 1}, \qquad p = \frac{r_\perp}{r_\parallel} \tag{2.9a,b}$$

D_r is the preaveraged diffusivity or isotropic rotary diffusivity independent of $\mathbf{Q}$, U is the nematic potential, and β is the shape factor. To specify the molecular geometry we approximate the disc-like shape of molecule of discotic mesophases with an oblate spheroid of aspect ratio p ($p < 1$) where $r_\parallel$ is the length of the shortest and distinct semiaxis, and $r_\perp$ the length of the two longest and equal semiaxes. The ideal flat disc corresponds to $p = 0$ ($\beta = -1$), and the sphere corresponds to $p = 1$ ($\beta = 0$). $\mathbf{A}$ and $\mathbf{W}$ are the rate of deformation and vorticity tensor respectively, and for the considered simple shear flow are given as:

$$\mathbf{A} = \tfrac{1}{2}\left(\nabla\mathbf{v} + \nabla\mathbf{v}^{\mathrm{T}}\right) = \frac{1}{2}\begin{bmatrix} 0 & \dot{\gamma} & 0 \\ \dot{\gamma} & 0 & 0 \\ 0 & 0 & 0 \end{bmatrix}, \tag{2.9c}$$

$$\mathbf{W} = \tfrac{1}{2}\left(\nabla\mathbf{v} - \nabla\mathbf{v}^{\mathrm{T}}\right) = \frac{1}{2}\begin{bmatrix} 0 & \dot{\gamma} & 0 \\ -\dot{\gamma} & 0 & 0 \\ 0 & 0 & 0 \end{bmatrix}. \tag{2.9d}$$

CE-2: The next modification uses a $\mathbf{Q}$ dependent rotary diffusivity, $\overline{D}_r$, which results in:

$$\hat{\mathbf{Q}} = \mathbf{F}_1(\mathbf{Q}, \nabla\mathbf{v}) + \mathbf{H}\left(\mathbf{Q}, \overline{D}_r(\mathbf{Q})\right) \tag{2.10}$$

where

$$\overline{D}_r = D_r \left[1 - \tfrac{3}{2} (\mathbf{Q}:\mathbf{Q}) \right]^{-2} \tag{2.11}$$

The flow contribution in CE-2 is the same as that in CE-1, and the modified thermodynamic contribution in CE-2 (eqn. (2.10)) is given as:

$$\mathbf{H}\left(\mathbf{Q}, \overline{D}_r(\mathbf{Q})\right) = -6\overline{D}_r\left[\left(1-\tfrac{U}{3}\right)\mathbf{Q} - U\mathbf{Q}\cdot\mathbf{Q} + U\left\{(\mathbf{Q}:\mathbf{Q})\mathbf{Q} + \tfrac{1}{3}(\mathbf{Q}:\mathbf{Q})\delta\right\}\right] \tag{2.12}$$

CE-3: In CE-3 the flow contribution is modified by including the full contribution of $\mathbf{Q}^2$ terms while in the thermodynamic contribution rotary diffusivity is assumed to be independent of $\mathbf{Q}$ (same as in CE-1), and is given by:

$$\hat{\mathbf{Q}} = \mathbf{F}_2(\mathbf{Q}, \nabla\mathbf{v}) + \mathbf{H}(\mathbf{Q}) \tag{2.13}$$

where the modified flow contribution is:

$$\begin{aligned}\mathbf{F}_2(\mathbf{Q}, \nabla\mathbf{v}) = {} & \tfrac{2}{3}\beta\mathbf{A} + \beta\left[\mathbf{A}\cdot\mathbf{Q} + \mathbf{Q}\cdot\mathbf{A} - \tfrac{2}{3}(\mathbf{A}:\mathbf{Q})\delta\right] - \\ & \frac{\beta}{2}\left[(\mathbf{A}:\mathbf{Q})\mathbf{Q} + \mathbf{A}\cdot\mathbf{Q}\cdot\mathbf{Q} + \mathbf{Q}\cdot\mathbf{A}\cdot\mathbf{Q} + \mathbf{Q}\cdot\mathbf{Q}\cdot\mathbf{A} - \left\{(\mathbf{Q}\cdot\mathbf{Q})\mathbf{A}\right\}\delta\right]\end{aligned} \tag{2.14}$$

CE-4: The fourth and final CE is similar to CE-3, however, the rotary diffusivity is assumed to a function of $\mathbf{Q}$. The CE-4 comprises of flow term as that in CE-3 and thermodynamic term as that in CE-2, and is given as:

$$\hat{\mathbf{Q}} = \mathbf{F}_2(\mathbf{Q}, \nabla\mathbf{v}) + \mathbf{H}\left(\mathbf{Q}, \overline{D}_r(\mathbf{Q})\right) \tag{2.15}$$

The flow contribution is not modified further to include higher order terms than $\mathbf{Q}^2$ as the original Doi's theory does not contain terms which would yield, on quadratic closure approximation, terms with order higher than $\mathbf{Q}^2$. Also, the curvature elastic effects (i.e., Frank elasticity) are neglected in the present investigation.

The CEs in the non-dimensional form along with the dimensionless parameters are given in Appendix A.

In this paper we analyze and evaluate the CEs using bifurcation analysis as employed by Farhoudi and Rey (1993b) and Rey (1995a, b). For bifurcation analysis of the CEs we use AUTO94©, a software for continuation and bifurcation analysis for

ordinary differential equations (Doedel et al., 1996). The equations solved are a set of five nonlinear coupled algebraic equations given by the right hand side of the ODEs (A.1 to A.4). The long time dynamic response (steady or periodic) was used for the continuation of stable branch(es), the unstable branches were traced by the subsequent continuation of the bifurcation points. For continuation the dimensionless shear rate or Peclet number, Pe, is used as the free parameter. The outputs from AUTO94© are the components of the steady state tensor order parameter $\mathbf{Q}_{ss}(Pe)$ which is transformed to principal form to determine its eigenvalues (to evaluate steady state alignments S_{ss} and P_{ss}) and eigenvectors or steady state orientations ($\mathbf{n}_{ss}$, $\mathbf{m}_{ss}$, $\mathbf{l}_{ss}$). As AUTO94© was unable to confirm the stability and sometimes the existence of some branches (periodic or steady), dynamic simulations are used to augment and confirm the bifurcation results obtained from AUTO94©. For dynamic simulations the set of time dependent dimensionless equations (presented in the Appendix A) are integrated using an implicit predictor-corrector first order Euler integration method with adaptable time step. The implicit predictor corrector method transforms the set of coupled nonlinear ordinary differential equations into a set of coupled nonlinear algebraic equations. The resulting algebraic equations are solved using the Newton-Raphson iteration scheme; the predictor step generates a first guess for iteration which forms the corrector step itself. The adopted convergence criteria is that the length of the difference vector between the calculated solution vectors corresponding to two successive iterations is less than 10^{-8}. The transient solution vector resulting from the numerical solutions consists of a set of five independent components of the tensor order parameter $\mathbf{Q}(t^*)$ as a function of dimensionless time $t^* = |6D_r|\, t$. The numerically obtained tensor order parameter $\mathbf{Q}(t^*)$ is subsequently transformed into the principal form, given by equation (2.2), to evaluate its eigenvalues and eigenvectors.

To compute the dynamic response of CEs, the model discotic nematics are assumed to be uniaxial ($P = 0$, and $\mathbf{m}, \mathbf{l} \rightarrow$ undefined; Singh and Rey, 1995b) prior to the imposition of the shear flow, and the initial conditions in the eigenvalue-eigenvector form are given as:

$$@t = 0: \quad \mathbf{n} = \mathbf{n}_0 ; \quad S = S_0 = S_{eq}(U) \tag{2.16}$$

where $S_{eq}(U)$ is the equilibrium uniaxial alignment of normal ($S > 0$) uniaxial nematic phase, given by Doi and Edwards (1986):

$$S_{eq} = \frac{1}{4} + \frac{3}{4}\sqrt{\left(1 - \frac{8}{3U}\right)} \tag{2.17}$$

For $U < 8/3$ the stable phase is isotropic, for $8/3 \leq U \leq 3$ there is biphasic equilibrium, and for the higher values of uniaxial nematic potential U the phase is uniaxial nematic. Higher values of U correspond to stronger uniaxial alignment. In this paper we use the following values of the parameters: $U = 6.0$, and $\beta = -0.8$. The range of initial uniaxial director orientation, $\mathbf{n}_0$, for the dynamic simulations performed in this work is: $0° \leq \theta_{n0} \leq 360°$, $5° \leq \phi_{n0} \leq 85°$.

2.4 Results and Discussion

This section describes and discusses the bifurcation and dynamic simulation results for the four CEs. This section is divided into two major subsections: bifurcation phenomena, and dynamic simulations; the former is further subdivided into four parts, one for each CE. In each part we present the computed bifurcation diagrams of the tensor order parameter $\mathbf{Q}_{ss}$ as a function of Pe. To facilitate the discussion the eigenvalues and eigenvectors of the $\mathbf{Q}_{ss}$ are computed; the eigenvalues of $\mathbf{Q}_{ss}$ are used to calculate S_{ss} and P_{ss}, and the eigenvectors ($\mathbf{n}_{ss}$, $\mathbf{m}_{ss}$, $\mathbf{l}_{ss}$) are used to distinguish between the various stable states predicted by the bifurcation computations for each CE. The following conventions are used to plot the bifurcation results: solid lines for stable steady state branch intervals, dot-dash lines for stable periodic branch intervals, short-dash lines for unstable (steady or periodic) branch intervals, empty squares to mark the bifurcation points, and filled squares for Hopf bifurcation points. While showing the bifurcation diagrams for various CEs, the maxima/minima corresponding to the periodic (or oscillatory) states are not plotted as a function of the continuation parameter Pe. At the Hopf bifurcation point, the steady state branch exchanges stability with the periodic branch. Locally, close to the Hopf bifurcation point, the stable periodic orbits encircle an unstable steady state solution

branch, and the unstable periodic orbits encircle a stable steady state solution branch. In both cases, the stable or unstable steady state part of the branch does not necessarily represent the mean values of the periodic oscillations. Thus the variable values represented by dot-dash lines (for stable oscillatory/periodic states) do not necessarily correspond to mean values of the oscillatory dynamic response. In the following discussion the solution branch means the plotted solution vector (computed components of $\mathbf{Q}_{ss}$, or the calculated S_{ss} or P_{ss}) as a function of Pe. The solution branches are classified into two main categories: in-plane branches (such as IP-1, IP-2) and out-of-plane branches (OP-1, OP-2, OP-3), such that the latter always have a non-zero z-component of $\mathbf{n}$ (i. e., $n_z \neq 0$). The numbers associated with the branch categories (i.e., 1, 2 with IP and 1, 2, 3 with OP) are used merely to differentiate the different branches belonging to the same category. The two intrinsic changes that may occur in different intervals of the same solution branch are changes in the stability and in the nature of the attractor. For example if the attractor loses stability in an interval of Pe, the corresponding solution branch will also become unstable in the same interval; and if the nature of the attractor changes in an interval then the corresponding orientation state represented by the solution branch will also change. The orientation state or simply the state means the corresponding uniaxial director dynamics, as shown in Figure 2.3, represented by a particular solution branch. In what follows we discuss only the stable steady and stable periodic states represented by various solution branches.

2.4.1 Bifurcation Phenomena

2.4.1.1 Constitutive Equation 1

Figure 2.4 shows the components of the steady state tensor order parameter $\mathbf{Q}_{ss}$ as a function of Pe. The bifurcation phenomena exhibited by CE-1 is represented by two in-plane branches, IP-1 and IP-2, and two out-of-plane branches, OP-1 and OP-2. The bifurcation phenomena shown in Figure 2.4 are summarized in Table 2.1. We note that here and in the rest of the paper the bifurcation phenomena exhibited by each CE is best explained by simultaneous consideration of the bifurcation diagrams and the tables.

There are four rows in Table 2.1, one for each branch defining the stability/instability intervals with respect to the Peclet number *Pe*, and the corresponding stable states in the stable intervals. The in-plane branch IP-1 is unstable for very low *Pe*, for intermediate *Pe* the IP-1 branch is stable in a narrow range and it corresponds to the stable PDO state (see Figure 2.3f). The stable PDO states emerge on the shear plane but with a very slight increase in *Pe* they move away from the shear plane; disappearance of PDOs is through another Hopf bifurcation, as shown in Figure 2.4, after which IP-1 again becomes unstable. As PDOs evolve from the shear plane, from the in-plane solution branch IP-1, they are classified based on the solution branch of their birth. For high *Pe*, the IP-1 is stable and corresponding stable state is ISS (see Figure 2.3a). The out-of-plane branch OP-1 predicts LRS (see Figure 2.3d) for very low *Pe*, for intermediate *Pe* the KO (see Figure 2.3e) states emerge and remain stable till $Pe \approx 3.7$ where OP-1 loses stability, folds at $Pe \approx 4$, and remains unstable till it extinguishes at $Pe = 0$. The out-of-plane branch OP-2 persists in a very narrow range of *Pe*, and is partly stable. The stable KOs, emerging from OP-1, extinguish on OP-2 through a Hopf bifurcation. The stable OP-2 exchanges stability with the unstable part of IP-1, thereafter IP-1 exhibits a stable ISS (see Figure 2.4). The in-plane branch IP-2 is unstable throughout the range of *Pe* it persists.

Figure 2.5 shows the steady state (a) uniaxial alignment S_{ss} and (b) biaxial alignment P_{ss} as a function of *Pe*. The two stable states on IP-1 are the periodic orbit PDO (see Figure 2.3f), and the steady state ISS (see Figure 2.3a). For the PDO, S_{ss} and P_{ss} both represent oscillatory stable states oscillating around values below S_{eq} and above zero respectively. The stable states on OP-1 are LRS (see Figure 2.3d) and KO (see Figure 2.3e). In case of KO, S_{ss} and P_{ss} oscillate around values below S_{eq} and above zero respectively. In LRS, S_{ss} decreases and remains below S_{eq} while P_{ss} increases.

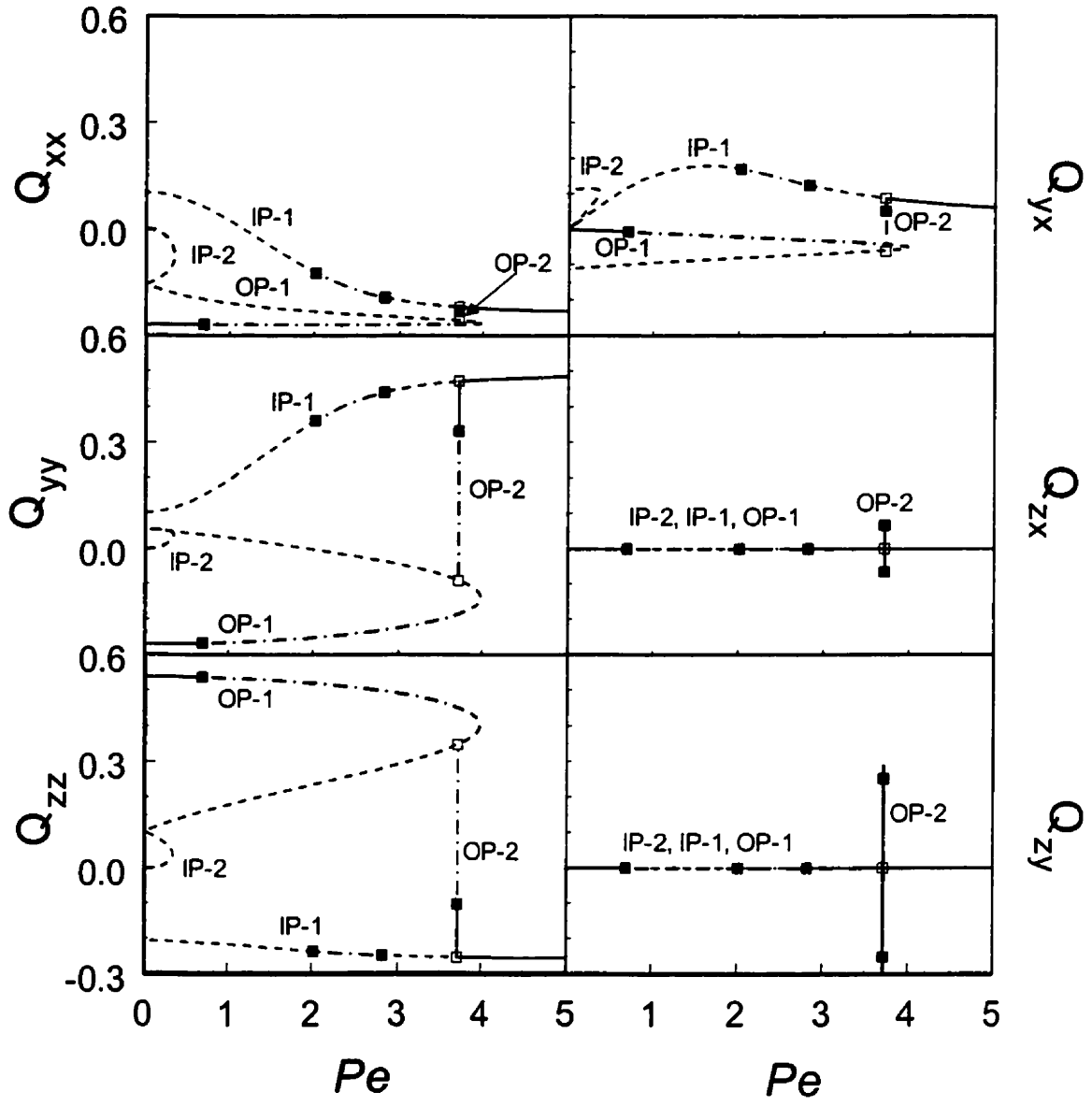

Figure 2.4: Computed steady state components of the tensor order parameter, $\mathbf{Q}_{ss}$, as a function of dimensionless shear rate Pe for $U = 6$, $\beta = -0.8$, as predicted by CE-1 for DNs subjected to simple shear flows. The bifurcation phenomena exhibited by CE-1 under simple shear are given by two in-plane solution branches, IP-1 and IP-2, and two out-of-plane solution branches, OP-1 and OP-2. The summary of stability/instability of the solution branches in various intervals along with the corresponding stable orientation states is given in Table 2.1. For details see text.

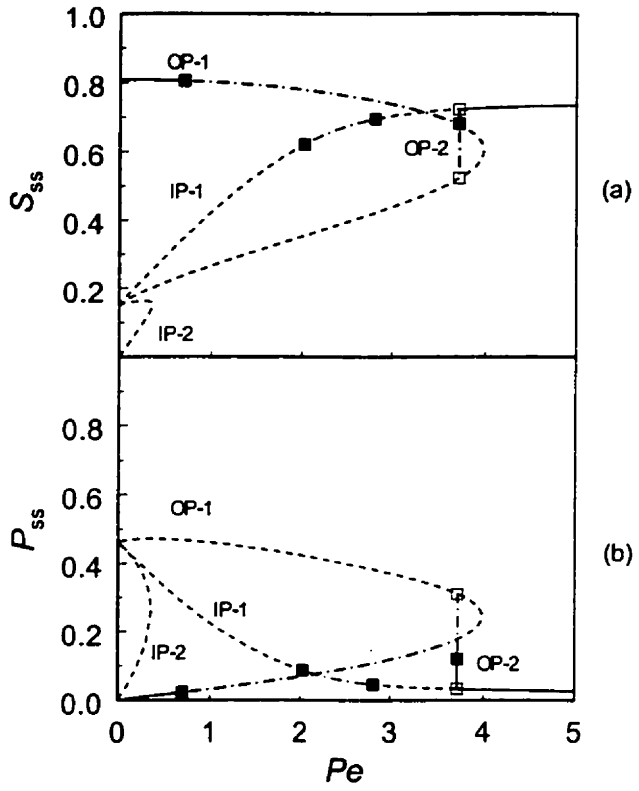

Figure 2.5: (a) Steady state uniaxial alignment S_{ss}, and (b) biaxial alignment P_{ss} as a function of dimensionless shear rate Pe for $U = 6$, $\beta = -0.8$, predicted by CE-1 for DNs subjected to simple shear flows. The bifurcation phenomena exhibited by CE-1 are given by two in-plane solution branches, IP-1 and IP-2, and two out-of-plane solution branches, OP-1 and OP-2. The summary of stability/instability of the solution branches in various intervals along with the corresponding stable orientation states is given in Table 2.1. A comprehensive summary of changes in S and P with Pe for the various stable orientation states is given in Table 2.5. For details see text.

TABLE 2.1

Summary of Bifurcation Phenomena for CE-1 (equation (2.6))

Branch	Stability features			
IP-1	$0 < Pe < 2$ Unstable	$2.0 < Pe < 2.8$ Stable (PDO)	$2.8 < Pe < 3.7$ Unstable	$Pe > 3.7$ Stable (ISS)
IP-2	Unstable throughout			
OP-1	$0 < Pe < 0.7$ Stable (LRS)		$0.7 < Pe < 3.7$ Stable (KO)	
OP-2	Exists for very narrow range of Pe (see text)			

Pe: Peclet number; IP-1: in-plane branch 1; IP-2: in-plane branch 2; OP-1: out-of-plane branch 1; OP-2: out-of-plane branch 2; LRS: log rolling state; KO: kayaking orbit; PDO: period doubling orbit; ISS: in-plane steady state

The stable state dynamics of **n** predicted by CE-1 are summarized in Table 2.1, and can be described as follows: for very low *Pe* there is only one stable state corresponding to LRS; for intermediate *Pe* the main stable state is KO, however, in a narrow range of *Pe* PDO also becomes stable along with KO; finally for high *Pe* the only stable state is ISS. The stable attractors for CE-1 are the vorticity axis, the kayaking orbits, the shear plane and the period doubling orbits.

The CE-1 neither predicts ITO and IWS states nor the classical ITO → IWS and IWS → ISS transitions. The orientation predictions by CE-1 for shear flows are not consistent with the predictions of the molecular (Larson and Ottinger, 1991) and macroscopic theories (Farhoudi and Rey, 1993). Also the LRS state is stable for a very short range of *Pe* and is not stable together with ISS as has been observed in the shear experiments of the representative discotics by Hammouda et al. (1995). Thus CE-1 cannot be employed to govern the microstructure response of discotic mesophases.

2.4.1.2 Constitutive Equation 2

Figure 2.6 shows the components of the tensor order parameter $\mathbf{Q}_{ss}$ as a function of *Pe*. The bifurcation phenomena exhibited by CE-2 are captured by two in-plane branches, IP-1 and IP-2, and two out-of-plane branches, OP-1 and OP-2. The bifurcation phenomena shown in Figure 2.6 are summarized in Table 2.2. There are four rows in Table 2.2, one for each branch, describing the stability/instability of the various intervals with respect to *Pe*, and the corresponding stable orientation states. The in-plane branch IP-1 is unstable for low *Pe*, for intermediate *Pe* it exhibits the ITO orientation state (see Figure 2.3a), which changes to stable IWS (see Figure 2.3b) for high *Pe*. No ISS (see Figure 2.3a) is encountered in the analyzed range of *Pe* ($Pe < 52$). The out-of-plane branch OP-1 is stable and corresponds to LRS (see Figure 2.3d) till $Pe \approx 14.3$ where it loses stability, folds and remains unstable till it extinguishes at $Pe = 0$. The in-plane branch IP-2 and out-of-plane branch OP-2 are unstable throughout.

Figure 2.7 shows the steady state (a) uniaxial alignment S_{ss} and (b) biaxial alignment P_{ss} as a function of *Pe*. The stable part of IP-1 is periodic in nature and the corresponding stable states are ITO and IWS for which S_{ss} and P_{ss} are oscillatory in

nature. The only stable state represented by OP-1 is LRS for which S_{ss} and P_{ss} follow the same trends as those stated in CE-1.

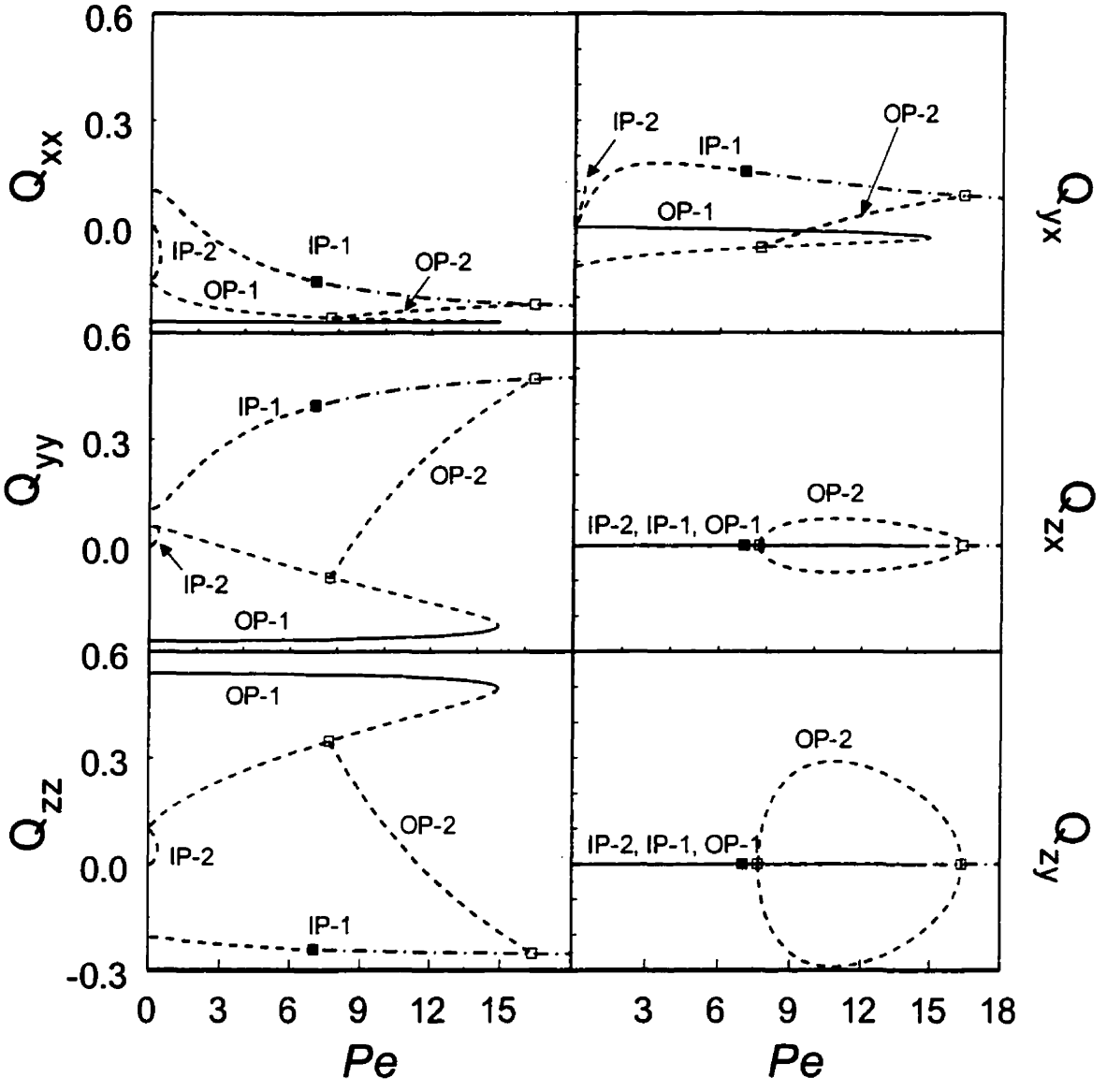

Figure 2.6: Computed steady state components of the tensor order parameter, $\mathbf{Q}_{ss}$, as a function of dimensionless shear rate Pe for U = 6, β = -0.8, as predicted by CE-2 for DNs subjected to simple shear flows. The bifurcation phenomena exhibited by CE-2 under simple shear are given by two in-plane solution branches, IP-1 and IP-2, and two out-of-plane solution branches, OP-1 and OP-2. The summary of stability/instability of the solution branches in various intervals along with the corresponding stable orientation states is given in Table 2.2. For details see text.

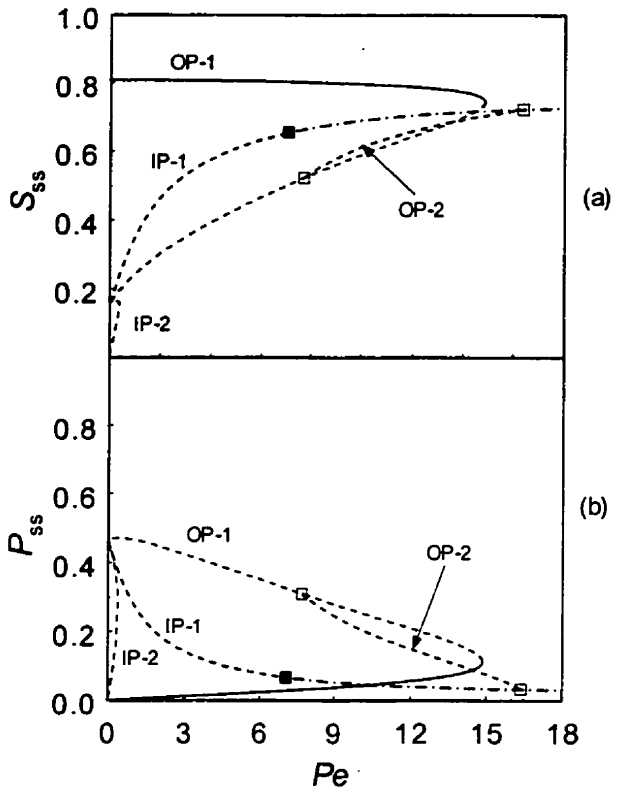

Figure 2.7: (a) Steady state uniaxial alignment S_{ss}, and (b) biaxial alignment P_{ss} as a function of dimensionless shear rate Pe for $U = 6$, $\beta = -0.8$, predicted by CE-2 for DNs subjected to simple shear flows. The bifurcation phenomena exhibited by CE-2 are given by two in-plane solution branches, IP-1 and IP-2, and two out-of-plane solution branches, OP-1 and OP-2. The summary of stability/instability of the solution branches in various intervals along with the corresponding stable orientation states is given in Table 2.2. A comprehensive summary of changes in S and P with Pe for the various stable orientation states is given in Table 2.5. For details see text.

TABLE 2.2

Summary of Bifurcation Phenomena for CE-2 (equation (2.10))

Branch	Stability features		
IP-1	$Pe < 7$ Unstable	$7 < Pe < 9$ Stable (ITO)	$Pe > 9$ Stable (IWS)
IP-2	Unstable throughout		
OP-1	$0 < Pe < 14.3$ Stable (LRS)		
OP-2	Unstable throughout		

Pe: Peclet number; IP-1: in-plane branch 1; IP-2: in-plane branch 2; OP-1: out-of-plane branch 1; OP-2: out-of-plane branch 2; LRS: log rolling state; ITO: in-plane tumbling orbit; IWS: in-plane wagging state

The stable state dynamics of **n** predicted by CE-2 are given by Table 2.2 and are summarized as follows: for low *Pe* there is only one stable state corresponding to LRS, for intermediate *Pe* LRS along with ITO are the stable states, for high *Pe* LRS and IWS are the stable states, and for very high *Pe* there is only one stable state corresponding to IWS. The stable attractors for CE-2 are the vorticity axis and the shear plane.

The CE-2 neither predicts ISS under shear for significant range of *Pe* nor the IWS $\rightarrow$ ISS transition, which is not in agreement with the theoretical predictions (based on molecular and macroscopic theories) and experimental data (Hammouda et al., 1995) for representative discotic under shear flows. Thus this CE-2 cannot be used to represent the microstructure phenomena in discotic mesophases, and hence is rejected.

2.4.1.3 Constitutive Equation 3

Figure 2.8 shows the components of the steady state tensor order parameter $\mathbf{Q}_{ss}$ as a function of *Pe*. The bifurcation phenomena exhibited by the CE-3 are represented by two in-plane branches, IP-1 and IP-2, and three out-of-plane branches, OP-1, OP-2 and OP-3. The bifurcation phenomena shown in Figure 2.8 are summarized in Table 2.3. There are five rows in Table 2.3, one for each branch, defining stability/instability of various intervals with respect to *Pe*, and the corresponding stable orientation states. The in-plane branch IP-1 is unstable for very low *Pe*, for intermediate *Pe* the IP-1 branch is stable in a narrow range and it corresponds to the stable PDO orientation state (see Figure 2.3f). The formation and disappearance of these PDOs follows the same phenomenon as those stated in case of CE-1. The IP-1 is unstable for rest of the intermediate *Pe*, and for high *Pe* it remains stable with ISS (see Figure 2.3c) being the corresponding stable steady state. The out-of-plane branch OP-1 is stable throughout the considered range of *Pe* and the stable state corresponds to LRS (see Figure 2.3d). The in-plane branch IP-2 and the out-of-plane branches OP-2 and OP-3 are unstable throughout.

Figure 2.9 shows the steady state (a) uniaxial alignment S_{ss} and (b) biaxial alignment P_{ss} as a function of *Pe*. The two stable state on IP-1 are the periodic orbit PDO and the steady state ISS. A Summary of the long time dynamical response of PDO is

given in Table 2.5. The stable state represented by OP-1 corresponds to LRS for which S_{ss} and P_{ss} follow the same trends as those stated in CE-1.

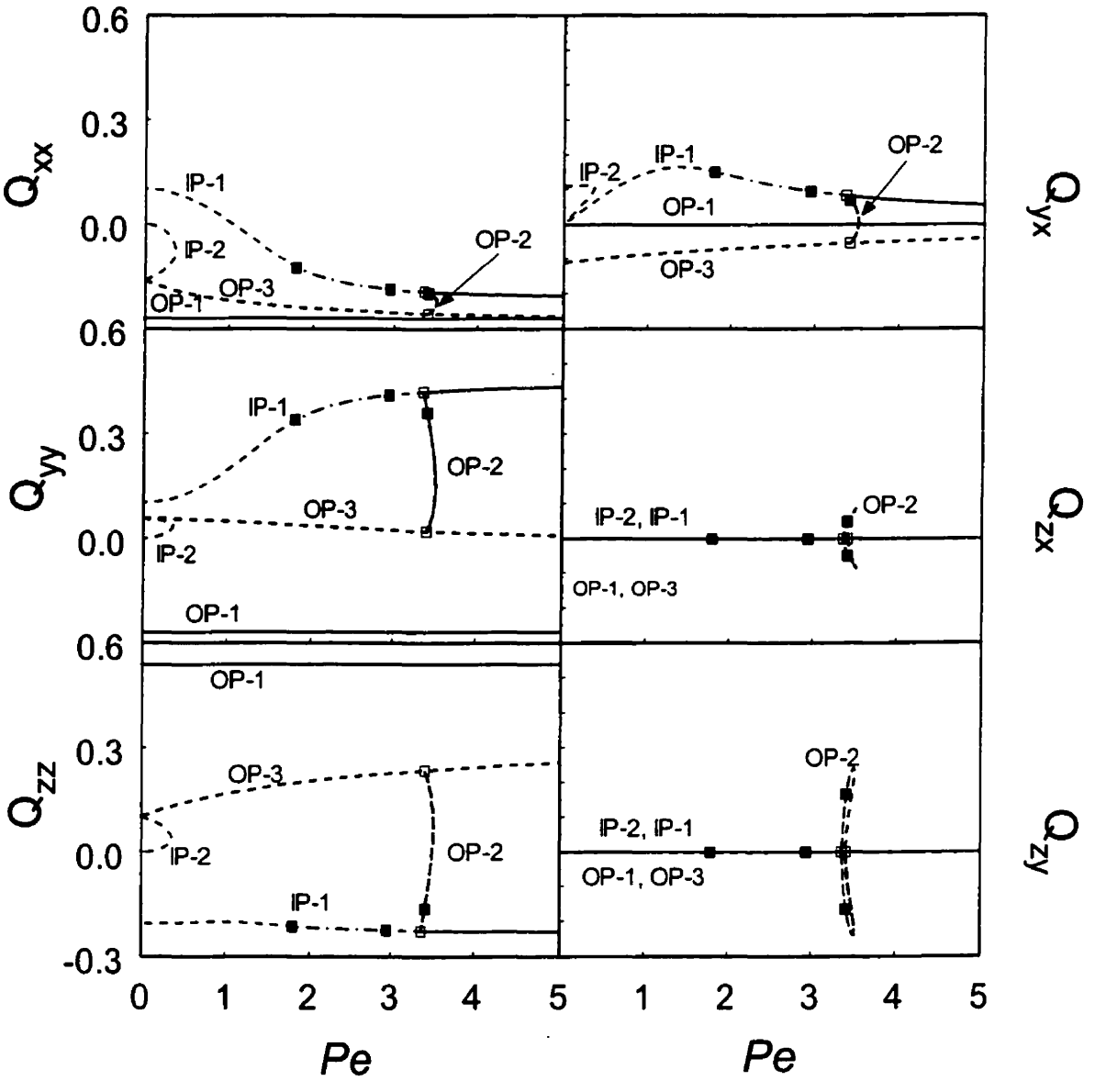

Figure 2.8: Computed steady state components of the tensor order parameter, $\mathbf{Q}_{ss}$, as a function of dimensionless shear rate *Pe* for $U = 6$, $\beta = -0.8$, as predicted by CE-3 for DNs subjected to simple shear flows. The bifurcation phenomena exhibited by CE-3 under simple shear are given by two in-plane solution branches, IP-1 and IP-2, and three out-of-plane solution branches, OP-1, OP-2 and OP-3. The summary of stability/instability of the solution branches in various intervals along with the corresponding stable orientation states is given in Table 2.3. For details see text.

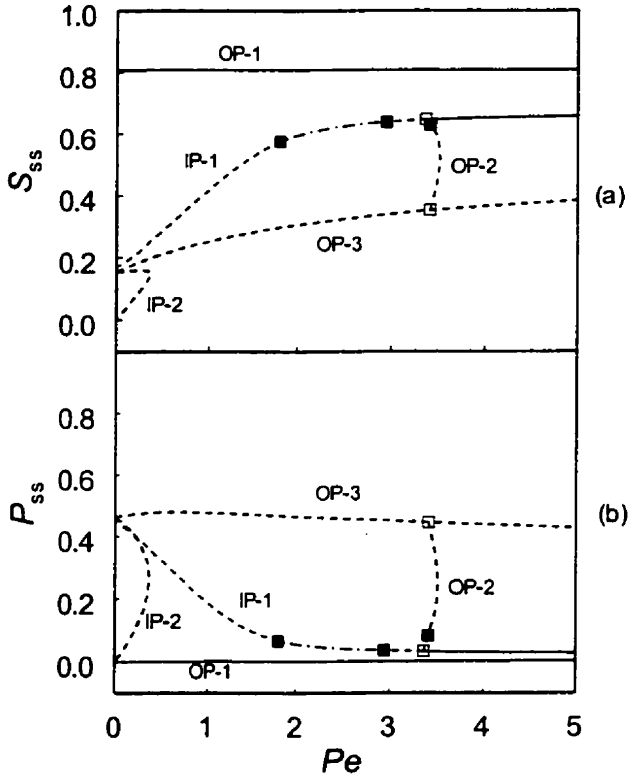

Figure 2.9: (a) Steady state uniaxial alignment S_{ss}, and (b) biaxial alignment P_{ss} as a function of dimensionless shear rate Pe for $U = 6$, $\beta = -0.8$, predicted by CE-3 for DNs subjected to simple shear flows. The bifurcation phenomena exhibited by CE-3 are given by two in-plane solution branches, IP-1 and IP-2, and three out-of-plane solution branches, OP-1, OP-2 and OP-3. The summary of stability/instability of the solution branches in various intervals along with the corresponding stable orientation states is given in Table 2.3. A comprehensive summary of changes in S and P with Pe for the various stable orientation states is given in Table 2.5. For details see text.

TABLE 2.3
Summary of Bifurcation Phenomena for CE-3 (equation (2.13))

Branch	Stability features			
IP-1	$0 < Pe < 1.8$ Unstable	$1.8 < Pe < 2.9$ Stable (PDO)	$2.9 < Pe < 3.4$ Unstable	$Pe > 3.4$ Stable (ISS)
IP-2	Unstable throughout			
OP-1	$Pe > 0$ Stable throughout (LRS)			
OP-2	Unstable throughout			
OP-3	Unstable throughout			

Pe: Peclet number; IP-1: in-plane branch 1; IP-2: in-plane branch 2; OP-1: out-of-plane branch 1; OP-2: out-of-plane branch 2; OP-3: out-of-plane branch 3; LRS: log rolling state; PDO: period doubling orbit; ISS: in-plane steady state.

The dynamics of **n** predicted by CE-3 are given by Table 2.3 and can be summarized as follows: for low *Pe* there is only one stable state corresponding to LRS, for intermediate *Pe* the main stable state is LRS, however, in a small range of *Pe* PDO also becomes stable state along with LRS, and for high *Pe* LRS and ISS correspond to the stable states predicted by CE-3. The stable attractors for CE-3 are the vorticity axis, the shear plane, and the eccentric period doubling orbits.

The CE-3 neither predicts ITO and IWS states nor the classical ITO → IWS and IWS → ISS transitions, and hence is not consistent with the predictions of the molecular (Larson and Ottinger, 1991) and macroscopic theories (Farhoudi and Rey, 1993). Thus CE-3 cannot be employed to represent the microstructure phenomena in discotic mesophases, and hence is rejected.

2.4.1.4 Constitutive Equation 4

Figure 2.10 shows the components of the steady state tensor order parameter $\mathbf{Q}_{ss}$ as a function of *Pe*. The bifurcation phenomena exhibited by CE-4 are captured by two in-plane branches, IP-1 and IP-2, and three out-of-plane branches, OP-1, OP-2 and OP-3. The bifurcation phenomena shown in Figure 2.10 are summarized in Table 2.4. Table 2.4 contains five rows, one for each branch, describing the stability/instability of the various intervals with respect to *Pe*, and the corresponding stable states. The in-plane branch IP-1 is unstable for low *Pe*, for intermediate *Pe* the IP-1 branch is stable with ITO (see Figure 2.3a) as the corresponding stable state, which changes to IWS (see Figure 2.3b) for high *Pe*. IP-1 is stable and predicts ISS (see Figure 2.3c) for very high *Pe*. The out-of-plane branch OP-1 is stable throughout the considered range of *Pe* and the stable state corresponds to LRS (see Figure 2.3d). The in-plane branch IP-2 and the out-of-plane branches OP-2 and OP-3 are unstable throughout.

Figure 2.11 shows the steady state (a) uniaxial alignment S_{ss} and (b) biaxial alignment P_{ss} as a function *Pe*. In IP-1 there is a typical in-plane transition from ITO to IWS and finally to ISS as predicted by many molecular and macroscopic theories. Here S_{ss} and P_{ss} show oscillatory states for ITO and IWS, and steady state for ISS. LRS is the

stable steady state represented by OP-1 for which variations in S_{ss} and P_{ss} with increasing *Pe* are the same as discussed before, and are summarized in Table 2.5.

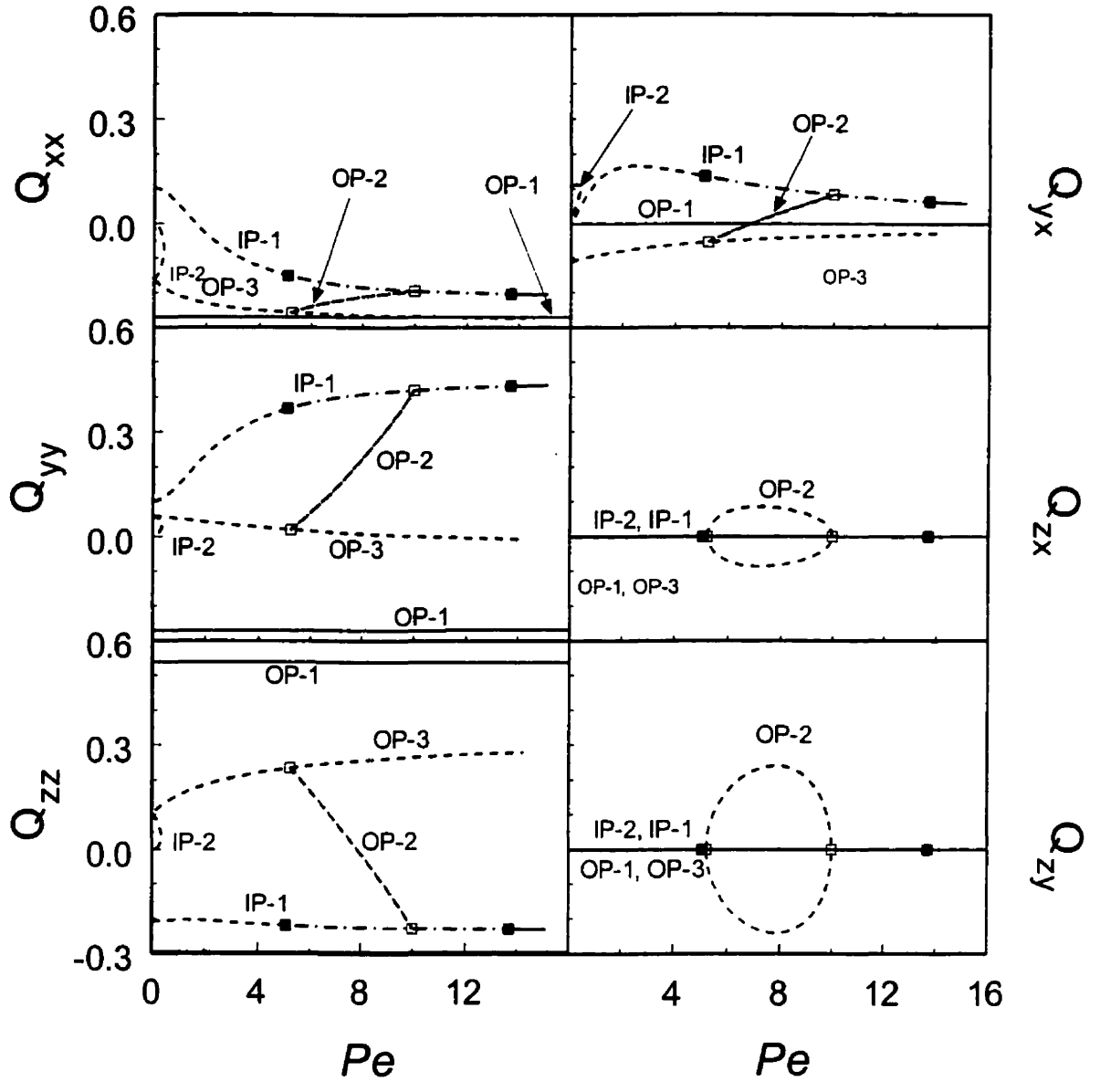

Figure 2.10: Computed steady state components of the tensor order parameter, $\mathbf{Q}_{ss}$, as a function of dimensionless shear rate *Pe* for $U = 6$, $\beta = -0.8$, as predicted by CE-4 for DNs subjected to simple shear flows. The bifurcation phenomena exhibited by CE-4 under simple shear are given by two in-plane solution branches, IP-1 and IP-2, and three out-of-plane solution branches, OP-1, OP-2 and OP-3. The summary of stability/instability of the solution branches in various intervals along with the corresponding stable orientation states is given in Table 2.4. For details see text.

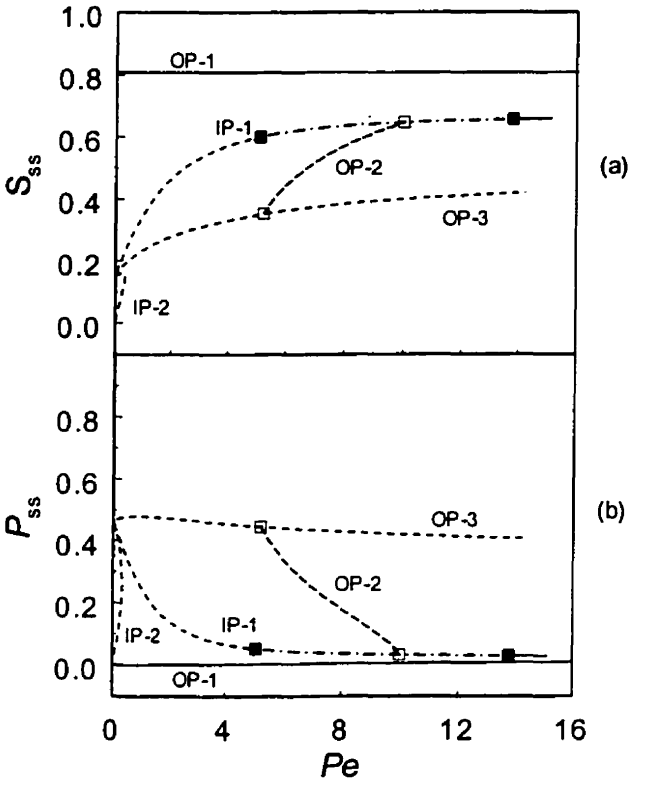

Figure 2.11: (a) Steady state uniaxial alignment S_{ss}, and (b) biaxial alignment P_{ss} as a function of dimensionless shear rate Pe for $U = 6$, $\beta = -0.8$, predicted by CE-4 for DNs subjected to simple shear flows. The bifurcation phenomena exhibited by CE-4 are given by two in-plane solution branches, IP-1 and IP-2, and three out-of-plane solution branches, OP-1, OP-2 and OP-3. The summary of stability/instability of the solution branches in various intervals along with the corresponding stable orientation states is given in Table 2.4. A comprehensive summary of changes in S and P with Pe for the various stable orientation states is given in Table 2.5. For details see text.

TABLE 2.4

Summary of Bifurcation Phenomena for CE-4 (equation (2.15))

Branch	Stability features			
IP-1	$Pe < 4.5$ Unstable	$4.5 < Pe < 5.5$ Stable (ITO)	$5.5 < Pe < 14$ Stable (IWS)	$Pe > 14$ Stable (ISS)
IP-2	Unstable throughout			
OP-1	$Pe > 0$ Stable throughout (LRS)			
OP-2	Unstable throughout			
OP-3	Unstable throughout			

Pe: Peclet number; IP-1: in-plane branch 1; IP-2: in-plane branch 2; OP-1: out-of-plane branch 1; OP-2: out-of-plane branch 2; OP-3: out-of-plane branch 3; LRS: log rolling state ITO: in-plane tumbling orbit; IWS: in-plane wagging state; ISS: in-plane steady state.

The dynamics of **n** predicted by CE-4 are summarized in Table 2.4 and can be summarized as follows: for low *Pe* there is only one stable state corresponding to LRS, for intermediate *Pe* LRS along with ITO are the stable states, for high *Pe* LRS and IWS are the stable states, and for very high *Pe* there are two stable states corresponding to LRS and ISS. The stable attractors for CE-4 are the vorticity axis and the shear plane.

The CE-4 predicts the major and essential stable steady and periodic states along with the classical ITO → IWS and IWS → ISS transitions as predicted by macroscopic (Farhoudi and Rey, 1993) and molecular theories (Larson and Ottinger, 1991). The multi-stabilities of the various stable states and their phase diagrams are qualitatively the same as those shown by Larson and Ottinger (1991). Moreover the simulations results of CE-4 under shear are consistent with the experimental results on representative discotics under shear (Hammouda et al. 1995). Also, as mentioned in the introduction, the preferred orientation of the disc-like molecules (close to the walls of slit) of discotic mesophase pitches, flowing in a thin rectangular channel, corresponds to LRS. Thus CE-4 can be considered as the most appropriate choice for describing the microstructural response of the discotic mesophases. The relevance of the predicted microstructure response in discotic mesophase pitches in explaining some of the observed microstructural features in mesophase carbon fibers will be established in future work.

2.4.2 Dynamic Simulations

As mentioned above the dynamic simulations were employed to confirm the stability of the various branches obtained by bifurcation analysis of the various CEs under shear flows. The results of the bifurcation analysis are organized and classified in terms of the uniaxial director **n** dynamics, given in Figure 2.3, but a more complete characterization must include the remaining two eigenvectors. Moreover, the maxima/minima corresponding to the periodic states are not plotted either in terms of director triad (**n**, **m**, **l**) or in terms of alignments S and P. Hence to further understand the long time dynamic response of periodic states in terms of either director triad (**n**, **m**, **l**) or alignments S and P, dynamic simulations were performed.

TABLE 2.5

Summary of long time dynamic response of stable states predicted by four CEs for DNs under shear flows for $U = 6$, $\beta = -0.8$

State type	Long time dynamic response of				
	uniaxial director **n**	biaxial director **m**	biaxial director **l**	uniaxial alignment S	Biaxial alignment P
LRS	$\phi_{nss} = 0°$	$\phi_{mss} = 90°$ $90° \le \theta_{mss} \le 135°$ $Pe\uparrow$: $\theta_{mss} \to 90°$ or $270°$	$\phi_{lss} = 90°$ $0° \le \theta_{lss} \le 45°$ $Pe\uparrow$: $\theta_{lss} \to 0°$ or $180°$	$0 \le S_{ss} \le S_{eq}$ $Pe\uparrow$: $S_{ss}\downarrow$	$0 \le P_{ss} \le 1$ $Pe\uparrow$: $P_{ss}\uparrow$
KO	$\phi_n = (0°, 90°)$ $\theta_n = [0°, 360°]$ (out-of-plane orbits) $Pe\uparrow$: $L\downarrow$, $\phi_n \to \approx 90°$	$\phi_m = (0°, 180°)$ $\theta_m = [135°, 225°]$ (out-of-plane orbits) $Pe\uparrow$: $L\downarrow$	$\phi_l = (0°, 180°)$ $\theta_l = [45°, 135°]$ (out-of-plane orbits) $Pe\uparrow$: $L\downarrow$	Oscillates $0 \le S \le S_{eq}$ $Pe\uparrow$: $L\downarrow$, $A\uparrow$	Oscillates $0 \le P \le 1$ $Pe\uparrow$:$L\downarrow$,$A\uparrow$
PDO	$\phi_n = (0°, 90°)$ $\theta_n = [45°, 135°]$ (out-of-plane orbits) $Pe\uparrow$: $L\uparrow$, $A\downarrow$	$\phi_m = (0°, 90°)$ $\theta_m = [135°, 225°]$ (out-of-plane orbits) $Pe\uparrow$: $L\uparrow$, $A\downarrow$	$\phi_l = (0°, 90°)$ $\theta_l = [45°, 135°]$ (out-of-plane orbits) $Pe\uparrow$: $L\uparrow$, $A\downarrow$	Oscillates $0 \le S \le S_{eq}$	Oscillates $0 \le P \le 1$
ITO	$\phi_n = 90°$ $\theta_n = [0°, 360°]$ (rotates in shear plane) $Pe\uparrow$: $L\downarrow$	same as **n** (since **n**$\perp$**m**)	$\phi_{lss} = 0°$	Oscillates around S_{eq} $Pe\uparrow$: $L\downarrow$, $A\uparrow$	Oscillates around values above 0 $Pe\uparrow$: $L\downarrow$, $A\uparrow$
IWS	$\phi_n = 90°$ $\theta_n = [45°, 135°]$ (oscillates in shear plane) $Pe\uparrow$: $L\downarrow$, $A\downarrow$	$\phi_m = 90°$ $\theta_m = [135°, 225°]$ $Pe\uparrow$: $L\downarrow$, $A\downarrow$	$\phi_{lss} = 0°$	Oscillates $0 \le S \le S_{eq}$ $Pe\uparrow$: $L\downarrow$, $A\uparrow$	Oscillates $0 \le P \le 1$ $Pe\uparrow$: $L\downarrow$, $A\uparrow$
ISS	$\phi_{nss} = 90°$ $90° \le \theta_{nss} \le 135°$ $Pe\uparrow$: $\theta_{nss} \to 90°$ or $270°$	$\phi_{mss} = 90°$ $0° \le \theta_{mss} \le 45°$ $Pe\uparrow$: $\theta_{mss} \to 0°$ or $180°$	$\phi_{lss} = 0°$	$0 \le S_{ss} \le S_{eq}$ $Pe\uparrow$: $S_{ss}\uparrow$	$0 \le P_{ss} \le 1$ $Pe\uparrow$: $P_{ss}\downarrow$

L: Period of oscillations; A: Amplitude of oscillations; Pe: Peclet number; ϕ_a (**a** = **n**, **m**, **l**): director polar angle; θ_a (**a** = **n**, **m**, **l**): director azimuthal polar angle; LRS: log rolling state; KO: kayaking orbit; PDO: period doubling orbit; ITO: in-plane tumbling orbit; IWS: in-plane wagging state; ISS: in-plane steady state; subscript "ss": steady state; subscript "eq": equilibrium value

Here we present the main features of the director triad (**n**, **m**, **l**) and alignment (S, P) computed by dynamic simulations corresponding to all the CEs. The main dynamic features of the uniaxial and biaxial orientation and alignments are summarized in Table 2.5, which contains 6 rows, one for every stable state represented in Figure 2.3, and five columns to describe the long time dynamics of the director triad (**n**, **m**, **l**) and alignment (S, P). All the symbols appearing in the table are defined in the captions. The superscript "ss" indicates that the corresponding long time dynamic solution is a steady state, and in this case the range of steady state orientation and alignment along with the asymptotic values are given. For example, LRS is a steady state, the uniaxial director **n** aligns along the vorticity axis ($\theta_{nss} = 0°$), the biaxial director **m** aligns in the region ($90° \leq \theta_{mss} \leq 135°$) in the shear plane ($\phi_{mss} = 90°$), and for very high Pe it approaches its asymptotic orientation ($\theta_{mss} \rightarrow 90°$). For periodic states (ITO, IWS, KO and PDO) the range of oscillation along with changes in amplitude, A, and period of oscillations, L, with increasing Pe is given. For example, IWS the uniaxial director oscillates in the shear plane ($\phi_n = 90$), the amplitude of oscillations is within the regions ($\theta_n = [45°, 135°]$), and as Pe increases the amplitude as well as period of oscillations decreases; $Pe \uparrow$: $L \downarrow$, $A \downarrow$. In partial summary Table 2.5 gives a comprehensive data base of all the characteristics of all the stable states predicted by all the CEs, investigated in this paper, under for shear flow at any arbitrary shear rate for a nematic discotic phase composed of molecules with a shape factor of $\beta = -0.8$. Although not discussed in the paper, it was found that as the shape factor β increases the tendency of DNs to tumble increases.

2.5 Conclusions

Out of four proposed CEs, an appropriate CE (eqn. (2.15)) has been selected for discotic mesophases by implementing an iterative process that is based on a set of criteria that consists of theoretical results and experimental data. The selected CE is able to capture all the experimental features and is consistent with the theoretical results, and will be used to develop the fundamental understanding of rheology of discotic mesophases in general and that of carbonaceous mesophase pitches, used in the manufacturing of mesophase carbon fibers, in particular.

The selected CE (eqn. (2.15)) is found to predict, qualitatively, almost all the necessary orientation features (except KO in case of Larson and Ottinger, 1991) based on the molecular theories, and therefore the terms with order $\mathbf{Q}^2$ are sufficient to construct an appropriate CE for DNs. A complete summary of all stable states (periodic or steady) and the corresponding stable intervals in terms of *Pe* is presented in Table 2.6. The last row of Table 2.6 contains information regarding the absent orientation modes in each CE. CE-4 does not predict the out-of-plane orientation states KO or PDO (see Figure 2.3e, f). The former orientation state KO is shown to be stable only in a very narrow range by Larson and Öttinger (1991), whereas the latter PDO has never been predicted or observed earlier, and hence this deficiency apparently does not impart a serious flaw on the predictions of CE-4. Moreover, though no molecular simulation for DNs subjected to various flows exist, the selected constitutive equation, i.e. CE-4, when adopted to rod-like nematics develops the same phenomenology as shown by Larson and Öttinger (1991), thus lending strong support to the validity of the CE-4.

The bifurcational analysis reveals that the various proposed CEs predict a great variety of dynamical microstructural behavior for discotic mesophases, and show multi-stabilities of various orientation modes through a series of complex bifurcations. Therefore, the theoretical investigation of rheology of these materials requires advanced mathematical tools such as bifurcation methods. The present investigation found that the bifurcation analysis is an effective but not sufficient tool for similar complex problems. Dynamic simulations must always be performed to check the stability of the various states.

Table 2.7 contains a complete summary of all the stable attractors for the four CEs investigated in this paper. All the presented CEs when subjected to simple shear flows predicted the shear plane and the vorticity axis as major stable attractors, whereas kayaking orbits and period doubling orbits are stable attractors only in those CEs which are based on $\mathbf{Q}$ independent diffusivity. Moreover, the CEs with the $\mathbf{Q}$ independent diffusivity do not predict the in-plane periodic stable states (such as ITO and IWS), which is not in agreement with the predictions of molecular theories (Larson and Ottinger,

1991). Hence the constant (**Q** independent) diffusivity is not an appropriate assumption while selecting a CE for nematics.

TABLE 2.6

Summary of the stable states predicted by four CEs

State type	Microstructure Constitutive Equation			
	CE-1	CE-2	CE-3	CE-4
LRS	$0 < Pe < 0.7$	$0 < Pe < 14.3$	$Pe > 0$	$Pe > 0$
KO	$0.7 < Pe < 3.7$	—	—	—
PDO	$2.0 < Pe < 2.8$	—	$1.8 < Pe < 2.9$	—
ITO	—	$7 < Pe < 9$	—	$4.5 < Pe < 5.5$
IWS	—	$Pe > 9$	—	$5.5 < Pe < 14$
ISS	$Pe > 3.7$	—	$Pe > 3.4$	$Pe > 14$
Stable states not predicted	ITO IWS	ISS KO PDO	ITO IWS KO PDO	KO PDO

Pe: Peclet number; LRS: log rolling state; KO: kayaking orbit; PDO: period doubling orbit; ITO: in-plane tumbling orbit; IWS: in-plane wagging state; ISS: in-plane steady state

TABLE 2.7

Summary of various stable attractors for four CEs

Type of main attractors	CE-1	CE-2	CE-3	CE-4
Shear plane	Yes	Yes	Yes	Yes
Vorticity axis	Yes	Yes	Yes	Yes
Out-of-plane kayaking orbit	Yes	No	No	No
Out-of-plane period doubling orbit	Yes	No	Yes	No

Bibliography

N.C. Andrews, B.J. Edwards and A.J. McHugh, "Continuum dynamic behavior of homogeneous liquid-crystalline polymers under the imposition of shear and magnetic fields", *Journal of Rheology*, **39** 1161 (1995).

H. Baals and S. Hess, "The viscosity coefficients of oriented nematics and nematic discotic liquid crystals: affine transformation model", *Z Naturforsch*, **43A** 662 (1988).

A.N. Beris and B.J. Edwards, "Thermodynamics of flowing systems: with internal microstructure", *Oxford University Press*, New York, USA (1994).

T. Carlsson, "The possibility of the existence of a positive Leslie viscosity α_2. proposed flow behavior of a disk-like nematic liquid crystals", *Mol. Cryst. Liq. Cryst.*, **89** 57 (1982).

T. Carlsson, "Remarks on the flow alignment of disk like nematics", *J. Physique*, 909 (1983).

S. Chandrasekhar, "Liquid crystals of disc-like molecules", *Mol. Cryst. Liq. Cryst.*, **63** 171 (1981).

S. Chandrasekhar, "Liquid Crystals", *Cambridge University Press*, Cambridge (1992).

P.G. deGennes, "The Physics of Liquid Crystals", *Oxford University Press*, London (1975).

C. Destrade, N.H. Tinh, H. Gasparoux, J. Malthete and A.M. Levelut, "Disc-like mesogen: A classification", *Mol. Cryst. Liq. Cryst.* **71** 111 (1981).

E.J. Doedel, X.J. Wang and T.F. Fairgrieve, "AUTO94©: Software for continuation and bifurcation problems in ordinary differential equations", *Applied Mathematics Report*, California Institute of Technology, Pasadena (1995).

M. Doi and S.F. Edwards, "The Theory of Polymer Dynamics", *Oxford University Press* New York. 358-362

Farhoudi Y, Rey AD (1993a) Ordering effects in shear flows of discotic polymers. Rheol Acta 32:207-217 (1986).

Y. Farhoudi and A.D. Rey, "Shear flow of nematic polymers. Part I. Orienting modes, bifurcations and steady rheological predictions", *J Rheo* **37** 289 (1993b).

B. Hammouda, J. Mang and S. Kumar, "Shear-induced orientational effects in discotic-liquid-crystal micelles", *Phys Rev E* **51** 6282 (1995).

A.S.K. Ho and A.D. Rey, "Orienting properties of discotic nematic liquid crystals in Jeffrey-Hamel flows", *Rheo. Acta* **30** 77 (1991).

R.G. Larson, "Constitutive Equations for Polymer Melts and Solutions", *Butterworths*, Boston (1988).

R.G. Larson and H.C. Öttinger, "Effect of molecular elasticity on out-of-plane orientations in shearing flows of liquid-crystalline polymers", *Macromolecules* **24** 6270 (1991).

F.M. Leslie, "Theory of flow phenomena in liquid crystals", *In: Brown HG (ed.) Advances in Liquid Crystals*, vol. 4. Academic Press, New York, 1-81 (1979).

P.L. Maffettone and S. Crescitelli, "Bifurcation analysis of a molecular model for nematic polymers in shear flows", *JNNFM* **59** 73 (1995).

G. Marrucci and F. Greco, "Flow behavior of liquid crystalline polymers", *Adv. Chem. Phys.* **86** 331(1993).

J.J. McHugh, "The development of orientation in mesophase pitch during fiber formation", Ph.D. thesis, Clemson University, Clemson, SC, USA (1994).

J.J. McHugh and D.D. Edie, "The orientation of mesophase pitch during fully developed channel flow" *Carbon* **34** 1315 (1996).

T.W. Ooi and T. Sridhar, "Uniaxial extensional of a lyotropic liquid crystalline polymer solution", *Ind Eng Chem Res* **33** 2368 (1994).

S. Otani and A. Oya, "Progress of pitch-based carbon fibers in Japan, in petroleum derived carbons", Bacha JD, Newman JW , White JL (Eds.), *ACS Symp. Ser No. 303*, American Chemical Society, Washington DC, USA 322 (1986).

T.J. Phillips and V. Minter, "On the observation of flow-induced order in the isotropic phase of a nematic discogen", *Liq Cryst* **20** 243 (1996).

A.D. Rey, "Bifurcational analysis of the isotropic-discotic nematic phase transition in the presence of extensional flow", *Liq Cryst* **19** 325 (1995a).

A.D. Rey, "Bifurcational analysis of the isotropic-nematic phase transition of rigid rod polymers subjected to biaxial stretching flow", *Macro. Theo. Sim.* **4** 857 (1995b).

L.S. Singer, "The mesophase in carbonaceous pitches", *Faraday Discuss. Chem. Soc.* **79** 265 (1985).

A.P. Singh and A.D. Rey, "Extensional dynamics of discotic nematics of variable order: geodesic flow and viscoelastic relaxation", *J Phys II France* **4** 645 (1994).

A.P. Singh and A.D. Rey, "Computer simulation of dynamics and morphology of discotic mesophases in extensional flows", *Liq. Cryst.* **18** 219 (1995a).

A.P. Singh and A.D. Rey, "Theory and simulation of extensional flow-induced biaxiality in discotic mesophases", *J Phys II France* **5** 1321 (1995b).

G.E. Volovik, "Relationship between molecule shape and hydrodynamics in a nematic substance", *JETP Lett.* **31** 273 (1980).

J.E. Zimmer and J.L. White, "Disclinations structures in the carbonaceous mesophase", In: Brown HG (ed.) *Advances in Liquid Crystals, vol. 5*, Academic Press, New York (1982)

[1]CHAPTER 3

Microstructure Constitutive Equation for Discotic Nematic Liquid Crystalline Materials

Part II: Microstructure-Rheology Relations

In the previous chapter a microstructure constitutive equation (CE) of discotic mesophases was formulated by taking into account the full microstructural characteristics. In this chapter the hydrodynamic constitutive equation or stress tensor equation complimenting the microstructure governing equation for discotic mesophases is formulated from first principles. The shear rheological properties predictions are presented and assessed within the context of nematorheology. The predicted apparent shear viscosity of discotic mesophases is qualitatively similar to that reported in the literature (Fleurot, 1998). The present work is the first attempt to establish the relations among rheological material functions, flow-induced microstructure, processing conditions, and material properties. A sufficiently number of distinguishing features have been identified that are specific to the discotic nature of the nematic phase, and augment the number of quantitative and qualitative differences between discotic and rod-like nematics that had been noted in the literature (Farhoudi and Rey, 1993c).

---

[1] This chapter appeared as an original article in *Rheological* Acta **37**(4) p374-386 (1998).

3.0 Abstract

The rheological material functions predicted by a previously selected constitutive equation (CE) for discotic mesophases are presented. The predicted relations among rheological properties, shear-induced microstructure, processing conditions and material parameters of discotic mesophases are characterized and discussed. The first and second normal stress differences corresponding to planar (i.e., 2-D orientation) microstructure mode of discotic nematics are found to be qualitatively similar to those for rod-like nematics despite the existing differences in flow-orientation characteristics. The first (second) normal stress difference for discotic mesophases corresponding to non-planar (i.e., 3-D orientation) microstructure mode is always positive (positive or negative depending on viscous effects); and is found to be due to flow-induced biaxiality. The effect of change in nematic potential (or temperature) on rheological properties of discotic mesophases is also presented. The apparent shear viscosities for various microstructure modes and material properties are also presented and shown to agree qualitatively with the available experimental data. Though only restricted validation of the predicted results with the actual experimental data of discotics is possible, the present study provides essential theoretical feedback to the on-going experimental work being pursued in understanding the processing behavior of mesophase pitches.

3.1 Introduction

Carbonaceous mesophases or mesophase pitches are an important class of low cost precursor materials that are used to manufacture high performance mesophase pitch-based carbon fibers which posses excellent mechanical and thermal transport properties (Singer, 1985; Peebles, 1994; Edie et al. 1994). These fibers are used to produce a new generation of composite materials that are revolutionizing the space, aircraft, electronics and automotive industries. The superior properties of these mesophase carbon fibers depend on the textures that evolve during the spinning process of mesophase pitches. During the spinning process, the mesophase pitches are subjected to various flow deformations and thermal stresses which result in a variety of fiber textures under different processing conditions (Oya and Otani, 1986; Mochida et al., 1993; Lafdi et al.

1993; Fatholahi and White, 1994; McHugh and Edie 1995, Fleurot, 1998). However, their flow behavior under such complex external fields is not known, and that knowledge is essential for their further development. Though the process optimization and texture selection may be achieved by trial and error, the variability of mesophase feed stocks and variations in process equipment geometry requires the use of generalized principles.

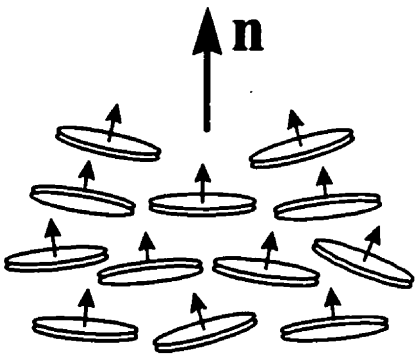

Figure 3.1: Definition of director orientation of a uniaxial discotic nematic liquid crystalline material. The director **n** is the average orientation of the unit normals to the disk-like molecules in a discotic nematic phase.

Mesophase pitches consist of poly-aromatic, flat, disk-like molecules that are rigid enough to display long range orientation order or liquid crystallinity, and tend to adopt a uniaxial discotic nematic phase, N_D (Chandrashekhar 1981, 1992; Destrade et al. 1981). In the discotic nematic phase, the unit normals to the flat disk-like molecules orient more or less along a common direction called (uniaxial) director or orientation **n**, as shown in Figure 3.1. The average degree of alignment of the unit normals to the disk-like molecules along the director **n** is defined by the (uniaxial) scalar order parameter or alignment S. This paper deals with rheology of discotic nematics that are uniaxial at rest but are biaxial under imposed flow. The effect of flow induced biaxiality of uniaxial discotic nematics under shear and extensional flows have been extensively explored (Singh and Rey, 1995, 1998; Rey, 1995).

It is well established, through extensive experimental measurements (Baek et al., 1993, 1994) and theoretical simulations (Marrucci and Maffetone, 1989; Larson and Öttinger, 1991; Marrucci and Greco, 1993; Beris and Edwards, 1994; Andrews et al., 1995) that liquid crystalline materials orient in the presence of magnetic, electric or flow

fields. This inherent property of liquid crystalline materials is exploited to manufacture highly oriented materials with superior properties that are not possible to achieve from their isotropic counterparts (Singer, 1985; Peebles 1994; Edie et al., 1994; McHugh and Edie, 1995). The rheology and flow properties of liquid crystalline materials are crucial to their end use since it is their flow-induced alignment that provides high strength and high modulus in the final product. It is well established that the rheology of liquid crystalline materials strongly depends on their internal microstructure along with external variables such as processing conditions and geometry. Numerous experimental (Baek et al., 1993, 1994) and theoretical (Marrucci and Maffetone, 1989; Larson and Öttinger, 1991; Marrucci and Greco, 1993; Andrews et al., 1995) studies have been performed relating the rheology of the rod-like nematics with their internal microstructure. However, it has been noted that the same is lacking for discotic nematics. In this work modeling and simulation is used to improve the current understanding of the rheology-microstructure relations for discotic mesophases.

Next we summarize some known important differences and similarities between rod-like and discotic nematics with regard to rheology-microstructure relations. Volovik (1980), and Carlsson (1982, 1983) studied the rheology of aligning low molecular weight uniaxial discotic mesophases and noted the particular material parameters that are affected in algebraic sign by molecular shape. The important difference in algebraic sign and magnitude of the material parameters for rod-like and discotic mesophases was found to be due to the fact that the former orient their largest molecular dimension along the director whereas the latter orient their shortest dimension along the director. The orienting properties of uniaxial nematics subjected to shear flows are governed by the sign and magnitude of the tumbling function λ, given by the negative ratio of the irrotational torque coefficient (γ_2) and the rotational viscosity (γ_1) such that for aligning disks (rods) $\lambda < -1$ ($\lambda > 1$) and for non-aligning disks (rods) $-1 < \lambda < 0$ ($0 < \lambda < 1$). Farhoudi and Rey (1993c) focused on the orienting properties of non-aligning uniaxial discotic nematics in simple shear flows and by using a macroscopic theory showed that the uniaxial director **n** tumbles, oscillates or aligns according to the flow strength, and the transitions among various regimes are similar to that predicted by molecular theories for

rod-like nematics (Marrucci and Maffetone, 1989; Larson and Öttinger, 1991). In a previous study, Singh and Rey (1998) presented the complete bifurcation phenomena along with the flow-induced biaxiality for uniaxial discotic mesophases under shear flows as predicted by a macroscopic theory. Along with the planar microstructure modes, the existence of non-planar microstructure mode (log-rolling state), similar to that predicted by Larson and Öttinger (1991) for rod-like nematics, was shown to be stable for discotics as well (Singh and Rey, 1998). The shear-induced microstructure features, both steady and periodic, are different in rod-like and discotic nematics. For example in discotic (rod-like) nematics under simple shear flows the director **n** rotates in the shear plane in the low shear rate tumbling regime during which it slows down near the velocity gradient (flow) direction, oscillates around velocity gradient (flow) direction in the intermediate shear rate wagging regime, and aligns near velocity gradient (flow) direction in the high shear rate steady state regime.

The relations among the planar microstructure phenomena and the corresponding rheological properties of rod-like nematics are well explained and documented in the literature (Marrucci and Maffetone, 1989; Larson, 1990; Marrucci and Greco, 1993; Farhoudi and Rey, 1993a, 1993b; Baek et al. 1994). However, similar studies are entirely absent for discotic nematics, and are essential for their continuing development. The effect of different orientation features in discotic nematics, from those in rod-like nematics, on their rheological properties has not been explored so far.

Next we present a brief summary of the known rheological properties of rod-like nematics. The Doi's theory predicts two sign changes in the first and second normal differences (N_1 and N_2) for rod-like nematics under simple shear flows (Larson 1990; Baek et al., 1993, 1994; Marrucci and Greco, 1993). For low shear rates or in the tumbling regime N_1 (N_2) is positive (negative), for intermediate shear rates or in the wagging regime N_1 (N_2) is negative (positive) due to the low values of order parameter, and finally at high shear rates or in the steady state regime the order parameter increases and N_1 (N_2) again becomes positive (negative) (Larson 1990; Baek et al., 1993, 1994; Marrucci and Greco, 1993). Larson and Ottinger (1991) performed the three dimensional orientational calculations and predicted the non-planar stable states (kayaking state and

log rolling state) in which the corresponding normal stress differences (N_1 and N_2) were found to be positive, comparable in magnitude with those for the planar orientation mode, and increasing with shear rate at low shear rates. Andrews et al. (1995) worked with a modified Doi's theory (using a quadratic closure approximation) and predicted the first sign transition in N_1, however, their modified theory was unable to predict the second sign change in N_1, and both of the sign transitions in N_2. Farhoudi and Rey (1993b, c) by using a macroscopic theory for LCP, which is similar in spirit to that used by Andrews et al. (1995), successfully predicted the two sign changes in N_1 and N_2, for rod-like nematics, by choosing proper material parameters that resulted in a tumbling function λ with a local minima (Farhoudi and Rey, 1993a).

In the previous paper (Singh and Rey, 1998), a set of microstructure constitutive equations (CEs) were formulated for discotic mesophases, and their microstructure response to simple shear flows were simulated. Out of the set, a CE that was consistent with known experimental data and theoretical predictions was selected. In this paper the predicted rheological response and properties of the selected CE of discotic mesophases will be presented. The main objective is to develop fundamental relations among the rheology and internal microstructure of discotic mesophases. The emphasis is to present the shear induced rheological properties of discotic mesophases and their relations with internal flow-induced microstructures, processing conditions, and material properties. The particular objectives of this paper are to:

1. Formulate an expression for the stress tensor corresponding to the already selected microstructure constitutive equation (Singh and Rey, 1998) for discotic nematics;
2. Characterize the relations among rheology-microstructure modes;
3. Characterize the relations among rheology-processing conditions;
4. Characterize the relations among rheology-material parameters.

The organization of this paper is as follows. In the following section we present the governing equations that describe the microstructural response of liquid crystalline materials and derive the corresponding stress tensor equation. Next, we present a classification of discotic mesophases based on their microstructure behavior under shear

flows. Subsequently, the simulated results are used to characterize the relations among shear rheology and microstructural modes, processing conditions, and material parameters. Finally, conclusions are presented.

3.2 Governing Equations

The microstructure of discotic mesophases is characterized by a second order tensor, known generally as the tensor order parameter **Q**:

$$\mathbf{Q} = S\left(\mathbf{nn} - \tfrac{1}{3}\delta\right) + \tfrac{1}{3}P(\mathbf{mm} - \mathbf{ll}) \tag{3.1a}$$

where the following restrictions apply:

$$\mathbf{Q} = \mathbf{Q}^{\mathrm{T}} \ , \quad tr(\mathbf{Q}) = 0 \ , \quad -\tfrac{1}{2} \le S \le 1 \ , \quad -\tfrac{3}{2} \le P \le \tfrac{3}{2} \ , \tag{3.1b,c,d,e}$$

$$\mathbf{n}\cdot\mathbf{n} = \mathbf{m}\cdot\mathbf{m} = \mathbf{l}\cdot\mathbf{l} = 1 \ , \quad \mathbf{nn} + \mathbf{mm} + \mathbf{ll} = \delta = \begin{bmatrix} 1 & 0 & 0 \\ 0 & 1 & 0 \\ 0 & 0 & 1 \end{bmatrix} \tag{3.1f,g}$$

The first eigenvector of **Q**, known as the uniaxial director **n**, corresponds to the largest eigenvalue $\frac{2}{3}S$, the biaxial director **m** corresponds to the intermediate eigenvalue $-\frac{1}{3}(S-P)$, and the second biaxial director **l** ($=\mathbf{n}\times\mathbf{m}$) corresponds to the smallest eigenvalue $-\frac{1}{3}(S+P)$. The orientation is defined completely by the orthogonal director triad (**n**, **m**, **l**). The magnitude of the uniaxial alignment S is a measure of the molecular alignment along the uniaxial director **n**, and is given as $S = \frac{3}{2}(\mathbf{n}\cdot\mathbf{Q}\cdot\mathbf{n})$. The magnitude of the biaxial alignment P is a measure of the molecular alignment in a plane perpendicular to uniaxial director **n**, and is given by $P = \frac{3}{2}(\mathbf{m}\cdot\mathbf{Q}\cdot\mathbf{m} - \mathbf{l}\cdot\mathbf{Q}\cdot\mathbf{l})$. Details on uniaxial ($S$) and biaxial ($P$) alignments and their interrelations are given in (Singh and Rey, 1995). The present work is restricted to normal nematics ($0 \le S \le 1$, $0 \le P \le 1$). The order parameter **Q** is assumed to be spatially uniform.

Figure 3.2(a) shows a schematic of homogeneous steady shear flow. The flow direction is along the x-axis, the velocity gradient direction is along the y-axis, and the vorticity axis (neutral axis) is along the z-axis. The shear plane is subdivided into four

quadrants as shown in Figure 3.2(b). The unit sphere description of the director triad (**n**, **m**, **l**), shown in Figure 3.2(c), where:

$$\mathbf{a} = \left(a_x,\ a_y,\ a_z\right) = \left(\sin\phi_a\cos\theta_a, \sin\phi_a\sin\theta_a, \cos\phi_a\right) \tag{3.2}$$

a (= **n**, **m**, **l**) is a unit vector given completely by azimuthal angle $\theta_a (0 \le \theta_a \le 2\pi)$, and polar angle $\phi_a (0 \le \phi_a \le \pi)$. In terms of angles, the equator lies in the shear plane and is given as $\left(\theta_a,\ \phi_a\right) = \left(\left[0,\ 2\pi\right],\ \pm\pi/2\right)$, and the north pole and the south pole are located along the vorticity axis and are given by $\phi_a = 0$ and $\phi_a = \pi$ respectively. We use this parametrization to present the results of uniaxial (**n**) and biaxial (**m**, **l**) orientations in a simple and direct way. In the rest of the paper all angles are reported in degrees.

3.2.1 Constitutive Equation

The microstructure response of liquid crystalline polymers, as described by Doi's mesoscopic nematodynamic theory (Doi and Edwards, 1986), is given as:

$$\hat{\mathbf{Q}} = \mathbf{F}(\mathbf{Q}, \nabla\mathbf{v}) + \mathbf{H}\left(\mathbf{Q},\ \overline{D}_r(\mathbf{Q})\right) \tag{3.3}$$

where $\nabla\mathbf{v}$ is the velocity gradient tensor and $\hat{\mathbf{Q}}$ is the corotational derivative of $\mathbf{Q}$ and is defined as:

$$\hat{\mathbf{Q}} = \frac{\partial\mathbf{Q}}{\partial t} + (\mathbf{v}\cdot\nabla)\mathbf{Q} - \mathbf{W}\cdot\mathbf{Q} + \mathbf{Q}\cdot\mathbf{W} \tag{3.4}$$

$\mathbf{F}(\mathbf{Q}, \nabla\mathbf{v})$ and $\mathbf{H}\left(\mathbf{Q},\ \overline{D}_r(\mathbf{Q})\right)$ represent the flow and the short range elastic contributions respectively, and are given as (Singh and Rey, 1998):

$$\begin{aligned}\mathbf{F}(\mathbf{Q}, \nabla\mathbf{v}) = {} & \tfrac{2}{3}\beta\mathbf{A} + \beta\left[\mathbf{A}\cdot\mathbf{Q} + \mathbf{Q}\cdot\mathbf{A} - \tfrac{2}{3}(\mathbf{A}:\mathbf{Q})\delta\right] - \\ & \tfrac{1}{2}\beta\left[(\mathbf{A}:\mathbf{Q})\mathbf{Q} + \mathbf{A}\cdot\mathbf{Q}\cdot\mathbf{Q} + \mathbf{Q}\cdot\mathbf{A}\cdot\mathbf{Q} + \mathbf{Q}\cdot\mathbf{Q}\cdot\mathbf{A} - \left\{(\mathbf{Q}\cdot\mathbf{Q}):\mathbf{A}\right\}\delta\right]\end{aligned} \tag{3.5}$$

$$\mathbf{H}\left(\mathbf{Q},\ \overline{D}_r(\mathbf{Q})\right) = -6\overline{D}_r\left[\left(1 - \tfrac{1}{3}U\right)\mathbf{Q} - U\mathbf{Q}\cdot\mathbf{Q} + U\left\{(\mathbf{Q}:\mathbf{Q})\mathbf{Q} + \tfrac{1}{3}(\mathbf{Q}:\mathbf{Q})\delta\right\}\right] \tag{3.6}$$

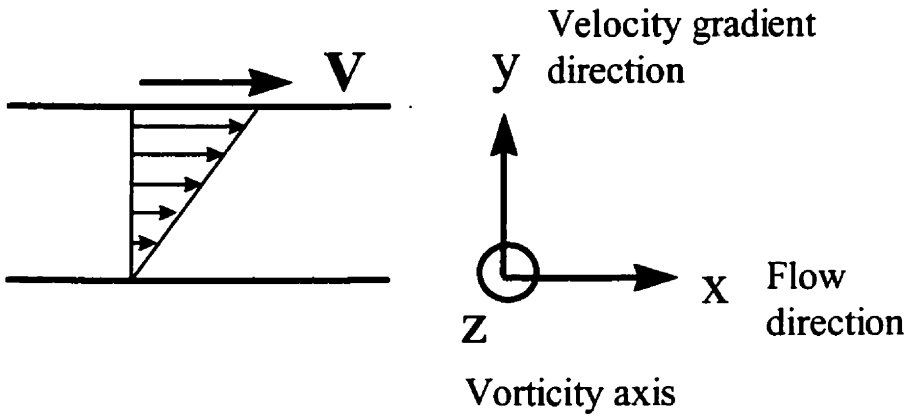

(a)

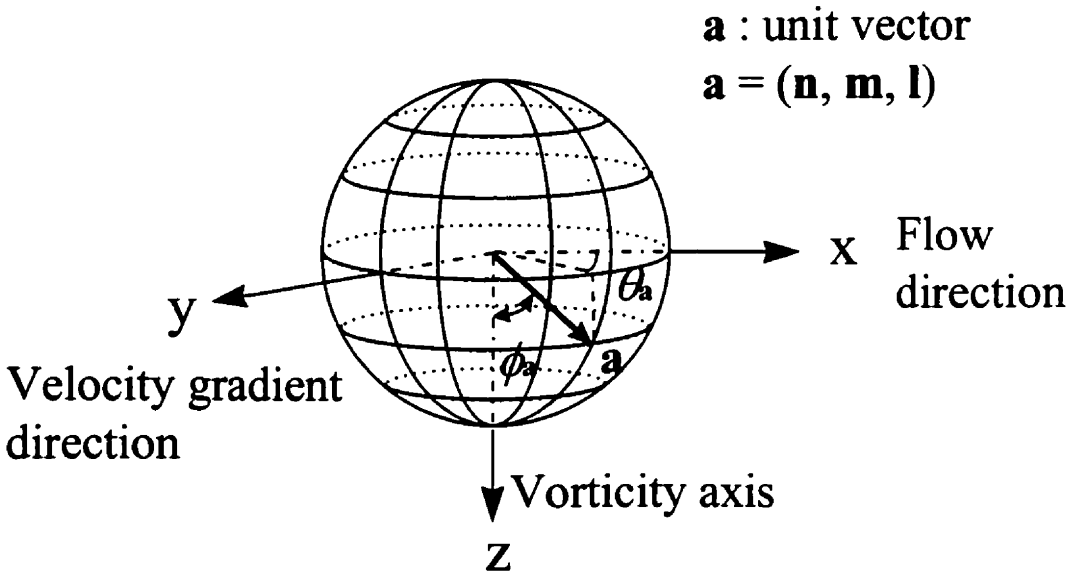

(b)

Figure 3.2: (a) Definition of simple shear flow deformation, and (b) coordinate system. The x-axis is the flow direction, the y-axis is the velocity gradient direction, and the z-axis (out of the plane of the paper) is the vorticity axis. (c) Unit sphere description of director triad (**n**, **m**, **l**). Unit vector **a** (**a** = **n**, **m**, **l**) is completely defined by the azimuthal angle $\theta_a (0 \le \theta_a \le 2\pi)$ and the polar angle $\phi_a (0 \le \phi_a \le \pi)$. In terms of unit vector angles, the equator lies in the shear plane and is given as $(\theta_a, \phi_a) = \left([0,2\pi], \pm \pi/2\right)$, and the north pole and the south pole are located on the vorticity axis and are given by $\phi_a = 0$ and $\phi_a = \pi$ respectively.

$$\text{where } \overline{D}_r = D_r\left[1 - \tfrac{3}{2}(\mathbf{Q}:\mathbf{Q})\right]^{-2}, \quad \beta = \frac{p^2-1}{p^2+1}, \quad p = \frac{r_\perp}{r_\parallel}, \qquad (3.7a,b,c)$$

$$\mathbf{A} = \tfrac{1}{2}\left(\nabla\mathbf{v} + \nabla\mathbf{v}^T\right) = \frac{1}{2}\begin{bmatrix} 0 & \dot\gamma & 0 \\ \dot\gamma & 0 & 0 \\ 0 & 0 & 0 \end{bmatrix}, \quad \mathbf{W} = \tfrac{1}{2}\left(\nabla\mathbf{v} - \nabla\mathbf{v}^T\right) = \frac{1}{2}\begin{bmatrix} 0 & \dot\gamma & 0 \\ -\dot\gamma & 0 & 0 \\ 0 & 0 & 0 \end{bmatrix}. \qquad (3.7d,e)$$

$\overline{D}_r$ is the averaged diffusivity, D_r is the preaveraged diffusivity or isotropic rotary diffusivity of an hypothetical isotropic fluid under same conditions, U is the nematic potential, and β is the shape factor. To specify the molecular geometry we approximate the disk-like shape of molecule of discotic mesophases with an oblate spheroid of aspect ratio p ($p < 1$) where $r_\parallel$ is the length of the shortest and distinct semi axis, and $r_\perp$ the length of the two longest and equal semi axes. For an ideal flat disc $p = 0$ ($\beta = -1$), for a sphere $p = 1$ ($\beta = 0$), and for infinitely long rod $p \to \infty$ ($\beta = 1$). $\mathbf{A}$ and $\mathbf{W}$ are the rate of deformation and vorticity tensor respectively for the considered simple shear flow, and $\dot\gamma$ is the constant shear rate.

3.2.2 Stress Tensor

The extra stress tensor $\mathbf{t}'$ for liquid crystalline materials is given by the sum of symmetric stress tensor $\mathbf{t}^s$ and anti-symmetric stress tensor $\mathbf{t}^a$. The symmetric visco-elastic stress tensor $\mathbf{t}^s$ for thermotropic liquid crystals is expressed as a sum of viscous stress contribution $\mathbf{t}^v$ and elastic stress contribution $\mathbf{t}^e$ (Doi and Edwards, 1986; Larson and Doi, 1991; deGennes and Proust, 1993; Larson, 1996) as:

$$\mathbf{t}' = \mathbf{t}^s + \mathbf{t}^a; \qquad \mathbf{t}^s = \mathbf{t}^v + \mathbf{t}^e \qquad (3.8a,b)$$

In the absence of spatial gradients, the tensor $\mathbf{H}\cdot\mathbf{Q}$ ($\mathbf{H}$ is given by equation(3.6)) is symmetric with the consequence that the antisymmetric stress tensor $\mathbf{t}^a$ vanishes (Farhoudi and Rey, 1993a). In this paper we assume that $\mathbf{Q}$ is spatially homogeneous, therefore $\mathbf{t}' = \mathbf{t}^s$. The symmetric contribution of the extra stress tensor, $\mathbf{t}^s$, is given by equation (3.8b) as a sum of elastic $\mathbf{t}^e$ and viscous $\mathbf{t}^v$ stress contributions. The expression for the elastic stress contribution $\mathbf{t}^e$, derived using the standard equation of

fluxes $\left(\mathbf{t}^s,\ \hat{\mathbf{Q}}\right)$ in terms of forces (**A**, **H**) (deGennes and Proust, 1993), for the presented CE (equation (3.3)) is:

$$\begin{aligned}\mathbf{t}^e &= (c\kappa T)\left[-\tfrac{2}{3}\beta\mathbf{H} - \beta\left\{\mathbf{H}\cdot\mathbf{Q}+\mathbf{Q}\cdot\mathbf{H}-\tfrac{2}{3}(\mathbf{H}:\mathbf{Q})\delta\right\}\right] + \\ &\quad (c\kappa T)\ \tfrac{1}{2}\beta\left[(\mathbf{H}:\mathbf{Q})\mathbf{Q}+\mathbf{H}\cdot\mathbf{Q}\cdot\mathbf{Q}+\mathbf{Q}\cdot\mathbf{H}\cdot\mathbf{Q}+\mathbf{Q}\cdot\mathbf{Q}\cdot\mathbf{H}-\left\{(\mathbf{Q}\cdot\mathbf{Q})\mathbf{H}\right\}\delta\right]\end{aligned} \tag{3.9}$$

where

$$\mathbf{H}(\mathbf{Q})=\frac{1}{6\overline{D}_r}\,\mathbf{H}\left(\mathbf{Q},\overline{D}_r(\mathbf{Q})\right)=-\left[\left(1-\tfrac{1}{3}U\right)\mathbf{Q}-U\mathbf{Q}\cdot\mathbf{Q}+U\left\{(\mathbf{Q}:\mathbf{Q})\mathbf{Q}+\tfrac{1}{3}(\mathbf{Q}:\mathbf{Q})\delta\right\}\right] \tag{3.10}$$

and c is concentration of molecules per unit volume, κ the Boltzmann constant and T the absolute temperature. Equation (3.9) is similar to that proposed by Andrews et al. (1995). The viscous stress contribution $\mathbf{t}^v$ is given by:

$$\begin{aligned}\mathbf{t}^v &= \nu_1\mathbf{A}+\nu_2\left\{\mathbf{Q}\cdot\mathbf{A}+\mathbf{A}\cdot\mathbf{Q}-\tfrac{2}{3}(\mathbf{Q}:\mathbf{A})\delta\right\}+ \\ &\quad \nu_3\left[(\mathbf{A}:\mathbf{Q})\mathbf{Q}+\mathbf{A}\cdot\mathbf{Q}\cdot\mathbf{Q}+\mathbf{Q}\cdot\mathbf{A}\cdot\mathbf{Q}+\mathbf{Q}\cdot\mathbf{Q}\cdot\mathbf{A}+\left\{(\mathbf{Q}\cdot\mathbf{Q})\mathbf{A}\right\}\delta\right]\end{aligned} \tag{3.11}$$

where ν_1, ν_2 and ν_3 are viscosity coefficients. Mapping the above expression with that given in Doi and Edwards (1986), Larson and Doi (1991) and Larson (1996), in which the viscous contribution to stress tensor contains contributions from $\mathbf{Q}^2$ terms only, we arrive at:

$$\mathbf{t}^v = \mu\left[(\mathbf{A}:\mathbf{Q})\mathbf{Q}+\mathbf{A}\cdot\mathbf{Q}\cdot\mathbf{Q}+\mathbf{Q}\cdot\mathbf{A}\cdot\mathbf{Q}+\mathbf{Q}\cdot\mathbf{Q}\cdot\mathbf{A}+\left\{(\mathbf{Q}\cdot\mathbf{Q}):\mathbf{A}\right\}\delta\right] \tag{3.12}$$

where $\nu_1=\nu_2=0$ and $\nu_3=\mu$. Combining equations (3.9) and (3.12), the symmetric extra stress tensor $\mathbf{t}^s$ is given by:

$$\begin{aligned}\frac{\mathbf{t}^s}{(c\kappa T)} &= \xi_v\ Pe\left[(\tilde{\mathbf{A}}:\mathbf{Q})\mathbf{Q}+\tilde{\mathbf{A}}\cdot\mathbf{Q}\cdot\mathbf{Q}+\mathbf{Q}\cdot\tilde{\mathbf{A}}\cdot\mathbf{Q}+\mathbf{Q}\cdot\mathbf{Q}\cdot\tilde{\mathbf{A}}-\left\{(\mathbf{Q}\cdot\mathbf{Q})\tilde{\mathbf{A}}\right\}\delta\right]+ \\ &\quad \left[-\tfrac{2}{3}\beta\mathbf{H}-\beta\left\{\mathbf{H}\cdot\mathbf{Q}+\mathbf{Q}\cdot\mathbf{H}-\tfrac{2}{3}(\mathbf{H}:\mathbf{Q})\delta\right\}+\right. \\ &\quad \left.\tfrac{1}{2}\beta\left[(\mathbf{H}:\mathbf{Q})\mathbf{Q}+\mathbf{H}\cdot\mathbf{Q}\cdot\mathbf{Q}+\mathbf{Q}\cdot\mathbf{H}\cdot\mathbf{Q}+\mathbf{Q}\cdot\mathbf{Q}\cdot\mathbf{H}-\left\{(\mathbf{Q}\cdot\mathbf{Q})\mathbf{H}\right\}\delta\right]\right]\end{aligned} \tag{3.13}$$

where $\xi_v = \dfrac{\mu\, 6D_r}{c\kappa T}$ is a dimensionless constant representing the ratio of the viscous $\mathbf{t}^v$ to the elastic $\mathbf{t}^e$ stress contributions, previously introduced by Larson (1996);

$Pe = \dfrac{\dot{\gamma}}{6D_r}$ is Peclet number or the dimensionless shear rate, and $\tilde{\mathbf{A}}$ is dimensionless rate of deformation tensor. At low shear rates elastic stress contributions are proportional to $1/D_r$ whereas the viscous contributions are proportional to μ (Larson, 1996).

The first normal stress difference (N_1), the second normal stress difference (N_2), and the apparent shear viscosity (η) are non-dimensionalized as follows:

$$N_1^* = \frac{N_1}{c\kappa T} = \frac{t_{xx}^s - t_{yy}^s}{c\kappa T} \tag{3.14a}$$

$$N_2^* = \frac{N_2}{c\kappa T} = \frac{t_{yy}^s - t_{zz}^s}{c\kappa T} \tag{3.14b}$$

$$\eta^* = \frac{\eta}{(c\kappa T)\,Pe} = \frac{6D_r}{c\kappa T}\,\frac{t_{xy}^s}{\dot{\gamma}} \tag{3.14c}$$

where the superscript "*" represents the corresponding dimensionless variable. For parametric studies three values of ξ_v (=0.001, 0.1, 0.2) are used. The calculated numerical values of N_1^* and N_2^* are scaled with their corresponding values at $Pe \to \infty$ and $\xi_v = 0.2$, whereas η^* is scaled with the zero shear viscosity, i.e., $Pe \to 0$ and $\xi_v = 0.2$. The normalized values are given as:

$$N_{1,\,\text{norm}}^* = \frac{N_1^*}{\left|N_{1,\,Pe\to\infty,\,\xi_v=0.2}^*\right|} \tag{3.15a}$$

$$N_{2,\,\text{norm}}^* = \frac{N_2^*}{\left|N_{2,\,Pe\to\infty,\,\xi_v=0.2}^*\right|} \tag{3.15b}$$

$$\eta_{\text{norm}}^* = \frac{\eta^*}{\left|\eta_{Pe\to 0,\,\xi_v=0.2}^*\right|} \tag{3.15c}$$

The values of $\left|N_{1,\,Pe\to\infty,\,\xi_v=0.2}^*\right|$, $\left|N_{2,\,Pe\to\infty,\,\xi_v=0.2}^*\right|$ and $\left|\eta_{Pe\to 0,\,\xi_v=0.2}^*\right|$ for the considered cases, discussed later, are given in Table 3.1. For simplicity, we drop the subscript "norm" for the scaled numerical values in the following discussion.

Table 3.1

Normalized Asymptotic values of Rheological Functions

	$N^{\bullet}_{1,\,Pe\to\infty,\,\xi_v=0.2}$	$N^{\bullet}_{2,\,Pe\to\infty,\,\xi_v=0.2}$	$\eta^{\bullet}_{Pe\to 0,\,\xi_v=0.2}$
$U=6$, $\beta=-0.8$ Planar microstructure mode Figure 3.4	-0.4563	0.4499	0.05027
$U=6$, $\beta=-0.8$ non-Planar microstructure mode Figure 3.5	0.04144	0.06847	0.02182
$U=3.5$, $\beta=-0.8$ Planar microstructure mode Figure 3.6	0.0433	-0.0426	0.016

3.3 Classification of Discotic Mesophases based on Microstructural Phenomena

Depending on the value of the tumbling function λ there are two different microstructure modes predicted by the presented theory for discotic mesophases in steady simple shear flows. Similar modes are predicted by macroscopic theories presented by Farhoudi and Rey (1993a, 1993b) for uniaxial rod-like nematics, but that study was restricted to the shear plane. The tumbling function λ for the present theory is given by (Tsuji and Rey, 1997):

$$\lambda = \beta \frac{\left(2 + S - \frac{1}{2}S^2 + P - \frac{1}{6}P^2\right)}{(3S - P)}. \tag{3.16}$$

Figure 3.3a shows the tumbling function, λ, as a function of both the uniaxial S and biaxial P alignments for discotic nematics with shape factor β = -0.8. The tumbling function λ, is negative (positive) for all values of biaxial alignment $P < 3S$ ($P > 3S$) with a discontinuity at $P = 3S$. The λ curve intersects the horizontal plane $\lambda = -1$ at some critical value of uniaxial $S^{\#}(U^{\#})$ and biaxial $P^{\#}$ alignments for a given shape factor β. From equation (3.16) we have:

$$-1 = \beta \frac{\left(2 + S^{\#} - \frac{1}{2}S^{\#2} + P^{\#} - \frac{1}{6}P^{\#2}\right)}{\left(3S^{\#} - P^{\#}\right)} \tag{3.16a}$$

For example for $\beta = -0.8$ and $P^{\#} = 0$, $S^{\#} = 0.66$ (see Figure 3.3c).

The (P - S) phase plane for nematics (Singh and Rey, 1995) in terms of S and P based on the restriction on the eigenvalues of order parameter **Q** is shown in Figure 3.3b. As mentioned above this study refers only to normal nematics, the sign of the tumbling function, λ, for normal discotics is marked in Figure 3.3b. The discontinuity occurs near the uniaxial nematics line where the largest and the intermediate eigenvalues of **Q** are equal. Furthermore, in this study we are restricted to the part of first quadrant of alignment (P - S) phase plane where the tumbling function λ is negative. In the region of negative λ, as the shape factor β increases the curves move upwards. This is shown in Figure 3.3c in which λ is plotted as a function of uniaxial alignment S at a fixed biaxial alignment ($P = 0$) for different shape factors $\beta = -0.9$ (full line), -0.8 (dash line) and -0.7 (triple dot-dash line). In the present model the tumbling function λ monotonically increases with increasing S in the range [0, 1] for all values of β, and has no local maxima as shown in Figure 3.3c.

Based on the nematic potential U value, discotic nematics with a given shape factor β show different microstructure phenomena, and are classified as aligning ($U < U^{\#}$) or non-aligning ($U > U^{\#}$) discotic nematics. As the shape factor β increases, the λ curve moves up and intersects the plane ($\lambda = -1$) at lower $S^{\#}$ ($U^{\#}$), thus decreasing (increasing) the range of U at which discotic nematics show aligning (non-aligning) characteristics.

3.3.1 Simple Aligning Discotics

Discotic nematics for which the director **n** reaches a unique stable steady state orientation within the shear plane ($n_z = 0$) for all magnitudes of Pe are termed aligning discotics, and are characterized by λ (S_{eq}, $P = 0$, β) < -1. Aligning discotics do not show any stable non-planar ($n_z \neq 0$) orientation mode under simple shear flows. The uniaxial director **n** aligns close to the velocity gradient direction in the second or fourth orientation quadrant. The angle between the steady orientation of **n** and the velocity gradient direction decreases with increasing Pe, and tends to zero as $Pe \rightarrow \infty$.

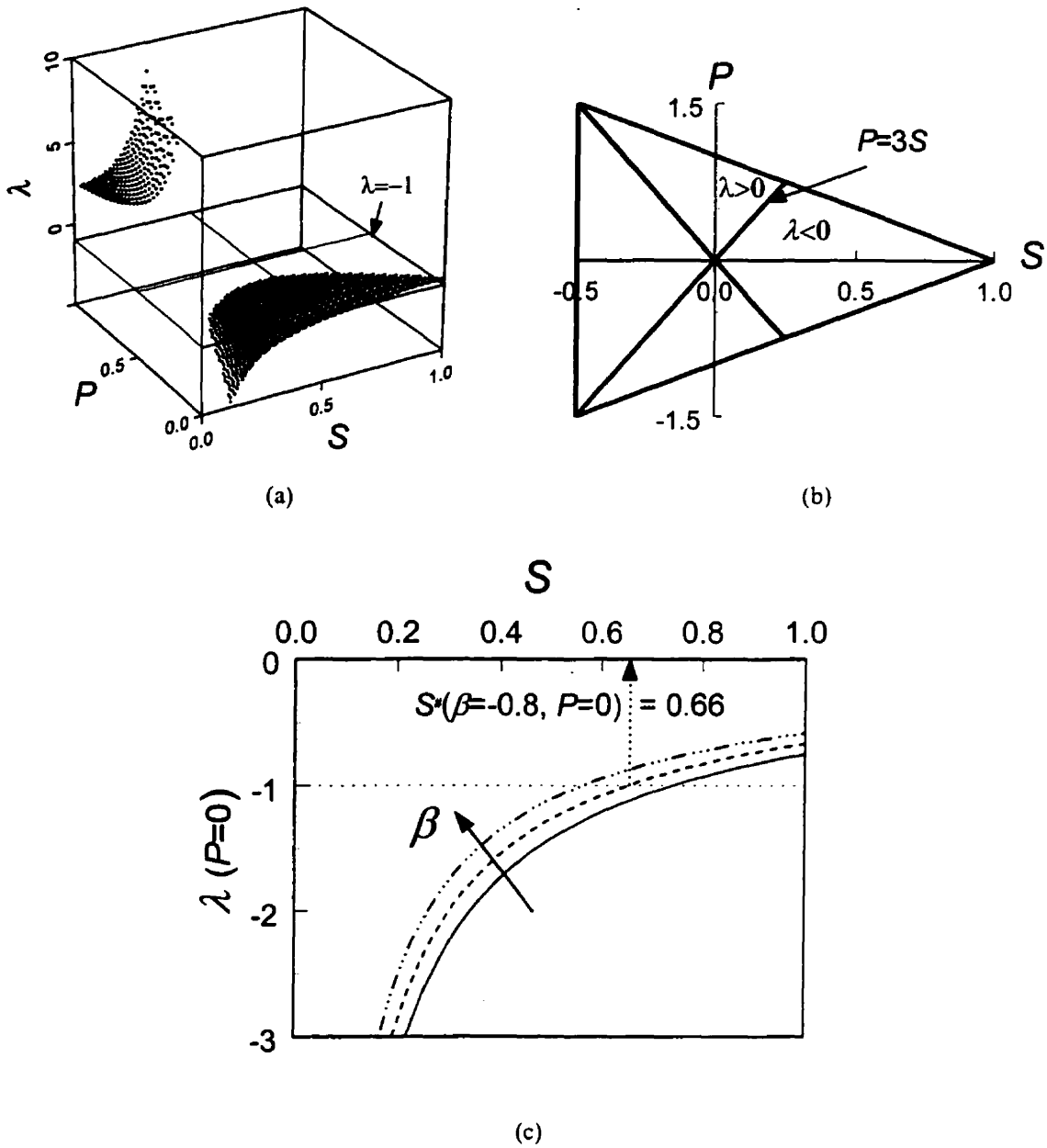

Figure 3.3: (a) Tumbling function λ as a function of uniaxial S and biaxial P alignments for β = -0.8. The λ surface monotonically decreases (increases) for $P < 3S$ ($P > 3S$), with a discontinuity at $P = 3S$. In discotic nematics planar steady state exists only if $\lambda < -1$. (b) The complete P - S phase plane showing regions where λ is positive or negative. This study is restricted to the normal discotic nematics for alignments values for which λ is negative. (c) λ as a function of uniaxial alignment S for $P = 0$, and for the shape factor β = -0.9 (full line), -0.8 (dash line), and -0.7 (triple dot-dash line). The λ curves move upwards and towards left with increasing β, diverge as $S \rightarrow 0$, and intersect the line $\lambda = -1$ at lower $S^{\#}$.

3.3.2 Non-Aligning Discotics

Discotic nematics for which all the three stable planar and one stable non-planar orientation states exist are classified as non-aligning discotic nematics, and are characterized by λ (S_{eq}, $P = 0$, β) > -1. The microstructural phenomena predicted by the CE for non-aligning discotics under shear flows have been presented previously (Singh and Rey, 1998), and is summarized in what follows. The predicted stable orientation modes, in terms of uniaxial director **n** dynamics are: (a) ITO or in-plane tumbling orbit, (b) IWS or in-plane wagging state, (c) ISS or in-plane steady state, (d) LRS or log rolling state. The first two orientation states, ITO and IWS, are periodic modes whereas the last two, ISS and LRS, are stationary modes. All orientation states except LRS are in-plane or planar orientation modes (i. e., $n_z = 0$). In case of planar steady state, the director **n** aligns close to the velocity gradient direction in the first or third orientation quadrant. The angle between the steady orientation of **n** and the velocity gradient direction decreases with increasing Pe, and tends to zero as $Pe \rightarrow \infty$.

The effect of biaxial orientation is not considered in the above classification. However, some differences are apparent, for example in aligning (non-aligning) discotics in the stationary planar state, the biaxial director **m** (**l**) aligns along the vorticity axis and vice versa.

3.4 Numerical Results and Discussion

In this section we present the rheological predictions, and the relations among shear rheological properties, microstructure modes, processing conditions and material properties of discotic mesophases under simple shear flows.

3.4.1 Microstructure Modes-Rheology Relations

As mentioned above the CE predicts one non-planar steady state mode (log-rolling), two planar time periodic modes (tumbling and wagging) and one planar steady state mode. In order to compute average values of the rheological properties for the tumbling and wagging modes, time averaging is performed. In this sub-section first we

present rheological properties corresponding to planar and non-planar microstructure modes, which will be followed by their comparison.

3.4.1.1 Planar Mode of Non-Aligning Discotic Nematics

Figure 3.4 shows the microstructure-rheology relations for non-aligning discotic nematics under shear flows corresponding to planar modes (tumbling, wagging and flow-aligning). Figure 3.4(a) shows the uniaxial alignment S (full line), biaxial alignment P (dash line) and uniaxial director **n** azimuthal angle θ_n (triple dot-dash line) as a function of dimensionless shear rate Pe, for $\beta = -0.8$ and $U = 6$. The various flow regimes, based on the uniaxial orientation **n** dynamics are also indicated. In this planar orientation mode the uniaxial director **n** and biaxial director **m** lie in the shear plane ($\phi_n = \phi_m = 90$, $\theta_n = \theta_m = [0, 360]$) and the biaxial director **l** aligns along the vorticity axis ($\phi_l = 0$). The biaxial directors **m** and **l** are not represented in Figure 3.4(a) as **m**$\perp$**n** and the orientation of **l** is independent of shear rate. The full microstructure description in terms of director triad (**n**, **m**, **l**) can be given in terms of the corresponding polar and azimuthal angles as:

n: $\phi_n = 90$, $\theta_n = [0, 360]$; (3.17a,b)

m: $\phi_m = 90$, $\theta_m = [0, 360]$; (3.17c,d)

l: $\phi_l = 0$. (3.17e)

The average uniaxial orientation of discotic nematics is near the velocity gradient direction for all planar periodic as well as steady states. The uniaxial (biaxial) alignments show three regions: low and high shear rate plateaus with an intermediate power law region. For the steady state regime, the values of S, P and θ_n are plotted on the same axis represented by $\langle S \rangle$, $\langle P \rangle$ and $\langle \theta_n \rangle$ respectively in Figure 3.4a.

Figure 3.4b shows the scaled dimensionless first normal stress difference N_1^* as a function of Pe corresponding to Figure 3.4a for $\xi_v = 0.001$ (full line), 0.1 (dash line), and 0.2 (triple dot-dash line). The first normal stress difference N_1^* is positive for low shear rates, in the tumbling regime, and becomes negative near the transition from tumbling to

wagging regime. N_1^* remains negative for the higher values of shear rates in the oscillatory and steady state regimes. The high *Pe* plateaus remain negative, and increase with increasing ξ_v. The phenomenon is qualitatively similar to that presented by Andrews et al. (1995) for rod-like nematics using a similar CE, however, it was unable to predict second sign transition in N_1^*. The present model also has this limitation for both rod-like as well as discotic nematics.

Figure 3.4c shows the scaled dimensionless second normal stress difference N_2^* as a function of *Pe* corresponding to Figure 3.4a, for ξ_v = 0.001 (full line), 0.1 (dash line), and 0.2 (triple dot-dash line). N_2^* is nearly zero for low *Pe*, in the tumbling regime, and then increases exponentially with intermediate *Pe* in the wagging regime before reaching a high *Pe* plateau in the steady state regime. The high *Pe* plateaus and the exponential increase at intermediate *Pe* increases with increasing ξ_v. N_2^* corresponding to the planar mode for discotic nematics does not show any sign transition, and does not resemble that of rod -like nematics. The theory used by Andrew et al. (1995) failed to predict any sign transition in case of rod-like nematics. However, the present theory when used for rod-like nematics predicts the first sign transition, but fails to predict the second at high *Pe*, reported by Marrucci and Maffetone (1989) and Baek et al. (1993, 1994).

The sign transitions in N_1^* and N_2^* for planar microstructure mode are attributed due to the coupling between director orientation $\mathbf{n}$ and alignment S (Marrucci and Maffettone, 1989; Larson, 1990; Farhoudi and Rey 1993a). Also, Marrucci and Mafettone (1989) suggested that alignment S rather than orientation plays a more dominant role in the sign transition in N_1^* by showing that the negative N_1^* persists beyond shear rates at which orientation angle becomes positive, and the negative N_1^* is due to the low alignment. Farhoudi and Rey (1993a) used a macroscopic theory with a set of material parameters that results in a tumbling function λ with a local minima for rod-like nematics, predicted both sign transitions in N_1^* and N_2^*, and the second sign change is shown to be due to the increase in the alignment above the equilibrium values

at high shear rates (Farhoudi and Rey, 1993a) which is attributed due to the 'U' shape of λ curve for rod-like nematics. In the work of Andrews et al. (1995) and in the present model there is only one adjustable parameter, the shape factor β, and there is no local maxima (minima) in λ for the useful limits ($0 \le S \le 1$, $0 \le P \le 1$) of alignments for discotic (rod-like) nematics as shown in figure 3.3c. As is well known in case of discotic (rod-like) nematics, steady state exists only when $\lambda < -1$ ($\lambda > 1$). In the present study, in steady state regime alignment S is always less than the equilibrium alignment S_{eq} (see Singh and Rey, 1998). Hence the present theory is unable to predict the second transition in N_1^* or the positive N_1^* at high shear rates as predicted by other molecular or mesoscopic theories for rod-like nematics. The results presented here for low and intermediate *Pe* suggest that N_1^* is qualitatively similar for both rod-like and discotic nematics despite the reversals in other material functions.

Figure 3.4d shows the scaled dimensionless apparent shear viscosity η^* as a function *Pe* corresponding to Figure 3.4a for ξ_v = 0.001 (full line), 0.1 (dash line), and 0.2 (triple dot-dash line). The scaled apparent viscosity η^* has three distinct regions: low and high shear rate plateaus, and an intermediate power law regime. The difference, $\Delta\eta^* = \eta_l^* - \eta_h^*$, between the low ($\eta_l^*$) and high ($\eta_h^*$) shear rate viscosities increases with increasing ξ_v. The low *Pe* plateau persists till the end of tumbling regime for which the average values of uniaxial and biaxial alignments ($\langle S \rangle$, $\langle P \rangle$) are independent of *Pe*. For the intermediate *Pe* the average value of uniaxial (biaxial) alignment increases (decreases), and is reflected in the shear thinning region of η^*. High shear rate independency of η^* is qualitative similar to a majority of reported viscosity data for mesophase pitches (McHugh et al., 1992; Fatholahi and White, 1994; Edie et al., 1994; Fleurot et al., 1995).

The predicted profiles of η^* are qualitatively similar to those for rod-like nematics shown by Larson (1990) in which the low shear rate plateau ends at $\dot{\gamma} < 0.003$. Baek et al. (1994) also predicted a low shear rate plateau along with a shear thinning region for a range of viscous to elastic stress ratios. The shear rate range for the lower

plateau can be easily evaluated for a known D_r from the relationship $\dot{\gamma} = 6 D_r Pe$. The rotational diffusivity D_r for discotic mesophase pitches is unknown, but it can be evaluated from either experimental rheological data using methods employed by Ooi and Sridhar (1994), and Baek et al. (1993) or by employing NMR techniques (Janik et al., 1977; Franklin, 1977; Khabibullaev et al., 1994). The experimental data for rotational diffusivity D_r is available for a wide range of rod-like low molecular weight liquid crystals (Janik et al., 1977; Franklin, 1977) and liquid crystalline polymers (Mori et al., 1982; Ooi and Sridhar, 1994; Baek et al., 1993).

3.4.1.2 Non-Planar (Log-Rolling) Mode of Non-Aligning Discotic Nematics

The bifurcation analysis of equation (3.3) revealed that the log-rolling steady state is stable for all shear rates, and thus equation (3.3) predicts multistability at all shear rates (Singh and Rey, 1998). In this section we present microstructure-rheology relations for the log-rolling state, shown in Figure 3.5, for non-aligning discotic nematics.

Figure 3.5(a) shows the uniaxial alignment S (full line), biaxial alignment P (dash line), and biaxial director **m** azimuthal angle θ_m (triple dot-dash line) as a function of dimensionless shear rate Pe, for β = -0.8 and U = 6. In this microstructure mode the uniaxial director **n** aligns along the vorticity axis ($\phi_n = 0$) and the biaxial directors **m** and **l** lie on the shear plane ($\phi_m = \phi_l = 90$). As shown in the Figure 3.5a at low Pe the biaxial director **m** (**l**) lies in the middle of fourth or third (first or second) quadrant. As Pe increases the steady state orientation of the uniaxial director **n** remains along vorticity axis however, that of the biaxial director **m** (**l**) shifts, exponentially for the intermediate Pe, towards the velocity gradient (flow) direction. For very high Pe the uniaxial and biaxial directors (**n**, **m**, **l**) lie along the vorticity direction, velocity gradient direction and flow direction respectively. The biaxial director **l** is not represented on Figure 3.5a since $\mathbf{m} \perp \mathbf{l}$. The complete microstructure description in terms of the director triad (**n**, **m**, **l**) can be presented in terms of the corresponding polar and azimuthal angles as:

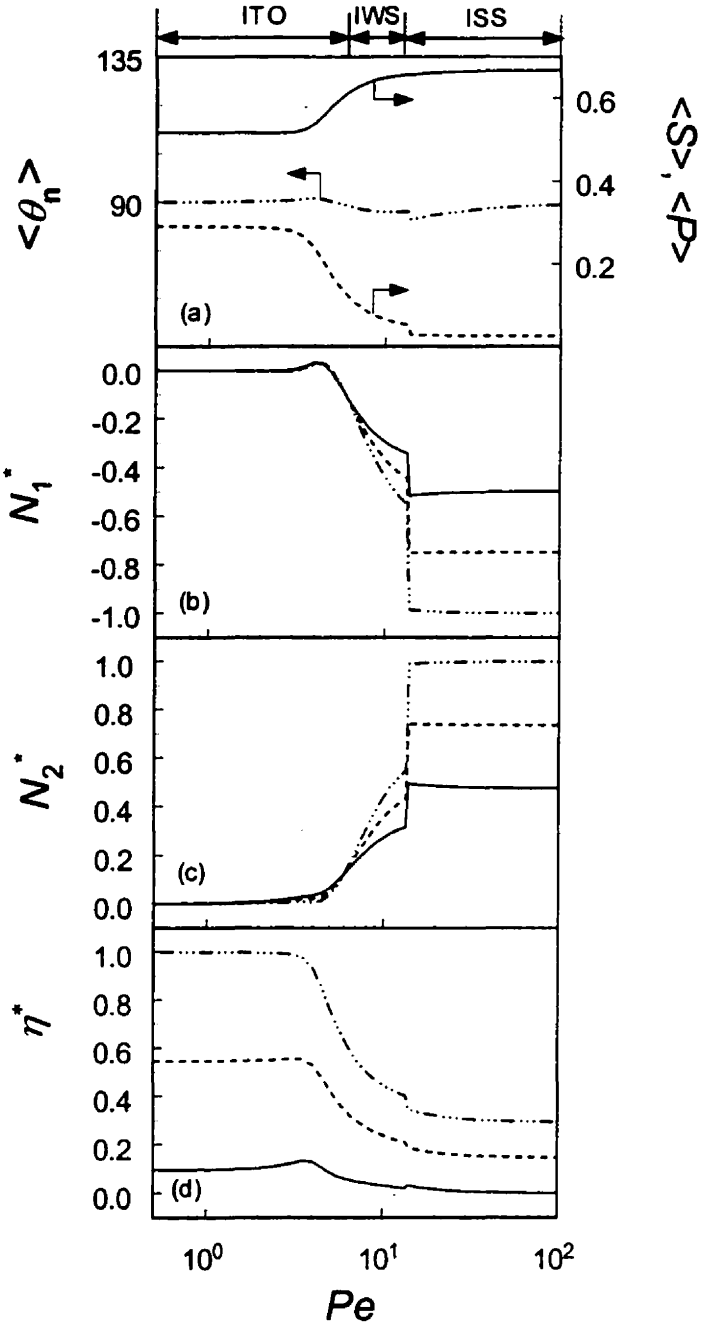

Figure 3.4: Microstructure-rheology relations for non-aligning discotic mesophases for the planar microstructure mode. (a) Microstructure features of non-aligning discotic mesophases for the planar orientation mode: uniaxial alignment S (full line), biaxial alignment P (dash line) and uniaxial director **n** azimuthal angle θ_n (triple dot-dash line) as a function of Pe, for β = -0.8 and U = 6. Corresponding rheological predictions: (b) scaled dimensionless first normal stress difference N_1^*, (c) scaled dimensionless second normal stress difference N_2^*, and (d) scaled dimensionless apparent shear viscosity η^* as a function of Pe for ξ_v = 0.001 (full line), 0.1 (dash line), and 0.2 (triple dot-dash line). For planar mode the first normal stress difference is similar to that of corresponding rod-like nematics. The apparent shear viscosity η^* shows three regions.

n: $\phi_n = 0$; (3.18a)

m: $\phi_m = 90$, $\theta_m = [90, 135]$ or $[-45, -90]$; (3.18b,c)

l: $\phi_l = 90$, $\theta_l = [180, 225]$ or $[0, 45]$. (3.18d,e)

The uniaxial (biaxial) S (P) alignment decreases (increases) with increasing Pe, however, the drop in S is much smaller than the rise in P.

Figure 3.5b shows the scaled dimensionless first normal stress difference N_1^* as a function of Pe corresponding to Figure 3.5a for $\xi_v = 0.001$ (full line), 0.1 (dash line), and 0.2 (triple dot-dash line). N_1^* is always positive and can be characterized in terms of three different regions: two plateaus at low and high Pe and an intermediate power law region. The low Pe plateau is independent of ξ_v, while the slope of the power law region and the magnitude of the high Pe plateau increases with increasing ξ_v. Larson and Ottinger (1991) also predicted positive N_1^* corresponding to the non-planar orientation mode for rod-like nematics.

Figure 3.5c shows the scaled dimensionless second normal stress difference N_2^* as a function of Pe corresponding to Figure 3.5a, for $\xi_v = 0.001$ (full line), 0.1 (dash line), and 0.2 (triple dot-dash line). N_2^* is also marked by two low and high shear rate plateaus with one highly dependent intermediate shear rate region. N_2^*, like N_1^*, is independent of ξ_v at low Pe but exhibits very strong dependence on ξ_v at intermediate and high Pe. At low ξ_v (= 0.001), N_2^* has mainly elastic contributions, and decreases with increasing intermediate Pe before reaching the high Pe plateau. At higher ξ_v (= 0.2), the viscous contributions increase and N_2^* reaches a positive high shear rate plateau. The high Pe plateaus increase, going from negative values to positive, with increasing ξ_v. The sign of the high Pe plateau in N_2^* may also be used as an indication of the relative contribution of the viscous stresses. For example, the positive high Pe plateau in N_2^* shows that the viscous contributions dominate the total induced stresses.

The complex phenomena in N_1^* and N_2^* are due to the coupling among uniaxial and biaxial alignments, and biaxial orientations. The uniaxial orientation is fixed along the vorticity axis, and the change in uniaxial alignment, see Figure 3.5a is much smaller than that in biaxial alignment. Hence, the rheological properties in this microstructure mode are affected mainly by flow-induced biaxiality.

Figure 3.5d shows the scaled dimensionless apparent shear viscosity η^* as a function of *Pe* corresponding to Figure 3.5a for $\xi_v = 0.001$ (full line), 0.1 (dash line), and 0.2 (triple dot-dash line). η^* is independent of shear rates at low ξ_v, however for higher values of ξ_v there is a slight shear thinning region at intermediate *Pe* which increases with increasing ξ_v. The predicted shear viscosity resembles qualitatively with that reported in the literature for mesophase pitches (McHugh et al., 1992; Edie et al., 1994; Fatholahi and White, 1994; Fleurot et al., 1995).

Comparison of Figures 3.4, and 3.5 reveals that the rheological properties depend strongly on the microstructure modes. As discussed above the rheological properties corresponding to the log-rolling mode are mainly due to the flow induced biaxiality, whereas those for planar microstructure mode are a uniaxial phenomena. At low shear rates N_1^* and N_2^* are comparable in magnitude for both microstructure modes. Hence as suggested by Larson and Ottinger (1991), the average of rheological properties at low shear rates will represent the combined effect from both microstructure modes. The apparent log-rolling shear viscosity η^* is roughly half in magnitude than that of planar mode at low *Pe*, whereas the high *Pe* plateaus in both of the microstructure modes are comparable.

3.4.2 Processing Condition-Rheology Relations

In this subsection rheological predictions for discotic nematics at low U (for aligning discotics) are presented, and compared with those at high U presented in the previous section. For thermotropic materials the nematic potential U is inversely proportional to temperature T. At low U (high T) the non-planar log-rolling state is unstable, and there is only one planar stable flow-aligning steady state.

Figure 3.6a shows the uniaxial alignment S (full line), biaxial alignment P (dash line) and uniaxial director **n** azimuthal angle θ_n (triple dot-dash line) as a function of the dimensionless shear rate Pe, for β = -0.8, and U = 3.5. In this microstructure mode the uniaxial (biaxial) director **n** (**l**) aligns in the shear plane near the velocity gradient (flow) direction in the second or fourth orientation quadrant, and the biaxial director **m** lies along the vorticity axis. The complete microstructure description in terms of director triad (**n**, **m**, **l**) can be given in terms of polar and azimuthal angles as:

$$\mathbf{n}: \qquad \phi_n = 90 \ , \quad \theta_n = [90,\ 135] \ \text{or} \ [-45,\ -90] \ ; \tag{3.19a,b}$$

$$\mathbf{m}: \qquad \phi_m = 0 \ ; \tag{3.19c}$$

$$\mathbf{l}: \qquad \phi_l = 90 \ , \quad \theta_l = [0,\ 45] \ \text{or} \ [180,\ 225] \ . \tag{3.19d,e}$$

As shown in Figure 3.6a, for low Pe, uniaxial director **n** shifts towards the velocity gradient direction as Pe increases. The uniaxial (biaxial), S (P), alignment slightly increases (decreases) with increasing Pe. The flow induced biaxiality P is close to zero, hence the discotic nematic phase is essentially uniaxial under shear flow.

Figures 3.6b and 3.6c show the scaled dimensionless first normal stress difference N_1^* and the dimensionless second normal stress difference N_2^*, respectively, as a function of Pe corresponding to Figure 3.6a for ξ_v = 0.001 (full line), 0.1 (dash line), and 0.2 (triple dot-dash line). N_1^* (N_2^*) is always positive (negative) for all values of Pe, and increases (decreases) at low and intermediate shear rates before reaching high shear rate plateau. The phenomena is qualitative similar to that for aligning rod-like nematics by Farhoudi and Rey (1993b, 1993c). As the ratio ξ_v increases, N_1^* (N_2^*) also increases (decreases) both at low and high shear rates, however, the difference in values of N_1^* and N_2^* with increasing ξ_v is more at high Pe is more than that at low Pe, thereby showing the relative dominance of viscous contribution at high shear rates.

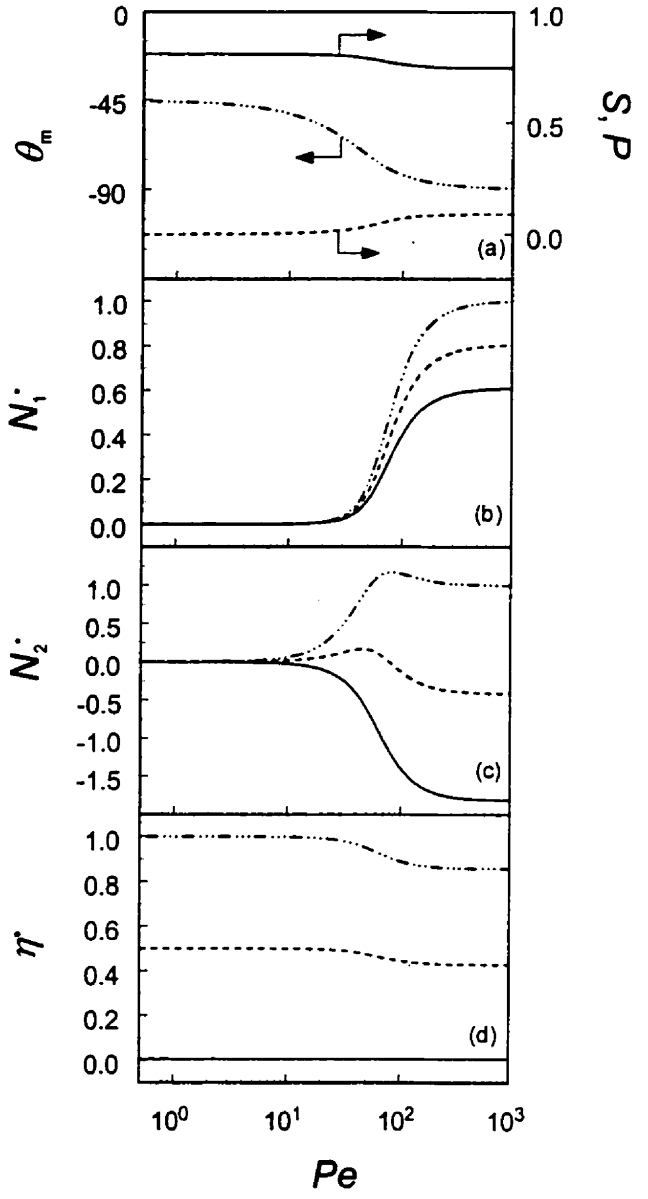

Figure 3.5: Microstructure-rheology relations for non-aligning discotic mesophases for the non-planar log-rolling mode. (a) Microstructure features for the log-rolling orientation mode: uniaxial alignment S (full line), biaxial alignment P (dash line) and biaxial director **m** azimuthal angle θ_m (triple dot-dash line) as a function of Pe for β = -0.8 and U = 6. Corresponding rheological predictions: (b) scaled dimensionless first normal stress difference N_1^*, (c) scaled dimensionless second normal stress difference N_2^*, and (d) scaled dimensionless apparent shear viscosity η^* as a function of Pe for ξ_v = 0.001 (full line), 0.1 (dash line), and 0.2 (triple dot-dash line). N_1^* (N_2^*) show three regions: two plateaus at low and high Pe with an intermediate power law (shear rate dependent) region. The high Pe plateau for N_2^* depends strongly on ξ_v. η^* is essentially independent of shear rate. The rheological properties in this mode are governed by the flow-induced biaxiality.

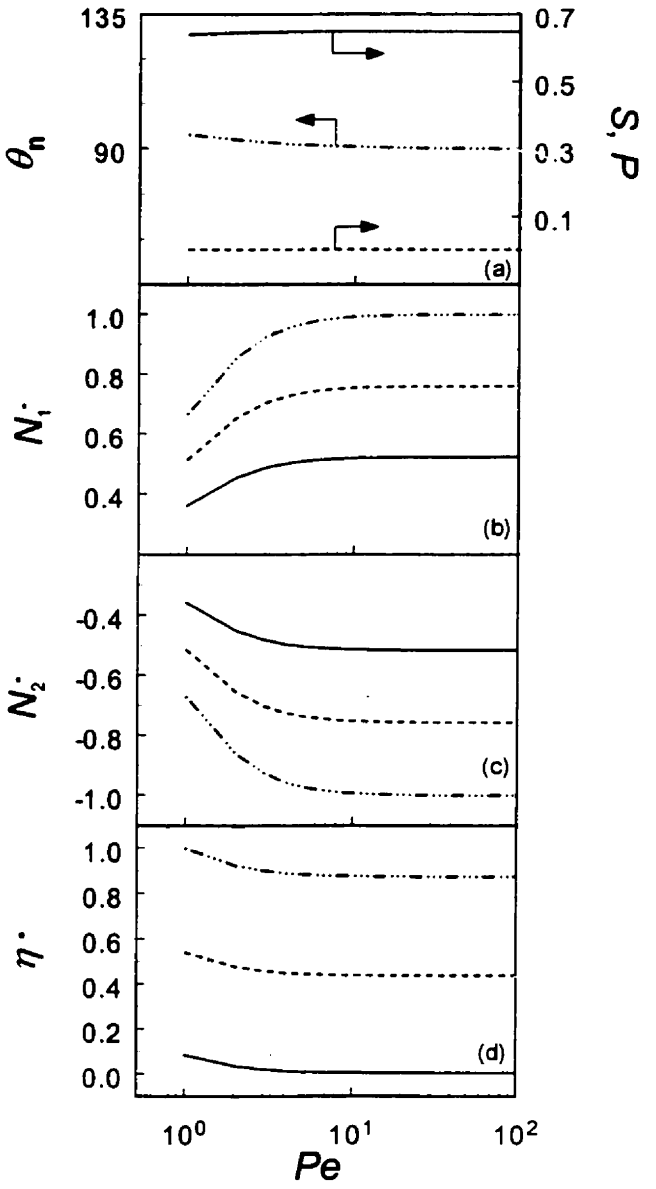

Figure 3.6: Microstructure-rheology relations for aligning discotic mesophases. (a) Microstructure features under simple shear flows: uniaxial alignment S (full line), biaxial alignment P (dash line) and uniaxial director **n** azimuthal angle θ_n (triple dot-dash line) of aligning discotic nematics as a function of Pe for β = -0.8 and U = 3.5. Corresponding rheological predictions: (b) scaled dimensionless first normal stress difference N_1^*, (c) scaled dimensionless second normal stress difference N_2^*, and (d) scaled dimensionless apparent shear viscosity η^* as a function of Pe for ξ_v = 0.001 (full line), 0.1 (dash line), and 0.2 (triple dot-dash line). N_1^* (N_2^*) is always positive (negative) which is similar to those of rod-like nematics. The dimensionless apparent viscosity η^* decreases exponentially for low shear rates but for intermediate and high shear rates is independent of Pe. N_1^* and η^* (N_2^*) increase (decreases) with increasing ξ_v.

Figure 3.6d shows the scaled dimensionless apparent shear viscosity η^* as a function of dimensionless shear rate *Pe* corresponding to Figure 3.6a for $\xi_v = 0.001$ (full line), 0.1 (dash line), and 0.2 (triple dot-dash line). The apparent shear viscosity η^* drops at low shear rates, but essentially remains independent of shear rates at intermediate and high shear rates at all values of ratio ξ_v. The effect ξ_v on η^* follows the same trend as mentioned above, however, the relative effect of ξ_v at low and high shear rates is roughly the same. The apparent shear viscosity η^* in this case resembles that reported by Fleurot (1998) for mesophase pitches.

The comparison of predicted rheological properties of discotics of same shape parameter (β = -0.8) reveals that as U ($U \propto 1/T$, T : temperature) increases, or equivalently as T decreases, beyond a critical value the following transitions may occur depending on the magnitude of the *Pe*: tumbling → flow alignment, wagging → flow alignment, log-rolling → flow alignment. Depending on the value of *Pe*, a decrease in temperature causes a change in the rheological material functions that can be deduced directly from the presented results. For example, if thermal change produces the log-rolling to flow-alignment transition, then N_1^* (N_2^*) will show monotonic increase (decrease) at low *Pe* and high *Pe* plateau.

3.4.3 Material Parameter - Rheology Relations

In this subsection the effect of material parameter or shape factor β on rheological properties is discussed. As shown in Figure 3.3c, with increasing β the tumbling function λ curve shifts upwards and towards left, and thus intersects the line $\lambda = -1$ at lower $S^{\#}$ ($U^{\#}$). Therefore as β increases the range of S_{eq} (U_{eq}), for which discotic mesophases display non-aligning (aligning) microstructural behavior also increases (decreases). In other words, discotic mesophases with higher β have more tendencies to display non-aligning behavior than those with the lower β. For a fixed U (= U_{eq}) and with increasing β, the shear induced microstructural features of discotic mesophases will change from non-aligning to aligning at a critical $\beta^{\#}$. Hence, the corresponding rheological properties

(N_1^*, N_2^* and η^*) will also change, as explained in the previous section. For a given nematic potential U_{eq} = 3.75 (see Figure 3.3c), the discotic nematics with β = -0.7 display simple aligning microstrucutral features and hence the corresponding rheological properties are those for aligning discotics (discussed above), whereas the discotic nematics with β = -0.9 display complex non-aligning microstructural features and hence the corresponding rheological properties are those for non-aligning discotics. Thus for a fixed U or alternatively for fixed T, as shape factor β increases, the corresponding rheological properties change.

3.5 Conclusions

Predictions of rheological properties of discotic mesophases are presented. The predicted rheological properties of discotic mesophases are discussed and assessed within the context of nematorheology.

The predicted first normal stress difference N_1 corresponding to the planar microstructure mode of non-aligning discotics is similar to that corresponding to the rod-like nematics at low shear rates. At higher shear rates the present theory does not accurately predict N_1 corresponding to planar mode of non-aligning rod-like nematics , hence no comparison can be drawn between them. N_1 for non-planar mode is always positive and increases exponentially for intermediate shear rates before reaching high shear rate plateau, and is mainly due to flow-induced biaxiality. For non-aligning discotic nematics, N_1 corresponding to the planar and the non-planar microstructure modes are comparable at low shear rates. As the more accurate representation of N_1 is to take average of both values corresponding to planar and non-planar modes (Larson and Öttinger, 1991) of non-aligning discotics, which may result in the disappearance of negative N_1 in discotics in which viscous contribution dominates. Thus sign transition in N_1 may not be a correct check for non-aligning discotics. Also N_1 of aligning discotics is similar to that of rod-like nematics at all shear rates. N_1 is always positive for discotic mesophase at lower values of U (aligning nematics).

The predicted apparent shear viscosity of discotic mesophases at low U (or high T) is qualitatively similar to that reported in the literature at all shear rates (Fleurot 1998);

whereas that at high U (low T) is qualitatively similar to that reported in literature for intermediate and high shear rates (McHugh et al. 1992; White and Fatholahi, 1994; Fleurot et al. 1995; Fleurot, 1998).

The present work is the first attempt to establish the relations between flow-induced microstructure with rheological material functions. A sufficiently number of distinguishing features have been identified that are specific to the discotic nature of the nematic phase, and augment the number of quantitative and qualitative differences between discotic and rod-like nematics that had been noted in the literature (Farhoudi and Rey, 1993c). How this distinguishing rheological features operate in the carbon fiber texture selection during spinning of carbonaceous mesophases is a topic of on going investigation.

Bibliography

N.C. Andrews, B.J. Edwards and A.J. McHugh, "Continuum dynamic behavior of homogeneous liquid-crystalline polymers under the imposition of shear and magnetic fields", *J Rheo* **39** 1161 (1995).

S.-G. Baek, J.J. Magda and R.G. Larson, "Rheological differences among liquid-crystalline polymers. I. The first and second normal stress differences of PBG solutions", *J Rheol* **37** 1201 (1993).

S.-G. Baek, J.J. Magda, R.G. Larson and S.D. Hudson, "Rheological differences among liquid-crystalline polymers. II. Disappearance of negative N_1 in densely packed lyotropes and thermotropes" *J Rheol* **38** 1473 (1994).

A.N. Beris and B.J. Edwards, "Thermodynamics of flowing systems: with internal microstructure", *Oxford University Press*, New York (1994).

T. Carlsson, "The possibility of the existence of a positive Leslie viscosity α_2. proposed flow behavior of a disk-like nematic liquid crystals", *Mol Cryst Liq Cryst* **89** 57 (1982).

T. Carlsson, "Remarks on the flow alignment of disk like nematics", *J. Physique* **44** 909 (1983).

S. Chandrasekhar, "Liquid crystals of disc-like molecules", *Mol Cryst Liq Cryst* **63** 171 (1981).

S. Chandrasekhar, "Liquid Crystals", 2nd edition, *Cambridge University Press*, Cambridge (1992).

P.G. deGennes and J. Proust, "The Physics of Liquid Crystals". 2nd edition, *Oxford University Press*, Oxford (1993).

C. Destrade, N.H. Tinh, H. Gasparoux, J. Malthete and A.M. Levelut, "Disc-like mesogen: A classification", *Mol Cryst Liq Cryst* **71** 111 (1981).

M. Doi and S.F. Edwards, "The Theory of Polymer Dynamics", *Oxford University Press* New York 358-362 (1986).

D.D. Edie, K.E. Robinson, O. Fleurot, S.P. Jones and C.C. Fain, "High thermal conductivity ribbon fibers from Naphthalene-based mesophase", *Carbon* **32** 1045 (1994).

Y. Farhoudi and A.D. Rey, "Shear flow of nematic polymers. Part I. Orienting modes, bifurcations and steady rheological predictions", *J Rheol* **37** 289 (1993a).

Y. Farhoudi and A.D. Rey, "Shear flow of nematic polymers. Part II. Stationary regimes and start-up dynamics", *JNNFM* **49** 175 (1993b).

Y. Farhoudi and A.D. Rey, "Ordering effects in shear flows of discotic polymers", *Rheol Acta* **32** 207 (1993c).

B. Fatholahi and J.L. White, "Polarized-light observations of flow-induced microstructure in mesophase pitch", *J Rheo* **38** 1591 (1994).

O. Fleurot, "The viscoelastic flow behavior of pitches", Ph.D. Dissertation, Clemson University, Clemson, SC, USA (1998).

O. Fleurot, D.D. Edie and J.J. McHugh, "Elastic behavior of mesophase pitch", Extended abstract of 23rd biennial conference on carbon 268-269, USCD San Diego USA (1995).

W. Franklin, "Relations between rotational diffusion and frequency spectra of nematic liquid crystals", *Mol Cryst Liq Cryst* **40** 91 (1977).

J.A. Janik, J.M. Janik, K. Otnes, J. Krawczyk and K. Rosciszewski, "Quasielastic neutron scattering study of fast reorientations in nematic-Azoxyanisole", *Physica* **92B** 351 (1977).

P.K. Khabibullaev, E.V. Gevorkyana and A.S. Lagunov, "Rheology of Liquid Crystals", *Allerton Press*, New York, NY, USA (1994).

K. Lafdi, S. Bonnamy and A. Oberlin, "Texture and structures in heterogeneous pitch-based carbon fibers (as-spun, oxidized, carbonized, and graphitized)", *Carbon* **31** 29 (1993).

R.G. Larson, "Constitutive Equations for Polymer Melts and Solutions", *Butterworths*, Stoneham, MA, USA (1990).

R.G. Larson, "Arrested tumbling in shearing flows in liquid crystal polymers", *Macromolecules* **23** 3983 (1990).

R.G. Larson, "On the relative magnitudes of viscous, elastic and texture stresses in liquid crystalline PBG solutions", *Rheo Acta* **35** 150 (1996).

R.G. Larson and M. Doi, "Mesoscopic domain theory for textures liquid crystalline polymers" *J Rheol* **35** 539 (1991).

R.G. Larson and H.C. Öttinger, "Effect of molecular elasticity on out-of-plane orientations in shearing flows of liquid-crystalline polymers", *Macromolecules* **24** 6270 (1991).

G. Marrucci and F. Greco, "Flow behavior of liquid crystalline polymers", *Adv Chem Phys* **86** 331 (1993).

G. Marrucci and P.L. Maffettone, "Description of the liquid-crystalline phase of rodlike polymers at high shear rates", *Macromolecules* **22** 4076 (1989).

J.J. McHugh and D.D. Edie, "Orientation of mesophase pitch in capillary and channel flows", *Liq Cryst* **18** 327 (1995).

J.J. McHugh, G.Z. Liu and D.D. Edie, "An evaluation of Naphthalene-based mesophase as a carbon fiber precursor", *TANSO* **155** 417 (1992).

I. Mochida, S.-H. Yoon and Y. Korai, "Spinning characteristics of mesophase pitches derived from Naphthalene and Methylnaphthalene with HF/BF_3", *Carbon* **31** 849 (1993).

Y. Mori, N. Ookuba, R. Hayakawa and Y. Wada, "Low frequency and high frequency relaxations in dynamic electric birefringence of Poly(γ-benzyl-L-glutamate)in *m*-Cresol", *J Poly Phys* **20** 2111 (1982).

Y.W. Ooi and T. Sridhar, "Uniaxial extensional of a lyotropic liquid crystalline polymer solution", *Ind Eng Chem Res* **33** 2368 (1994).

S. Otani and A. Oya, "Progress of pitch-based carbon fibers in Japan, in petroleum derived carbons". Bacha JD, Newman JW , White JL (Eds.), *ACS Symp. Ser No. 303*, American Chemical Society, Washington, DC, 322 (1986).

L.H. Peebles, "Carbon Fibers Formation, Structures and Properties", *CRC Press*, Boca Raton, USA (1994).

A.D. Rey, "Bifurcational analysis of the isotropic-discotic nematic phase transition in the presence of extensional flow", *Liq Cryst* **19** 325 (1995).

L.S. Singer, "The mesophase in carbonaceous pitches", *Faraday Discuss Chem Soc* **79** 265 (1985).

A.P. Singh and A.D. Rey, "Theory and simulation of extensional flow-induced biaxiality in discotic mesophases", *J Phys II France* **5** 1321 (1995).

A.P. Singh and A.D. Rey, "Microstructure constitutive equation for discotic nematic liquid crystalline materials. Part I: Selection procedure and shear flow predictions", *Rheo Acta* **37** 30 (1998).

T. Tsuji and A.D. Rey, "Effect of long range order on sheared liquid crystalline materials. Part I: Compatibility between tumbling behavior and fixed anchoring", *JNNFM* **73** 127 (1997).

G.E. Volovik, "Relationship between molecule shape and hydrodynamics in a nematic substance", *JETP Lett* **31** 273 (1980).

[1]CHAPTER 4

Consistency of Predicted Shear-induced Orientation Modes with Observed Mesophase Pitch-Based Carbon Fiber Textures

In the previous chapters (chapter 2 and chapter 3) shear flow-induced microstructure of model discotic mesophases was presented. It was observed that at low temperature (high U) three in-plane (ITO, IWS, and ISS), and one out-of-plane (LRS) orientation modes are stable. Apart from the classical transition between the in-plane modes with increasing shear rate (ITO → IWS → ISS), there exists multistability among the in-plane and the out-of-plane modes. Moreover, at high temperature (low U) the complex bifurcations among the various orientation modes disappear, and the only stable orientation mode is ISS. The main theme of this chapter is to establish the consistency of the numerical results presented in chapters 2 and 3 with the observed mesophase pitch-based carbon fibers. It is shown that the present theoretical model is able to predict the fiber texture transition, radial to onion, with increasing temperature.

---

[1]This chapter appeared as an original article in *Carbon* **36**(12) p1855-1859 (1998).

4.1 Introduction

Carbon fibers made from mesophase pitches have superior mechanical and thermal transport properties, and are finding uses in a wide variety of applications ranging from space to electronic industry (Edie et al, 1994; Fleurot et al 1995; Fleurot and Edie, 1997; McHugh and Edie, 1992, 1994). These fibers are manufactured by melt-spinning discotic liquid crystalline mesophase pitches, and exhibit a spectrum of transverse textures depending on processing conditions. For example Otani and Oya (Otani and Oya, 1986) reported a transition from radial to onion texture as the spinning temperature increases along with multistability between random and mixed radial-onion textures at intermediate temperatures. Yoon et al. (1993) and Lafdi et al (1993) also reported that the radial fiber texture is prevalent at low spinning temperatures whereas the onion texture prevails as the spinning temperature rises. The basic understanding of evolution of the spectrum of carbon fiber textures during the spinning process is an active field of research (Edie et al, 1994; Fatholahi and White, 1994, 1995; Fleurot et al 1995; Fleurot and Edie, 1997; Lafdi et al, 1993; McHugh and Edie, 1992, 1994; Otani and Oya, 1986; Singh and Rey, 1995, 1998; Wang and Rey 1997; Yoon et al, 1993), and is of practical importance for their further development. Numerous experimental studies have been performed to elucidate the effects of various processing conditions and geometry on the flow induced microstructure (Edie et al, 1994; Fatholahi and White, 1994 1995; Fleurot and Edie, 1997; Fleurot et al 1995; Lafdi et al, 1993; McHugh and Edie, 1992, 1994; Otani and Oya, 1986; Yoon et al, 1993). Mathematical modeling and simulation provides an economical alternative to the trial and error experimental methodologies and have been performed by Edie and McHugh (1992, 1994), and Wang and Rey (1997). Edie and McHugh (1992, 1994) using Leslie-Ericksen theory for liquid crystalline materials predicted that the radial texture exists inside the spinneret capillary. However, the same study (McHugh and Edie, 1992, 1994) did not address the stability of the predicted radial orientation mode, the existence of other equivalent textures, e.g. onion, random etc., and the observed transition in textures with changing processing conditions. Rey and Wang (1997) predicted the transition from radial $\rightarrow$ random $\rightarrow$ onion textures with increasing

temperature by solely considering the effects of long-range orientation elasticity while neglecting any viscous or short range molecular elastic effects.

Flow is a mechanism that induces molecular orientation in mesophase pitches while it passes through the spin-pack (Fatholahi and White, 1994, 1995; Fleurot and Edie, 1997; McHugh and Edie, 1992, 1994). During the melt spinning process mesophase pitches are subjected to strong shear flows in the filter, inhomogeneous mixed shear and extensional flows through converging cone and the leading capillary, and strong extensional flows in the spin-line. Fatholahi and White (1994, 1995), McHugh and Edie (1992, 1994), and Flourot and Edie (1997) observed and proposed that the fiber texture is likely to develop inside the spin-pack (converging cone and capillary), and the strong extensional flow in the spin-line accentuates the already induced orientation in the spin pack. Mesophases pitches are anisotropic visco-elastic materials (Fleurot et al 1995; Fleurot and Edie, 1997; McHugh and Edie, 1992, 1994), therefore both viscous as well as elastic effects are expected to contribute to the selection and development of fiber textures. A rigorous visco-elastic flow model that has all the microstructural features corresponding to the observed fiber textures has been proposed by Singh and Rey (1998). The simulated results of the proposed model have been characterized and validated (Singh and Rey, 1998). In this paper, we present the predicted shear-induced microstructure in mesophase pitches considering only the viscous and short range molecular elasticity, and compare the simulated results with the observed molecular orientation in fiber textures. The consistency of the predicted results with the observed fiber textures will be discussed, as well as the role of viscous shear flow on the texture selection mechanism. This communication is part of an ongoing program to develop a process simulator for fiber spinning of mesophase pitches.

This is the first modeling effort in this field that puts forth a tensor model for discotics that is able to predict, under simple shear flow (test flow), all the essential orientation features necessary to capture all the observed fiber textures. To convey this message is the prime objective of this letter.

The particular objectives of this manuscript are: (1) to convey the elements of consistency between the predicted shear-induced orientation modes (Singh and Rey, 1998) by the proposed constitutive equation for mesophase pitches and the experimental observations (Fatholahi and White, 1994, 1995; Fleurot and Edie, 1997; Fleurot et al 1995; Lafdi et al, 1993; McHugh and Edie, 1992, 1994; Otani and Oya, 1986; Yoon et al, 1993), and (2) based on that compatibility to analyze the predicted multistability and transitions in orientation modes with varying process conditions within the context of experimental results (Lafdi et al, 1993; Otani and Oya, 1986; Yoon et al, 1993).

4.2 Mathematical Model

Figure 4.1 shows the schematic presentation of mesophase pitches consisting of poly-aromatic, flat, disk-like molecules that are rigid enough to display long range orientation order, and that tend to adopt a uniaxial discotic nematic phase, N_D. In discotic nematics, the unit normals to the flat disk-like molecules orient more or less along a common direction called the director $\mathbf{n}$, see Figure 4.1. The average degree of alignment of unit normals to the disk-like molecules is defined by the (uniaxial) scalar order parameter S. The microstructure of discotic mesophases is characterized by a symmetric, traceless second order tensor, known generally as tensor order parameter $\mathbf{Q}$:

$$\mathbf{Q} = S\left(\mathbf{nn} - \tfrac{1}{3}\boldsymbol{\delta}\right) + \tfrac{1}{3}P(\mathbf{mm} - \mathbf{ll}) \tag{4.1a}$$

where the following restrictions apply:

$$\mathbf{Q} = \mathbf{Q}^{\mathrm{T}} \ , \quad tr(\mathbf{Q}) = 0 \ , \quad -\tfrac{1}{2} \le S \le 1 \ , \quad -\tfrac{1}{2} \le P \le \tfrac{1}{2} \ , \tag{4.1b,c,d,e}$$

$$\mathbf{n}\cdot\mathbf{n} = \mathbf{m}\cdot\mathbf{m} = \mathbf{l}\cdot\mathbf{l} = 1 \ , \quad \mathbf{nn} + \mathbf{mm} + \mathbf{ll} = \boldsymbol{\delta} \tag{4.1f,g}$$

Being a second order tensor $\mathbf{Q}$ has three eigenvalues and eigenvectors. The first eigenvector or uniaxial director $\mathbf{n}$ corresponds to the largest eigenvalue $\frac{2}{3}S$, the biaxial director $\mathbf{m}$ corresponds the intermediate eigenvalue $-\frac{1}{3}(S-P)$, and the second biaxial director $\mathbf{l}$ $(=\mathbf{n}\times\mathbf{m})$ corresponds to the smallest eigenvalue $-\frac{1}{3}(S+P)$. Details on uniaxial (S) and biaxial (P) alignments and their interrelations are given in (Singh and Rey, 1995, 1998).

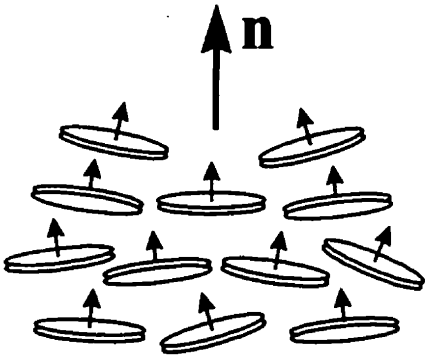

Figure 4.1: Definition of director orientation of a uniaxial discotic nematic liquid crystalline material. The director **n** in a discotic nematic phase is the average orientation of the unit normals to the disk-like molecules.

The microstructure response of liquid crystalline polymers, as described by Doi's mesoscopic nematodynamic theory (Doi and Edwards, 1986), is given as (Singh and Rey, 1998):

$$\hat{\mathbf{Q}} = \mathbf{F}(\mathbf{Q}, \nabla\mathbf{v}) + \mathbf{H}\left(\mathbf{Q}, \overline{D}_r(\mathbf{Q})\right) \tag{4.2}$$

where $\nabla\mathbf{v}$ is the velocity gradient tensor and $\hat{\mathbf{Q}}$ is the corotational derivative of $\mathbf{Q}$ and is defined as:

$$\hat{\mathbf{Q}} = \frac{\partial \mathbf{Q}}{\partial t} + (\mathbf{v}\cdot\nabla)\mathbf{Q} - \mathbf{W}\cdot\mathbf{Q} + \mathbf{Q}\cdot\mathbf{W} \tag{4.3}$$

$\mathbf{F}(\mathbf{Q}, \nabla\mathbf{v})$, and $\mathbf{H}\left(\mathbf{Q}, \overline{D}_r(\mathbf{Q})\right)$ represent the flow or viscous contributions, and the short range molecular elasticity respectively, and are given by (Singh and Rey, 1998):

$$\begin{aligned}\mathbf{F}(\mathbf{Q}, \nabla\mathbf{v}) = {} & \tfrac{2}{3}\beta\mathbf{A} + \beta\left[\mathbf{A}\cdot\mathbf{Q} + \mathbf{Q}\cdot\mathbf{A} - \tfrac{2}{3}(\mathbf{A}:\mathbf{Q})\delta\right] - \\ & \tfrac{1}{2}\beta\left[(\mathbf{A}:\mathbf{Q})\mathbf{Q} + \mathbf{A}\cdot\mathbf{Q}\cdot\mathbf{Q} + \mathbf{Q}\cdot\mathbf{A}\cdot\mathbf{Q} + \mathbf{Q}\cdot\mathbf{Q}\cdot\mathbf{A} - \{(\mathbf{Q}\cdot\mathbf{Q}):\mathbf{A}\}\delta\right]\end{aligned} \tag{4.4}$$

$$\mathbf{H}\left(\mathbf{Q}, \overline{D}_r(\mathbf{Q})\right) = -6\overline{D}_r\left[\left(1 - \tfrac{1}{3}U\right)\mathbf{Q} - U\mathbf{Q}\cdot\mathbf{Q} + U\left\{(\mathbf{Q}:\mathbf{Q})\mathbf{Q} + \tfrac{1}{3}(\mathbf{Q}:\mathbf{Q})\delta\right\}\right] \tag{4.5}$$

$$\text{where } \overline{D}_r = D_r\left[1 - \tfrac{3}{2}(\mathbf{Q}:\mathbf{Q})\right]^{-2}, \quad \beta = \frac{p^2-1}{p^2+1}, \quad p = \frac{r_\parallel}{r_\perp} \tag{4.6a,b,c}$$

The long-range orientation elasticity, known as Frank elasticity (DeGennes and Proust, 1993), is not considered in this paper. In equations (4.2-4.6), $\overline{D_r}$ is the averaged diffusivity, D_r is the preaveraged diffusivity or isotropic rotary diffusivity of an hypothetical isotropic fluid at the same conditions, U is the nematic potential which is inversely proportional to temperature T, and β is the shape factor respectively. To specify the molecular geometry we approximate the disc-like shape of molecule of discotic mesophases with an oblate spheroid of aspect ratio p ($p < 1$) where in equation (4.6c) $r_{\parallel}$ is the length of the shortest and distinct semiaxis, and $r_{\perp}$ the length of the two longest and equal semiaxes. The ideal flat disc corresponds to $p = 0$ ($\beta = -1$), and the sphere corresponds to $p = 1$ ($\beta = 0$). **A** and **W** are the rate of deformation and vorticity tensor respectively. Since there are only two processes in the model, we have only one dimensionless number, Pe, the Peclet number or dimensionless shear rate, which is defined as (Singh and Rey, 1998):

$$Pe = \frac{\dot{\gamma}}{|6D_r|} \tag{4.7}$$

where $\dot{\gamma}$ is constant shear rate. Only uniaxial orientation modes are discussed here, further details on biaxial orientation modes (**m**, **l**) and uniaxial and biaxial alignments (S, P) are documented in (Singh and Rey, 1998). In what follows uniaxial orientation (i.e., the orientation of the director **n**) will be referred to simply as orientation.

4.3 Summary of Predicted Orientation Modes and Consistency with Observed Textures

Below we summarize the microstructure phenomena predicted by the CE, equation (4.2), for discotic mesophases under simple shear flow. The coordinate system is shown in Figure 4.2. The flow direction is along the x-axis, the velocity gradient direction is along the y-axis, and the vorticity axis is along the z-axis.

The predicted orientation modes, in terms of uniaxial director **n** dynamics are: (a) ITO or in-plane tumbling orbit, (b) IWS or in-plane wagging state, (c) ISS or in-plane steady state, (d) LRS or log rolling state. The two dimensional schematic representations

of the orientation modes in terms of uniaxial director **n** are given in Figure 4.3. Figure 4.3a represents the in-plane tumbling orbit (ITO) in which the uniaxial director **n** rotates clockwise in the shear (x-y) plane. Figure 4.3b shows the in-plane wagging state (IWS), in which **n** oscillates around a point near the y-axis (velocity gradient direction), and in the shear (x-y) plane. Figure 4.3c represents the in-plane steady state (ISS) in which the uniaxial director **n** aligns near the y-axis (velocity gradient direction) in the shear (x-y) plane. Figure 4.3d shows the out-of-plane (non-planar) log rolling state (LRS) in which the uniaxial director **n** aligns along the vorticity axis (z-axis) perpendicular the shear plane. The first two orientation states, ITO and IWS, are the time-dependent states whereas the last two, ISS and LRS, are steady states. All orientation states except LRS are planar orientation modes (i.e., $n_z = 0$). A detailed analysis of these orientation states in terms of uniaxial **n** and biaxial (**m**, **l**) directors, and uniaxial S and biaxial P alignments are given in (Singh and Rey, 1998).

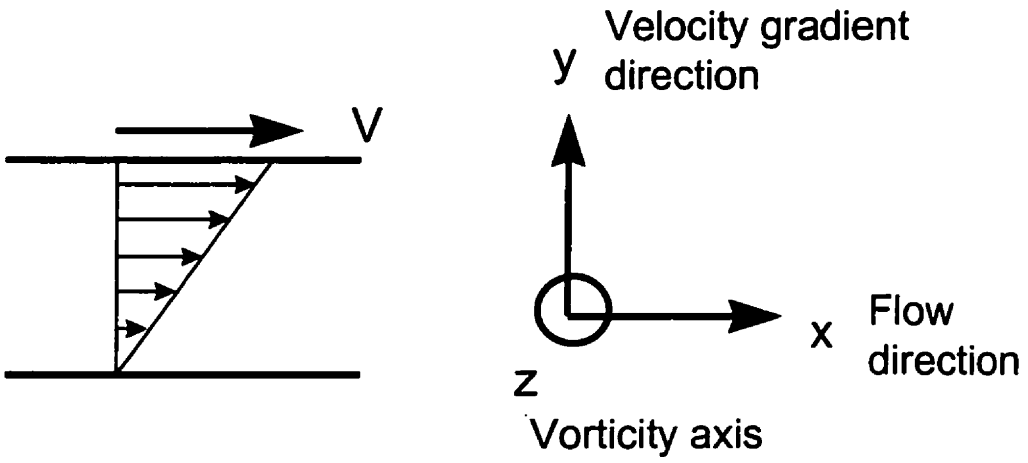

Figure 4.2: Definition of homogeneous simple shear flow deformation. The x-axis is the flow direction, the y-axis is the velocity gradient direction, and the z-axis (out of the plane of the paper) is the vorticity axis or neutral direction.

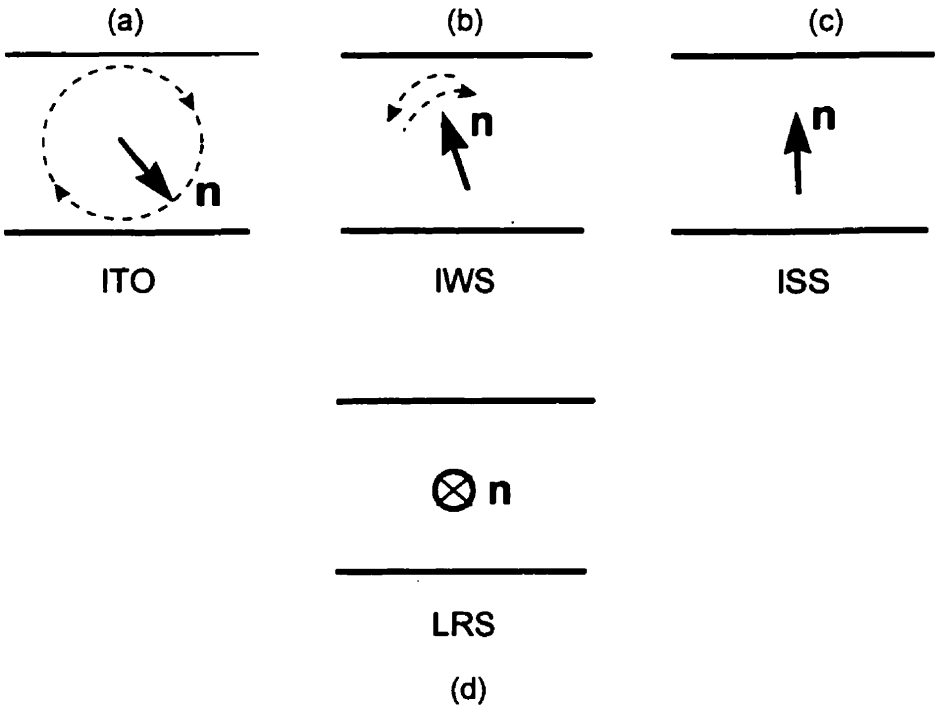

Figure 4.3: The representative schematics of the stable uniaxial orientation modes of discotic mesophases under homogeneous simple shear flow predicted by constitutive equation (2). The four stable orientation modes are : (a) ITO or in-plane tumbling orbit, (b) IWS or in-plane wagging state, (c) ISS or in-plane steady state, (d) LRS or log rolling state. The top row represents the planar orientation modes and the bottom row non-planar mode. As shear rate increases there exists transition among planar orientation modes such that with increasing shear rate: ITO → IWS → ISS. Also there exists multistability among planar and non-planar orientation modes. For more details see the text and Table 4.1.

Table 4.1

Multistability and Transition among various predicted orientation modes for $\beta = -0.8$

	High U (= 6)				Low U(=3.5)
Stable orientation mode/s	LRS —	LRS ITO	LRS IWS	LRS ISS	— ISS
Shear rate range	$0 < Pe < 4.5$	$4.5 \leq Pe < 5.5$	$5.5 \leq Pe < 14$	$Pe \geq 14$	$Pe > 0$

Pe: Peclet number or dimensionless shear rate; β: shape factor; U: nematic potential; LRS: log rolling state; ITO: in-plane tumbling orbit; IWS: in-plane wagging state; ISS: in-plane steady state. U is inversely proportional to temperature T.

For a given shape factor β, at sufficiently high U ($U > U^{\#}$) or alternatively at sufficiently low T ($T < T^{\#}$) all four orientation modes are stable, and there exists multistability between planar and non-planar orientation modes as given in Table 4.1, $U^{\#}$ and $T^{\#}$ represent critical values of U and T. For example for $\beta = -0.8$, at low U ($U = 3.5$), there is only one stable orientation mode, ISS, for whole range of dimensionless shear rate Pe. On the other hand at high U ($U = 6$) all four orientation modes are stable, and there exists multistability among planar and non-planar orientation modes. More details are given in (Singh and Rey, 1998). The complex multistability phenomena at higher U is summarized in Table 4.1 and can be described as follows: for low shear rates there is only one stable orientation mode corresponding to LRS; for intermediate Pe, LRS along with ITO are the stable modes; for high Pe, LRS and IWS are the stable orientation modes; and for very high Pe there are two stable modes corresponding to LRS and ISS. Though not shown here, however, similar multistability exists at higher values of U for all values of shape factor β, and at lower values of U the complex bifurcations disappear and there is only one stable orientation mode, ISS, at all shear rates. The co-existence of stable steady planar and non-planar orientation modes at all shear rates (at high values of the nematic potential) is predicted for the first time by the presented model. This multistability of stable planar and stable non-planar orientation modes at higher shear rate is an essential feature of the presented model that is absent in the all the existing vector theories and is an essential feature required to capture the reported orientation modes in fiber textures. Thus the letter is geared to convey to the audience that a highly useful model for discotics is now available, and its predictions under simple test flow match the main characteristics of the fiber textures.

Next the consistency among the above mentioned shear-induced microstructure predictions and the observed fiber microstructures will be shown. This will be achieved by comparing the shear induced orientational response of the model discotic mesophases with the localized orientation field in observed carbon fiber textures (Fatholahi and White, 1994, 1995; Fleurot and Edie, 1997; Fleurot et al 1995; Lafdi et al, 1993; McHugh and Edie, 1992, 1994; Otani and Oya, 1986; Yoon et al, 1993).

4.4 Thermal Effects

As mentioned above, it has been noted that the microstructure is likely to develop in the spin-pack (converging cone and the capillary), and the extensional flow in the spin-line merely accentuates the achieved orientation in the spin-pack (Fatholahi and White, 1994, 1995; Fleurot and Edie, 1997; McHugh and Edie, 1992, 1994). Figure 4.4 shows the schematics of the main observed fiber textures, which exist in the capillary. Considering the flow in the circular capillary section. In terms of cylindrical coordinate system (see Figure 4.4a), the fiber axis can be assumed to lie along the z′ direction, which is also the flow direction, the radial direction (r) is the velocity gradient direction, and the azimuthal direction (θ) is the vorticity or neutral direction. The various lines in Figure 4.4(b,c) represent the locus of the side view of the disk like molecules. In the textures, shown in Figure 4.4, the unit normals to the disk like molecules lie in the plane perpendicular to the fiber axis (z' direction). Thus the localized director orientation in the shown fiber textures is given by $\mathbf{n} = (n_r, n_\theta, n_{z'}) = (n_r, n_\theta, 0)$. Also, in the radial (onion) texture the normals to the disk-like molecules orient along the azimuthal (radial) direction. Using this terminology, in the onion texture the unit normals orient along the radial direction or along the velocity gradient direction, whereas in the radial texture the unit normals align along the azimuthal direction or the vorticity axis. Thus the observed radial (onion) texture is consistent with the predicted shear-induced LRS (ISS) orientation mode. Table 4.2 contains a complete summary of these comparisons. Also, as presented in Table 4.1, at high U (low T), both ISS as well as LRS exist together at high shear rates, thus under these conditions the model predicts multistability in radial and onion textures. From the above discussion, it is directly inferred that the predicted shear-induced microstructure phenomena is consistent with the observed textures, thus the simulated results are consistent with those found in the literature (Fatholahi and White, 1994, 1995; Fleurot and Edie, 1997; Fleurot et al 1995; Lafdi et al, 1993; McHugh and Edie, 1992, 1994; Otani and Oya, 1986).

As mentioned above as U (T) decreases (increases) the complex transitions among the planar and non-planar orientation modes, stated above, disappear and the only stable

orientation mode is ISS. Therefore following the preceding discussion, we notice that at low (high) U (T) the only flow-induced stable texture is the onion texture. This transition from radial texture at low temperature to an onion one at high temperature has been observed experimentally (Lafdi et al, 1993; Otani and Oya, 1986; Yoon et al, 1993) and predicted theoretically (Wang and Rey, 1997) based on long-range elasticity without consideration of flow effects. Thus the proposed visco-elastic flow model for discotic mesophases under simple shear flows has the features that are consistent with the experimental observations and theoretical results.

4.5 Conclusions

In summary, we have established the consistency of the flow-induced microstructure predicted by the presented CE with that observed experimentally. The CE successfully predicts the transition from radial to onion texture with increasing temperatures. The validation of the shear-induced microstructure phenomena predicted by the presented CE suggests that it is a reliable contribution towards the formulation of a process model for mesophase pitch spinning.

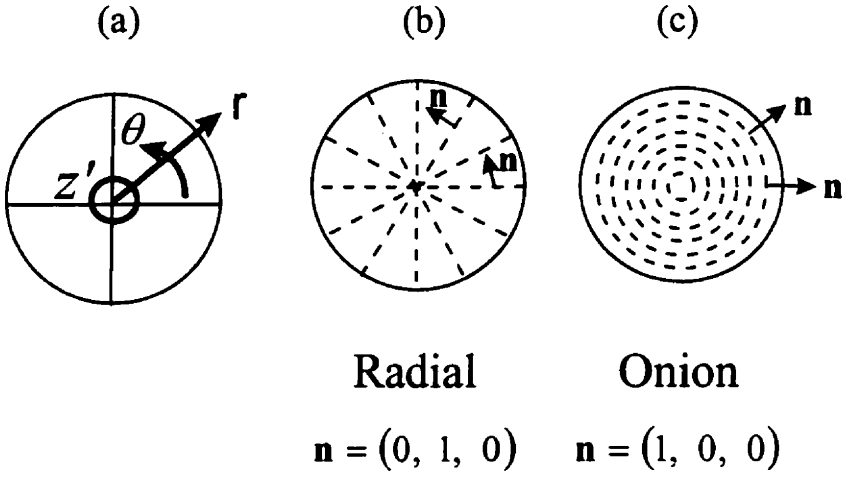

Figure 4.4: Schematics of (a) cylindrical coordinate system, and the observed fiber microstructures: (b) radial, and (c) onion. In the radial (onion) texture, the unit normals to the disk-like molecules orient along the azimuthal θ (radial r) direction.

Table 4.2

Consistencies among predicted and observed orientation modes in fiber textures

Fiber texture	Localized uniaxial director field	Corresponding predicted consistent orientation mode (Singh and Rey, 1998)
Radial texture[§]	$\mathbf{n} = (n_r, n_\theta, n_z) = (0, 1, 0)$ $\mathbf{n}$ along vorticity direction $(\mathbf{n} \parallel \mathbf{v} \times \nabla \mathbf{v})$	LRS
Onion texture[ϰ]	$\mathbf{n} = (n_r, n_\theta, n_z) = (1, 0, 0)$ $\mathbf{n}$ along velocity gradient direction $(\mathbf{n} \parallel \nabla \mathbf{v})$	ISS

$\mathbf{n}$: uniaxial director orientation; ISS: in-plane steady state; LRS: out-of-plane log rolling state; $\mathbf{v}$: velocity direction; $\nabla \mathbf{v}$: velocity gradient direction

[§](Fatholahi and White, 1994, 1995; Fleurot and Edie, 1997; Fleurot et al 1995; Lafdi et al, 1993; McHugh and Edie, 1992, 1994; Otani and Oya, 1986; Yoon et al, 1993)

[ϰ] (Lafdi et al, 1993; Otani and Oya, 1986; Yoon et al, 1993)

Bibliography

P.G. deGennes and J. Proust, *The Physics of Liquid Crystals. 2nd edition, Oxford University Press, Oxford*, (1993)

M. Doi and S.F. Edwards, *The Theory of Polymer Dynamics. Oxford University Press New York*, 358 (1986)

D.D. Edie, K.E. Robinson, O. Fleurot, S.P. Jones and C.C. Fain, "High thermal conductivity ribbon fibers from Naphthalene-based mesophase." *Carbon*, **32**, 1045 (1994).

B. Fatholahi and J.L. White, "Polarized-light observation of flow-induced microstructures in mesophase pitch." *Journal of Rheology*, **38**, 1591 (1994)

B. Fatholahi and J.L. White, *Carbon '95*, 60 (1995)

O. Fleurot and D.D. Edie, *Carbon '97*, (1997)

O. Fleurot, D.D. Edie and J.J. McHugh, *Carbon '95*, 265 (1995)

K. Lafdi, S. Bonnamy and A. Oberlin, "Textures and structures in heterogeneous pitch-based carbon fibres (as-spun, oxidized, carbonized, and graphitized)" *Carbon*, **31**, 29 (1993)

J.J. McHugh and D.D. Edie, *Carbon '92*, 683, (1992)

J.J. McHugh and D.D. Edie, "Orientation of mesophase pitch in capillary and channel flows." *Liquid Crystals*, **18**, 327 (1995).

S. Otani and A. Oya, *Progress of Pitch-based Carbon Fibers in Japan*, in Petroleum derived carbon, J.D. Bacha, J.W. Newman and J.L. White, Eds., ACS Symp. Ser. No. 303, American Chemical Society, Washigton D.C., 322 (1986)

A.P. Singh and A.D. Rey, "Theory and simulation of extensional flow-induced biaxiality in discotic mesophases" *Journal de Physique II France*, **5**, 1321 (1995)

A.P. Singh and A.D. Rey, "Microstructure constitutive equation for discotic nematic liquid crystalline materials Part I: Selection procedure and shear flow predictions" *Rheolgica Acta*, **37**, 30 (1998).

L. Wang and A.D. Rey, "Pattern selection mechanism in mesophase carbon fibres" *Modelling Simul. Mater. Eng.*, **5**, 67 (1997)

S.-H. Yoon, Y. Korai and I. Mochida, "Spinning characteristics of mesophase pitches derived from naphthalene and methylnaphthalene with HF/BF_3." *Carbon*, **31**, 849 (1993)

[1]CHAPTER 5

Theoretical Analysis of Texture Dependent Extensional Viscosity of Discotic Mesophases

In the previous chapters the microstructural and rheological response of the constitutive equation (CE) for discotic mesophases was explored by subjecting it to homogeneous shear flows only. The present chapter is solely geared towards analyzing and characterizing the uniaxial extensional rheological predictions of the CE. It is found that two distinct uniaxial extensional viscosity parameters are needed to fully characterize extensional rheological functions of discotic mesophases. The discotic mesophases are found to be non-Troutonian, and show strain thinning or strain thickening behavior based on the temperature, and the ratio of viscous to elastic effects. It will be shown that the elastic stresses impart strain-thinning characteristics to the discotic mesophases, whereas the viscous stresses result in a strain thickening behavior. The rheological analysis is used to put forth the relations between extensional viscosities, and the classical mesophase fiber textures.

---

[1] This chapter appeared as an original article in *Liquid Crystals* **26**(7) p999-1005 (1999).

5.0 Abstract

Rheological functions for uniaxial extensional flows predicted by a previously selected and validated constitutive equation (CE) for discotic mesophases are presented. The predicted relations among extensional viscosities, flow-induced microstructure, processing conditions, and material parameters of discotic mesophases are characterized and discussed. It is found that in contrast to rod-like nematics, two distinct uniaxial extensional viscosities need to be defined to completely characterize the extensional rheological functions of discotic mesophases. The model predicts non-Troutonian extensional viscosities of discotic nematics, such as strain thinning and strain thickening, depending on the process temperature, and the ratio of viscous to elastic stress contributions. The uniaxial extensional viscosities are also found to depend strongly on the flow-induced microstructure. The rheological analysis is then used to characterize the relations between extensional flow viscosities and the classical microstructures that arise during the industrial fiber spinning of discotic mesophase pitches.

5.1 Introduction

Mesophase pitches are used to manufacture high performance carbon fibers (Edie et al, 1994; Fatholahi et al, 1992; Fatholahi and White, 1994; Fleurot and Edie, 1997; McHugh and Edie, 1992, 1995; Peebles, 1994). These fibers possess superior mechanical and thermal transport properties and find uses in a wide variety of applications ranging from space to electronics industry (Peebles, 1994). Conventional high speed melt spinning process is employed in which the mesophase pitch is melted and then extruded through spinneret capillaries to form fibers which are subsequently drawn in the spin-line to accentuate the axial orientation (Fatholahi et al, 1992; Fatholahi and White, 1994; Fleurot and Edie, 1997; McHugh and Edie, 1992, 1995). Since the mesophase pitches have finite memory, the relative intensity of the various process steps and their sequence (i.e., conical section → capillary → die exit → spin-line) have a profound effect on the final microstructure of the carbon fibers. Also, spinning temperature is reported to have significant effect on the selection of fiber texture (Peebles, 1994). The spinning process

inherently involves extensional flows both inside the spin-pack and in the spin-line, therefore it is important to understand the behavior of mesophases pitches under these flows (Edie et al, 1994; Fatholahi et al., 1992; Fatholahi and White, 1994; Fleurot and Edie, 1997; McHugh and Edie, 1992, 1995; Peebles, 1994). In addition the molecular orientation of discotic mesophases in the spin-line gives rise to characteristic textures, such as radial and onion (Peebles, 1994), see Figure 5.4, and relation between extensional viscosities and fiber textures has not been yet characterized. This paper presents for the first time the theory and simulation of uniaxial extensional viscosities of discotic mesophases, based on a validated tensorial model, and its relationships with the flow-induced microstructure, processing conditions, and molecular geometry corresponding to those of carbonaceous mesophase pitches.

Mesophase pitches consist of flat, disk-like, aromatic molecules that tend to adopt a uniaxial discotic nematic phase N_D, with unit normals to the disc-like molecules more or less aligned along a common direction (see Figure 5.1) represented by the uniaxial director $\mathbf{n}$; in what follows we use $\mathbf{n}$ and uniaxial orientation interchangeably. The degree of alignment of the unit normals along $\mathbf{n}$ is given by the scalar order parameter S; in what follows we use S and uniaxial alignment interchangeably. The flow-induced biaxiality in discotic mesophases is characterized in terms of biaxial directors/orientation $\mathbf{m}$ and $\mathbf{l}$, and biaxial scalar order parameter or alignment P, the details are given in (Singh and Rey, 1995a).

It is well known that the extensional flows are strong orienting flows (Singh and Rey, 1994, 1995a, 1995b). The basic flow orienting phenomena of nematics in extensional flows depend on the molecular geometry due to the fact that discotic (rod-like) nematics orients their shortest (longest) direction along the director $\mathbf{n}$. For discotic nematics the tumbling function or the reactive parameter is negative $\lambda < 0$, and uniaxial extensional flows orient the uniaxial director $\mathbf{n}$ anywhere in the compression plane, normal to the extension axis (Singh and Rey, 1994, 1995a, 1995b). This flow-induced orientation naturally induces biaxiality (Singh and Rey, 1995a) since the major axis (extension direction) of the rate of strain tensor ellipsoid is perpendicular to the main axis ($\mathbf{n}$) of the tensor order parameter ellipsoid. On the other hand for rod-like nematics the

reactive parameter is positive $\lambda > 0$, and **n** aligns along the extension direction, and the tensor order parameter is uniaxial.

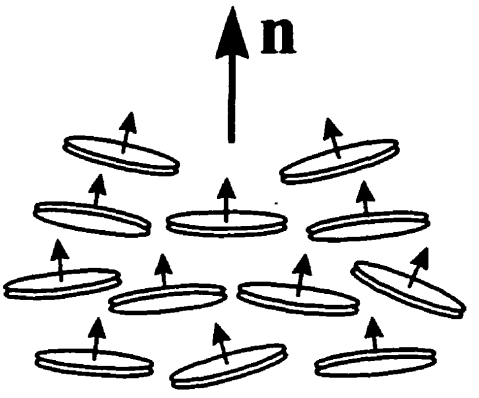

Figure 5.1: The uniaxial director orientation **n** of the uniaxial discotic nematic liquid crystals. The director **n** is the average orientation of the unit normals to the disc-like molecules.

The main objective of this paper is to present the extensional rheological properties of discotic mesophases. The particular objectives of the paper are to:

1. Identify the important extensional rheological parameters for discotic mesophases;
2. Characterize the dependence of rheological material properties of discotic mesophases on their extensional flow-induced microstructure;
3. Establish the relationship among extensional rheological functions, flow-induced microstructure, processing conditions, and molecular geometry.

Although numerical predictions of this paper are not directly validated due to the lack of available experimental data, yet a high degree of confidence can be expected since: (1) the present model has been shown to capture the distinctive and experimentally observed shear-induced microstructure modes (McHugh and Edie, 1995), and flow instability of discotic mesophases (Fatholahi et al, 1992), (2) the model presented in this paper has shown to capture all the complex nonlinear rheological phenomena actually exhibited by discotic as well as rod-like nematics (Fatholahi et al, 1992; McHugh and Edie, 1995). This paper is a continuation of our effort to increase the understanding of rheology of discotic mesophases, and to provide the theoretical guidelines to the experimental work being pursued to understand the microstructure-processing-product

property relationships to develop new high performance engineering materials.

The organization of this paper is as follows. The next section presents the theory, the coordinate system and kinematics along with the microstructure governing CE and stress tensor equation. In section 3 we present, discuss, and characterize the uniaxial extensional viscosity of discotic mesophases. Also, the relations among extensional viscosity, microstructure, processing conditions, and materials parameters are given. Finally conclusions are presented. Appendix A contains a brief analysis, based on L-E theory, of extensional viscosity of rod-like and discotic nematics.

5.2 Theory and Governing Equations

5.2.1 Definition of Microstructure, Kinematics and Coordinates

In tensor theories the complete description of microstructure of liquid crystalline materials is conveniently given by a symmetric and traceless second order tensor, generally known as tensor order parameter **Q** given in principal form as:

$$\mathbf{Q} = \lambda_{\mathbf{n}}\mathbf{nn} + \lambda_{\mathbf{m}}\mathbf{mm} + \lambda_{\mathbf{l}}\mathbf{ll} \tag{5.1a}$$

where $\lambda_{\mathbf{n}} = \frac{2}{3}S$, $\lambda_{\mathbf{m}} = -\frac{1}{3}(S-P)$, $\lambda_{\mathbf{l}} = -\frac{1}{3}(S+P)$, and $-\frac{1}{3} \le \lambda_{\mathbf{a}} \le \frac{2}{3}$ (5.1b,c,d,e)

The eigenvalues $\lambda_{\mathbf{a}}$ ($\mathbf{a} = \mathbf{n}, \mathbf{m}, \mathbf{l}$) correspond to the unit eigenvectors ($\mathbf{n}, \mathbf{m}, \mathbf{l}$) respectively, the latter forming a right handed orthogonal triad. The orientation is completely defined by the director triad ($\mathbf{n}, \mathbf{m}, \mathbf{l}$). The magnitude of uniaxial alignment $S = \frac{3}{2}\mathbf{n}\cdot\mathbf{Q}\cdot\mathbf{n}$ is a measure of molecular alignment along the uniaxial director **n** and that of the biaxial alignment $P = \frac{3}{2}\mathbf{m}\cdot\mathbf{Q}\cdot\mathbf{m} - \frac{3}{2}\mathbf{l}\cdot\mathbf{Q}\cdot\mathbf{l}$ is a measure of molecular alignment in a plane perpendicular to uniaxial director **n**. Details on uniaxial (S) and biaxial (P) alignments and their interrelations are given in (Singh and Rey, 1995a). The present work is restricted to normal nematics ($0 \le S \le 1$, $0 \le P \le 1$). The order parameter **Q** is assumed to be spatially uniform and Frank elasticity is not considered.

Figure 5.2 shows the deformations of an element of discotic mesophase subjected at time $t = 0$ to a uniaxial extensional flow of constant extension rate $\dot{\varepsilon}$. As shown, the extension direction is along the z-axis and r-θ is the compression plane. The velocity field for the considered flow field is given as:

$$v_r = -\tfrac{1}{2}\dot{\varepsilon} r H(t) \quad v_\theta = 0 \quad v_z = \dot{\varepsilon} z H(t) \quad \text{where } H(t) = \begin{cases} 0 & t < 0 \\ 1 & t \geq 0 \end{cases} \qquad \text{(5.2a,b,c,d)}$$

In this paper we use the velocity field given by equation (5.2) and perform only a steady state analysis, i.e., $t \to +\infty$.

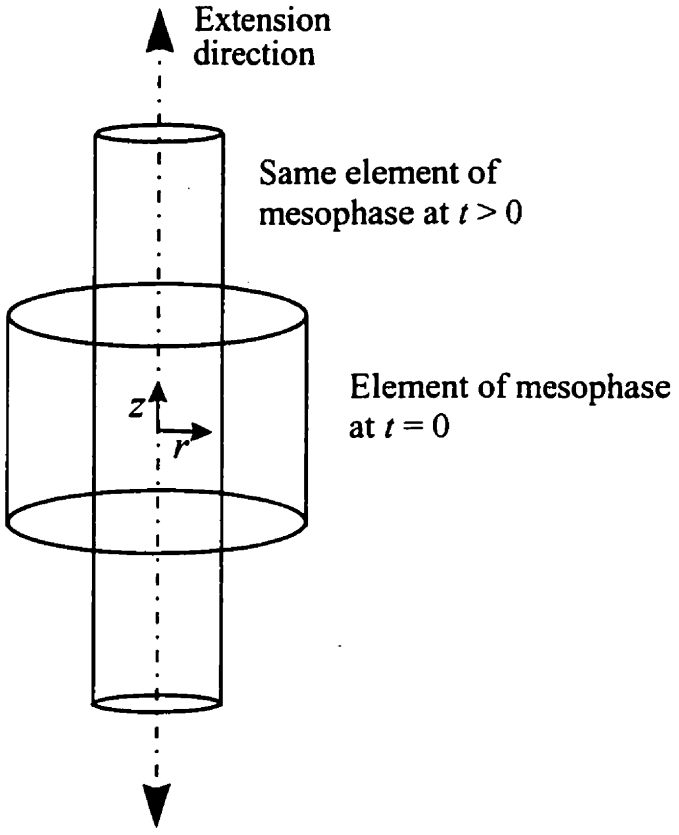

Figure 5.2: Deformation of a unit cylinder of discotic mesophase subjected at time $t = 0$ to a uniaxial extensional flow deformation. The extension direction is along the z-axis, and the $r-\theta$ plane contains the uniform compression.

5.2.2 Microstructure Constitutive Equation

The microstructure response of liquid crystalline polymers, as described by Doi's mesoscopic nematodynamic theory (Doi and Edwards, 1986), is given as:

$$\hat{\mathbf{Q}} = \mathbf{F}(\mathbf{Q}, \nabla\mathbf{v}) + \mathbf{H}(\mathbf{Q}, \overline{D}_r(\mathbf{Q})) \tag{5.3}$$

where $\nabla\mathbf{v}$ is the velocity gradient tensor and $\hat{\mathbf{Q}}$ is the corotational derivative of $\mathbf{Q}$ and is defined as:

$$\hat{\mathbf{Q}} = \frac{\partial \mathbf{Q}}{\partial t} + (\mathbf{v}\cdot\nabla)\mathbf{Q} - \mathbf{W}\cdot\mathbf{Q} + \mathbf{Q}\cdot\mathbf{W} \tag{5.4}$$

$\mathbf{F}(\mathbf{Q}, \nabla\mathbf{v})$ and $\mathbf{H}(\mathbf{Q}, \overline{D}_r(\mathbf{Q}))$ represent the flow and the short range elastic contributions respectively, and are given as (Singh and Rey, 1998a):

$$\begin{aligned}\mathbf{F}(\mathbf{Q}, \nabla\mathbf{v}) = {} & \tfrac{2}{3}\beta\mathbf{A} + \beta\left[\mathbf{A}\cdot\mathbf{Q} + \mathbf{Q}\cdot\mathbf{A} - \tfrac{2}{3}(\mathbf{A}:\mathbf{Q})\delta\right] - \\ & \tfrac{1}{2}\beta\left[(\mathbf{A}:\mathbf{Q})\mathbf{Q} + \mathbf{A}\cdot\mathbf{Q}\cdot\mathbf{Q} + \mathbf{Q}\cdot\mathbf{A}\cdot\mathbf{Q} + \mathbf{Q}\cdot\mathbf{Q}\cdot\mathbf{A} - \{(\mathbf{Q}\cdot\mathbf{Q}):\mathbf{A}\}\delta\right]\end{aligned} \tag{5.5}$$

$$\mathbf{H}(\mathbf{Q}, \overline{D}_r(\mathbf{Q})) = -6\overline{D}_r\left[(1 - \tfrac{1}{3}U)\mathbf{Q} - U\mathbf{Q}\cdot\mathbf{Q} + U\{(\mathbf{Q}:\mathbf{Q})\mathbf{Q} + \tfrac{1}{3}(\mathbf{Q}:\mathbf{Q})\delta\}\right] \tag{5.6}$$

$$\text{where } \overline{D}_r = D_r\left[1 - \tfrac{3}{2}(\mathbf{Q}:\mathbf{Q})\right]^{-2}, \quad \beta = \frac{p^2 - 1}{p^2 + 1}, \quad p = \frac{r_\perp}{r_\parallel}, \tag{5.7a,b,c}$$

$\overline{D}_r$ is the averaged diffusivity, D_r is the preaveraged diffusivity or rotary diffusivity of an hypothetical isotropic fluid under the same conditions, U ($\propto 1/T$, T temperature) is the nematic potential, and β is the shape factor. To specify the molecular geometry we approximate the disk-like shape of molecule of discotic mesophases with an oblate spheroid of aspect ratio p ($p < 1$) where $r_\parallel$ is the length of the shortest and distinct semiaxis, and $r_\perp$ the length of the two longest and equal semiaxes. For an ideal flat disc $p = 0$ ($\beta = -1$), for a sphere $p = 1$ ($\beta = 0$), and for infinitely long rod $p \to \infty$ ($\beta = 1$). For discotics ($-1 < \beta < 0$), as β increases the constituting aromatic disk-like molecules tend to become thicker. $\mathbf{A}$ and $\mathbf{W}$ are the rate of deformation and vorticity tensor respectively. For uniaxial extensional flows the vorticity tensor $\mathbf{W}$ is zero, and $\mathbf{A}$ is calculated using equations (5.2).

5.2.3 Symmetric Visco-Elastic Stress Tensor for Nematics

The symmetric extra stress tensor $\mathbf{t}^s$ for thermotropic liquid crystalline materials is expressed as a sum of viscous $\mathbf{t}^v$ and elastic $\mathbf{t}^e$ stress contributions (deGenne and Proust, 1993; Doi and Edwards, 1986; Larson, 1996) as:

$$\mathbf{t}^s = \mathbf{t}^v + \mathbf{t}^e \tag{5.8}$$

The expression for the elastic stress contribution $\mathbf{t}^e$, derived by using the standard equation of fluxes $\left(\mathbf{t}^s, \hat{\mathbf{Q}}\right)$ in terms of forces (**A**, **H**) (deGenne and Proust, 1993; Singh and Rey, 1998b; Tsuji and Rey, 1997), for the presented CE (equation (5.3)) is:

$$\begin{aligned}\mathbf{t}^e = (c\kappa T)\Big[&-\tfrac{2}{3}\beta\mathbf{H} - \beta\left\{\mathbf{H}\cdot\mathbf{Q} + \mathbf{Q}\cdot\mathbf{H} - \tfrac{2}{3}(\mathbf{H}:\mathbf{Q})\delta\right\} + \\ &\tfrac{1}{2}\beta\left\{(\mathbf{H}:\mathbf{Q})\mathbf{Q} + \mathbf{H}\cdot\mathbf{Q}\cdot\mathbf{Q} + \mathbf{Q}\cdot\mathbf{H}\cdot\mathbf{Q} + \mathbf{Q}\cdot\mathbf{Q}\cdot\mathbf{H} - ((\mathbf{Q}\cdot\mathbf{Q}):\mathbf{H})\delta\right\}\Big]\end{aligned} \tag{5.9}$$

where

$$\mathbf{H}(\mathbf{Q}) = \frac{1}{6\overline{D}_r}\mathbf{H}\left(\mathbf{Q}, \overline{D}_r(\mathbf{Q})\right) = -\left[\left(1 - \tfrac{1}{3}U\right)\mathbf{Q} - U\mathbf{Q}\cdot\mathbf{Q} + U\left\{(\mathbf{Q}:\mathbf{Q})\mathbf{Q} + \tfrac{1}{3}(\mathbf{Q}:\mathbf{Q})\delta\right\}\right] \tag{5.10}$$

and c is concentration of molecules per unit volume, κ the Boltzmann constant and T the absolute temperature. The viscous stress contribution $\mathbf{t}^v$ is given by:

$$\begin{aligned}\mathbf{t}^v = \Xi:\mathbf{A} = \; &\nu_1\mathbf{A} + \nu_2\left[\mathbf{Q}\cdot\mathbf{A} + \mathbf{A}\cdot\mathbf{Q} - \tfrac{2}{3}(\mathbf{Q}:\mathbf{A})\delta\right] + \\ &\nu_3\left[(\mathbf{A}:\mathbf{Q})\mathbf{Q} + \mathbf{A}\cdot\mathbf{Q}\cdot\mathbf{Q} + \mathbf{Q}\cdot\mathbf{A}\cdot\mathbf{Q} + \mathbf{Q}\cdot\mathbf{Q}\cdot\mathbf{A} + ((\mathbf{Q}\cdot\mathbf{Q}):\mathbf{A})\delta\right]\end{aligned} \tag{5.11}$$

where Ξ is the fourth order tensor, and ν_1, ν_2 and ν_3 are viscosity coefficients. Mapping the above expression to those given in (Doi and Edwards, 1986; Larson, 1996), in which the viscous contribution to stress tensor contains contributions from $\mathbf{Q}^2$ terms only, we arrive at:

$$\mathbf{t}^v = \mu\left[(\mathbf{A}:\mathbf{Q})\mathbf{Q} + \mathbf{A}\cdot\mathbf{Q}\cdot\mathbf{Q} + \mathbf{Q}\cdot\mathbf{A}\cdot\mathbf{Q} + \mathbf{Q}\cdot\mathbf{Q}\cdot\mathbf{A} + ((\mathbf{Q}\cdot\mathbf{Q}):\mathbf{A})\delta\right] \tag{5.12}$$

where $\nu_1 = \nu_2 = 0$ and $\nu_3 = \mu$. Combining equations (5.9) and (5.12), the dimensionless symmetric extra stress tensor $\tilde{\mathbf{t}}^s$ is given by (Singh and Rey, 1998b):

$$\tilde{\mathbf{t}}^s = \frac{\mathbf{t}^s}{c\kappa T} = \xi_v De\left[(\tilde{\mathbf{A}}:\mathbf{Q})\mathbf{Q} + \tilde{\mathbf{A}}\cdot\mathbf{Q}\cdot\mathbf{Q} + \mathbf{Q}\cdot\tilde{\mathbf{A}}\cdot\mathbf{Q} + \mathbf{Q}\cdot\mathbf{Q}\cdot\tilde{\mathbf{A}} - ((\mathbf{Q}\cdot\mathbf{Q}):\tilde{\mathbf{A}})\boldsymbol{\delta}\right] + \beta\left[-\tfrac{2}{3}\mathbf{H} - \{\mathbf{H}\cdot\mathbf{Q} + \mathbf{Q}\cdot\mathbf{H} - \tfrac{2}{3}(\mathbf{H}:\mathbf{Q})\boldsymbol{\delta}\} + \tfrac{1}{2}\{(\mathbf{H}:\mathbf{Q})\mathbf{Q} + \mathbf{H}\cdot\mathbf{Q}\cdot\mathbf{Q} + \mathbf{Q}\cdot\mathbf{H}\cdot\mathbf{Q} + \mathbf{Q}\cdot\mathbf{Q}\cdot\mathbf{H} - ((\mathbf{Q}\cdot\mathbf{Q}):\mathbf{H})\boldsymbol{\delta}\}\right] \quad (5.13)$$

where $\xi_v = \frac{\mu\ 6D_r}{c\kappa T}$ is a dimensionless constant representing the ratio of the viscous $\mathbf{t}^v$ to the elastic $\mathbf{t}^e$ stress contributions, previously introduced by Larson (Larson, 1996); $De = \frac{\dot{\varepsilon}}{6D_r}$ is Deborah number or the dimensionless strain rate, and $\tilde{\mathbf{A}}$ ($\tilde{\mathbf{A}} = \mathbf{A}/\dot{\varepsilon}$) is dimensionless rate of strain tensor, and $\dot{\varepsilon}$ is the extension rate.

5.2.4 Uniaxial Extensional Viscosities of Discotic Nematics

The classical definition of uniaxial extensional viscosity for isotropic materials, also referred to as elongational viscosity or tensile viscosity, is given by Dealy (1994):

$$\eta_E(\dot{\varepsilon}) = \lim_{t\to\infty}\left[\frac{\sigma_E(t,\dot{\varepsilon})}{\dot{\varepsilon}}\right] \quad (5.14)$$

where $\sigma_E = t^s_{zz} - t^s_{rr}$ is the tensile modulus. However, for discotic nematic liquid crystals the above definition is incomplete because there are two different extensional viscosities, as explained below and shown in Appendix A. These two extensional viscosities are defined as follows:

$$\eta_{zr} = \frac{t^s_{zz} - t^s_{rr}}{\dot{\varepsilon}}, \quad \eta_{z\theta} = \frac{t^s_{zz} - t^s_{\theta\theta}}{\dot{\varepsilon}} \quad (5.15a,b)$$

and in dimensionless form as:

$$\eta^*_{zi} = \frac{\eta_{zi}}{(c\kappa T)De} = \frac{6D_r}{c\kappa T}\frac{t^s_{zz} - t^s_{ii}}{\dot{\varepsilon}} = \frac{\tilde{t}^s_{zz} - \tilde{t}^s_{ii}}{De} \quad \text{where } i = r \text{ and } \theta. \quad (5.16)$$

For simplicity, in what follows the superscript "*"is dropped. It is important to note that for rod-like nematics only one extensional viscosity is needed because $\mathbf{n}$ orients along the extension direction (z-axis). On the other hand, in discotic nematics $\mathbf{n}$ orients normal to

the extension direction and anywhere in the compression plane (r-θ), so that the symmetry of the compression plane is broken, and therefore two viscosities are needed. In what follows we show the relations between the two extensional viscosities (equations (5.15)) and the microstructures that arise in the spinning of carbonaceous mesophases (McHugh and Edie, 1995).

5.3 Results and Discussion

This section is subdivided into two subsections. The first subsection discusses the microstructure features (orientation and alignment) of discotic mesophases subjected to uniaxial extensional flows needed to explain extensional flow rheology. The second subsection presents the extensional rheological properties of discotic mesophases.

5.3.1 Orientation and Alignment of Discotic Mesophases under Extensional flows

The detailed dynamic analysis of orientation director triad (**n**, **m**, **l**) and uniaxial S and biaxial P alignments of discotic mesophases under extensional flows are given in (Singh and Rey, 1995a). As mentioned above, here we study only the steady state rheological features of discotic mesophases under extensional flows. At steady state the uniaxial $\mathbf{n}_{ss}$, and biaxial $\mathbf{m}_{ss}$ directors lie in the compression plane (r-θ plane) whereas the biaxial director $\mathbf{l}_{ss}$ lies along the extension direction (z axis). The steady state orientation of the director triad ($\mathbf{n}_{ss}$, $\mathbf{m}_{ss}$, $\mathbf{l}_{ss}$) is independent of extensional rate (De), nematic potential (U), and shape factor (β). However, the dynamics of the orientation director triad are functions of these parameters (Singh and Rey, 1994, 1995a, 1995b).

In this work we have obtained the stable steady state solutions to equations (5.3) for a velocity field given by equations (5.2). The output consists of the components of the steady state tensor order parameter $\mathbf{Q}_{ss}(De)$ which is transformed to principal form to determine its eigenvalues (to evaluate steady state alignments S_{ss} and P_{ss}) and eigenvectors or steady state orientation triad ($\mathbf{n}_{ss}$, $\mathbf{m}_{ss}$, $\mathbf{l}_{ss}$). The parametric study is performed by choosing two values, low and high, of the nematic potential U (U = 3, 6),

and the shape factor β (β = -0.8, -0.6). In the present case, i.e., in the absence of spatial gradients, both S_{ss} and P_{ss} are independent of the steady state director triad orientation ($\mathbf{n}_{ss}$, $\mathbf{m}_{ss}$, $\mathbf{l}_{ss}$). Figure 5.3 shows the steady state uniaxial S_{ss} and biaxial P_{ss} scalar order parameters as a function of De for U = 6 (full line) and U = 3 (dash-line) for β = -0.8 (upper), and β = -0.6 (lower). S_{ss} increases monotonically with the dimensionless strain rate De at all values of U and β. P_{ss} at higher U (U = 6) follows the similar trend and increases monotonically with De for both values of β, however at lower U (U = 3) there is a local minima for intermediate values of De thereafter it increases monotonically with De. For discotic mesophases with a given shape factor β, S_{ss} at high U is always greater than that at low U, however, the difference $\Delta S_{ss} = S_{ss,highU} - S_{ss,lowU}$ between values at high and low U decreases with increasing De. Whereas P_{ss} at high U is less than that at low U, and the difference $\Delta P_{ss} = P_{ss,lowU} - P_{ss,highU}$ increases with De. Both S_{ss} and P_{ss} for discotic mesophases consisting of thicker disks, β = -0.6, are less than those with the relatively thinner disks, β = -0.8 for all U and De. Though not shown in Figure 5.3, as $De \rightarrow 0$, uniaxiality is recovered, i.e. $P_{ss} \rightarrow 0$, for all values of nematic potential, U (U = 6, 3) and shape factor β (β = -0.6, -0.8) considered here.

In this paper the spatial variation of order parameter is not considered when capturing the extensional viscosities corresponding to the characteristic textures of discotic mesophase fibers. As is well known (deGenne and Proust, 1993), the intrinsic length scale of the model ζ, where there are variations in order parameter, is given as:

$$\zeta = \sqrt{\frac{L}{\left(d^2 \Lambda_H / dS^2\right)\Big|_{S_B}}} \tag{5.17}$$

where L is the elastic constant, Λ_H is the homogeneous free energy density (Rey, 1997), and S_B the bulk order parameter. For liquid crystals systems this correlation length is less than 10^{-2} μm and thus significantly smaller than the fiber radius (~ 1 μm), and to simplify the analysis we can assume as a first approximation that $\nabla \lambda_i = 0$ (i = **n**, **m**, **l**). Therefore in what follows we use the homogeneous scalar order parameter

(i.e., $\nabla S = \nabla P = \mathbf{0}$) results obtained in this section to calculate extensional viscosities in the presence of the orientation gradients (i.e., $\nabla \mathbf{n} \neq \mathbf{0}, \nabla \mathbf{m} \neq \mathbf{0}$) that arise in cylindrical coordinates (see Figure 5.4).

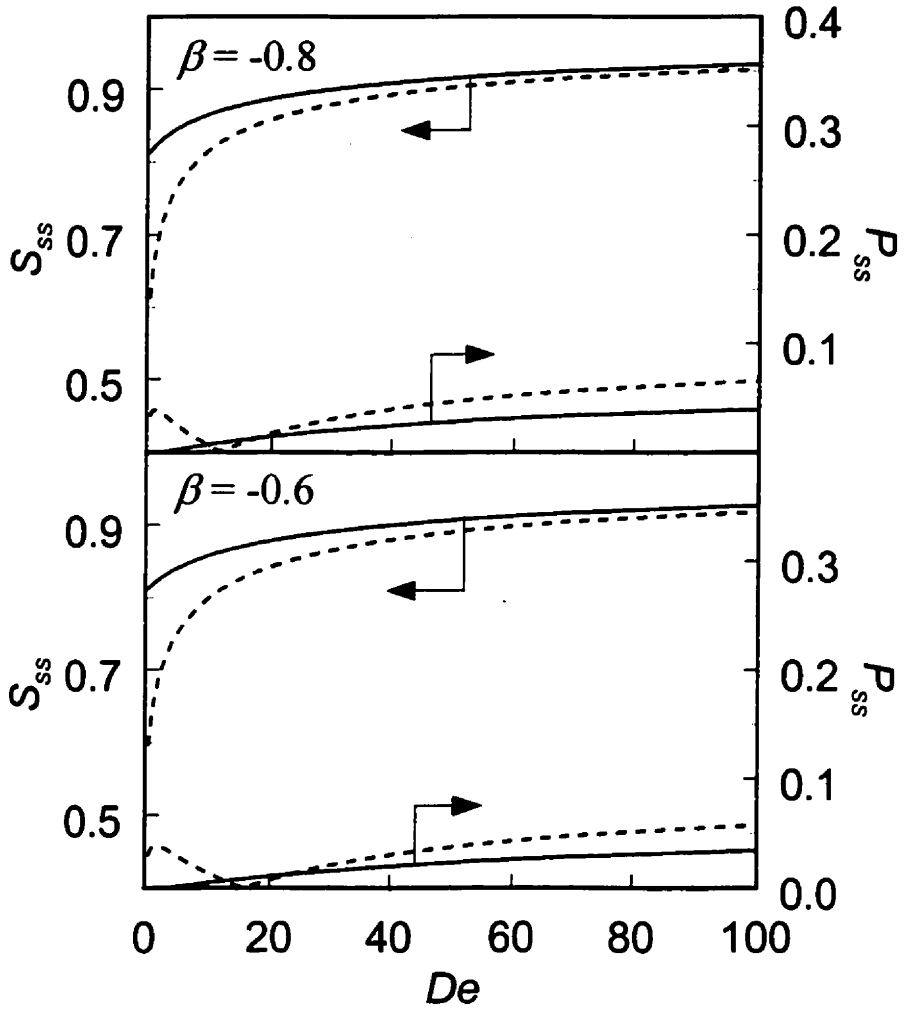

Figure 5.3: Steady state uniaxial S_{ss} and biaxial P_{ss} scalar order parameters as a function of De for $U = 6$ (full line) and $U = 3$ (dash-line) for $\beta = -0.8$ (upper), and $\beta = -0.6$ (lower). S_{ss} increases monotonically with the dimensionless strain rate De at all values of U and β. P_{ss} at higher U ($U = 6$) follows the similar trend, however at lower U ($U = 3$) there is a local minima. Both S_{ss} and P_{ss} for discotic mesophases consisting of thicker molecules, $\beta = -0.6$, are less than those with the relatively thinner molecules, $\beta = -0.8$.

5.3.2 Uniaxial Extensional Viscosity of Discotic Mesophases

This section presents the predicted extensional viscosity and its relations with the flow-induced internal microstructure (**Q**), processing conditions ($U \propto 1/T$), and material parameters (β), of relevance to the industrial fiber spinning of mesophase pitches. It is well documented that during this process the fiber cross section may exhibit the onion or radial textures (Peebles, 1994), shown in Figure 5.4. The figure shows schematics of the radial and onion microstructure mode with respect to the cylindrical coordinate system with the z-axis (extensional direction) perpendicular to the page. The dotted lines show the side view of the disk-like molecules, such that for radial (onion) mode, the unit normals to the disk-like molecules orient along the azimuthal θ (radial r) direction. These two modes also exist as the prevalent transverse fiber textures in mesophase carbon fibers (Peebles, 1994). To study the effect of processing conditions and material parameters, the same parametric values for U and β, as stated above, are used.

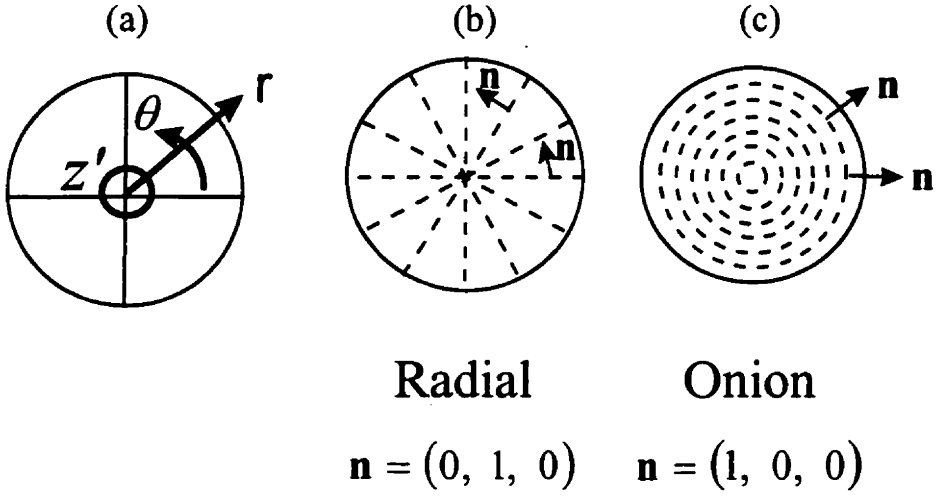

Figure 5.4: Schematics of (a) cylindrical coordinate system, and the two main representative mesophase pitch-based carbon fiber transverse textures: (b) radial, and (c) onion. In the radial (onion) texture, the unit normals to the disk-like molecules orient along the azimuthal θ (radial r) direction. These textures are observed in the spinning of carbonaceous mesophases (Peebles, 1994).

As shown in Appendix A the Leslie-Ericksen (Leslie, 1979) theory for discotic mesophases indicates that two uniaxial extensional viscosities need to be defined to

completely characterize their extensional rheological functions, in contrast to rod-like nematics, which need only one. Thus to characterize the extensional viscosities for discotic nematics with the two observed microstructures, radial and onion, we use the following nomenclature:

$$\eta^i_{zj} = \frac{t^i_{zz} - t^i_{jj}}{De} \tag{5.18}$$

where $i = r$, o represents the radial and onion texture respectively, and $j = r$, θ representing the two axis in the cylindrical coordinate system, see Figure 5.4a. For example the two extensional viscosities corresponding to the radial texture are: η^r_{zr} and $\eta^r_{z\theta}$, the former is given as the ratio of the difference of the diagonal components of extra stress tensor $\mathbf{t}^s$ along z and r directions to the strain rate, and the latter by the ratio of the difference of the diagonal components of extra stress tensor $\mathbf{t}^s$ along z and θ directions to the strain rate. In the present model, the extension viscosity is a function of flow-induced microstructure ($\mathbf{Q}$), nematic potential (U), strain rate (De) and the shape factor (β), and can be represented as below:

$$\eta^i_{zj} = \Psi\left(\beta, U, De, \mathbf{Q}^i\right) \tag{5.19}$$

where the microstructure tensor $\mathbf{Q}^i$ ($i = r$ (radial), $i = o$ (onion)) for radial ($\mathbf{Q}^r$) and onion ($\mathbf{Q}^o$) texture is given as:

$$\mathbf{Q}^r = \lambda_m \hat{\delta}_r \hat{\delta}_r + \lambda_n \hat{\delta}_\theta \hat{\delta}_\theta + \lambda_1 \hat{k}\hat{k} \tag{5.20}$$

$$\mathbf{Q}^o = \lambda_n \hat{\delta}_r \hat{\delta}_r + \lambda_m \hat{\delta}_\theta \hat{\delta}_\theta + \lambda_1 \hat{k}\hat{k} \tag{5.21}$$

where $\hat{\delta}_r$, $\hat{\delta}_\theta$ and $\hat{k}$ are the unit vectors along the three cylindrical coordinates; the superscript in $\mathbf{Q}$ represents the texture: $i = r$ (radial), o (onion).

Figure 5.5 shows the computed dimensionless uniaxial extensional viscosities η^i_{zr} and $\eta^i_{z\theta}$ ($i = r$ (radial texture), $i = o$ (onion texture)) of discotic mesophase as a function of De for $\xi_v = 0.001$ (full line), 0.1 (dash line), and 0.2 (triple dot-dash line); for

β = -0.8 and U = 6 ((a), (b)), and U = 3 ((c), (d)). The extensional viscosity η^i_{zr} ($\eta^i_{z\theta}$) for the radial mode η^r_{zr} ($\eta^r_{z\theta}$) is always less (greater) than for the onion mode η^o_{zr} ($\eta^o_{z\theta}$), i.e. $\eta^r_{zr} < \eta^o_{zr}$ ($\eta^r_{z\theta} > \eta^o_{z\theta}$), at all *De* for all values U and β. Please also note that $\eta^r_{zr} = \eta^o_{z\theta}$, and $\eta^o_{zr} = \eta^r_{z\theta}$, therefore we have $\eta^r_{zr} = \eta^o_{z\theta} < \eta^o_{zr} = \eta^r_{z\theta}$. The dependence of uniaxial extensional viscosities, η^r_{zr} and η^o_{zr}, for the radial and the onion textures on U, β and *De* are summarized in Table 5.1. For high U (U = 6), η^i_{zr} (each η^r_{zr} and η^o_{zr}) is independent of low *De*, but exhibits slight strain thinning for ξ_v = 0.001, and strain thickening for ξ_v = 0.1, and 0.2 at high *De*. It is found that the strain thinning (thickening) is due to elastic (viscous) stress contribution, since as the viscous contribution to total stress increases the discotic mesophases exhibit stronger strain thickening characteristics. This phenomenon is more apparent at low U (higher T). As shown in Table 5.1, η^r_{zr} follows the same trend at low and high U. However, at low U, η^o_{zr} exhibits strain thinning at low *De* with saturation at high *De* for ξ_v = 0.001, and strain thinning for low *De* and strain thickening at high *De* with transition from thinning to thickening at intermediate *De* for ξ_v = 0.1, and 0.2. At low *De* the departure from equilibrium is higher at low U (see Figure 5.4), thus elastic stress contributes more at low U at low *De*, thereby showing strain thinning at low strain rates, with strain thickening at high rates. Also, as elastic (viscous) stress dominates at low (high) *De*, therefore strain thinning (thickening) is seen at low (high) strain rates, with an intermediate *De* strain thinning → thickening transition (see Figure 5.5d and Table 5.1). Though extensional viscosities at very low *De* are not presented here, however, at very low *De* (*De* → 0) the visco-elastic effects on microstructure and stress vanish and the viscosities are constant. The terminology for low/high *De* is used just to explain the most important results presented in Figure 5.5.

Although not shown, the effect of the shape factor β on both the extensional viscosities has been characterized. It is found that as β increases the extensional viscosities η^i_{zr} and $\eta^i_{z\theta}$ decrease. For a fixed director triad orientation (radial or onion in the present case), the extensional viscosities are functions of the steady state eigenvalues

(λ_n, λ_m, λ_l) or the uniaxial S_{ss} and biaxial P_{ss} alignments; see equations (5.1, 5.19). As explained above and shown in Figure 5.3, both S_{ss} and P_{ss} decrease with increasing β, hence η^i_{zr} and $\eta^i_{z\theta}$ decrease with increasing β. All the above-mentioned equalities, i.e. $\eta^r_{zr} = \eta^o_{z\theta}$ and $\eta^o_{zr} = \eta^r_{z\theta}$, and inequalities, i.e. $\eta^r_{zr} < \eta^o_{zr}$ and $\eta^r_{z\theta} > \eta^o_{z\theta}$, also follow at higher β (β = -0.6).

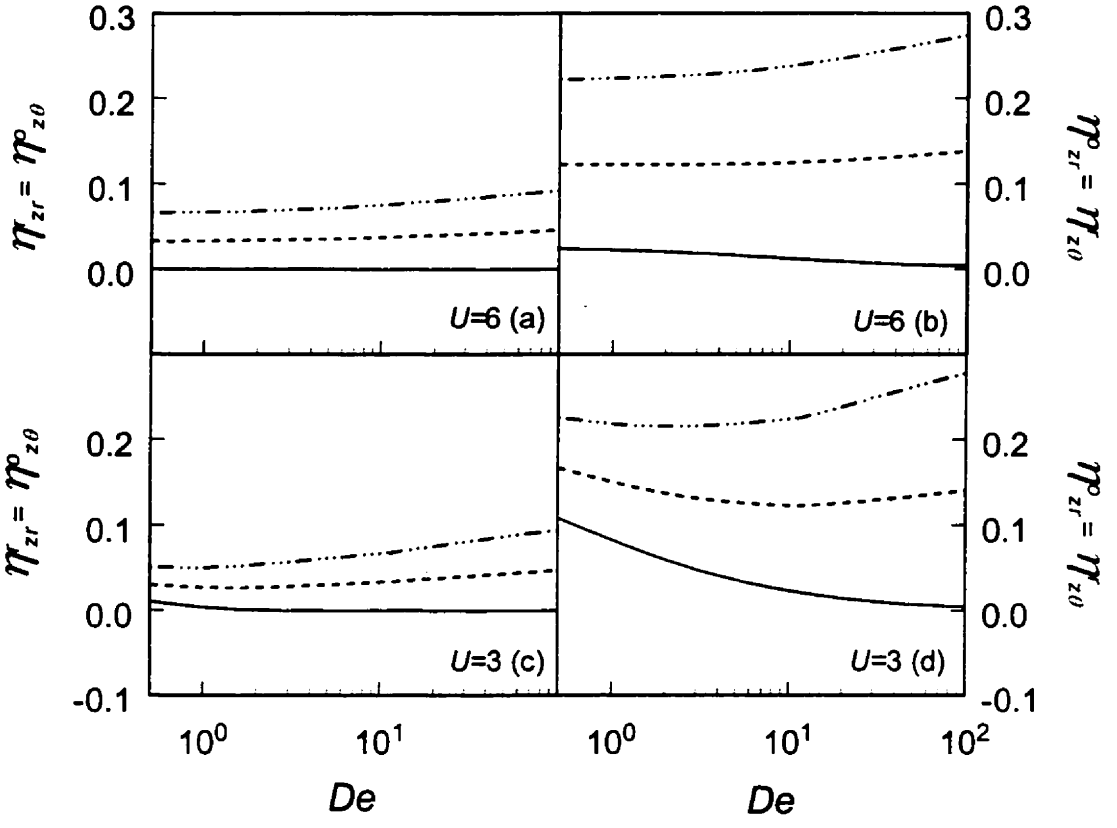

Figure 5.5: Dimensionless uniaxial extensional viscosities η^i_{zr} and $\eta^i_{z\theta}$ ($i = r$ (radial), $i = o$ (onion)) of discotic mesophase as a function of *De* for ξ_v = 0.001 (full line), 0.1 (dash line), and 0.2 (triple dot-dash line); for β = -0.8 and U = 6 ((a), (b)), and U = 3 ((c), (d)). The extensional viscosity η^i_{zr} ($\eta^i_{z\theta}$) for the radial texture η^r_{zr} ($\eta^r_{z\theta}$) is always less (greater) than for the onion texture η^o_{zr} ($\eta^o_{z\theta}$), i.e. $\eta^r_{zr} < \eta^o_{zr}$ ($\eta^r_{z\theta} > \eta^o_{z\theta}$). Also note that $\eta^r_{zr} = \eta^o_{z\theta}$, and $\eta^o_{zr} = \eta^r_{z\theta}$, therefore $\eta^r_{zr} = \eta^o_{z\theta} < \eta^o_{zr} = \eta^r_{z\theta}$, for details see text.

TABLE 5.1

Effect of processing conditions on uniaxial extensional viscosities of discotic mesophases

U	6 (high)				3 (low)			
ξ_v	0.001		0.1, 0.2		0.001		0.1, 0.2	
De	low	High	Low	high	low	high	low	high
$\eta^r_{zr} = \eta^o_{z\theta}$	—	↓	—	↑	—	↓	—	↑
$\eta^o_{zr} = \eta^r_{z\theta}$	—	↓	—	↑	↓	—	↓	↑

'—': strain rate independent viscosity, '↓': strain thinning, '↑': strain thickening, U: nematic potential ($\propto$ 1/T, temperature), ξ_v: ratio of viscous to elastic stress contributions, De: dimensionless strain rate, η^r_{zr}, $\eta^r_{z\theta}$, η^o_{zr}, $\eta^o_{z\theta}$: dimensionless uniaxial extensional viscosities of discotic mesophases.

The above discussed viscosity-microstructure relationships can be summarized as follows:

Inequalities within a given texture: $\eta^r_{z\theta} > \eta^r_{zr}$; $\eta^o_{zr} > \eta^o_{z\theta}$ (5.22,a,b)

Equalities between two different textures: $\eta^r_{z\theta} = \eta^o_{zr}$; $\eta^r_{zr} = \eta^o_{z\theta}$ (5.23a,b)

To understand the above equalities and inequalities we use symmetry. The extensional viscosities for discotic mesophase depend on the microstructure **Q**, the nematic potential U, the strain rate De, and the shape factor β:

$$\eta^r_{z\theta} = \Psi(\beta, U, De, \lambda_n, \lambda_l), \quad \text{and} \quad \eta^o_{zr} = \Psi(\beta, U, De, \lambda_n, \lambda_l) \tag{5.24a,b}$$

where λ_n, λ_m, λ_l are the eigenvalues of **Q**; see equation (5.1). Since the eigenvalue, λ_n, along θ direction for the radial texture is equal to the eigenvalue, λ_n, along r for the onion texture, and since λ_l is common to both we find:

$$\eta^r_{z\theta} = \eta^o_{zr} \tag{5.25}$$

Similarly

$$\eta_{zr}^{r} = \Psi(\beta, U, De, \lambda_m, \lambda_1), \qquad \text{and} \qquad \eta_{z\theta}^{o} = \Psi(\beta, U, De, \lambda_m, \lambda_1) \tag{5.26a,b}$$

Since the eigenvalue, λ_m, along r direction for the radial texture is equal to the eigenvalue, λ_m, along θ for the onion texture, and since λ_1 is common to both we have:

$$\eta_{zr}^{r} = \eta_{z\theta}^{o} \tag{5.27}$$

Next, we will establish the origin of the inequalities (equations (5.22)) in the uniaxial extensional viscosities within a given texture. From equations (5.19-5.21), (5.24a) and (5.26a), since $\lambda_n > \lambda_m$, we have the inequality:

$$\eta_{z\theta}^{r} > \eta_{zr}^{r} \tag{5.28}$$

Likewise from equations (5.19-5.21), (5.24b) and (5.26b), and $\lambda_n > \lambda_m$, the second inequality follows:

$$\eta_{zr}^{o} > \eta_{z\theta}^{o} \tag{5.29}$$

We note that even in the uniaxial approximation ($\lambda_n \neq \lambda_m = \lambda_1$), there will be two distinct extensional viscosities for discotic mesophases, and the inequalities between the uniaxial extensional viscosities for discotic mesophases presented above will hold. Appendix B shows that the texture dependent equalities and inequalities between the viscosity coefficients hold in the uniaxial limits also using L-E theory.

5.4 Conclusions

Predictions of uniaxial extensional rheological functions of discotic mesophases are presented and classified. The predicted rheological functions are discussed and assessed within the context of nematorheology.

For discotic mesophases two uniaxial extensional viscosities, termed here as η_{zr} and $\eta_{z\theta}$, are needed to completely characterize their extensional rheological functions. The extensional viscosities depend strongly on the microstructure such that $\eta_{zr}^{r} < \eta_{zr}^{o}$ and

$\eta^r_{z\theta} > \eta^o_{z\theta}$. The extensional viscosities are different within a given texture, for example, for radial (onion) texture $\eta^r_{zr} < \eta^r_{z\theta}$ ($\eta^o_{zr} > \eta^o_{z\theta}$). The discotic mesophases are found to be non-Troutonian, and show strain thinning or thickening based on temperature and ratio of viscous to elastic stress contributions. The elastic (viscous) stresses result in strain thinning (thickening) characteristics to the discotic mesophases.

The microstructure dependency of the extensional viscosity of discotic mesophases has direct impact on the selection of experimental technique to measure the extensional viscosity. The preferred microstructure (radial, onion, mixed radial onion, or folded) develops inside the spinneret capillaries, and the strong extensional flows accentuate the axial orientation of the molecules (Fatholahi et al, 1992; Fatholahi and White, 1994; Fleurot and Edie, 1997; McHugh and Edie, 1992, 1995). Thus if spinning devices are employed to measure the extensional viscosity, then prevailing microstructure in the thread-line needs to be specified along with the extensional viscosity data.

Bibliography

J.M. Dealy, "Official nomenclature for material functions describing the response of a viscoelastic fluid to various shearing and extensional deformations" *J. Rheol.*, **38**, 179 (1994).

P.G. deGenne and J. Proust, In *The Physics of Liquid Crystals*, 2nd edition, (Oxford University Press), London (1993).

M. Doi and S.F. Edwards, 1986, In *The Theory of Polymer Dynamics* (Oxford University Press), New York, USA.

D.D. Edie, K.E. Robinson, O. Fleurot, S.P. Jones and C.C. Fain, "High thermal conductivity ribbon fibers from Naphthalene-based mesophase." *Carbon*, **32**, 1045 (1994).

B. Fatholahi, M.K. Gopalakrishnan and J.L. White, *Carbon '92*, 36 (1992).

B. Fatholahi and J.L. White, "Polarized-light observation of flow-induced microstructures in mesophase pitch." *Journal of Rheology*, **38**, 1591 (1994).

O. Fleurot and D.D. Edie, *Carbon '97* (1997).

R.G. Larson, "On the relative magnitudes of viscous, elastic and texture stresses in liquid crystalline PBG solutions" *Rheol. Acta*, **35**(2), 150 (1996).

F.M. Leslie, *Theory of flow phenomena in liquid crystals*, in *Advances in Liquid Crystals*, (Academic Press), New York, USA, (1979).

J.J. McHugh, "The development of orientation in mesophase pitch during fiber formation" Ph.D. Dissertation, Clemson University, Clemson, SC, USA (1994).

J.J. McHugh and D.D. Edie, *Carbon '92*, 683 (1992).

J.J. McHugh and D.D. Edie, "Orientation of mesophase pitch in capillary and channel flows." *Liquid Crystals*, **18**, 327 (1995).

L.H. Peebles, In *Carbon Fibers Formation, Structures and Properties*, CRC Press, Boca Raton, USA (1994).

A.D. Rey, "Fiber stability analysis for in-situ liquid crystalline polymer composites" *Polymer Composites*, **18**, 687 (1997).

A.P. Singh and A.D. Rey, "Extension dynamics of discotic nematics of variable order: geodesic flow and viscoelastic relaxation", *Journal de Physique II France* **4**, 645 (1994).

A.P. Singh and A.D. Rey, "Theory and simulation of extensional flow-induced biaxiality in discotic mesophases", *Journal de Physique II France* **5**, 1321 (1995a).

A.P. Singh and A.D. Rey, "Computer simulation of dynamics and microstructure of discotic mesophases in extensional flows", *Liquid Crystals* **18**(2), 230 (1995b).

A.P. Singh and A.D. Rey, "Microstructure constitutive equation for discotic nematic liquid crystalline materials Part I: Selection procedure and shear flow predictions", *Rheologica Acta* **37**(1), 30 (1998a).

A.P. Singh and A.D. Rey, "Microstructure constitutive equation for discotic nematic liquid crystalline materials Part II: Rheological predictions", *Rheologica Acta* **37**(4), 374 (1998b).

T. Tsuji and A.D. Rey, "Effect of long range order on sheared liquid crystalline materials .1. compatibility between tumbling behavior and fixed anchoring" *JNNFM*, **73**, 127 (1997).

G.E. Volovik, "Relationship between molecule shape and hydrodynamics in a nematic substance" *JETP Lett.*, **31**, 273 (1980).

[1]CHAPTER 6

Effect of Long Range Elasticity and Boundary Conditions on Microstructural Response of Sheared Discotic Mesophases

In the previous chapters we explored the flow-induced microstructural and rheological response of the selected CE under homogeneous flows. This chapter presents comprehensive analysis of non-homogeneous shear flow-induced microstructure response of discotic mesophases in the presence of curvature elasticity in different planar surface anchorings. Four different planar microstructure modes, steady state and periodic, are shown to be stable. The microstructure phase diagram reveals that the four stable microstructure regimes co-exist at one point, called qua-critical point. It is shown that the bulk molecular orientation is along the velocity gradient direction irrespective of the surface anchorings. Novel scaling laws relating the microstructure mode domains with the Frank elasticity are presented. This chapter puts forth a systematic study of flow induced microstructural behavior of discotic mesophases, and provides a useful fundamental understanding of the flow of discotic mesophases of use in the processing of carbonaceous mesophases.

---

[1] This chapter appeared as an original article in *Journal of Non-Newtonian Fluid Mechanics* **94**(2-3) p87-111 (2000).

6.0 Abstract

A comprehensive analysis of shear flow-induced microstructure phenomena exhibited by discotic mesophases is presented using a complete generalized non-linear theory that takes into account short-range order elasticity, long-range elasticity, and viscous flow effects. The following four distinct shear-induced stable planar non-homogeneous microstructure modes are found: (1) long-range elasticity-induced steady state, (2) bulk tumbling–boundary wagging state, (3) bulk wagging state, and (4) viscous flow induced steady state. The stability of the microstructure modes is presented in terms of a rheological phase plane spanned by the Ericksen number Er (ratio of viscous flow to long-range elasticity), and the ratio of short-range to long-range elasticity (R). The steady and dynamical features of the various microstructure regimes are thoroughly characterized and analyzed. Two strong surface anchoring conditions, along the velocity gradient direction, and along the flow direction, are employed to investigate their effect on the stability and range of various microstructure regimes on the Er-R phase plane. The average bulk orientation for all the modes is found to be close to the velocity gradient direction. The fixed anchoring along the velocity gradient direction transmits the anchoring conditions into the bulk more strongly than that by the fixed anchoring along the flow direction. The effects of long-range elasticity on the flow-induced microstructure features are characterized. These simulations provide useful information to process carbonaceous mesophases by identifying the principles that govern shear flow-induced orientation in discotic mesophases.

6.1 Introduction

Carbonaceous mesophases or mesophase pitches are being employed as precursor materials to manufacture high performance mesophase carbon fibers and as matrix materials in carbon-carbon composites. The excellent end product property profiles are due to the anisotropic nature of the mesophase pitches. For example mesophase carbon fibers have been known to possess very high axial thermal conductivity and elastic modulus, and thus are very suitable for industrial processes requiring high thermal transport and stiffness. As is well known (Chandrasekhar, 1981, 1992; Zimmer et al.,

1982; Carlsson, 1983; Singer, 1985; McHugh et al., 1992; Edie et al., 1994; McHugh and Edie, 1995, 1994; Peebles, 1994), it is possible to induce and control preferred molecular alignment in anisotropic carbonaceous mesophases during processing, thereby imparting superior properties to the end products. Mesophase pitches are discotic liquid crystalline materials and have been shown (Singer, 1985; Chandrasekhar, 1992; McHugh et al., 1992; Edie et al., 1994; McHugh and Edie, 1995; Peebles, 1994) to exhibit symmetry breaking typical of the nematic phase. Mesophases pitches consist of disc-shaped aromatic molecules that are flat and large enough to exhibit nematic characteristics, and are termed discotic nematics, N_D. Figure (6.1) shows a schematic of a uniaxial discotic nematic phase. The unit normals to the disk-like molecules orient along a preferred direction given by a unit vector $\mathbf{n}$ commonly known as director or average orientation, and the extent of alignment of the unit normals along the director $\mathbf{n}$ is given by a scalar S called uniaxial scalar order parameter or uniaxial alignment.

Numerous experimental (Baek et al., 1993, 1994) and theoretical studies (Marrucci and Maffettone, 1989; Larson and Öttinger, 1991; Andrews et al., 1995; Marrucci and Greco, 1993; Tsuji and Rey, 1997, 1998, 2000; Rey and Tsuji, 1998) have been performed to unravel the fundamental principles governing the flow-induced microstructural phenomena of rod-like nematics. A similar understanding is not yet available for discotic nematics, but is required for making further technological advances in the manufacturing of carbon fiber using carbonaceous mesophase precursors. The present work is aimed towards developing such scientific database for discotic mesophases, and extends our previous work (Tsuji and Rey, 1997, 1998, 2000; Rey and Tsuji, 1998) to discotic nematics.

In industrial processing, precursor materials are subjected to complex flows, involving various combinations of shear and extensional deformations, in complex geometries. In order to control the molecular orientation or microstructure a fundamental understanding of the material behavior subjected to the prevailing complex flow is required. In this paper we study and characterize the distinct microstructural features exhibited by discotic mesophases under rectilinear shear flow.

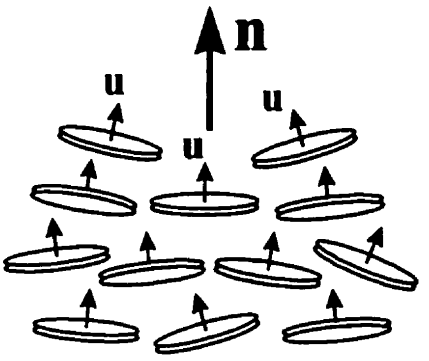

Figure 6.1: Definition of uniaxial director/orientation **n** of a uniaxial discotic nematic liquid crystalline phase. The director **n** is the average orientation of the unit normals **u** to the disc-like molecules.

In our previous works (Singh and Rey, 1998a, 1998b) a constitutive equation (CE) for discotic mesophases was formulated based on Doi's theory of nematodynamics (Doi and Edwards, 1986) by taking into account full microstructural features (Singh and Rey, 1998a, 1998b). The CE under homogeneous shear flow predicted the classical stable planar 2D (tumbling, wagging and aligning) modes as well as non-planar 3D (log-rolling) mode. These microstructure modes in sheared discotic mesophases are similar to those for rod-like nematics, yet possess inherent differences which are attributes of different molecular shape. For example in the planar stationary high shear rate regime, the director **n** aligns near the velocity gradient (velocity) direction for discotic (rod-like) nematics. Similarly, in the planar periodic, rotational and oscillatory, modes the director **n** spends most time along the velocity gradient direction in sheared discotic mesophases (Singh and Rey, 1998a, 1998b). Our previous work (Singh and Rey, 1998a, 1998b) was restricted to ideal homogeneous microstructure fields, however actual processing flows have finite boundaries that affect strongly the microstructure fields through surface forces and torques. Thus it is necessary to include the geometry effects to complete the current understanding of flowing discotic mesophases. These surface effects are implemented using a previously developed model (Singh and Rey, 1998a, 1998b) by incorporating long-range (Frank) elasticity terms. Tsuji and Rey (Tsuji and Rey, 1997, 1998; Rey and Tsuji, 1998) have successfully undertaken the same approach for sheared rod-like nematics.

The general aim of this paper is to characterize the effect of long-range order elasticity on the rectilinear shear-induced microstructure phenomena in discotic mesophases. The particular objectives are:

1. To present comprehensive characterization of all the planar spatially non-homogeneous microstructure modes of discotic mesophases subjected to rectilinear shear flow,
2. To characterize and explain the differences in the microstructural response of sheared discotic nematics under two representative surface anchoring conditions,
3. To summarize the planar microstructure features of the sheared discotic mesophases in terms of rheological phase diagrams,
4. To analyze the effect of elastic anisotropy on the microstructure features of sheared discotics.

The organization of the paper is as follows. In the next section we present the theory, coordinate system, assumptions used in problem formulation, governing equations, and a brief description of computational methods employed to solve the governing equation. Section 6.3 contains the numerical results and their discussion. Section 6.4 presents the conclusions.

6.2 Problem Formulation

6.2.1 Theory and Governing Equations

The microstructure of discotic mesophases, N_D, is described conveniently in terms of a second order, symmetric and traceless tensor order parameter **Q** (deGennes and Proust, 1993):

$$\mathbf{Q} = \int \left(\mathbf{uu} - \frac{\mathbf{I}}{3} \right) f \, d^2\mathbf{u} \tag{6.1}$$

where **u** is the unit vector normal to the disk-like molecules (see Figure 6.1), **I** is second order unit tensor, and f is the orientation distribution function. Alternatively **Q** can also be defined in terms of three eigenvectors (**n**, **m** and **l**) and three eigenvalues

(λ_n, λ_m and λ_l):

$$\mathbf{Q} = \lambda_n \mathbf{nn} + \lambda_m \mathbf{mm} + \lambda_l \mathbf{ll} \tag{6.2}$$

The main eigenvector **n** of **Q** represents the uniaxial director. Uniaxial scalar order parameter or alignment S, is a measure of the molecular alignment along the uniaxial director **n**, and is given by $S = \frac{3}{2}\mathbf{Q}:\mathbf{nn}$. Biaxial alignment P is a measure of molecular alignment along the eigenvector **m** in a plane perpendicular to **n**, and is calculated as $P = \frac{3}{2}(\mathbf{Q}:\mathbf{mm} - \mathbf{Q}:\mathbf{ll})$.

The evolution of microstructure tensor order parameter **Q** is given by a combination of three competitive contributions:

1. Flow contribution **F** accounts for effect of fluid rate of deformation and fluid vorticity on molecular field in terms of microstructure **Q**, molecular shape β, and flow field $\nabla\mathbf{v}$ (**v** is the velocity vector).
2. Short-range elastic contribution **H** arises directly from the intermolecular attractive and repulsive forces such as van der Walls forces and excluded volume effects, and controls the isotropic-nematic phase transition. **H** is given in terms of microstructure **Q**, nematic potential $U(1/T)$, and rotational diffusivity D_r.
3. Long-range elastic contribution **B**, commonly known as Frank elasticity, arises due to secondary effect of the nematic intermolecular forces, and transmits the surface anchoring effects from the boundaries into the bulk. This effect is necessary to describe the textures and defects invariably observed in practice (Zimmer et al., 1982; Larson, 1999).

A linear combination of these three fundamental contributions determines the microstructure response of discotic nematics under arbitrary flow as follows (Tsuji and Rey, 1997, 1998, 2000; Rey and Tsuji, 1998; Singh and Rey, 1998a, 1998b):

$$\hat{\mathbf{Q}} = \mathbf{F}(\mathbf{Q}, \nabla\mathbf{v}) + \mathbf{H}(\mathbf{Q}, \overline{D}_r(\mathbf{Q})) + \mathbf{B}(\nabla\mathbf{Q}) \tag{6.3}$$

where

$$\mathbf{F}(\mathbf{Q},\nabla\mathbf{v}) = \tfrac{2}{3}\beta\mathbf{A} + \beta[\mathbf{A}\cdot\mathbf{Q} + \mathbf{Q}\cdot\mathbf{A} - \tfrac{2}{3}(\mathbf{A}:\mathbf{Q})\mathbf{I}] - \tfrac{1}{2}\beta[(\mathbf{A}:\mathbf{Q})\mathbf{Q} + \mathbf{A}\cdot\mathbf{Q}\cdot\mathbf{Q} + \mathbf{Q}\cdot\mathbf{A}\cdot\mathbf{Q} + \mathbf{Q}\cdot\mathbf{Q}\cdot\mathbf{A} - \{(\mathbf{Q}\cdot\mathbf{Q}):\mathbf{A}\}\mathbf{I}] \tag{6.3a}$$

$$\mathbf{H}(\mathbf{Q},\overline{D}_r(\mathbf{Q})) = -6\overline{D}_r[(1-\tfrac{1}{3}U)\mathbf{Q} - U\mathbf{Q}\cdot\mathbf{Q} + U\{(\mathbf{Q}:\mathbf{Q})\mathbf{Q} + \tfrac{1}{3}(\mathbf{Q}:\mathbf{Q})\mathbf{I}\}] \tag{6.3b}$$

$$\mathbf{B}(\mathbf{Q}) = 6\overline{D}_r\left[\frac{L_1}{c\kappa T}\nabla^2\mathbf{Q} + \tfrac{1}{2}\frac{L_2}{c\kappa T}\left[\nabla(\nabla\cdot\mathbf{Q}) + \{\nabla(\nabla\cdot\mathbf{Q})\}^T - \tfrac{2}{3}tr\{\nabla(\nabla\cdot\mathbf{Q})\}\mathbf{I}\right]\right] \tag{6.3c}$$

$$\overline{D}_r = D_r\left[1 - \tfrac{3}{2}(\mathbf{Q}:\mathbf{Q})\right]^{-2}, \quad \beta = \frac{p^2-1}{p^2+1}, \quad p = \frac{r_\perp}{r_\parallel}. \tag{6.3e, f, g}$$

$$\hat{\mathbf{Q}} = \frac{\partial\mathbf{Q}}{\partial t} + (\mathbf{v}\cdot\nabla)\mathbf{Q} - \mathbf{W}\cdot\mathbf{Q} + \mathbf{Q}\cdot\mathbf{W} \tag{6.3h}$$

where $\hat{\mathbf{Q}}$ is the Jaunmann derivative of $\mathbf{Q}$, $\overline{D}_r$ is the microstructure dependent rotational diffusivity, D_r is the pre averaged rotational diffusivity or isotropic diffusivity independent of $\mathbf{Q}$, U is the nematic potential, and β the shape factor. The disk-like molecules of discotic nematics are approximated with oblate spheroids of aspect ratio p ($p < 1$), equation (3f), where $r_\parallel$ is the length of shorter and distinct semiaxis, and $r_\perp$ the length of the two longer and equal semi-axes such that for an ideal flat disc-like molecule $p = 0$ ($\beta = -1$), for sphere $p = 1$ ($\beta = 0$), and for infinitely long rod $p \to \infty$ ($\beta = 1$). For discotics, the material parameter varies from $-1 < \beta < 0$. L_1 and L_2 are Landau coefficients or elastic moduli, and are related to the macroscopic curvature elasticity of uniaxial nematics as follows:

$$L_1 = \frac{K_{22}}{2S^2},\ L_2 = \frac{K - K_{22}}{S^2} \text{ where } K = K_{11} = K_{33};\ L_1 + \frac{2}{3}L_2 \geq 0,\ L_1 \geq 0 \tag{6.4}$$

K_{11}, K_{22} and K_{33} are Frank elastic constants for splay, twist and bend elasticity respectively. It has been observed experimentally, and predicted from molecular simulations and theory for representative discotic nematic materials (Stelzer et al., 1997; de Castro et al., 1999; Singh and Pandey, 1998) that there exists a reversal in the well known ordering of Frank elastic constants as compared to that in rod-like nematics. For discotics the ordering in Frank constants is $K_{22} > K_{11} > K_{33}$ (Stelzer et al., 1997).

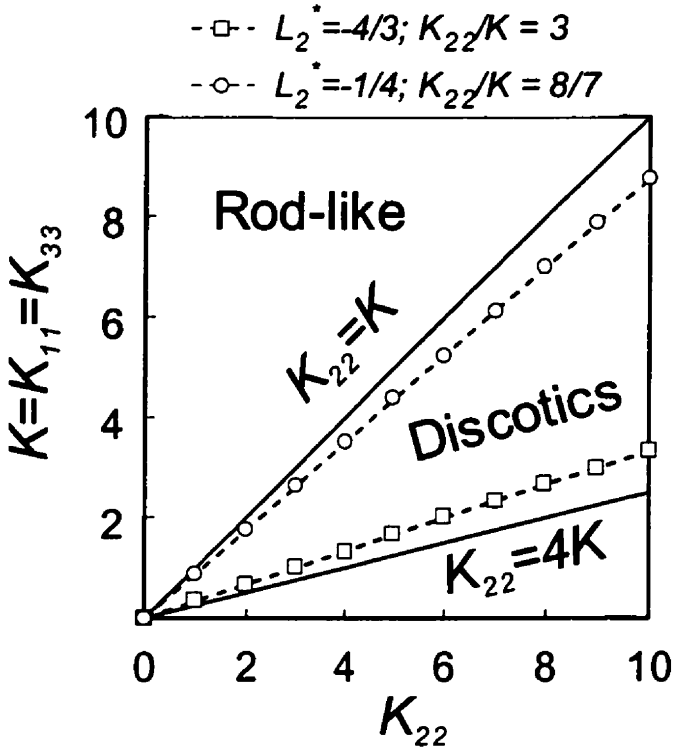

Figure 6.2: The parametric area in the K-K_{22} phase plane where the present theory, equation (3), is applicable for rod-like and discotic nematics. Please note that the theory is applicable for ideal discotic mesophases only in the closed range $K \le K_{22} \le 4K$. In this theory the bend and splay elastic constants are equal $K_{11} = K_{33} = K$. As shown, two different values of $L_2^* = L_2/L_1$ are used in the present analysis.

In the present theory the splay and bend elastic constants are equal, $K_{11} = K_{33}$ (deGennes and Proust, 1993; Beris and Edwards, 1994). Higher order theories are necessary to account for inequalities between K_{11} and K_{33}. To accomplish this six new terms must be added, rendering the computations nearly intractable. Since for discotic nematics the distinguished constant is K_{22}, the $K_{11} = K_{33}$ limitation is not as significant as for rod-like nematics. Figure (6.3) shows the parametric area in the K-K_{22} phase plane where the present theory (equation 6.3) is applicable for rod-like and discotic nematics. The present theory is applicable for ideal uniaxial discotic mesophases only in the following closed range:

$$1 \le \frac{K_{22}}{K} \le 4, \qquad -1.5 \le \frac{L_2}{L_1} \le 0. \tag{6.5}$$

Combining equations set (6.3), we find the following governing equations for the tensor order parameter **Q**:

$$\begin{aligned}\frac{d\mathbf{Q}}{dt} &= \mathbf{W}\cdot\mathbf{Q}-\mathbf{Q}\cdot\mathbf{W}+\tfrac{2}{3}\beta\mathbf{A}+\beta\left[\mathbf{A}\cdot\mathbf{Q}+\mathbf{Q}\cdot\mathbf{A}-\tfrac{2}{3}(\mathbf{A}:\mathbf{Q})\mathbf{I}\right]\\ &\quad-\tfrac{1}{2}\beta\left[(\mathbf{A}:\mathbf{Q})\mathbf{Q}+\mathbf{A}\cdot\mathbf{Q}\cdot\mathbf{Q}+\mathbf{Q}\cdot\mathbf{A}\cdot\mathbf{Q}+\mathbf{Q}\cdot\mathbf{Q}\cdot\mathbf{A}-\{(\mathbf{Q}\cdot\mathbf{Q}):\mathbf{A}\}\mathbf{I}\right]\\ &\quad-\frac{6D_r}{(1-\frac{3}{2}\mathbf{Q}:\mathbf{Q})^2}\left[(1-\tfrac{1}{3}U)\mathbf{Q}-U\mathbf{Q}\cdot\mathbf{Q}+U\{(\mathbf{Q}:\mathbf{Q})\mathbf{Q}+\tfrac{1}{3}(\mathbf{Q}:\mathbf{Q})\mathbf{I}\}\right]\\ &\quad+\frac{6D_r}{(1-\frac{3}{2}\mathbf{Q}:\mathbf{Q})^2}\left[\frac{L_1}{ckT}\nabla^2\mathbf{Q}+\frac{1}{2}\frac{L_2}{ckT}\left[\nabla(\nabla\cdot\mathbf{Q})+\{\nabla(\nabla\cdot\mathbf{Q})\}^T-\tfrac{2}{3}\mathrm{tr}\{\nabla(\nabla\cdot\mathbf{Q})\}\mathbf{I}\right]\right]\end{aligned} \tag{6.6}$$

The dimensionless form of the above equation is obtained by scaling as follows:

$$\begin{aligned}Er\frac{d\mathbf{Q}}{dt^*} &= Er\left[\mathbf{W}^*\cdot\mathbf{Q}-\mathbf{Q}\cdot\mathbf{W}^*+\frac{2}{3}\beta\mathbf{A}^*+\beta\left[\mathbf{A}^*\cdot\mathbf{Q}+\mathbf{Q}\cdot\mathbf{A}^*-\frac{2}{3}(\mathbf{A}^*:\mathbf{Q})\mathbf{I}\right]\right.\\ &\quad\left.-\frac{1}{2}\beta\left[(\mathbf{A}^*:\mathbf{Q})\mathbf{Q}+\mathbf{A}^*\cdot\mathbf{Q}\cdot\mathbf{Q}+\mathbf{Q}\cdot\mathbf{A}^*\cdot\mathbf{Q}+\mathbf{Q}\cdot\mathbf{Q}\cdot\mathbf{A}^*-\{(\mathbf{Q}\cdot\mathbf{Q}):\mathbf{A}^*\}\mathbf{I}\right]\right]\\ &\quad-R\frac{6}{(1-\frac{3}{2}\mathbf{Q}:\mathbf{Q})^2}\left[\left(1-\frac{1}{3}U\right)\mathbf{Q}-U\mathbf{Q}\cdot\mathbf{Q}+U\left\{(\mathbf{Q}:\mathbf{Q})\mathbf{Q}+\frac{1}{3}(\mathbf{Q}:\mathbf{Q})\mathbf{I}\right\}\right]\\ &\quad+\frac{1}{(1-\frac{3}{2}\mathbf{Q}:\mathbf{Q})^2}\left[\nabla^{*2}\mathbf{Q}+\frac{1}{2}L^*_2\left[\nabla^*(\nabla^*\cdot\mathbf{Q})+\{\nabla^*(\nabla^*\cdot\mathbf{Q})\}^T-\frac{2}{3}\mathrm{tr}\{\nabla^*(\nabla^*\cdot\mathbf{Q})\}\mathbf{I}\right]\right]\end{aligned} \tag{6.7}$$

$$t^*=\dot{\gamma}t,\quad \mathbf{A}^*=\frac{\mathbf{A}}{\dot{\gamma}},\quad \mathbf{W}^*=\frac{\mathbf{W}}{\dot{\gamma}},\quad \nabla^*=H\nabla,\quad L^*_2=\frac{L_2}{L_1}$$

The dimensionless quantities are represented by a superscript (*) in equation (6.7), and H is the characteristic distance between the two plates (see Figure 6.3). As there are three competing contributions controlling the microstructural response of discotic nematics, therefore we have two dimensionless numbers or scaling parameters:

$$Er=\frac{\dot{\gamma}H^2c\kappa T}{L_1 6D_r}=\frac{VHc\kappa T}{L_1 6D_r}=\frac{VH\mu_e}{L_1},\qquad \mu_e=\frac{c\kappa T}{6D_r} \tag{6.8a, b}$$

$$R=\frac{D_r H^2\mu_e}{L_1}=\frac{H^2}{6}\frac{c\kappa T}{L_1} \tag{6.9}$$

The Ericksen number Er is the ratio of the viscous flow effects to long-range order elasticity, whereas ratio R, introduced previously by Tsuji and Rey (1997), is the ratio of the short-range order elasticity to long-range order elasticity. As reported (Tsuji and Rey, 1997, 1998; Rey and Tsuji, 1998) the above-presented theory, equation (6.3), fills the gap between classical theories of liquid crystals, Leslie–Ericksen (L-E) theory (Leslie, 1968, 1979), and Doi's theory (Doi, 1981; Doi and Edwards, 1986). In summary, the above generalized theory is completely compatible with the L-E theory in the limit $R \to \infty$, on the other hand it is compatible with Doi's theory in the limit $Er \to \infty$, and transversely isotropic fluid (TIF) theory in the limit $R \to \infty$ and $Er \to \infty$ and (Tsuji and Rey, 1997, 1998; Rey and Tsuji, 1998). It is noted that the L-E theory has no restriction on the values of elastic constants, however, as mentioned above the present theory is restricted to $K_{11} = K_{33}$.

6.2.2 Definition of Coordinate System and Flow Field

The model discotic mesophases are subjected to the rectilinear simple shear flow, shown in Figure (6.3a). The lower plate (at $y = 0$) is stationary and the top plate ($y = H$), at distance H from the bottom plate, moves in the $+x$-direction with a known constant velocity V. The velocity gradient is along the y-axis, and vorticity along the z-axis. In this study we restrict our analysis to planar orientation such that two of the three eigenvectors of $\mathbf{Q}$ lie in the shear plane, and as a consequence the only non-zero components of tensor order parameter are Q_{xx}, Q_{xy}, Q_{yy}, Q_{zz}. The components along the vorticity direction, Q_{zx} and Q_{zy}, are set to zero. We note that eliminating components Q_{zx} and Q_{zy} does not restrict the uniaxial director $\mathbf{n}$ to the shear plane. The director $\mathbf{n}$ is still able to escape the shear plane and align along the vorticity direction even if $Q_{zx} = Q_{zy} = 0$. Expressing the components in terms of eigenvectors and eigenvalues, it is found:

$$Q_{zx} = \lambda_{\mathbf{n}} n_z n_x + \lambda_{\mathbf{m}} m_z m_x + \lambda_{\mathbf{l}} l_z l_x \tag{6.10}$$

$$Q_{zy} = \lambda_{\mathbf{n}} n_z n_y + \lambda_{\mathbf{m}} m_z m_y + \lambda_{\mathbf{l}} l_z l_y \tag{6.11}$$

and, it follows that the sufficient condition for both components Q_{zx} and Q_{zy} to be equal to

zero is $\mathbf{a} = (0, 0, 1)$, where **a** = **n**, **m**, **l**. In this work we have never observed a director escape from the shear plane. The planar director dynamics are given in terms of one azimuthal angle θ, measured in degrees, which **n** makes with the x-axis as shown in Figure (6.3b).

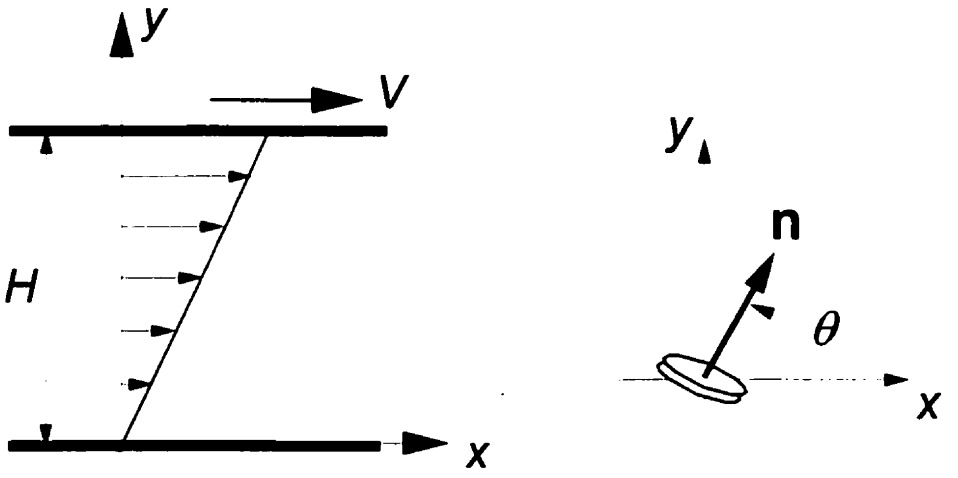

(a) (b)

Figure 6.3: (a) Definition of rectilinear simple shear flow. The discotic mesophase sample is placed between two infinitely long plates. The lower plate ($y = 0$) is stationary and the top plate ($y = H$) moves in the +x-direction with a known constant velocity V. The velocity gradient $\nabla \mathbf{v}$ is along the y-axis. (b) Definition of orientation angle θ that the primary eigenvector (uniaxial director) **n** of tensor order parameter **Q** makes with the x-axis.

6.2.3 Initial and Boundary Conditions

One of the objectives of this paper is to analyze the distinct microstructure features of sheared discotics pertaining to different boundary constraints. Two fixed anchoring modes are possible under the planar molecular orientation assumption:

BCVG: The director **n** is fixed along the velocity gradient direction (y-axis), such that:

$$\mathbf{n}_{S,BCVG} = (n_x, n_y, n_z) = (0,1,0) \tag{6.12}$$

BCF: The principal eigenvector $\mathbf{n}$ is fixed along the flow direction (x-axis), such that:

$$\mathbf{n}_{S,BCF} = (n_x, n_y, n_z) = (1, 0, 0) \tag{6.13}$$

Furthermore at the surface, it is assumed that the discotics are uniaxial ($P = 0$) and at equilibrium ($S = S_{eq}$). The equilibrium alignment depends on the surface nematic potential as:

$$S_{eq} = \frac{1}{4} + \frac{3}{4}\sqrt{1 - \frac{8}{3U}} \tag{6.14}$$

The resulting microstructure tensor order $\mathbf{Q}$ at the boundaries is given as:

$$\mathbf{Q}(y^* = 0) = \mathbf{Q}(y^* = 1) = S_{eq}\left(\mathbf{n}_S\mathbf{n}_S - \frac{\mathbf{I}}{3}\right) \tag{6.15}$$

The initial state is assumed to be uniaxial and at equilibrium ($P = 0$, $S = S_{eq}$). Initially (at time $t^* \leq 0$), the orientation of discotic nematic phase $\mathbf{n}_I(t^* = 0, 0 < y^* < 1)$ between the two plates is assumed to be parallel to the corresponding orientation $\mathbf{n}_S$. Small thermal fluctuations are imposed on the initial orientation by introducing infinitesimally small Gaussian noise in $\mathbf{n}_I$. Thus the initial condition in terms of $\mathbf{Q}$ is given as:

$$\mathbf{Q}(t^* = 0,\ 0 < y^* < 1) = S_{eq}\left(\mathbf{n}_I\mathbf{n}_I - \frac{\mathbf{I}}{3}\right) \tag{6.16}$$

Hence for BCVG:

$$\mathbf{n}_I = (n_x, n_y, n_z) = [\sin(\varepsilon\zeta), \cos(\varepsilon\zeta), 0], \text{ and} \tag{6.17}$$

for BCF:

$$\mathbf{n}_I = (n_x, n_y, n_z) = [\cos(\varepsilon\zeta), \sin(\varepsilon\zeta), 0] \tag{6.18}$$

where $\varepsilon = \frac{\pi}{180}10^{-3}$ radians, and ζ is Gaussian noise. We have found that the solutions are independent of ζ.

The model equation set (6.7) is solved numerically by using the finite element method for spatial discretization. The resulting set of non-linear time dependent ordinary differential, obtained after spatial discretization, is solved using the Newton-Raphson iteration scheme. The convergence is assumed to occur when the length of the difference between two successive solutions vectors is less than 10^{-6}. A finite difference method is used to discretize time, and a first order implicit Euler predictor-corrector method is used for time integration. To minimize computing time without losing accuracy, an adaptive time step control scheme is implemented. Standard methods are employed for mesh refinement, convergence, solution stability and consistency. The computations are performed for both boundary conditions and the set of parameters listed in Table 6.1.

Table 6.1

Simulation parameters used for model equation set (6.7)

Er	R	β	U	L_2^*
$1 \le Er \le 10^5$	$1 \le R \le 10^5$	-0.9	6	$-\frac{4}{3}$ $(K_{22} = 3K)$
				$-\frac{1}{4}$ $(K_{22} = 8/7\,K)$

Er: Ericksen number; R: ratio of short range elasticity to long range elasticity; β: shape factor; U: nematic potential; $L_2^* = L_2/L_2$, ratio of Landau coefficients; K_{22}: twist energy elastic constant; $K = K_{11} = K_{33}$ where K_{11}: splay energy elastic constant, K_{33}: bend energy elastic constant

6.3 Numerical Results and Discussion

An extensive numerical analysis of the governing equations (6.7), subjected to shear flow for both sets of boundary conditions, equations (6.12, 6.13), was performed. Firstly, the flow-induced microstructure modes are identified, analyzed and characterized. The effect of different anchoring conditions on the microstructure features are presented and characterized. Detailed microstructure phase diagrams in *R-Er* phase plane are also presented. Finally, the effect of the long-range curvature elastic anisotropy on shear-induced microstructure are discussed and characterized.

6.3.1 Shear-induced Microstructure Modes under Strong Anchoring Conditions

Four distinct stable in-plane (2D) microstructures, two steady and two periodic, modes were found to be stable in the (*Er*, *R*) phase plane. These four planar modes are: (1) long-range elasticity induced steady state (ESS), (2) bulk tumbling–boundary wagging state (TWS), (3) bulk wagging state (WS), and (4) viscous flow induced steady state (VSS). Similar modes have also been reported for planar shear flow of rod-like nematics (Tsuji and Rey, 1997). The nomenclature used in this paper is adopted from that given by Tsuji and Rey (1997, 1998). In this sub-section we present, characterize and discuss the four distinct shear induced microstructure modes for the two considered boundary conditions.

6.3.1.1 Long-Range Elasticity induced Steady State (ESS)

This steady state prevails at sufficiently low *Er* values and for all arbitrary values of *R*, and arises due to the dominance of long-range elasticity on the vorticity effects of imposed shear flow. Figure (6.4) shows the (a) in-plane director angle θ, (b) uniaxial alignment *S*, and (c) biaxial alignment *P* profiles for *Er* = 50, *R* = 1000 (solid line); *Er* = 50, *R* = 10 (dash line); and *Er* = 100, *R* = 1000 (dot-dash line). The spatial profiles are for BCVG, and *U* = 6, β = -0.9, and L_2^* = -4/3. In ESS, the orientation profiles are parabolic. The director angle at the centerline $\theta|_{y^*=0.5}$ decreases with increasing *Er*,

however, remains unaffected by changes in R. At a constant and low Er (Er = 50), the S profiles are also parabolic, but the value at the centerline $S|_{y^*=0.5}$ decreases with decreasing R. At low Er, two competing effects come into play: long-range order, which tries to impose the anchoring orientation and alignment on the bulk, and short-range order that keeps the equilibrium alignment S_{eq} everywhere in the system. At higher R, short-range order dominates and the bulk alignment is close to the equilibrium value ($S \approx S_{eq}$), however, as R decreases it is easier for the system to lower the alignment S in order to compensate for the higher long-range energy. As Er increases the flow torques gradually gain strength over long-range elasticity and thus are able to decrease $\theta|_{y^*=0.5}$ as shown in Figure (6.4). It is found that for R = 1000, $\theta|_{y^*=0.5}$ lies in the first quadrant till $Er < 70$, and the S profiles are parabolic. However, there exists a jump in the director angle profile near $Er \approx 70$ such that for $Er > 70$, $\theta|_{y^*=0.5}$ lies in the fourth quadrant which results in large gradients in both alignments (S, P). This well understood (Tsuji and Rey, 1997) apparent discontinuity is due to solution multiplicity, and is similar to that exhibited by L-E theory (Manneville, 1981). As shown in Figure (6.4) for Er = 100, R = 1000, $\theta|_{y^*=0.5} \approx$ -60 degrees, and the steady state uniaxial alignment $S > S_{eq}$ near the boundaries and in some portion of the central core. The nematic phase is nearly uniaxial ($P \approx 0$), however the spatial variations in P increase with decreasing R and increasing Er.

Figure (6.5) shows the (a) in-plane director angle θ angle, (b) uniaxial alignment S, and (c) biaxial alignment P profiles as a function of $y^* = y/H$ for BCF and U = 6, β = -0.9, and L_2^* = -4/3. The other parametric conditions are: R = 100, Er = 100 (solid line); R = 100, Er = 50 (dash dot line); R = 1000, Er = 50 (dash line). The orientation profiles are parabolic as for BCVG. However, orientation difference $\Delta\theta = \left|\theta|_{y^*=0.5} - \theta_S\right|$ in the orientation angle at the centerline $\theta|_{y^*=0.5}$ and at the surface θ_S is higher in BCF as compared to BCVG. The dominant long-range elasticity transmits the anchoring orientation in the bulk; the latter tends to rotate under the prevailing rotational torques. The net effect of the fixed boundary conditions to transmit the anchoring orientation into

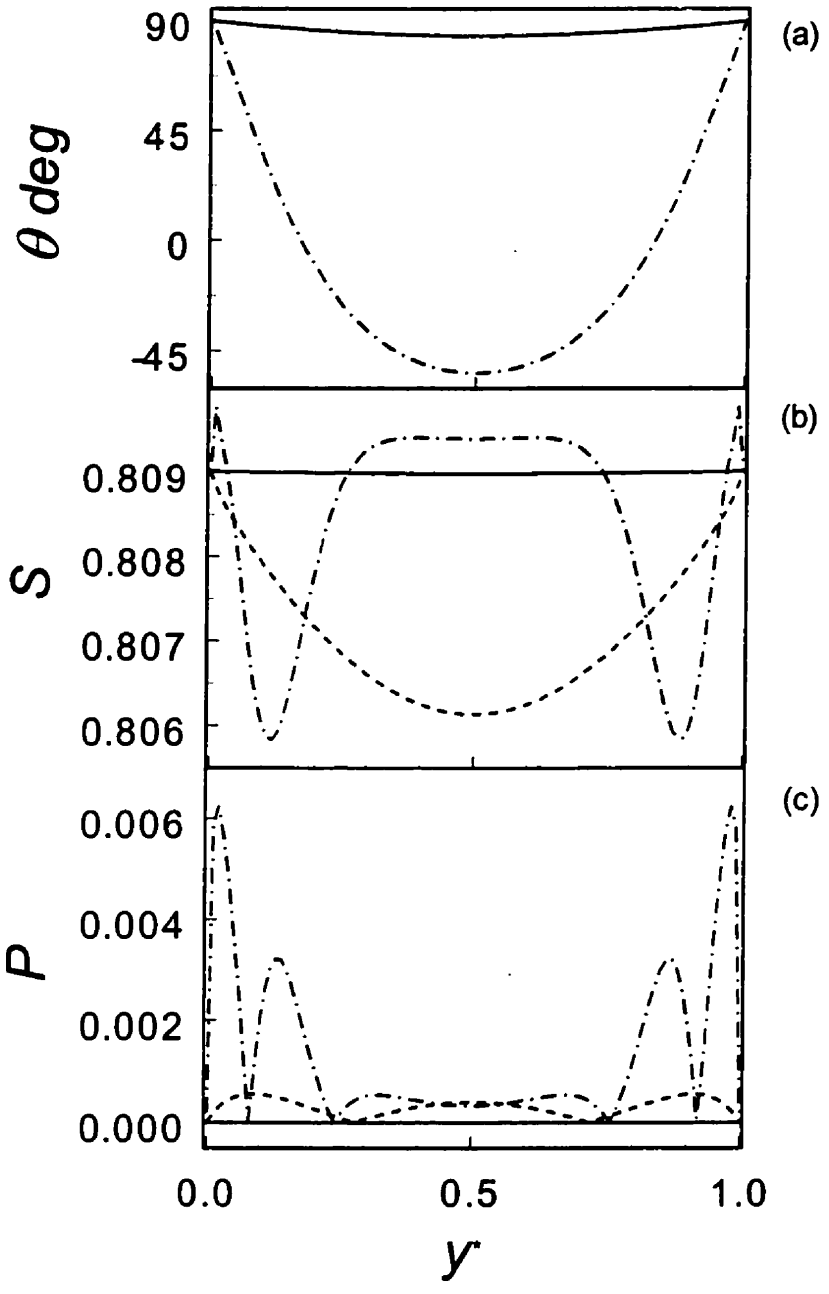

Figure 6.4: (a) In-plane director angle θ, (b) uniaxial alignment S, and (c) biaxial alignment P steady state spatial profiles for $U = 6$, $\beta = -0.9$, and $L_2^* = -4/3$. The parametric conditions are $Er = 50$, $R = 1000$ (solid line); $Er = 50$, $R = 10$ (dash line); and $Er = 100$, $R = 1000$ (dot-dash line). The shown profiles correspond to long-range elasticity induced steady state (ESS) for BCVG, $\mathbf{n}_{S,BCVG} = (0,1,0)$. The orientation profiles are parabolic. The director angle at the centerline $\theta|_{y^*=0.5}$ decreases with increasing Er, however, remains unaffected by changes in R. A decrease in ratio R, at constant Er, affects only alignments to compensate for higher long-range energy. The nematic phase is nearly uniaxial.

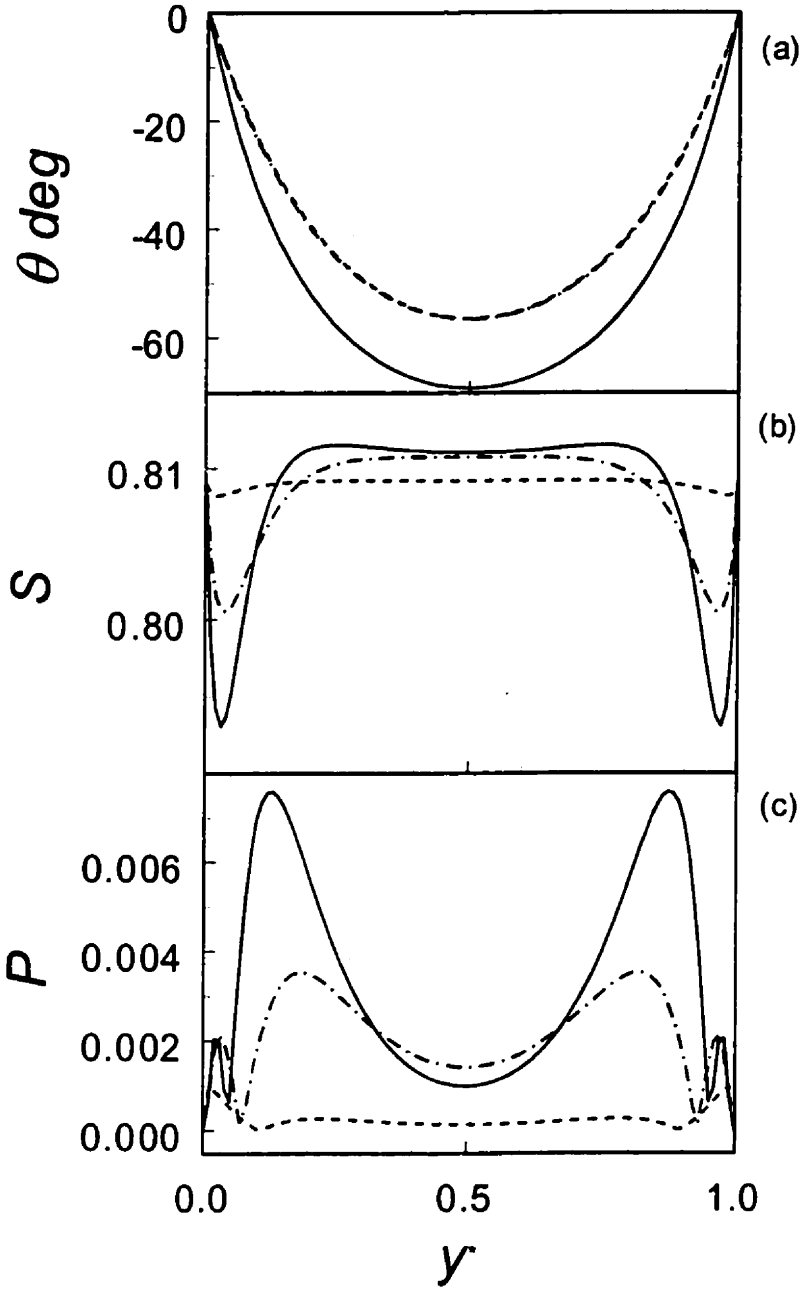

Figure 6.5: (a) In-plane director angle θ, (b) uniaxial alignment S, and (c) biaxial alignment P spatial profiles for BCF, $\mathbf{n}_{S,BCF} = (1,0,0)$, and for U = 6, β = -0.9, and $L_2^* = -4/3$. The parametric conditions are R = 100, Er = 100 (solid line); R = 100, Er = 50 (dash dot line); R = 1000, Er = 50 (dash line). The shown data corresponds to long-range elasticity induced steady state (ESS) for BCF. The orientation extends a larger angle in the bulk as compared to that in BCVG, $\mathbf{n}_{S,BCVG} = (0,1,0)$. The uniaxial profile is always marked a central core region where uniaxial S alignment is greater than *Seq*, and by two troughs near the plates where orientation gradients are large. The deviation in S increases with increasing Er and decreasing R. The nematic phase again is nearly uniaxial.

the bulk is stronger for BCVG as compared to BCF, as $(\Delta\theta)_{BCF} > (\Delta\theta)_{BCVG}$ under the same conditions. The uniaxial alignment S profiles, in the ESS mode for BCF, are characterized by two troughs near the two plates where orientation gradients are large, and by a bulk region at the center where $S > S_{eq}$. The alignment S is higher (lower) when the director is close to the velocity gradient (flow) direction. As R increases, at constant Er, the orientation profile remains unaltered but the alignments (S, P) tend to their equilibrium values since as $R \rightarrow \infty$, $S = S_{eq}$ and $P = 0$. The nematic is mostly uniaxial, however, the extent of flow-induced biaxiality under the same parametric conditions is higher for BCF than for BCVG. It is also noted from Figure (6.5) that in ESS, R does not have appreciable influence on orientation profiles, however, Er affects both orientation and alignment profiles.

The main characteristics of ESS for both BCs are: (a) the microstructure field is steady state, (b) ESS prevails at low Er and arbitrary R, and arises due to long-range elasticity which frustrates the shear flow vorticity torques, (c) the orientation profiles are parabolic, (d) the transients leading to ESS are overdamped and non-oscillatory.

The main differences in the ESS regime due to the two boundary conditions are: (a) for BCF the uniaxial alignment S profiles are always characterized by a central core region where $S > S_{eq}$ and by two troughs near the boundaries in which $S < Seq$, (b) the orientation gradients are always higher in BCF than in BCVG, (c) the ESS state prevails till higher values of Er in BCF than in BCVG.

6.3.1.2 Bulk Tumbling – Boundary Wagging State (TWS)

This stable periodic in-plane microstructure mode is stable at appropriate values of Er and R. This periodic microstructure mode arises as the long-range and short-range order elastic effects are unable to contain the strong rotational flow toques. Figure (6) shows the spatio-temporal profiles of: (a) the in-plane director angle θ, (b) the uniaxial alignment S, and (c) the biaxial alignment P, in 3-D box plots, for BCVG with: $R = 100$, $Er = 2000$, $U = 6$, $\beta = -0.9$, and $L_2^* = -4/3$. The director orientation is periodic and is characterized by the presence of three layers: one central bulk region where the director

continuously rotates clockwise, and two boundary regions where the director oscillates. The uniaxial S and biaxial P alignments also exhibit space dependent and periodic behavior, which is marked by coinciding sharp changes appearing near the bounding surfaces. The complex phenomena presented in Figure (6) can conveniently be expressed by scientific visualization of the tensor order parameter profiles, presented in Figure (7). The directions of the main orthogonal axes of the ellipsoid correspond to the directions of the eigenvectors (**n**, **m**), and the lengths of the semi-axes of the ellipsoid are proportional to the corresponding eigenvalues (λ_n, λ_m). The less aligned state is represented by an ellipsoid with a smaller (larger) major (minor) semi-axis. Figure (7) shows that the ellipsoids rotate with increasing time in the bulk region, and oscillate near the velocity gradient direction in two boundary layers. The average bulk orientation is along the velocity gradient direction as the time dependent orientation spends most of the time along the y-axis. There is a lowering in the alignment, represented in Figure (7) by nearly circular ellipsoids, when the orientation is away from the velocity gradient direction. The smooth and continuos transition between the director rotation in the bulk and the director oscillations in boundary regions is achieved by emergence of abnormal nematics, where the two eigenvalues are equal, $\lambda_n = \lambda_m > \lambda_l$, at which ellipsoid becomes a circle. This periodic emergence of the abnormal nematic state allows for the director resetting mechanism (Tsuji and Rey, 1997) that makes it possible to have continuous rotating bulk orientation in the presence of fixed surface anchoring conditions. The abnormal nematics emerge in pairs, one near each plate, at a distance δ from each plate that marks the boundary between the tumbling bulk and the two oscillating boundary layers. For the parametric condition used in Figures (6.6, 6.7) the boundary layer thickness $\delta \approx 0.09$, and the abnormal nematic states appear periodically with a space independent dimensionless time period $T_p \approx 16$. These results are consistent with those for rod-like nematics (Tsuji and Rey, 1997).

Figure (6.8) shows the time evolution of the (a) in-plane director angle θ, (b) uniaxial alignment S, and (c) biaxial alignment P, at $y^* = 0.5$ (solid line), $y^* = 0.08$ (dash line), and $y^* = 0.04$ (dot dash line), for the same parameters as for Figure (6.6).

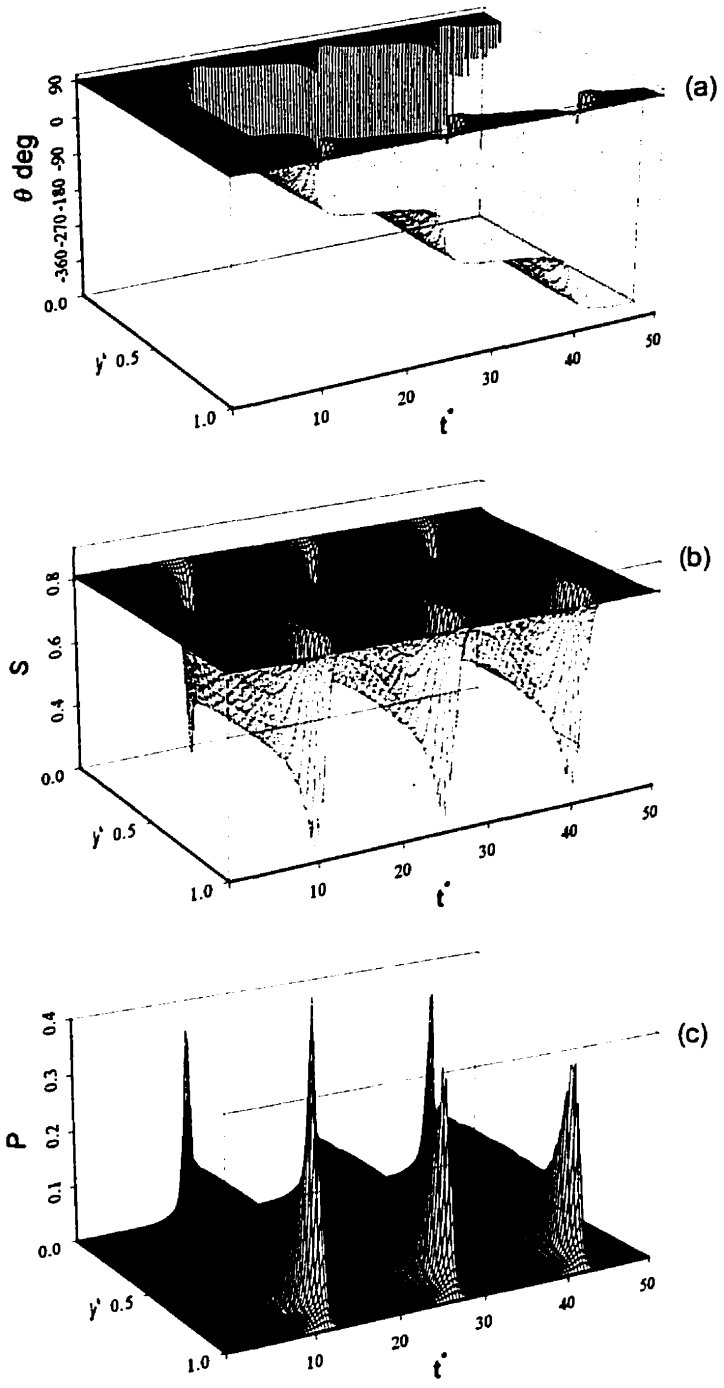

Figure 6.6: The temporal-spatial profiles of (a) orientation angle θ, (b) uniaxial alignment S, and (c) biaxial alignment P for BCVG, $\mathbf{n}_{S,BCVG} = (0, 1, 0)$, at $R = 100$, $Er = 2000$. The stable microstructural features are inhomogeneous and periodic, and typical of bulk tumbling-boundary wagging state (TWS). The director orientation is periodic and is marked by three layers: one central bulk region where the director rotates clockwise continuously, and two boundary regions where the director oscillates. The spatial-temporal response of alignments is marked by coinciding sharp changes that appear near the binding surfaces.

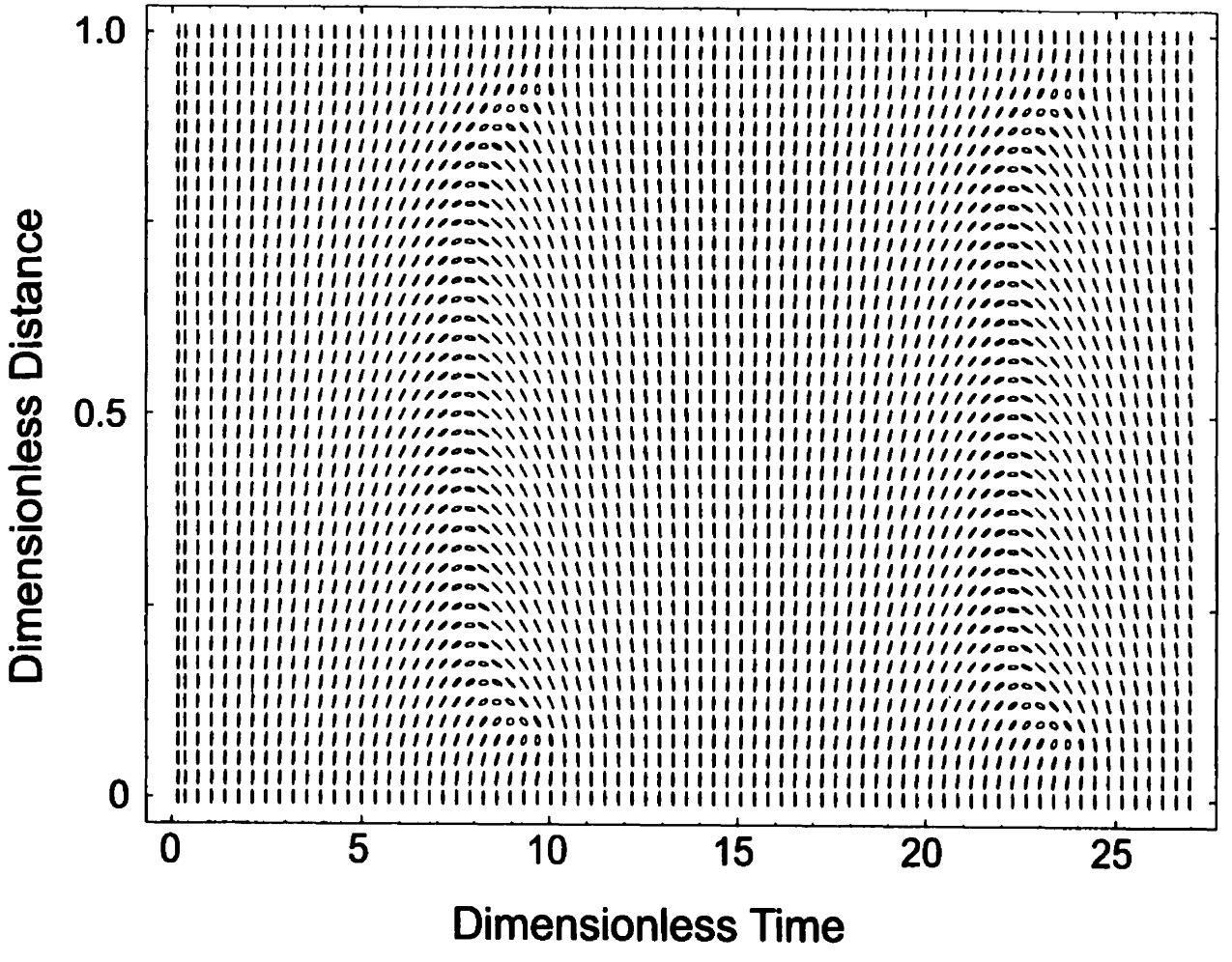

Figure 6.7: Scientific visualization of the spatial-temporal profiles of the tensor order parameter **Q** for BCVG, $\mathbf{n}_{S,BCVG} = (0,1,0)$, and for R = 1000, Er = 2000, U = 6, β = -0.9, and L_2/L_1 = -4/3. The bulk tumbling-boundary wagging state (TWS) is stable under these parametric conditions. The ellipsoids rotate clockwise in the central core, and oscillate with space dependent amplitude near velocity gradient directions in the two boundary layers. A pair of abnormal nematic states appears periodically at the boundary of tumbling core and oscillating boundary layers. The average molecular orientation is along the velocity gradient direction.

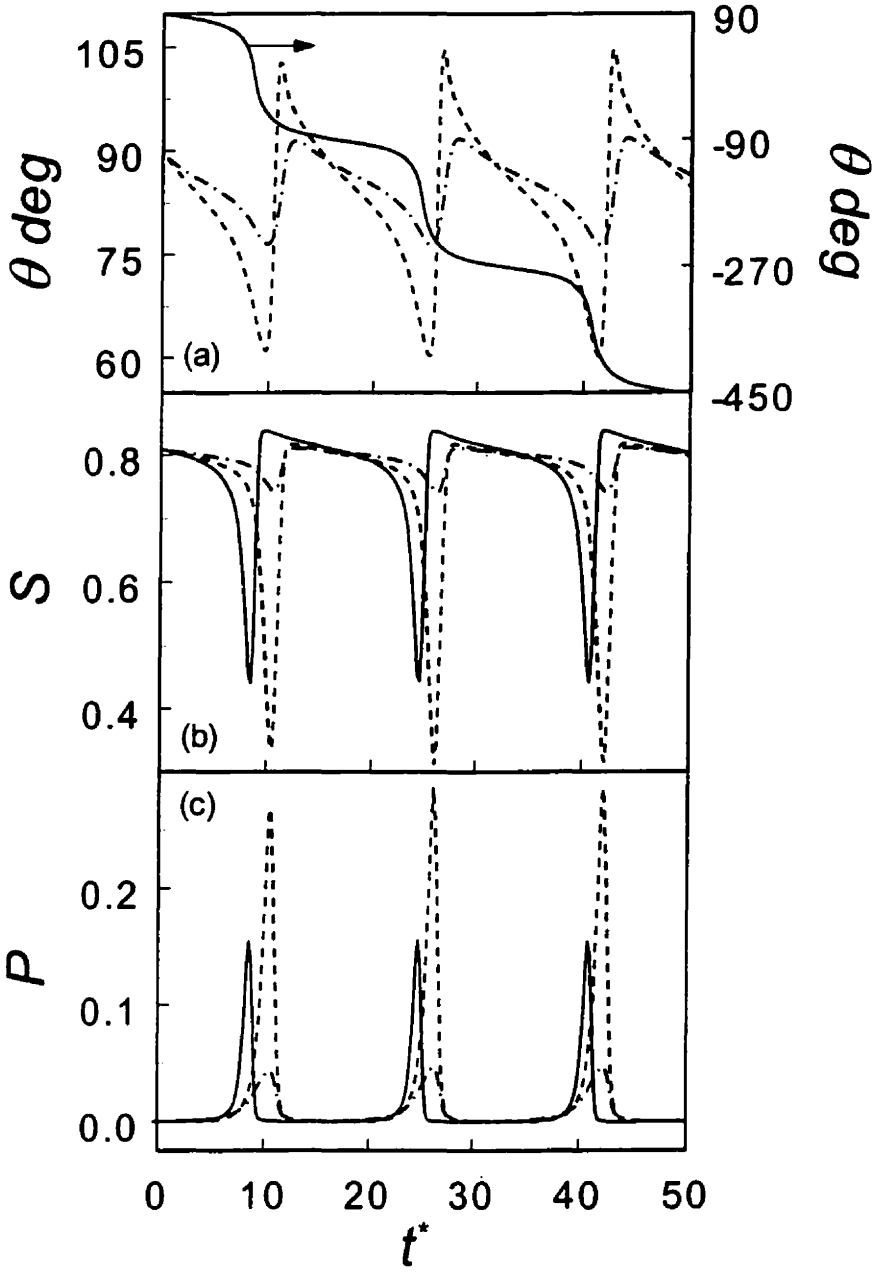

Figure 6.8: The time evolution of (a) orientation angle θ, (b) uniaxial alignment S, and (c) biaxial alignment P at $y^* = 0.5$ (solid line), $y^* = 0.08$ (dash line), and $y^* = 0.04$ (dot dash line) for the same parameters as for Figure (6.7). Clearly, the bulk near the centerline, $y^* = 0.5$, exhibits the classical tumbling step-like time evolution in which the director rotates clockwise in the shear plane by slowing down near the velocity gradient direction. In the oscillating boundary regions the orientation oscillates near the velocity gradient direction with space dependent amplitude that is maximum near the boundary between the tumbling-wagging layers, and decreases when approaching the either plate. There is a sharp change in the alignments when orientation is farthest away from the velocity gradient direction.

Clearly, the orientation at the centerline ($y^* = 0.5$) exhibits the classical tumbling step-like time evolution in which the director rotates clockwise in the shear plane and slows down near the velocity gradient direction (Singh and Rey, 1998a, 1998b). There is a sharp change in the alignments when the orientation is farthest away from the velocity gradient direction. The same phenomena are observed throughout in the tumbling bulk region ($\delta < y^* < 1-\delta$). In the two oscillating boundary layer regions ($0 < y^* < \delta$, $1-\delta < y^* < 1$), the orientation oscillates near the velocity gradient direction with a space dependent amplitude that is maximum near the boundary between the tumbling-wagging layers, and decreases when approaching the plate as shown in Figure (6.8). Also, as we move towards either boundary the alignment amplitude decreases. The oscillation amplitude is maximum near $y^* \approx \delta$ and $y^* \approx 1-\delta$. This tumbling-wagging transition phenomenon is the same as that observed in the homogeneous shear flow of discotics by increasing the shear rate. However, in TWS this transition (see Figures 6.6, 6.7, and 6.8) occurs at constant *Er*.

Figure (6.9) shows (a) the boundary layer thickness δ, and (b) dimensionless time period T_p as a function of *Er*, for BCVG, and at R = 25 (○), R = 50 (△), R = 100(▽), R = 500 (□), R = 1000 (◇). The boundary layer thickness δ increases with increasing *Er* and decreasing R. For a given R as *Er* increases the thickness δ increases until it approaches the centerline (y^* = 0.5). On the other hand for a given flow strength *Er*, δ decreases for increasing R and as $R \rightarrow \infty$, $\delta \rightarrow 0$, i.e. the entire bulk rotates, in accordance with Doi's theory (Doi, 1981; Doi and Edwards, 1986). Two pairs of abnormal nematic states emerge for every 2π rotation of the bulk. The dimensionless time period T_p decreases asymptotically with increasing *Er*, and the limiting value is independent of R. At the transition ESS → TWS transition the period T_p diverges. The results are consistent with those for rod-like nematics (Tsuji and Rey, 1997).

Figure (6.10) presents the scientific visualizations of computed tensor field profiles, $\mathbf{Q}(y^*, t^*)$ for BCF, *Er* = 2000, and R = 100. In this case the major semi-axis of the boundary ellipsoids are held fixed along the flow direction. As in BCVG, the periodic microstructure phenomena consist of three layers: bulk tumbling region, and two

oscillatory boundary layers. The director spends more time along the velocity gradient direction, as in BCVG, despite of fixed boundary anchoring along the flow direction. This is facilitated by the underlying microstructural phenomena in the boundary layer regions. Figure (6.11) shows the time evolution of the in-plane director angle θ at: $y^* = 0.025$ (solid line), $y^* = 0.05$ (dot dash line), $y^* = 0.1$ (dash line) $y^* = 0.2$ (long dash line), and $y^* = 0.5$ (dotted line), for BCF and for the same materials constants as of Figure (6.10). The director $\mathbf{n}$ rotates clockwise in the inner core, $y^* = 0.5$ (dotted line).

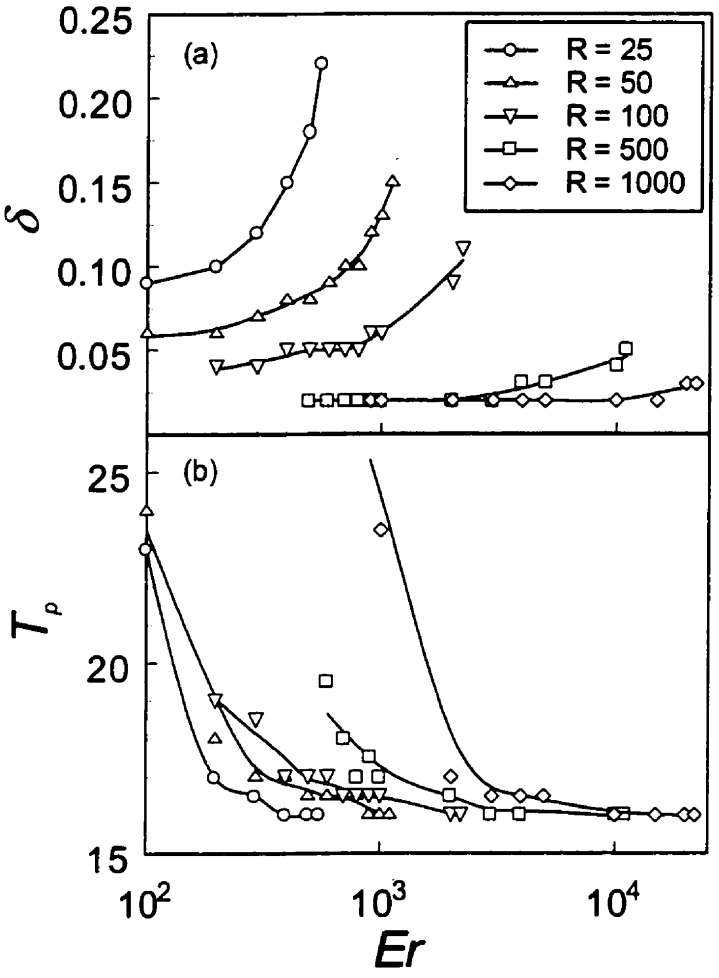

Figure 6.9: (a) Boundary layer thickness δ, and (b) dimensionless time period T_p as a function of Ericksen number Er for surface anchoring, $\mathbf{n}_{S,BCVG} = (0,1,0)$, for five different values of the ratio R. The boundary layer thickness δ increases with increasing Er and decreasing R; whereas, the dimensionless time period T_p decreases with increasing Er and R.

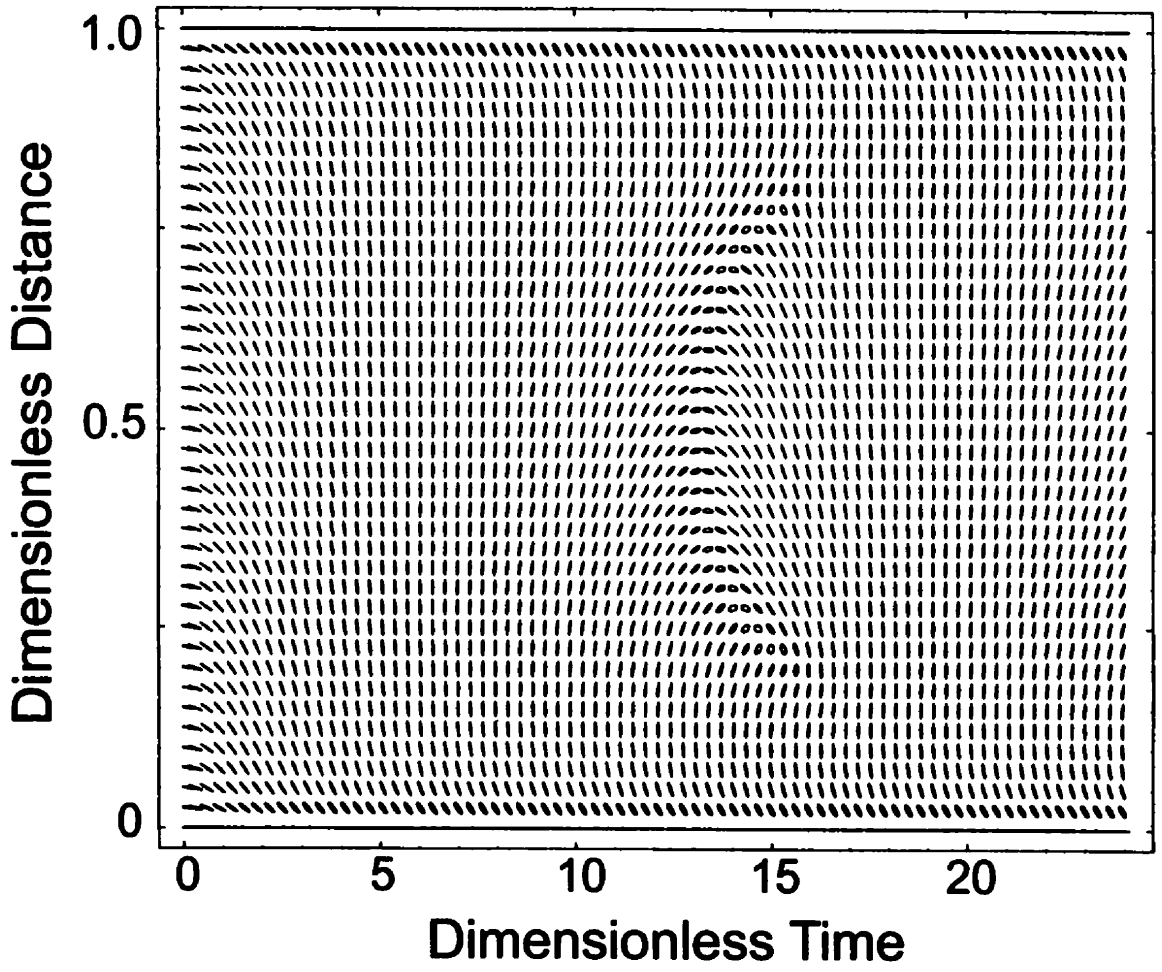

Figure 6.10: Scientific visualization of the spatial-temporal profiles of the tensor order parameter **Q** for BCF, $\mathbf{n}_{S,BCF} = (1,0,0)$, at R = 100, Er = 2000, U = 6, β = -0.9, and L_2^* = -4/3. The bulk tumbling-boundary wagging state (TWS) is stable under these conditions. In the central core the ellipsoids rotate clockwise, and spend most of the time along the velocity gradient direction as in BCVG, $\mathbf{n}_{S,BCVG} = (0,1,0)$. However, in the oscillating boundary layers the ellipsoids oscillate with space dependent amplitude along a space dependent direction, which is along the flow direction near the wall and along velocity gradient direction near the boundary between boundary layer and tumbling core.

In the outer oscillating boundary layers, the director oscillates with space dependent amplitude and around a space dependent direction as shown in Figure (6.11). Starting from the bottom plate the director oscillates around the flow direction, and as y^* increases the oscillation direction moves away from the flow direction towards the velocity gradient direction, finally as $y^* \to \delta$ the director oscillates very close to the velocity gradient direction and the microstructure dynamics are same as for BCVG. For example, at $y^* = 0.025$ the director oscillates around $\theta \approx -48\,\text{deg}$; at $y^* = 0.1$ along $\theta \approx -80\,\text{deg}$; and at $y^* = 0.2$ along $\theta \approx -98\,\text{deg}$. Figure (6.12) presents the boundary layer thickness δ as a function of the Ericksen number Er, for BCF for various values of the ratio R. The thickness δ for BCF is higher than that for BCVG for the same values of R. The tumbling core shrinks at the expense of the thicker boundary layer that is needed to allow for the director compatibility between the boundary anchoring (along flow direction) and the bulk director, that is mainly along velocity gradient direction.

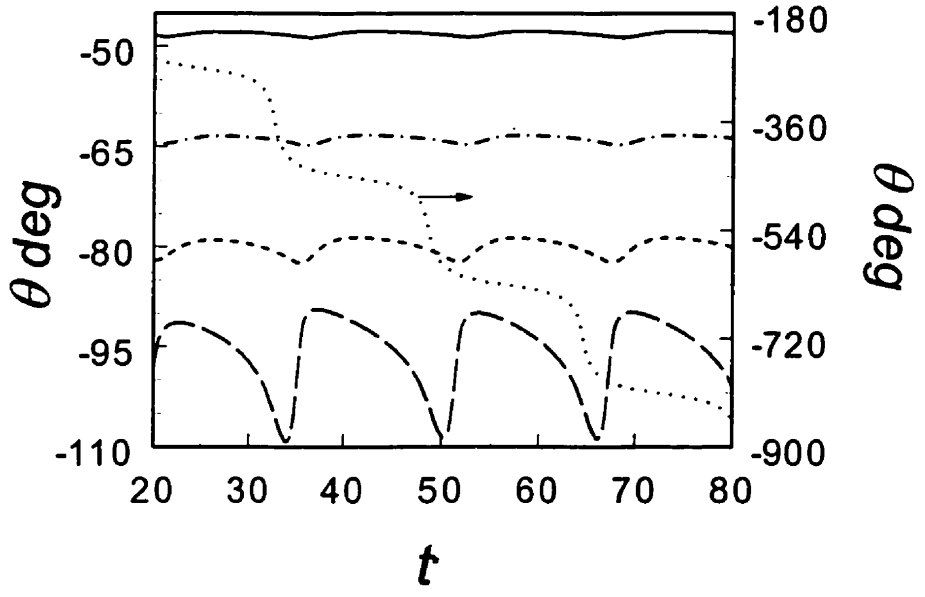

Figure 6.11: Time evolution of the in-plane director angle θ angle at $y^* = 0.025$ (solid line), $y^* = 0.05$ (dot dash line), $y^* = 0.1$ (dash line) $y^* = 0.2$ (long dash line), and $y^* = 0.5$ (dotted line) for BCF, $\mathbf{n}_{S,BCF} = (1, 0, 0)$, and with the parametric values of Figure (6.11). The director rotates clockwise in the inner core while spending most of the time along velocity gradient direction. In the outer oscillating boundary layers, the director oscillates with space dependent amplitude and around a space dependent direction. For details see text.

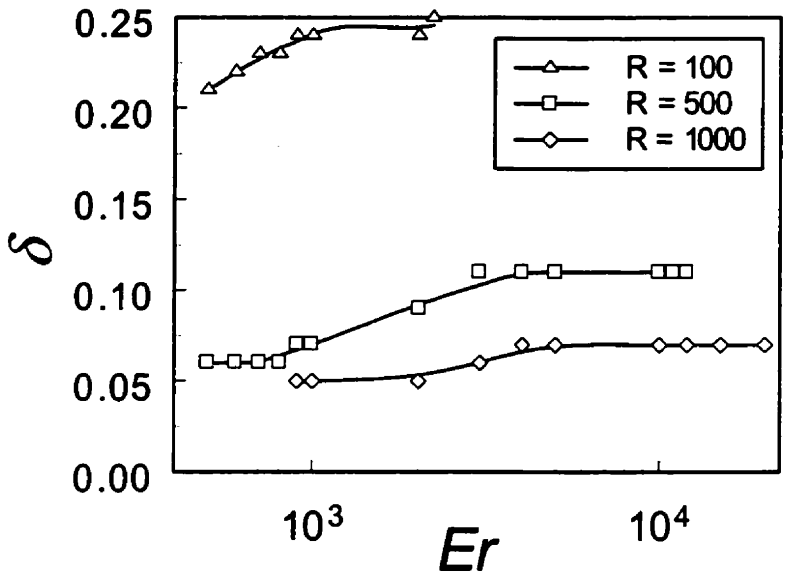

Figure 6.12: The boundary layer thickness δ as a function of Ericksen number Er, for BCF, $\mathbf{n}_{S,BCF} = (1, 0, 0)$, for various values of the ratio R. Please note that the thickness δ for BCF is higher than that for BCVG, $\mathbf{n}_{S,BCVG} = (0, 1, 0)$, for the same values of R.

The main characteristics of TWS for both BCs are: (a) the microstructure field is periodic, (b) TWS arises as the long-range and short-range order elastic effects are unable to contain the strong rotational toques due to the imposed shear flow, (c) the orientation dynamics are rotational in the core region and oscillatory in the two boundary layers, (d) a pair of abnormal nematic states appear periodically at the two boundaries between these three layer, (e) the abnormal states move towards the center-line with increasing Er and decreasing R, (f) the average orientation is along the velocity gradient direction.

The main microstructural differences between BCF and BCVG cases are: (a) the director oscillates around a space dependent direction in the oscillating boundary layers in BCF, (b) the boundary layer thickness δ is higher in BCF than that in BCVG, (c) the TWS mode is stable at higher values of R and Er in BCF than in BCVG.

6.3.1.3 Bulk Wagging State (WS)

As *Er* is further increased the tumbling core region of TWS is replaced by a new wagging periodic state called wagging state (WS) in which the orientation and alignments oscillate throughout the bulk. This stable periodic in-plane mode is stable at sufficiently high values of *Er* and *R*. The strong rotational torques of the shear flow still overpower the long-range elastic effects, but are increasingly challenged by the extensional torques of the shear flow. Figure (6.13) shows the computed scientific visualization of the spatial-temporal profiles of the tensor order parameter **Q** for BCVG, $R = 100$, $Er = 3000$, $U = 6$, $\beta = -0.9$, and $L_2^* = -4/3$. The ellipsoids oscillate with a space dependent amplitude that is a maximum at the centerline and zero at the boundaries. The director **n** oscillates near the velocity gradient direction, and the average bulk orientation is close to the velocity gradient direction. The alignments' (S, P) dynamics are also oscillatory with maximum amplitude at the centerline and zero at the either boundary. The uniaxial (biaxial) alignment reaches a minimum (maximum) when the orientation is farthest from the velocity gradient direction. The amplitude of oscillations decreases with increasing *Er* and decreasing *R*, and finally near WS → VSS transition the amplitude of oscillations is negligible. The oscillation amplitude is maximum at the TWS → WS transition.

Figure (6.14) shows the computed scientific visualization of the spatio-temporal profiles for BCF of the tensor order parameter **Q** for the same parameters as for Figure (6.13). The ellipsoids oscillate in the entire bulk with space dependent amplitude, which is the maximum at the center and zero at the boundaries, as in case of BCVG. The ellipsoids oscillate along a direction near the velocity gradient direction in the central core of the bulk, however in two boundary layers near the plates the direction of oscillation changes from being near the flow direction to that near the velocity gradient direction, as in the bulk.

A direct comparison of Figures (6.7) and (6.13) for BCVG, and Figures (6.10) and (6.14) for BCF reveals the main microstructural differences and similarities between TWS and WS. In TWS the bulk orientation angle θ rotates clockwise continuously and thus the difference between the orientation angle in the bulk and that in the boundary

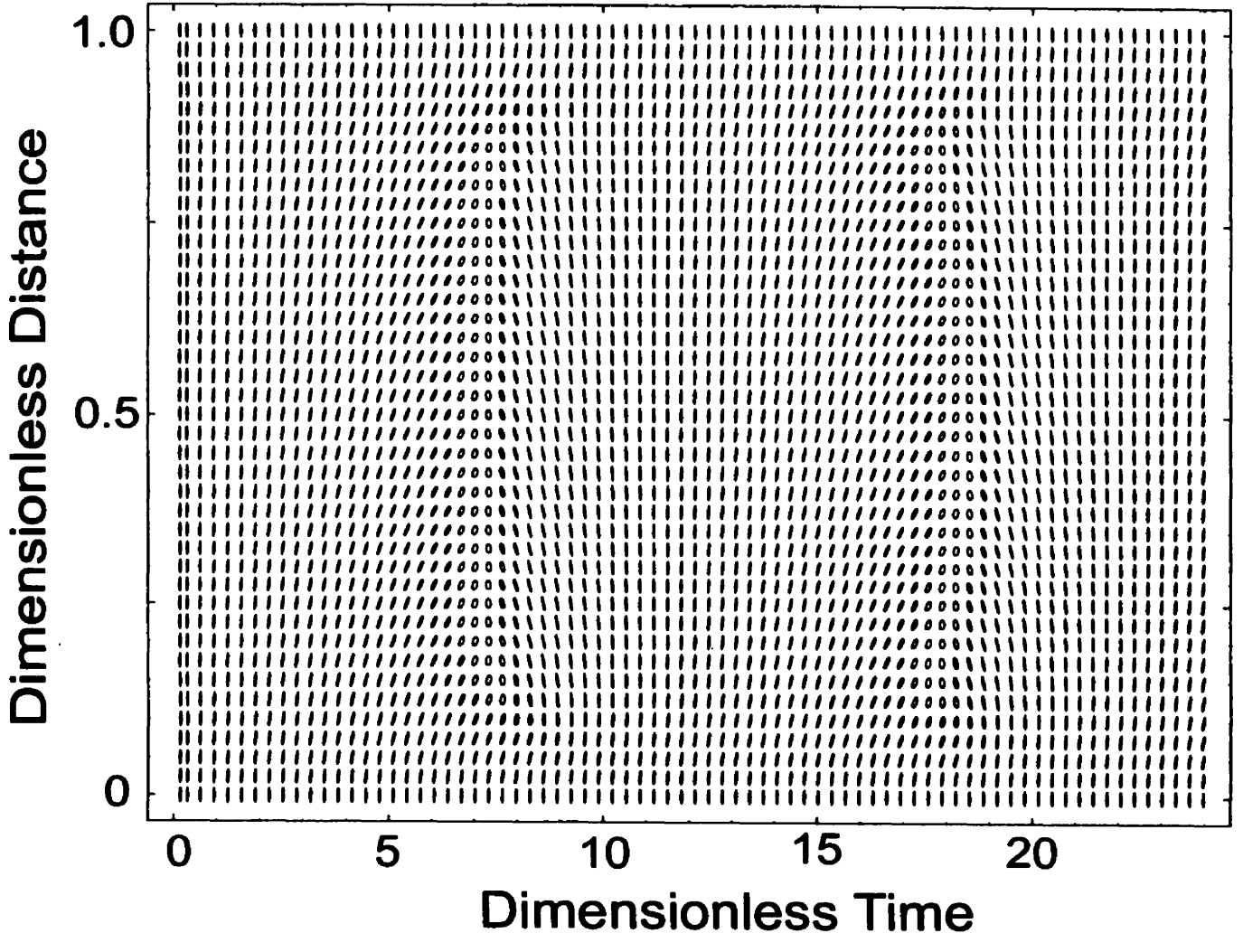

Figure 6.13: Scientific visualization of the spatial-temporal profiles of the tensor order parameter **Q** for BCVG, $\mathbf{n}_{S.BCVG} = (0,1,0)$, at R = 100, Er = 3000, U = 6, β = -0.9, and $L_2^* = -4/3$. The visualization is typical of the bulk wagging state (WS) under BCVG. The ellipsoids oscillate in the entire bulk with space dependent amplitude, which is the maximum at the center and zero at the either boundary, along a direction near velocity gradient direction.

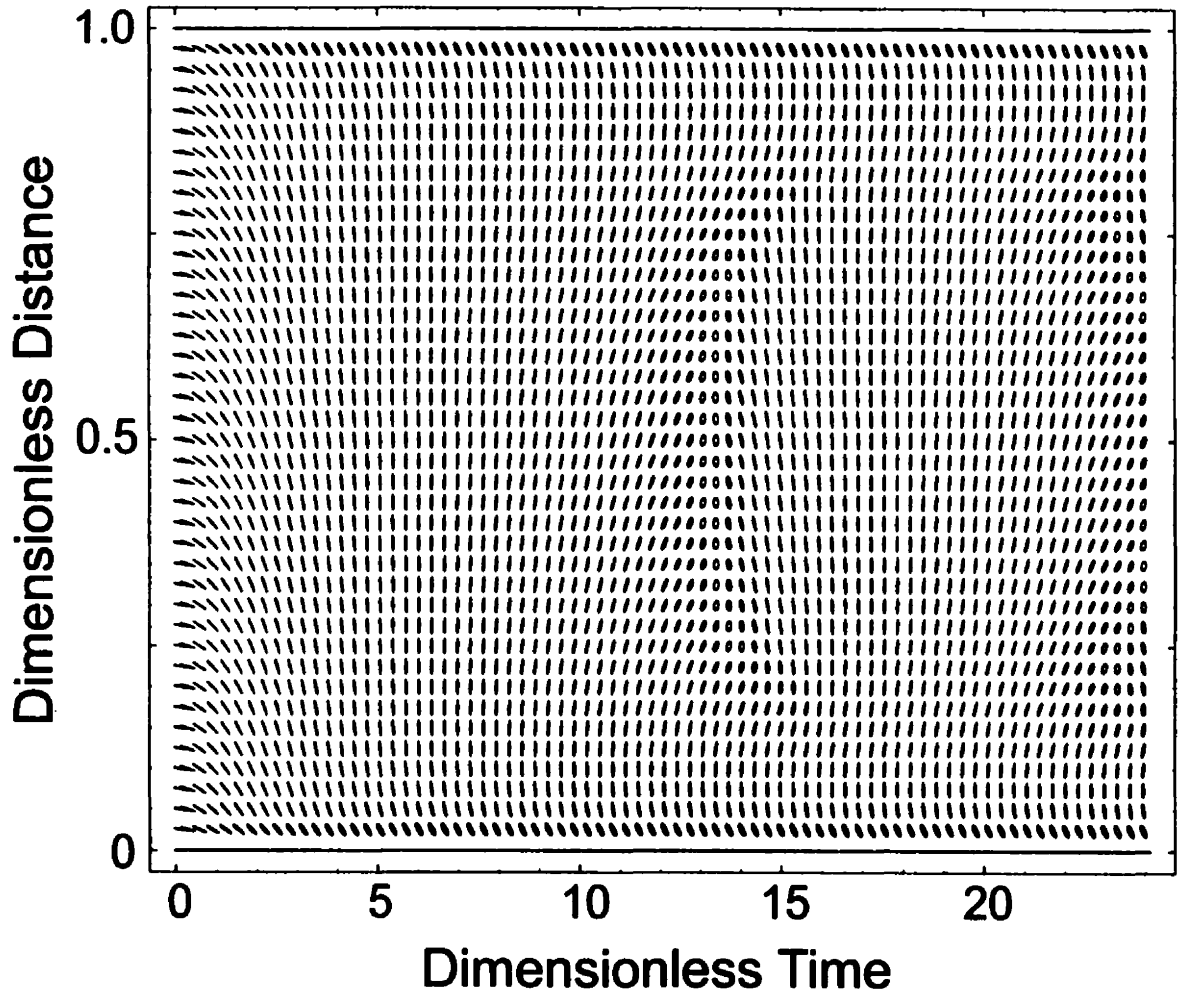

Figure 6.14: Scientific visualization of the spatial-temporal profiles of the tensor order parameter **Q** for BCF, $\mathbf{n}_{S,BCF} = (1, 0, 0)$, at R = 100, Er = 3000, U = 6, β = -0.9, and $L_2^* = -4/3$. The visualization is typical of the bulk wagging state (WS) under BCF. The ellipsoids oscillate in the entire bulk with space dependent amplitude, which is the maximum at the center and zero at the either boundary. The ellipsoids oscillate along a direction near the velocity gradient direction in major part of the bulk, however near the plates the direction of oscillation changes from being near the flow direction to the velocity gradient direction as in the bulk. The average bulk orientation is along the velocity gradient direction.

surfaces increases continuously with time, which gives rise to the emergence of a pair of abnormal nematics due to the director resetting mechanism. Whereas in the WS the orientation angle θ oscillates in the bulk within closed bounds ($0 \le \theta \le \pi$ or $\pi \le \theta \le 2\pi$) and thus the difference between the bulk orientation and the boundary surfaces is always finite and less than π. Also, no abnormal nematics appear in the WS regime.

The main characteristics of WS for both BCs are: (a) the microstructure field is periodic oscillatory and inhomogeneous, (b) the orientation and alignments oscillate thorough out the bulk with a space dependent amplitude that is maximum at the centerline and zero at the boundaries, (c) the period of oscillations decreases with increasing *Er* and decreasing *R*, (d) the average orientation in the bulk is around the velocity gradient direction.

The main microstructural difference in WS between BCF and BCVG cases is the presence, in the BCF case, of oscillating boundary layers in which the director oscillates around a space dependent direction that is along the flow direction near the plates and along the velocity gradient direction in the bulk.

6.3.1.4 Viscous Flow Induced Steady State (VSS)

This planar steady state is stable at large *Er* and appropriate *R*, and arises due to dominance of strong flow aligning torques over all other competing effects. Figure (6.15) shows the spatial profiles of the (a) in-plane director angle θ, (b) uniaxial alignment *S*, and (c) biaxial alignment *P*, under BCVG and for $U = 6$, $\beta = -0.9$, and $L_2^* = -4/3$. The shown curves are for $Er = 6000$, $R = 100$ (solid line); $Er = 10000$, $R = 100$ (dash line); and $Er = 10000$, $R = 10$ (dot-dash line). The orientation and alignment profiles exhibit typical boundary layer behavior, in which the aligned core, with a flat and homogeneous microstructure profile, is sandwiched between the two layers with sharp changes near the plates. Again the average orientation is near the velocity gradient direction. The orientation difference $\Delta\theta = \left|\langle\theta\rangle_{core} - \theta_S\right|$ in the average orientation angle in the flat core $\langle\theta\rangle_{core}$ and at surface θ_S decreases with increasing *Er* as stronger flow strength imposes orientation along the velocity gradient direction. The uniaxial alignment *S* in the bulk is

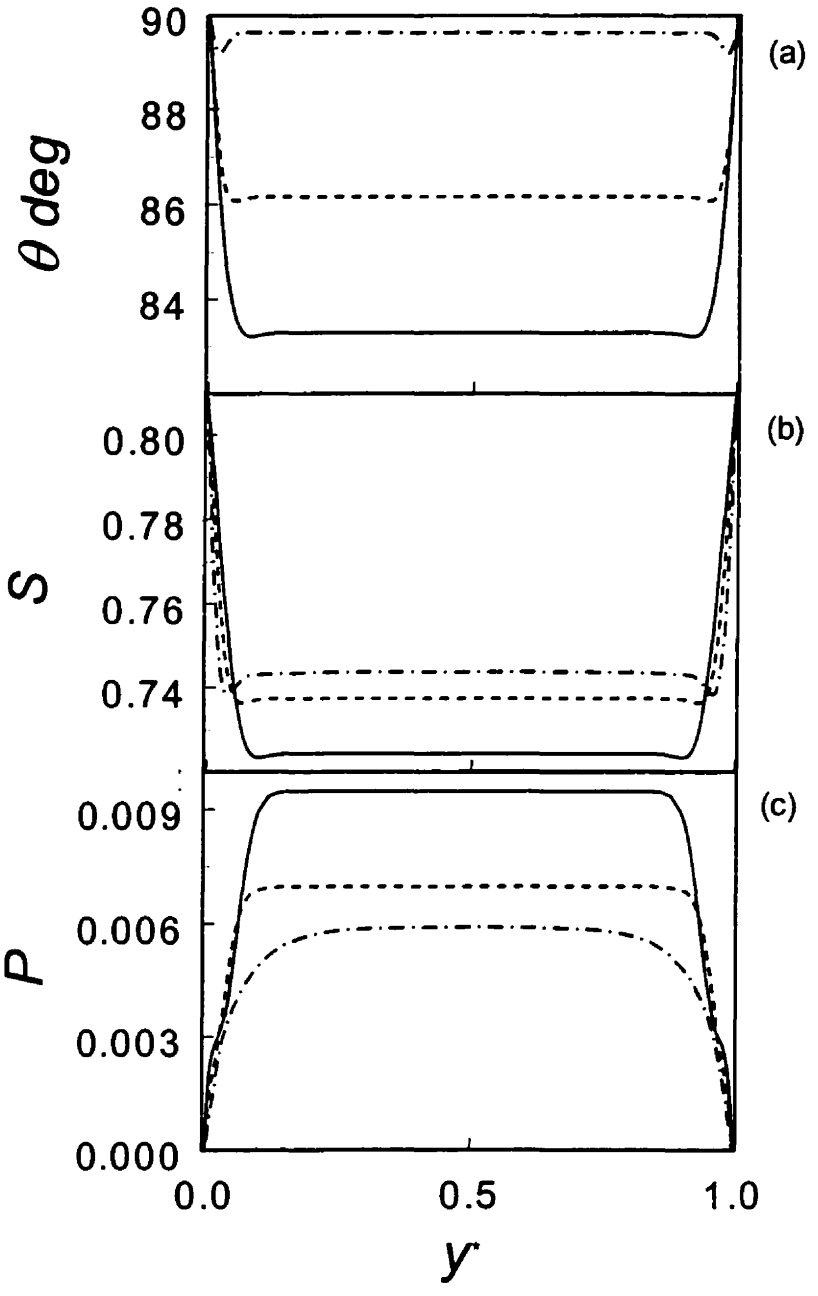

Figure 6.15: (a) In-plane director angle θ, (b) uniaxial alignment S, and (c) biaxial alignment P spatial profiles for BCVG, $\mathbf{n}_{S,BCVG} = (0,1,0)$, and for U = 6, β = -0.9, and $L_2^* = -4/3$. The parametric conditions are R = 100, Er = 6000 (solid line); R = 100, Er = 10000 (dash line); and R = 10, Er = 10000 (dot-dash line). The profiles are typical of viscous flow-induced steady state (VSS) under BCVG. The orientation θ and alignment (S, P) profiles are characterized by a flat profile within two boundary layers. The difference between surface orientation and the bulk-aligning angle decreases with increasing Er and decreasing R. The alignments show the similar dependence with Er and R. The sheared nematic phase is nearly uniaxial.

always less than S_{eq}. The nematic phase for BCVG is practically uniaxial, however the biaxial alignment P decreases with increasing Er and decreasing R. The thickness of the boundary layers also decreases with increasing Er and decreasing R.

Figure (6.16) shows the steady state spatial profiles of the in-plane director angle θ (solid line), the uniaxial alignment S (dash line), and the biaxial alignment P (dot-dash line), for $Er = 60000$, and $R = 100$. The shown profiles are typical of the VSS occurring under BCF. The orientation profile is characterized by two boundary layers with large orientation gradients leading to a flat orientation profile in the bulk. The average orientation is near the velocity gradient direction. Two local maximas and three local minimas characterize the alignment profiles. The alignment S (P) drops (jumps) sharply near the plates where large orientation gradients exist as director goes from the anchoring orientation, along the flow direction, to the central core bulk orientation along the velocity gradient direction. The nematic phase is highly biaxial near the plates; however, the central core remains mostly uniaxial ($P \approx 0$). The dependence of orientation angle in core on Er and R follows the same trends as in BCVG, discussed above.

The microstructural differences in ESS and VSS modes are attributed due to the nature of the stabilizing mechanisms that promotes the steady state. The main dynamical and steady state microstructural differences are: (a) the orientation profile in ESS is parabolic whereas that in VSS is characterized by a flat bulk and two boundary layers with sharp gradients; (b) the dynamics in ESS (VSS) mode are over-damped (under-damped); (c) the maximum bulk angle (at the centerline) in ESS (VSS) increases with increasing (decreasing) Er.

The main characteristics of VSS for both BCs are: (a) the microstructure field is non-homogeneous, steady state and arises due to the flow aligning torques at very high Er, (b) the orientation profiles are flat in the bulk with rapid gradients in the boundary layers, (c) the transients leading to VSS are under-damped and oscillatory, (d) the steady state orientation angle decreases with increasing Er and decreasing R, (e) the bulk orientation is near the velocity gradient direction.

The main differences in VSS mode for the two anchoring conditions are: (a) for BCVG the uniaxial alignment is always $S < S_{eq}$, whereas for BCF $S > S_{eq}$ near the boundary, (b) the nematic phase is highly biaxial near the plates in BCF whereas it is nearly uniaxial in BCVG, (c) the orientation gradients are always higher in BCF than in BCVG.

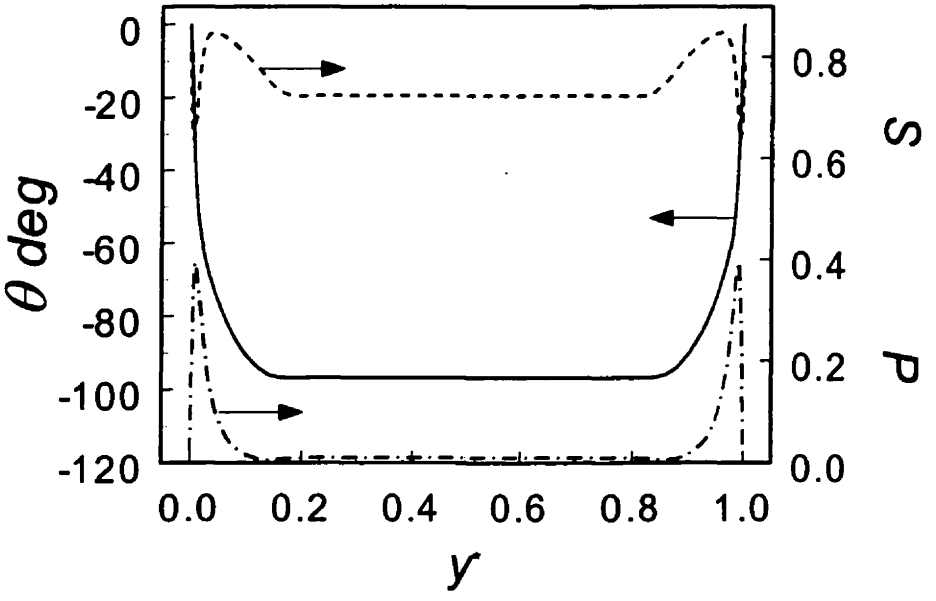

Figure 6.16: The steady state spatial profiles of the in-plane director angle θ (solid line), the uniaxial alignment S (dash line), and the biaxial alignment P (dot-dash line) for Er = 60000, R = 100. The shown profiles are typical of the viscous flow-induced steady state (VSS) occurring under BCF, $\mathbf{n}_{S,BCF} = (1, 0, 0)$. The bulk orientation profile is flat and nears the velocity gradient direction, as in BCVG, $\mathbf{n}_{S,BCVG} = (0, 1, 0)$. There are rapid gradients in the orientation field near the plates at which there are sharp changes in alignment fields. The uniaxial alignment reaches values greater than *Seq*, a peculiarity only observed in BCF. The nematic phase is highly biaxial near the boundary, however the bulk is mostly uniaxial ($P \approx 0$).

6.3.2 Microstructure Phase Diagram

In this section we present the microstructure phase diagram, in terms of *Er-R*, for both boundary conditions. The transition lines between the various microstructure regimes are not computed due to the unavailability of robust procedures to handle the coupled highly non-linear complex system of partial differential equations in hand. Nonetheless, the large number of computations performed at various values *Er* and *R*

provides the location of the transition boundaries accurately enough.

Figure (6.17) presents the microstructure phase diagram for (a) BCVG and (b) BCF for $U = 6$, $\beta = -0.9$, and $L_2^* = -4/3$. The figure shows parametric regions for the four stable planar microstructure modes: ESS (□), TWS (○), WS (△), and VSS (◇). The location of the boundaries between the various stable modes is apparent in the figure. The filled circle (●) represents the qua-critical point from which all the transition lines, marking the boundary between the various microstructure modes, emanate. In other words, all of the four flow regimes coexist at this point. The locations of the qua-critical points are:

$$\text{BCVG:} \quad (Er_{qc}, R_{qc}) \approx (70, 3) \tag{6.19a}$$

$$\text{BCF:} \quad (Er_{qc}, R_{qc}) \approx (450, 20) \tag{6.19b}$$

For $R > R_{qc}$ the system displays, for both BCs, all of the four flow regimes with increasing Er, whereas for $R < R_{qc}$ only steady state regimes, ESS and VSS, are encountered. Also for $Er > Er_{qc}$ the system displays all the four stable modes with various R. The ESS regime spreads to higher Er with increasing R, because for high R the short-range order elasticity dominates, the alignments remain close to their equilibrium values and remain unaffected by the rotational flow torques, thus relatively higher flow strength (higher Er) values are required to set up the rotational tumbling dynamics in the bulk of the system.

Moreover, at sufficiently low values of R, the sufficiently high values of Er induce a decrease in the uniaxial alignment S thereby giving rise to VSS. The VSS regime spreads to higher values of R with increasing Er, as higher flow strength is required to produce the alignment changes that produce VSS. The periodic modes TWS and WS appear only to the right and above of qua-critical point and prevail for parametric values $(Er, R) > (Er_{qc}, R_{qc})$. The parametric space where TWS and WS modes exist begins to pinch as qua-critical point is approached, and finally extinguishes at qua-critical point. Both Er and R are inversely proportional to long-range order curvature elasticity. Therefore as Er and R decrease the effect of log-range order begins to increase, thereby

dampening any periodic behavior. The various transition lines have positive slopes and the regions spread with increasing Er and R.

Comparison of Figures (6.17a) and (6.17b) reveals that for BCF the qua-critical point has shifted upwards and to the right in the phase space such that:

$$\left(Er_{qc}, R_{qc}\right)_{BCF} > \left(Er_{qc}, R_{qc}\right)_{BCVG} \tag{6.20a}$$

$$\frac{\left(Er_{qc}\right)_{BCF}}{\left(Er_{qc}\right)_{BCVG}} \approx \frac{\left(R_{qc}\right)_{BCF}}{\left(R_{qc}\right)_{BCVG}} \approx 6.5 \tag{6.20b}$$

The scaling given by equation (6.20b) states that the qua-critical point shifts along each parametric axis in the same ratio.

As is observed from Figure (6.17), the periodic regimes start from the qua-critical point. The TWS and WS modes appear when long-range elasticity is weak, and always appear in the absence of long-range order elasticity (Singh and Rey, 1998a, 1998b). The effect of long-range elasticity is to suppress the inherent periodic behavior of the nematic phase at lower and intermediate shear rates. Also, Er and R both scale inversely with long-range elasticity. Thus TWS and WS will appear at lower values of Er and R, provided the materials and thermodynamic parameters (U, β) are kept constant, if long-range elasticity is stronger and vice versa. Therefore shifting of the qua-critical point is a manifestation of the fact that the fixed anchoring conditions under BCF are less effective in transmitting the surface anchorings into the bulk. Moreover, the ESS regime under BCF extends till higher values of Er than in BCVG, which again is attributed to the weaker penetration effects of fixed boundary anchoring in case of BCF.

The main characteristics of the phase diagrams for both BCs are: (a) the phase plane presents the regions where various flow-induced modes are stable; (b) the transition lines between various regimes emanate from the qua-critical point; (c) all four regimes co-exist at the qua-critical point; (d) the system displays all the four modes for $R > R_{qc}$ and $Er > Er_{qc}$; and (e) all the regimes spread with increasing Er and R.

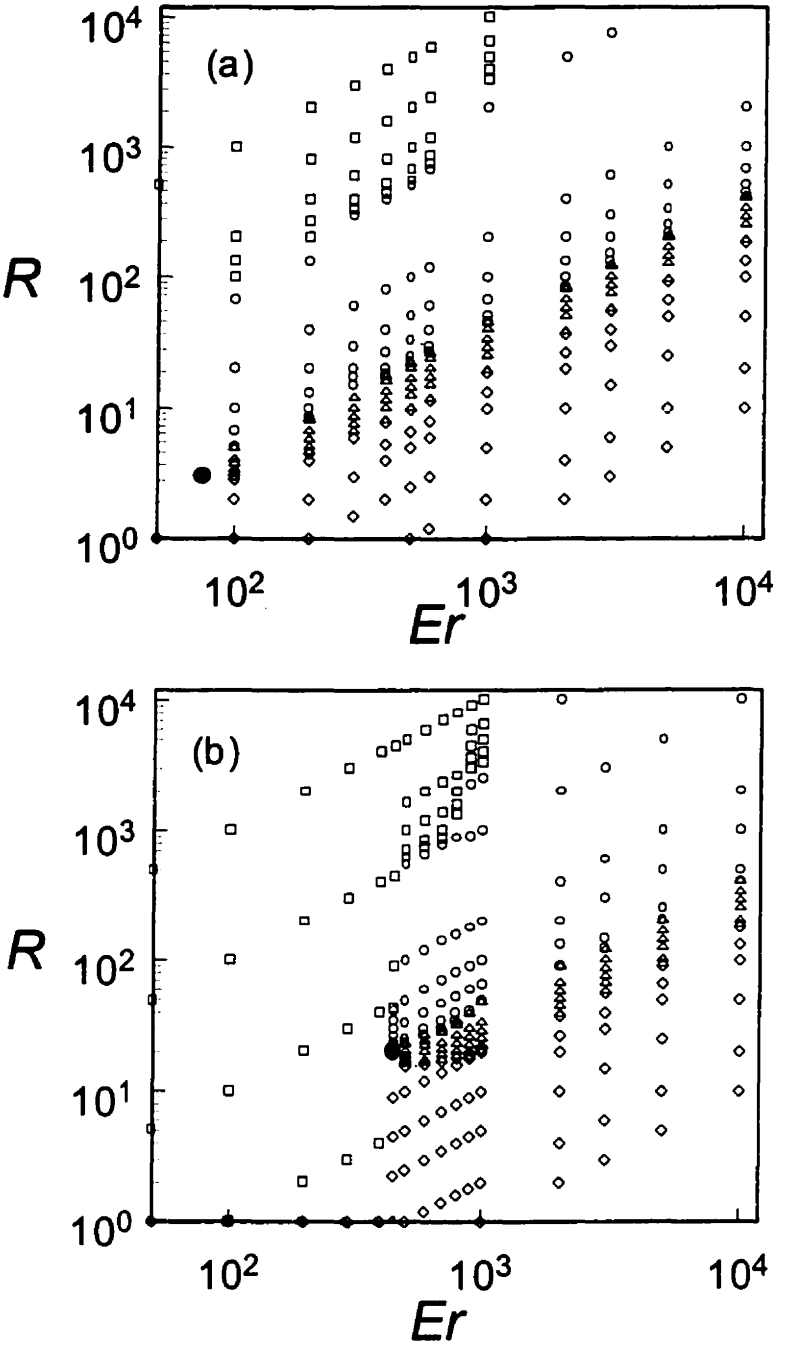

Figure 6.17: Microstructure phase diagram in the *R-Er* phase plane for (a) BCVG ($\mathbf{n}_{S,BCVG} = (0,1,0)$), and (b) BCF ($\mathbf{n}_{S,BCF} = (1,0,0)$) for $U = 6$, $\beta = -0.9$, and $L_2^* = -4/3$. The figure shows parametric regions for the four stable planar microstructure modes: ESS (□), TWS (○), WS (△), and VSS (◇). In BCF the phase plane is shifted towards right and upwards as compared to BCVG. The coordinates of the qua-critical points (●) for BCVG and BCF are $(Er_{qc}, R_{qc})_{BCVG} \approx (70,3)$ and $(Er_{qc}, R_{qc})_{BCF} \approx (450,20)$ respectively.

6.3.3 Effect of Long-Range Elastic Anisotropy

The above numerical results and discussion was based on one value of the long-range elasticity ratio parameter: $L_2^* = L_2/L_1 = -4/3$. To investigate the effect of long-range elasticity on microstructural phenomena of sheared discotic nematics, two values of $L_2^* = -4/3$, and -1/4 were used, corresponding to Frank elastic constants $K_{22} = 3K$, and $K_{22} = 8/7\,K$ respectively (see Figure 6.2). The long-range elastic anisotropy is higher for $L_2^* = -4/3$ ($K_{22} = 3K$) than for $L_2^* = -1/4$ ($K_{22} = 8/7\,K$). Figure (6.18) shows the microstructure phase diagram, in *Er-R* parametric phase space for BCVG, $L_2^* = -1/4$, U = 6, and β = -0.9. All of the four microstructure modes were found to exist in the clearly marked regions on the phase plane, as shown in Figure (18): ESS (□), TWS (○), WS (△), and VSS (◇). A filled circle represents the qua-critical point (●). The coordinates of the qua-critical point in Figure (6.18) are $(Er_{qc}, R_{qc}) \approx (180, 8)$.

A comparison of Figures (6.17a) and (6.18) reveals that the qua-critical point in Figure (6.18) has moved upwards and towards the right, such that:

$$(Er_{qc}, R_{qc})_{L_2^*=-\frac{1}{4}} > (Er_{qc}, R_{qc})_{L_2^*=-\frac{4}{3}}, \text{ and} \tag{6.21a}$$

$$\frac{(Er_{qc})_{L_2^*=-\frac{1}{4}}}{(Er_{qc})_{L_2^*=-\frac{4}{3}}} \approx \frac{(R_{qc})_{L_2^*=-\frac{1}{4}}}{(R_{qc})_{L_2^*=-\frac{4}{3}}} \approx \frac{\left(\frac{K_{22}}{K}\right)_{L_2^*=-\frac{4}{3}}}{\left(\frac{K_{22}}{K}\right)_{L_2^*=-\frac{1}{4}}} \approx 2.6. \tag{6.21b}$$

Based on the discussion in the previous section, the inequality (6.21a) is due to the fact that the extent of penetration of surface anchoring effects into the bulk is higher for $L_2^* = -1/4$ than for L_2^* = -4/3, and higher elastic anisotropy induces better penetration effects from the surface into the bulk. The above scaling law, equation (6.21b), states that the qua-critical point shifts along each parametric axis in the same ratio, and the shift ratio is given by the inverse ratio of the Frank elastic constant ratio K_{22}/K.

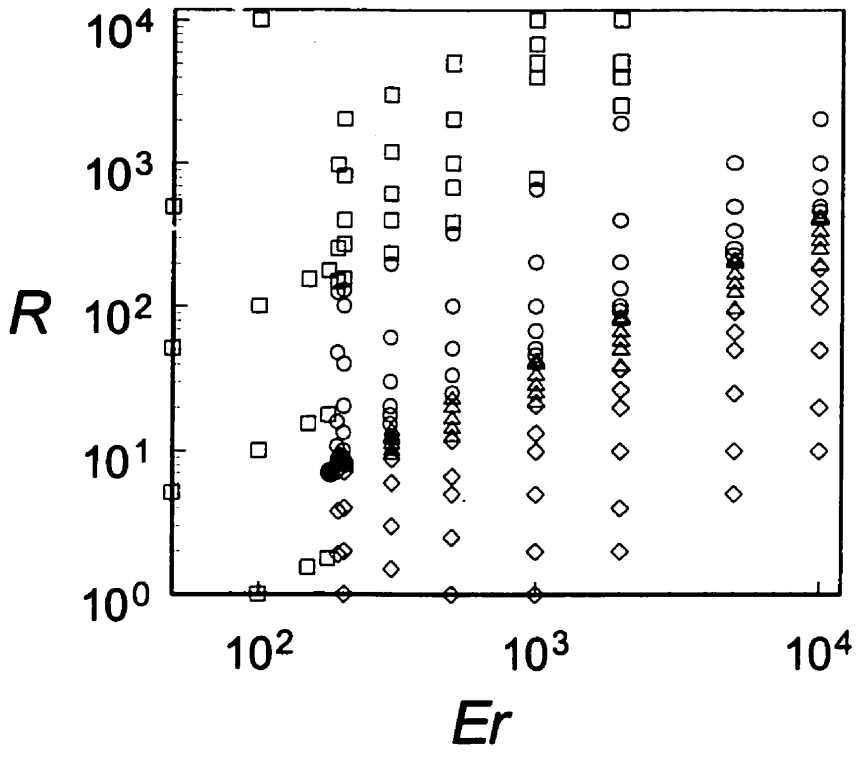

Figure 6.18: Microstructure phase diagram for BCVG, $\mathbf{n}_{S,BCVG} = (0,1,0)$, and for L_2^* = -1/4 ($K_{22} = 3K$), $U = 6$, and β = -0.9. The figure shows parametric regions for the four stable planar microstructure modes: ESS (□), TWS (○), WS (△), and VSS (◇). At higher value of L_2^*, lesser long range anisotropy, the phase diagram is shifted towards right and upwards as compared to Figure (6.19a) which is for L_2^*=-3/4 ($K_{22} = 8/7K$). The location of the qua-critical points (●) is $(Er_{qc}, R_{qc}) \approx (180, 8)$.

6.4 Conclusions

A comprehensive analysis of shear-induced microstructure phenomena exhibited by discotic mesophases is performed using a complete generalized theory that takes into account short-range elasticity, long-range elasticity and viscous effects. The theory predicts four distinct planar microstructure modes: (1) long-range elasticity induced steady state (ESS), (2) bulk tumbling–boundary wagging state (TWS), (3) bulk wagging state (WS), and (4) viscous flow induced steady state (VSS). In the ESS the microstructure is stabilized by the curvature elasticity through fixed orientation and alignments anchoring at the plates. The TWS is a periodic state and comprises of three spatial distinct regions: a continuously rotating core, and two oscillatory boundary layers.

At the boundary of the three regions a pair of abnormal nematic sates appear which bridges smoothly the winding core with the boundary layers through the director resetting mechanism. The thickness of the boundary layers increases with increasing Ericksen number *Er* and decreasing ratio *R*. The WS is a periodic state in which the orientation and alignments oscillate throughout the bulk with space dependent amplitude that is maximum at the centerline. The maximum amplitude of oscillations decreases with increasing Ericksen number *Er* and decreasing ratio *R*. The VSS is a spatially inhomogeneous steady state that is brought out by the aligning effects of the flow. In all the microstructure modes the average bulk orientation is along the velocity gradient direction.

The microstructure phase diagram spanned by Er and R that summarizes the complete in-plane microstructure phenomena of sheared discotic mesophases reveals that the four regimes coexist at a one point, called qua-critical point, in phase plane.

The effect of different planar surface anchoring conditions on flow-induced microstructural phenomena reveals that: (a) the average bulk orientation is along the velocity gradient direction irrespective of the surface anchoring, (b) the fixed anchoring along the velocity gradient direction is able to transmit the anchoring effects deeper into the bulk than the tangential case.

The effect of Frank elasticity is given in the form of a microstructure phase diagram. It is found that as strength of long-range anisotropy decreases the qua-critical point moves upwards and towards the right in the phase plane. A novel scaling law relating the magnitude of the shift was discovered, and states that the qua-critical point shifts along each parametric axis in the same ratio, and the shift ratio is given by the inverse ratio of the Frank elastic constant ratio K_{22}/K.

The present systematic study of flow induced microstructural behavior of discotic mesophases subjected to representative boundary conditions provides a useful fundamental understanding of the flow behavior of discotic mesophases of use in the processing of carbonaceous mesophases.

Bibliography

N.C. Andrews, B.J. Edwards and A.J. McHugh, "Continuum dynamic behavior of homogeneous liquid-crystalline polymers under the imposition of shear and magnetic fields", *J Rheo* **39** 1161 (1995).

S.-G. Baek, J.J. Magda and R.G. Larson, "Rheological differences among liquid-crystalline polymers. I. The first and second normal stress differences of PBG solutions", *J Rheol* **37** 1201 (1993).

S.-G. Baek, J.J. Magda, R.G. Larson and S.D. Hudson, "Rheological differences among liquid-crystalline polymers. II. Disappearance of negative N_1 in densely packed lyotropes and thermotropes" *J Rheol* **38** 1473 (1994).

A.N. Beris and B.J. Edwards, "Thermodynamics of flowing systems: with internal microstructure", *Oxford University Press*, New York (1994).

T. Carlsson, "Remarks on the flow alignment of disk like nematics", *J. Physique* **44** 909 (1983).

S. Chandrasekhar, "Liquid crystals of disc-like molecules", *Mol Cryst Liq Cryst* **63** 171 (1981).

S. Chandrasekhar, "Liquid Crystals", 2nd edition, *Cambridge University Press*, Cambridge (1992).

P.A. de Castro, A.J. Palangana, and L.R. Evangelista, "Micellar shape anisotropy and elastic constant in discotic lyotropic liquid crystals", *Physical Review E* **60**(5) p 6195-6198 (1999).

P.G. deGennes and J. Proust, "The Physics of Liquid Crystals". 2nd edition, *Oxford University Press*, Oxford (1993).

M. Doi, J. Polymer Physics Ed. **19** p229 (1981).

M. Doi and S.F. Edwards, "The Theory of Polymer Dynamics", *Oxford University Press* New York 358-362 (1986).

D.D. Edie, K.E. Robinson, O. Fleurot, S.P. Jones and C.C. Fain, "High thermal conductivity ribbon fibers from Naphthalene-based mesophase", *Carbon* **32** 1045 (1994).

R.G. Larson and H.C. Öttinger, "Effect of molecular elasticity on out-of-plane orientations in shearing flows of liquid-crystalline polymers", *Macromolecules* **24** 6270 (1991).

R.G. Larson, "The structure and rheology of complex fluids", *Oxford University Press*, NY (1999).

F.M. Leslie, Rat. Mech. Anal. **28** p265 (1968).

F.M. Leslie, "Theory of flow phenomena in liquid crystals", Advances in Liquid Crystals, *Academic Press*, New York (1979).

P. Manneville, *Mol. Cryst. Liq. Cryst.* **70** p 223 (1981)

G. Marrucci and P.L. Maffettone, "Description of the liquid-crystalline phase of rodlike polymers at high shear rates", *Macromolecules* **22** 4076 (1989).

G. Marrucci and F. Greco, "Flow behavior of liquid crystalline polymers", *Adv Chem Phys* **86** 331 (1993).

J.J. McHugh, G.Z. Liu and D.D. Edie, "An evaluation of Naphthalene-based mesophase as a carbon fiber precursor", *TANSO* **155** 417 (1992).

J.J. McHugh and D.D. Edie, "Orientation of mesophase pitch in capillary and channel flows", *Liq Cryst* **18** 327 (1995).

L.H. Peebles, "Carbon Fibers Formation, Structures and Properties", *CRC Press*, Boca Raton, USA (1994).

A.D. Rey and T. Tsuji, "Recent advances in theoretical liquid crystal rheology", Macromol. Theory Simul. **7** p623-639 (1998).

L.S. Singer, "The mesophase in carbonaceous pitches", *Faraday Discuss Chem Soc* **79** 265 (1985).

A.P. Singh and A.D. Rey, "Microstructure constitutive equation for discotic nematic liquid crystalline materials Part I: Selection procedure and shear flow predictions", *Rheologica Acta* **37**(1) p30-45 (1998a).

A.P. Singh and A.D. Rey, "Microstructure constitutive equation for discotic nematic liquid crystalline materials Part II: Rheological predictions", *Rheologica Acta* **37**(4) p374-386 (1998b).

K. Singh and N.S. Pandey, "Elastic constants of discotic (nematic) liquid crystals: effect of packing", *Liquid Crystals* **25**(3) p411-418 (1998).

J. Stelzer, M.A. Bates, L. Longa, and G.R. Luckhurst, "computer simulation studies of anisotropic systems. XXVII The direct pair correlation function of the Gay-Berne discotic nematic and estimates of its elastic constants", *J. Chemical Physics* **107**(18) p7483-7492 (1997).

T. Tsuji and A.D. Rey, "Effect of long-range order on sheared liquid crystalline materials. Part I: Compatibility between tumbling behavior and fixed anchoring", *JNNFM* **73** p127-152 (1998).

T. Tsuji and A.D. Rey, "Orientation mode selection mechanisms for sheared nematic liquid crystalline materials", *Physical Review E* **57**(5) p5609-5625 (1998).

T. Tsuji and A.D. Rey, "Effect of long range order on sheared liquid crystalline materials: Flow regimes, transitions, and rheological phase diagrams", *Physical Review E*, in press (2000).

J.E. Zimmer, J.L. White, in H.G. Brown (Ed.), Advances in Liquid Crystals, Volume 5, Academic Press, NY (1982) 157.

[1]CHAPTER 7

Microstructure Response of Sheared Discotic Mesophases in Hybrid Aligned Nematic (HAN) Cell

Chapter 6 presents detailed account of long-range elasticity effects, and boundary conditions on the shear-induced microstructural response of model discotic mesophases. However, same surface anchorings were used, such that the orientation was fixed in the same direction at the top and the bottom plate. In this chapter the microstructural response of sheared discotics subjected to mixed boundary conditions, equivalent of that in a hybrid aligned nematic (HAN) cell, is computed. The strong surface anchorings at both the plates correspond to the stable orientation configuration of discotic mesophases when subjected to homogeneous shear flows, such that the director **n** is anchored along the vorticity direction at the bottom stationary plate, and along the velocity gradient direction at the top moving plate. A novel model of continuous generation of defect-like structures in the bulk is discovered, and is due to asynchronous rotational kinematics. The simulation results are used to put forth the generation of more complex fiber textures, such as mixed texture (radial core with onion exterior), and skin-core textures observed during processing of a carbonaceous mesophase.

---

[1] This chapter appeared as an original article in XIII[th] Congress of Rheology "*Rheology 2000*", p117-119, Cambridge, U.K. (2000)

7.0 Abstract

Flow modeling of model mesophase pitches is performed using a complete phenomenological theory that takes into account short-range order elasticity, long-range curvature elasticity, and viscous flow effects. The theory is fully compatible with the well known Leslie-Ericksen and Doi theories, and thus fills the parametric gap where these classical theories are inapplicable. A novel shear-induced mode of continuous generation of defect-like structures in the bulk has been discovered. These structures emerge due to asynchronous rotational orientation kinematics. The numerical results are characterized mathematically as well as in terms of the basic physical mechanisms. The simulations are further used to put forth the fundamental principles that govern mesophase carbon fiber texture generation under shear.

7.1 Introduction

Mesophase pitches (MPs) have emerged into an important class of precursor materials to manufacture high performance mesophase carbon fibers, and as matrix materials in carbon-carbon composites. The excellent end product property profiles are due to the anisotropic nature of the MPs. For example, the mesophase carbon fibers have been known to possess very high axial thermal conductivity and elastic modulus, and thus are very suitable for industrial processes requiring high thermal transportation and stiffness. It is possible to induce and control preferred molecular alignment in anisotropic carbonaceous mesophases during processing, thereby imparting superior properties to the end products. The MPs consist of disc-shaped aromatic molecules that are flat and large enough to exhibit nematic characteristics, and are termed discotic nematics, N_D. Figure (7.1) shows a schematic of a uniaxial discotic nematic phase. The unit normals to the disk-like molecules orient along a preferred direction given by a unit vector $\mathbf{n}$ commonly known as director or average orientation, and the extent of alignment of the unit normals along the director $\mathbf{n}$ is given by a scalar S called uniaxial scalar order parameter or uniaxial alignment.

Numerous experimental and theoretical studies have been performed to unravel the fundamental principles governing the flow-induced microstructural phenomena of

rod-like nematics. A similar understanding is not yet available for N_D, but is required for making further technological advances in the manufacturing of carbon fibres using MP precursors. The present work is aimed towards developing such scientific database for MPs, and extends our previous work (Singh and Rey, 1998a, 199bb, 2000; Tsuji and Rey, 1998) to N_D.

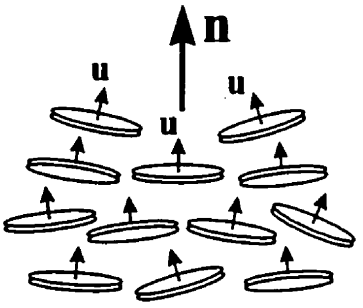

Figure 7.1: Definition of uniaxial director/orientation **n** of a uniaxial discotic nematic liquid crystalline phase. The director **n** is the average orientation of the unit normals **u** to the disc-like molecules.

In industrial processing, precursor materials are subjected to complex flows, involving various combinations of shear and extensional deformations, in complex geometries. In order to control the molecular orientation or microstructure a fundamental understanding of the material behavior subjected to the prevailing complex flow is required. In this paper we study and characterize the distinct microstructural features exhibited by discotic mesophases under rectilinear shear flow.

In our previous works (Singh and Rey, 1998a) a constitutive equation (CE) for discotic mesophases was formulated based on Doi's theory of nematodynamics by taking into account full microstructural features. The CE under homogeneous shear flow predicted the classical stable planar 2D (tumbling, wagging and aligning) modes as well as non-planar 3D (log-rolling) mode. These microstructure modes in sheared discotic mesophases are similar to those for rod-like nematics; yet possess inherent differences that are attributes of different molecular shape. In a subsequent work (Singh and Rey, 2000), a comprehensive characterization of all the planar spatially non-homogeneous microstructure modes of sheared N_D subjected to different boundary conditions is presented. The general aim of this paper is to characterize the effect of long-range order

elasticity on the rectilinear shear-induced microstructure phenomena in MPs subjected to mixed boundary conditions, and to use the results to identify the fundamental principles governing various MP-based carbon fiber textures.

7.2 Theory and Governing Equations

The evolution of microstructure, in terms of the tensor order parameter **Q**, in N_D subjected to shear flows is governed by the following microstructure constitutive equation (Singh and Rey, 2000; Tsuji and Rey, 1998):

$$\begin{aligned} Er\frac{d\mathbf{Q}}{dt} = Er\Big[& \mathbf{W}\cdot\mathbf{Q}-\mathbf{Q}\cdot\mathbf{W}+\frac{2}{3}\beta\mathbf{A}+\beta\Big[\mathbf{A}\cdot\mathbf{Q}+\mathbf{Q}\cdot\mathbf{A}-\frac{2}{3}(\mathbf{A}:\mathbf{Q})\mathbf{I}\Big] \\ & -\frac{1}{2}\beta\big[(\mathbf{A}:\mathbf{Q})\mathbf{Q}+\mathbf{A}\cdot\mathbf{Q}\cdot\mathbf{Q}+\mathbf{Q}\cdot\mathbf{A}\cdot\mathbf{Q}+\mathbf{Q}\cdot\mathbf{Q}\cdot\mathbf{A}-\{(\mathbf{Q}\cdot\mathbf{Q}):\mathbf{A}\}\mathbf{I}\big]\Big] \\ & -R\frac{6}{\left(1-\frac{3}{2}\mathbf{Q}:\mathbf{Q}\right)^2}\Big[\Big(1-\frac{1}{3}U\Big)\mathbf{Q}-U\mathbf{Q}\cdot\mathbf{Q}+U\Big\{(\mathbf{Q}:\mathbf{Q})\mathbf{Q}+\frac{1}{3}(\mathbf{Q}:\mathbf{Q})\mathbf{I}\Big\}\Big] \\ & +\frac{1}{\left(1-\frac{3}{2}\mathbf{Q}:\mathbf{Q}\right)^2}\Big[\nabla^2\mathbf{Q}+\frac{1}{2}\frac{L_2}{L_1}\Big[\nabla(\nabla\cdot\mathbf{Q})+\{\nabla(\nabla\cdot\mathbf{Q})\}^T-\frac{2}{3}\mathrm{tr}\{\nabla(\nabla\cdot\mathbf{Q})\}\mathbf{I}\Big]\Big] \end{aligned} \tag{7.1}$$

Here, **A**, **W**, L_i (i = 1,2), U, β are the dimensionless vorticity tensor, the dimensionless rate of deformation tensor, the Landau coefficients, the nematic potential and the molecular shape factor, respectively. For details see (Singh and Rey, 2000; Tsuji and Rey, 1998). The first term on the right hand side of equation (7.1) relates the microstructure with viscous flow deformations, the second term represents the short-range order elasticity effects which control the isotropic-nematic phase transition, and the last term represents the long-range order elasticity effects and transmits the surface anchoring effects from the boundaries into the bulk. The long-range elastic effect also known as Frank elasticity is necessary to describe the textures and defects invariably observed in practice. As there are three competing contributions controlling the microstructural response of N_D, therefore we have two dimensionless numbers or scaling parameters (Tsuji and Rey, 1998):

$$Er=\frac{VH\mu_e}{L_1}, \quad R=\frac{H^2}{6}\frac{c\kappa T}{L_1}, \tag{7.2a,b}$$

Where H is the characteristic distance between the two plates (see Figure 7.2), V is the constant velocity of the top plate, and μ_e is the viscosity (Singh and Rey, 2000; Tsuji and Rey, 1998). The Ericksen number Er is the ratio of the viscous flow effects to long-range order elasticity, whereas ratio R is the ratio of the short-range order elasticity to long-range order elasticity. As reported (Singh and Rey, 2000; Tsuji and Rey, 1998) the above-presented theory, equation (7.1), fills the gap between classical theories of liquid crystals, Leslie–Ericksen (L-E) theory and Doi's theory. In summary, the above generalized theory is completely compatible with the L-E theory in the limit $R \rightarrow \infty$, on the other hand it is compatible with Doi's theory in the limit $Er \rightarrow \infty$, and transversely isotropic fluid (TIF) theory in the limit $R \rightarrow \infty$ and $Er \rightarrow \infty$ (Singh and Rey, 2000; Tsuji and Rey, 1998).

In this work mixed fixed boundary conditions are used, such that the director **n** is anchored along the vorticity direction (z-axis) at the bottom stationary plate, and along the velocity gradient direction (y-axis) at the top moving plate, see Figure 7.2. The director orientation is characterized by an out-of-plane angle ϕ, and an in-plane angle θ. This set of BCs corresponds to the anchoring conditions in a hybrid aligned nematic (HAN) cell. Both BCs are along the stable attractors for model discotic nematics under homogeneous shear flows (Singh and Rey, 1998a). In the present work the parametric values are set at: $U = 6$, $\beta = -0.9$, $L_2/L_1 = -4/3$, and the simulations are performed for the ranges: $1 \le R \le 10^5$, and $1 \le Er \le 10^5$.

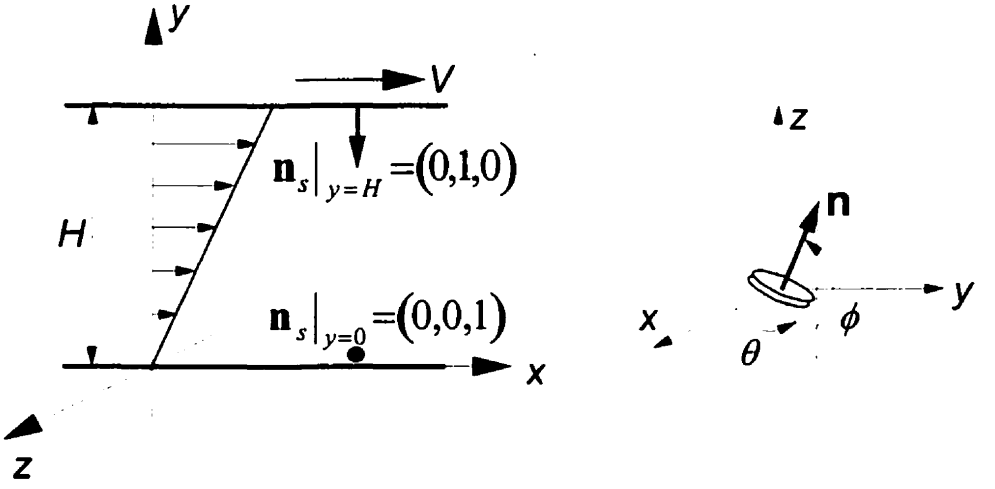

Figure 7.2: Definition of flow geometry, co-ordinate system and boundary conditions.

7.3 Numerical Results and Discussion

An extensive computational investigation of the governing equation (7.1) has been performed. The microstructure features of model MPs are characterised by one time dependent periodic state, and two steady states. A brief description of the relevant features of these three regimes is given below:

7.3.1 Elasticity-Driven Steady State (ESS)

This steady state prevails at sufficiently low *Er* and for all arbitrary values of *R*, and arises due to the dominance of long-range elasticity on the vorticity effects of imposed shear flow. Figure 7.3 shows the director out-of-plane angle ϕ spatial profiles for *Er* = 100, *R* = 10 (solid line), and *Er* = 1000, *R* = 100 (dash line). At low *Er* the out-of-plane angle changes monotonically from bottom plate to top plate, however, at high *Er* the director aligns near the vorticity axis in most of the domain ($0<y/H<0.75$), and decreases sharply near the top plate. The long-range elasticity effects are stronger at lower *Er* (*Er*=100) thereby maintaining lower spatial gradients than at higher *Er* (*Er*=1000). In this regime the uniaxial (biaxial) *S*(*P*) scalar order parameters are near their equilibrium values. The inset schematics represent the corresponding fiber textures discussed below.

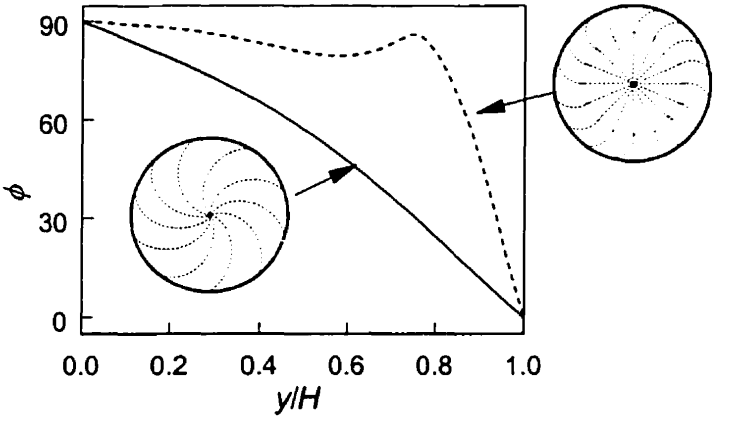

Figure 7.3: Director out-of-plane angle ϕ spatial profiles for *Er* = 100, *R* = 10 (solid line), and *Er* = 1000, *R* = 100 (dash line). The inset schematics represent the corresponding fiber textures.

The main features of the ESS regime are: (a) the microstructure field reaches steady state; (b) the steady state arises due to long-range elasticity, (c) the nematic phase is mostly uniaxial.

7.3.2 Composite Kayaking-Limit Cycle Periodic State (KLS)

This periodic state appears at sufficiently high Er and at appropriate values of R. Figure 7.4 shows (a) uniaxial alignment (S), and (b) biaxial alignment (P) as a function of dimensionless time (t) and distance (y/H) for Er =1000 and R = 20. The director dynamics are rotational, and the scalar order parameters (S, P) oscillate with the nucleation of an abnormal nematic state in the bulk (at $y^* = y/H \approx 0.84$ in this case). As R decreases the nucleation point moves away from the top plate towards the lower plate. The director rotates in the kayaking orbits in the region $0<y/H<y^*$, and in a out-of-plane limit cycles in the rest of the domain $y^*<y/H<1$, as shown in Figure 7.4(c). In the kayaking orbit the director rotates clockwise in a closed loop, which extends (shrinks) towards the velocity gradient (flow) direction, around the vorticity axis in which it slows down near the velocity gradient direction. For more details please see (Singh and Rey, 1998a). In the limit cycle the director trajectory also makes a closed loop that is eccentric to the vorticity axis as shown in Figure 7.4(c). The kayaking orbit and the limit cycle shrink as we move close to the walls. The abnormal nematic states nucleate where the kayaking orbit and the limit cycle merge.

The salient features of this periodic state are: (a) the director dynamics in the bulk are rotational and correspond to kayaking orbits near the bottom plate and to limit cycles near the top plate, (b) at the boundary between these two regions abnormal nematic states nucleate, (c) the abnormal nematic states emerge in the bulk.

7.3.3 Viscous-Driven Steady State (VSS)

This steady state appears at high Er and appropriate R, and arises due to dominance of the strong aligning viscous torques over all other competing effects. Figure 7.5 shows spatial profiles of the out-of-plane director angle ϕ for Er = 100, R = 1 (solid line), R = 0.1 (triple-dot dash line), and for Er = 1000, R = 1 (dash line). The bulk

orientation in the region $y/H<\delta_c$ is along the vorticity axis ($\phi \approx 90$), and that in the region $y/H>\delta_c$ is planar and along the velocity gradient direction ($\phi \approx 0$, $\theta \approx 90$). The sharp director reorientation in the bulk is compensated by a corresponding sharp dip (spike) in bulk alignment S (P). δ_c increases with decreasing R, and decreasing Er as shown in Figure 7.5.

The main features of the VSS regime are: (a) the microstructure field is non-homogeneous, steady state and arises due to the flow aligning torques at high Er, (b) there exists a discontinuity in the orientation field, and (c) the nematic phase is highly biaxial.

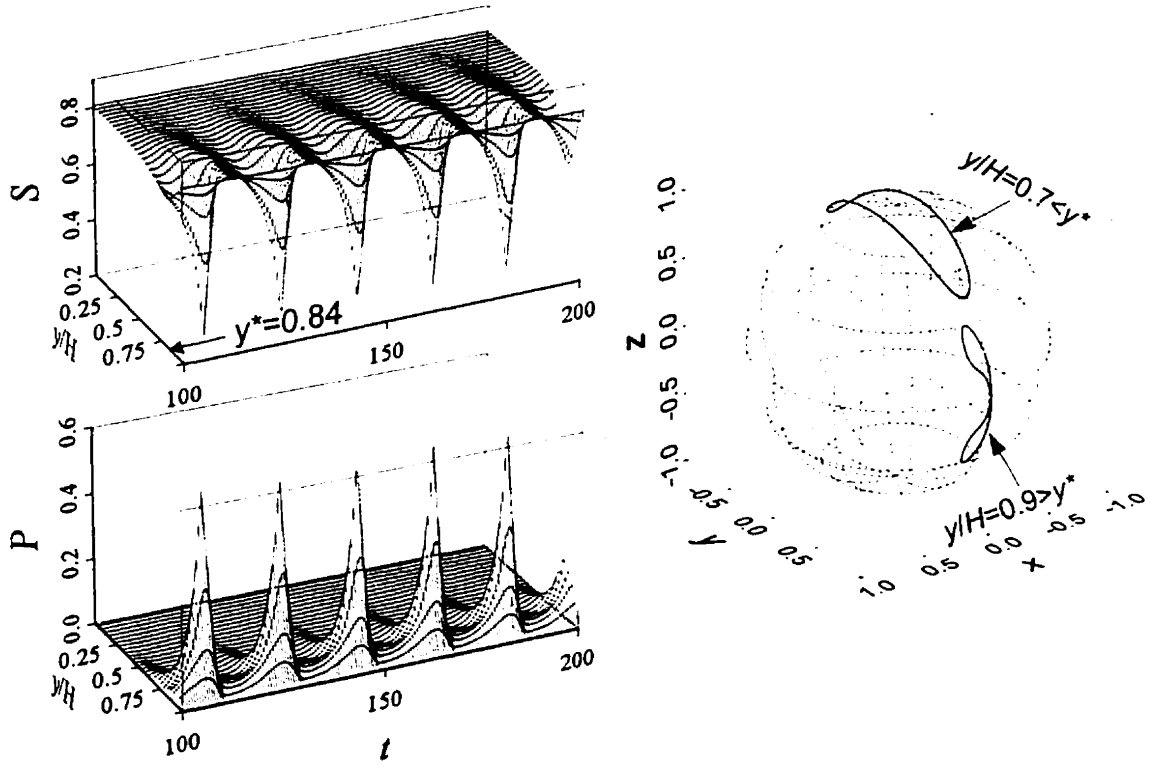

Figure 7.4: Uniaxial (S) and biaxial (P) scalar order parameter as a function of dimensionless time (t) and distance (y/H) for Er =1000 and R = 20. Director profiles on unit sphere at y/H = 0.7 (kayaking orbit) and y/H = 0.9 (limit cycle). Abnormal nematics appear at $y^* \approx 0.84$.

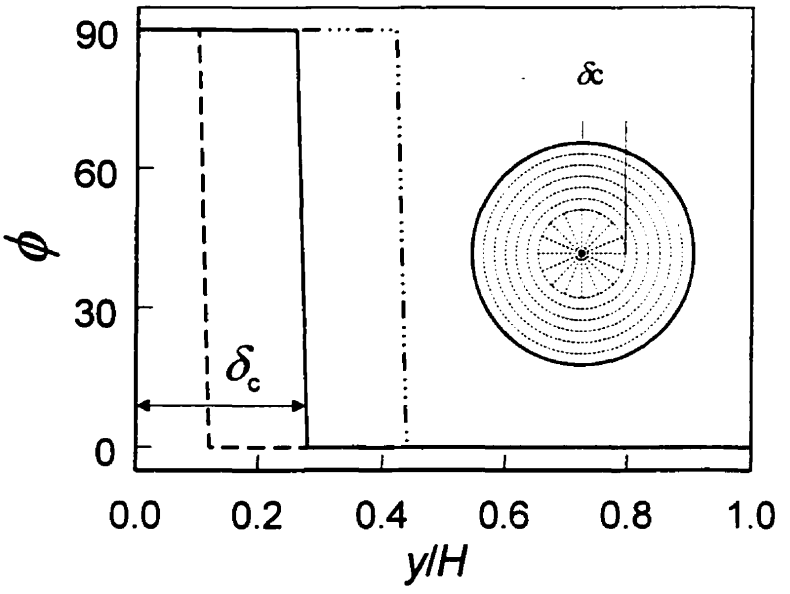

Figure 7.5: Director out-of-plane angle ϕ as a function of dimensionless distance (y/H) between the plates for Er = 100, and R = 1 (solid line), 0.1 (triple-dot dash line), Er = 1000, and R = 1 (dash line).

7.4 Implications of Numerical Results on Fiber Textures

Mesophase carbon fibers exhibit numerous transverse fiber textures (Peebles, 1994). We extend the numerical results, presented above, to explain the existence of some of the prevalent MP-based carbon fiber textures. It is presented in (Singh and Rey, 1998b) that the pure radial (onion) fiber texture is consistent with director orientation along vorticity (velocity gradient) direction. Using the same reasoning, we find that the director orientation in VSS corresponds to a mixed texture with a radial core and an onion exterior, shown in Figure 7.5. The size of the radial core δ_c is a function of R and Er as mentioned above. The presented model also predicts the textures with an onion core and a radial exterior. The orientation field in ESS corresponds to the skin-core textures (Peebles, 1994). The director orientation in ESS at high Er (Er=1000) corresponds to a texture with a fairly large radial core and folded outer layers as shown in Figure 7.3. At lower Er (Er=100) the continuous decrease in out-of-plane director orientation results in a folded texture morphology or skin-core texture, in which a small inner radial core is connected smoothly with the outermost onion layer.

Bibliography

L.H. Peebles, "*Carbon Fibers Formation, Structures and Properties*", CRC Press, Boca Raton, USA (1994).

A.P. Singh and A.D. Rey, "Microstructure constitutive equation for discotic nematic liquid crystalline materials. Part I: Selection procedure and shear flow predictions", *Rheologica Acta* **37**(1) 30 (1998a).

A.P. Singh and A.D. Rey, "Consistency of Predicted Shear-induced Orientation Modes with Observed Mesophase Pitch-Based Carbon Fibre Textures", *Carbon* **36** 1855 (1998b).

A.P. Singh and A.D. Rey, "Effect of Long Range Elasticity and Boundary Conditions on Microstructural Response of Sheared Discotic Mesophases", *JNNFM* **94**(2-3) 87 (2000).

T. Tsuji and A.D. Rey, "Effect of long-range order on sheared liquid crystalline materials. Part I: Compatibility between tumbling behavior and fixed anchoring", *JNNFM* **73** 127 (1998).

CHAPTER 8

Conclusions and Original Contributions to Knowledge

8.1 Thesis Summary

This thesis presents a detailed account of the development of a constitutive equation for generic discotic mesophases and for mesophase pitches, by adopting the well-known nematodynamics theories for rod-like nematics. The shear and extensional flow induced microstructural and rheological predictions of the selected constitutive equation are computed and analyzed. The numerical results are put forth to characterize the relations among microstructure modes, rheological parameters, processing conditions, and material properties. Furthermore, general principles governing the mesophase carbon fiber textures are elucidated.

This work is a first attempt to establish the relations between flow-induced microstructure, rheological material functions, processing conditions, and material parameters for discotic mesophases. A sufficiently number of distinguishing features have been identified that are specific to the discotic nature of the nematic phase, and augment the number of quantitative and qualitative differences between discotic and rod-like nematics that had been noted in the literature. How these distinguishing rheological

features operate in the carbon fiber texture selection during spinning of carbonaceous mesophases is a topic of ongoing investigation.

8.2 Thesis Conclusions

As stated earlier this thesis addresses three different facets of scientific study. The conclusions for each effort are given below:

8.2.1 Conclusions of Shear-induced Microstructure Characterization

A microstructure constitutive equation, CE, has been developed for mesophase pitches by implementing an iterative process that is based on a set of criteria that consists of theoretical results and experimental data. Four CEs for discotic nematics were proposed. A comprehensive bifurcation analysis reveals that the various proposed CEs predict a great variety of dynamical microstructural behaviors for discotic mesophases, and show multi-stabilities of various orientation modes through a series of complex bifurcations. All the CEs, when subjected to homogeneous simple shear flows, predicted the shear plane and the vorticity axis as major stable attractors, whereas kayaking orbits and period doubling orbits are stable attractors only in those CEs which are based on **Q** independent diffusivity. Moreover, the CEs with the **Q** independent diffusivity do not predict the in-plane periodic stable states (such as in-plane tumbling orbit, ITO, and in-plane wagging state, IWS), which is not in agreement with the predictions of molecular theories. Hence the constant (**Q** independent) diffusivity is not an appropriate assumption while selecting a CE for non-aligning discotic mesophases. A complete analysis and characterization of all the stable attractors, and their transition with dimensionless shear rate *Pe* for all the proposed CEs is presented. The complete summary of dynamical and steady state microstructure features of all the CEs under homogeneous shear rates is given in Tables 2.5, 2.6, and 2.7.

The selected CE for mesophase pitches predicts the major and essential stable steady and periodic states: ITO (in-plane tumbling), IWS (in-plane wagging state), ISS (in-plane steady state), and LRS (log-rolling state); along with the low temperature classical transitions ITO $\rightarrow$ IWS $\rightarrow$ ISS with shear rate. At high temperature the complex

bifurcations between the in-plane and out-of-plane orientation modes disappear and the only stable state is ISS. The CE also predicts the multistability among the in-plane and out-of-plane orientation modes at all shear rates and at low temperature.

The long-range Frank elasticity term is coupled with the selected CE to account for the microstructure gradients. A comprehensive analysis of shear-induced microstructure phenomena exhibited by discotic mesophases is performed using this complete generalized theory. Four distinct planar microstructure modes are predicted: (1) long-range elasticity induced steady state (ESS), (2) bulk tumbling–boundary wagging state (TWS), (3) bulk wagging state (WS), and (4) viscous flow induced steady state (VSS). In the ESS the microstructure is stabilized by the curvature elasticity through fixed orientation and alignments at the plates. The TWS is a periodic state and comprises of three spatial distinct regions: a continuously rotating core, and two oscillatory boundary layers. At the boundary of the three regions a pair of abnormal nematic sates appear which bridges smoothly the winding core with the boundary layers through the director resetting mechanism. The thickness of the boundary layers increases with increasing Ericksen number *Er* (dimensionless shear rate) and decreasing ratio *R* (ratio of short-range elasticity to long-range elasticity). The WS is a periodic state in which the orientation and alignments oscillate throughout the bulk with space dependent amplitude that is maximum at the centerline. The maximum amplitude of oscillations decreases with increasing Ericksen number *Er* and decreasing ratio *R*. The VSS is a spatially inhomogeneous steady state that is brought out by the aligning effects of the flow. In all the microstructure modes the average bulk orientation is along the velocity gradient direction. The microstructure phase diagram spanned by *Er* and *R* reveals that the four regimes coexist at a one point, called qua-critical point, in the phase plane.

The effect of Frank elasticity is given in the form of a microstructure phase diagram. It is found that as the strength of long-range anisotropy decreases the qua-critical point moves upwards and towards the right in the phase plane. A novel scaling law relating the magnitude of the shift was discovered, and states that the qua-critical point shifts along each parametric axis in the same ratio, and the shift ratio is given by the inverse ratio of the Frank elastic constant ratio K_{22}/K.

Further, the effect of different planar surface anchoring conditions on flow-induced microstructural phenomena reveals that: (a) the average bulk orientation is along the velocity gradient direction irrespective of the surface anchoring, (b) the fixed anchoring along the velocity gradient direction is able to transmit the anchoring effects deeper into the bulk than the tangential case.

The effect of mixed boundary conditions on sheared discotic mesophases is analyzed. Mixed surface anchorings along the two stable attractors are imposed, such that the director is along the velocity gradient at the bottom stationary plate and along the vorticity axis at the top moving plate. The shear-induced microstructural features under theses boundary conditions are characterized by three stables states: (1) Elasticity-driven steady state (ESS), (2) composite kayaking-limit cycle periodic state (KLS), and (3) viscous-driven steady state (VSS). In ESS, the uniaxial microstructure field reaches steady state due to long-range elasticity. In KLS, the orientational dynamics in the bulk are rotational, and correspond to kayaking orbits near the bottom plate, and to eccentric limit cycles near the top plate; defect like structures emerge, in the bulk, at the boundary of the two and are due to asynchronous rotational orientation kinematics. The discontinuous and highly biaxial microstructure field in VSS is non-homogeneous, steady and arises due to strong viscous torques.

8.2.2 Conclusions of Shear and Extensional Rheological Functions Characterization

A complete hydrodynamic constitutive equation or extra stress tensor equation is developed from first principles. The predicted relations among rheological properties, shear-induced microstructure, processing conditions, and material parameters of discotic mesophases are computed, analyzed, and characterized.

Under homogeneous shear flow conditions, the predicted first normal stress difference N_1 corresponding to the planar microstructure mode of non-aligning discotics is found to be similar to that corresponding to the rod-like nematics at low shear rates. At higher shear rates the present theory does not accurately predict N_1 corresponding to planar mode of non-aligning rod-like nematics, hence no comparison can be drawn.

N_1 for non-planar mode is always positive, and increases exponentially for intermediate shear rates before reaching high shear rate plateau, and is mainly due to flow-induced biaxiality. For non-aligning discotic nematics, N_1 corresponding to the planar and the non-planar microstructure modes are comparable at low shear rates. As the more accurate representation of N_1 is to take average of both values corresponding to planar and non-planar modes of non-aligning discotics, which may result in the disappearance of negative N_1 in discotics in which viscous contribution dominates. Thus sign transition in N_1 may not be a correct check for non-aligning discotics. Also N_1 of aligning discotics is similar to that of rod-like nematics at all shear rates. N_1 is always positive for discotic mesophase at lower values of nematic potential U (for aligning nematics). The predicted apparent shear viscosity of discotic mesophases at low U (or high T) is qualitatively similar to that reported in the literature at all shear rates; whereas that at high U (low T) is qualitatively similar to that reported in literature for intermediate and high shear rates.

It is shown that two unique uniaxial extensional viscosities, termed here as η_{zr} and $\eta_{z\theta}$, are needed for discotic mesophases to completely characterize their extensional rheological functions. The discotic mesophases are found to be non-Troutonian, and show strain thinning or thickening based on the temperature and the ratio of viscous to elastic stress contributions. The elastic stresses result in strain thinning characteristics to the discotic mesophases whereas viscous stresses cause strain thickening. The extensional viscosities are highly dependent on the fiber microstructures.

8.2.3 Conclusions of Fiber Texture Characterization

The simulation results are further employed to put forth the fundamental principles that govern the formation of main mesophase carbon fiber textures. It is shown that the homogeneous shear induced microstructure modes selected by the CE are consistent with the radial and onion fiber textures, observed experimentally. The transition from the radial to the onion texture with increasing temperatures is also successfully predicted. The simulated shear-induced microstructural features under mixed boundary conditions are used explain the formation of mixed textures (with radial core and onion exterior), and folded layer or skin-core textures. The size of the radial

core in the mixed texture is a function of *Er* and *R*, and increases with decreasing *R* and *Er*. The transition from a skin-core texture to a mixed texture takes place with decreasing *R* or increasing *Er*.

8.3 Original Contributions to Knowledge

The specific original contributions of this thesis to present scientific knowledge are as follows:

1. A microstructure constitutive equation, for discotic mesophase in general and for mesophase pitches in particular, is developed.
2. An exhaustive bifurcation analysis of shear-induced predictions of a series of constitutive equations is performed, and the results are characterized in terms orientation modes.
3. A comprehensive analysis of shear-induced microstructure phenomena exhibited by discotic mesophases is performed using a complete generalized theory that takes into account short-range elasticity, long-range elasticity and viscous effects is presented for the first time.
4. A new scaling law relating the strength of long-range anisotropic energy with magnitude of shift of qua-critical point in *R-Er* phase plane is discovered.
5. Shear rheological predictions for discotic mesophases are presented for the first time. The shear rheological relations among microstructure, processing conditions, and material properties are presented.
6. It is shown that two unique extensional viscosity functions need to be defined to fully characterize the extensional rheology of discotic mesophases, and that the uniaxial extensional rheological material functions are strong functions of the internal microstructure.
7. The fundamental principles governing the formation of major mesophase carbon fiber textures are presented for the first time.

APPENDIX A

Dimensionless Forms of Constitutive Equations

The dimensionless coupled, nonlinear, ordinary first-order differential equations governing the microstructural response of a discotic nematics, subjected to simple shear flows, for the four proposed constitutive equations (CEs) are given below:

CE-1

$$\frac{d\mathbf{Q}}{dt^*} = Pe\left[\tilde{\mathbf{W}}\cdot\mathbf{Q}-\mathbf{Q}\cdot\tilde{\mathbf{W}}+\tfrac{2}{3}\beta\tilde{\mathbf{A}}+\beta\left\{\tilde{\mathbf{A}}\cdot\mathbf{Q}+\mathbf{Q}\cdot\tilde{\mathbf{A}}-\tfrac{2}{3}\left(\tilde{\mathbf{A}}:\mathbf{Q}\right)\delta\right\}-2\beta\left(\mathbf{Q}:\tilde{\mathbf{A}}\right)\mathbf{Q}\right]- \left[\left(1-\tfrac{U}{3}\right)\mathbf{Q}-U\mathbf{Q}\cdot\mathbf{Q}+U\left\{(\mathbf{Q}:\mathbf{Q})\mathbf{Q}+\tfrac{1}{3}(\mathbf{Q}:\mathbf{Q})\delta\right\}\right] \tag{A.1}$$

CE-2

$$\frac{d\mathbf{Q}}{dt^*} = Pe\left[\tilde{\mathbf{W}}\cdot\mathbf{Q}-\mathbf{Q}\cdot\tilde{\mathbf{W}}+\tfrac{2}{3}\beta\tilde{\mathbf{A}}+\beta\left\{\tilde{\mathbf{A}}\cdot\mathbf{Q}+\mathbf{Q}\cdot\tilde{\mathbf{A}}-\tfrac{2}{3}\left(\tilde{\mathbf{A}}:\mathbf{Q}\right)\delta\right\}-2\beta\left(\mathbf{Q}:\tilde{\mathbf{A}}\right)\mathbf{Q}\right]- \left\{1-\tfrac{3}{2}(\mathbf{Q}:\mathbf{Q})\right\}^{-2}\left[\left(1-\tfrac{U}{3}\right)\mathbf{Q}-U\mathbf{Q}\cdot\mathbf{Q}+U\left\{(\mathbf{Q}:\mathbf{Q})\mathbf{Q}+\tfrac{1}{3}(\mathbf{Q}:\mathbf{Q})\delta\right\}\right] \tag{A.2}$$

CE-3

$$\frac{d\mathbf{Q}}{dt^*} = Pe\left[\begin{array}{l}\tilde{\mathbf{W}}\cdot\mathbf{Q}-\mathbf{Q}\cdot\tilde{\mathbf{W}}+\frac{2}{3}\beta\tilde{\mathbf{A}}+\beta\left\{\tilde{\mathbf{A}}\cdot\mathbf{Q}+\mathbf{Q}\cdot\tilde{\mathbf{A}}-\frac{2}{3}\left(\tilde{\mathbf{A}}:\mathbf{Q}\right)\delta\right\}- \\ \frac{\beta}{2}\left\{\left(\tilde{\mathbf{A}}:\mathbf{Q}\right)\mathbf{Q}+\tilde{\mathbf{A}}\cdot\mathbf{Q}\cdot\mathbf{Q}+\mathbf{Q}\cdot\tilde{\mathbf{A}}\cdot\mathbf{Q}+\mathbf{Q}\cdot\mathbf{Q}\cdot\tilde{\mathbf{A}}-\left(\left(\mathbf{Q}\cdot\mathbf{Q}\right):\tilde{\mathbf{A}}\right)\delta\right\}\end{array}\right]- \tag{A.3}$$
$$\left[\left(1-\frac{U}{3}\right)\mathbf{Q}-U\mathbf{Q}\cdot\mathbf{Q}+U\left\{\left(\mathbf{Q}:\mathbf{Q}\right)\mathbf{Q}+\frac{1}{3}\left(\mathbf{Q}:\mathbf{Q}\right)\delta\right\}\right]$$

CE-4

$$\frac{d\mathbf{Q}}{dt^*} = Pe\left[\begin{array}{l}\tilde{\mathbf{W}}\cdot\mathbf{Q}-\mathbf{Q}\cdot\tilde{\mathbf{W}}+\frac{2}{3}\beta\tilde{\mathbf{A}}+\beta\left\{\tilde{\mathbf{A}}\cdot\mathbf{Q}+\mathbf{Q}\cdot\tilde{\mathbf{A}}-\frac{2}{3}\left(\tilde{\mathbf{A}}:\mathbf{Q}\right)\delta\right\}- \\ \frac{\beta}{2}\left\{\left(\tilde{\mathbf{A}}:\mathbf{Q}\right)\mathbf{Q}+\tilde{\mathbf{A}}\cdot\mathbf{Q}\cdot\mathbf{Q}+\mathbf{Q}\cdot\tilde{\mathbf{A}}\cdot\mathbf{Q}+\mathbf{Q}\cdot\mathbf{Q}\cdot\tilde{\mathbf{A}}-\left(\left(\mathbf{Q}\cdot\mathbf{Q}\right):\tilde{\mathbf{A}}\right)\delta\right\}\end{array}\right]- \tag{A.4}$$
$$\left\{1-\frac{3}{2}\left(\mathbf{Q}:\mathbf{Q}\right)\right\}^{-2}\left[\left(1-\frac{U}{3}\right)\mathbf{Q}-U\mathbf{Q}\cdot\mathbf{Q}+U\left\{\left(\mathbf{Q}:\mathbf{Q}\right)\mathbf{Q}+\frac{1}{3}\left(\mathbf{Q}:\mathbf{Q}\right)\delta\right\}\right]$$

where $Pe=\dfrac{\dot{\gamma}}{|6D_r|}$ is the dimensionless number called Peclet number, $t^*=|6D_r|\,t$ is the dimensionless time, and $\tilde{\mathbf{A}}$ and $\tilde{\mathbf{W}}$ are dimensionless rate of deformation tensor and dimensionless vorticity tensor respectively, and are given as:

$$\tilde{\mathbf{A}}=\begin{bmatrix}0 & \frac{1}{2} & 0\\ \frac{1}{2} & 0 & 0\\ 0 & 0 & 0\end{bmatrix},\quad \tilde{\mathbf{W}}=\begin{bmatrix}0 & \frac{1}{2} & 0\\ -\frac{1}{2} & 0 & 0\\ 0 & 0 & 0\end{bmatrix} \tag{A.5}$$

APPENDIX B

Uniaxial Extensional Viscosity Predictions from Leslie-Ericksen Theory

The purpose of this appendix is to show, in context of a vector theory (Leslie-Ericksen theory (L-E)) (Leslie, 1979), that two extensional viscosities need to be defined to characterize the uniaxial extensional functions of discotic nematics, whereas only one extensional viscosity coefficient is needed for the rods-like nematics. Also ordering equalities and inequalities between uniaxial extensional viscosities with regard to textures in discotic nematics are also established using the L-E theory.

For anisotropic fluids, the stress tensor τ as given by the L-E theory (Leslie, 1979) is:

$$\tau = \alpha_1 \mathbf{A}:\mathbf{nnnn} + \alpha_4 \mathbf{A} + \alpha_5 \mathbf{nn}\cdot\mathbf{A} + \alpha_6 \mathbf{A}\cdot\mathbf{nn} + \alpha_2 \mathbf{nN} + \alpha_3 \mathbf{Nn} \tag{B.1}$$

where $\mathbf{N} = \dot{\mathbf{n}} - \mathbf{n}\cdot\mathbf{W}$ (B.2)

For extensional flows at steady state

$$\mathbf{W} = \mathbf{0}, \quad \dot{\mathbf{n}} = \mathbf{0}, \quad \therefore \quad \mathbf{N} = \mathbf{0} \tag{B.3a,b}$$

and $\mathbf{A}$ is given by equations (5.2). Equation (B.1) for extensional flows and at steady state reduces to:

$$\tau = \alpha_1 \mathbf{A}:\mathbf{nnnn} + \alpha_4 \mathbf{A} + \alpha_5 \mathbf{nn}\cdot\mathbf{A} + \alpha_6 \mathbf{A}\cdot\mathbf{nn} \tag{B.4}$$

For rod-like nematics:

$$\mathbf{n}_{ss} = (n_r, n_\theta, n_z) = (0,0,1) \tag{B.5}$$

The diagonal components of the stress tensor τ are given as

$$\tau_{rr} = \tau_{\theta\theta} = -\frac{\dot{\varepsilon}}{2}\alpha_4 \tag{B.5a,b}$$

$$\tau_{zz} = (\alpha_1 + \alpha_4 + \alpha_5 + \alpha_6)\dot{\varepsilon} \tag{B.5c}$$

where $\dot{\varepsilon}$ is strain rate. As $\tau_{rr} = \tau_{\theta\theta}$, therefore there is only one uniaxial extensional viscosity for rod-like nematics given as:

$$\eta_{uni,rods} = \tfrac{3}{2}\alpha_4 + \alpha_1 + \alpha_5 + \alpha_6 \tag{B.6}$$

Similarly for discotic mesophases subjected to uniaxial: extensional flows (Singh and Rey, 1994, 1995a, 1995b):

$$\mathbf{n}_{ss} = (n_r, n_\theta, n_z) = (n_r, n_\theta, 0) \tag{B.7}$$

The diagonal components of the stress tensor τ are given as

$$\tau_{rr} = -\frac{\dot{\varepsilon}}{2}\left[\alpha_4 + (\alpha_1 + \alpha_5 + \alpha_6)n_r^2\right] \tag{B.8a}$$

$$\tau_{\theta\theta} = -\frac{\dot{\varepsilon}}{2}\left[\alpha_4 + (\alpha_1 + \alpha_5 + \alpha_6)n_\theta^2\right] \tag{B.8b}$$

$$\tau_{zz} = \alpha_4\dot{\varepsilon} \tag{B.8c}$$

Clearly $\tau_{rr} \neq \tau_{\theta\theta}$, therefore there are two distinct uniaxial extensional viscosities for discotic mesophases, given by:

$$\eta_{zr,uni,disks} = \tfrac{3}{2}\alpha_4 + \tfrac{1}{2}(\alpha_1 + \alpha_5 + \alpha_6)n_r^2 \tag{B.9a}$$

$$\eta_{z\theta,uni,disks} = \tfrac{3}{2}\alpha_4 + \tfrac{1}{2}(\alpha_1 + \alpha_5 + \alpha_6)n_\theta^2 \tag{B.9b}$$

Thus to completely characterize the extensional rheological properties of discotic mesophases, both need to be specified. As the extensional viscosities of discotic mesophases are microstructure dependent, see equations (B.9a, B.9b), they can be directly related to the transverse fiber textures. For the ideal radial texture

($\mathbf{n}_{ss} = (0, 1, 0)$):

$$\eta^{r}_{zr,uni,disks} = \tfrac{3}{2}\alpha_4 \tag{B.10a}$$

$$\eta^{r}_{z\theta,uni,disks} = \tfrac{3}{2}\alpha_4 + \tfrac{1}{2}(\alpha_1 + \alpha_5 + \alpha_6) = \tfrac{3}{2}\alpha_4 + \tfrac{1}{2}(\alpha_1 + \alpha_2 + \alpha_3 + 2\alpha_6) \tag{B.10b}$$

For the ideal onion texture ($\mathbf{n}_{ss} = (1, 0, 0)$):

$$\eta^{o}_{zr,uni,disks} = \tfrac{3}{2}\alpha_4 + \tfrac{1}{2}(\alpha_1 + \alpha_5 + \alpha_6) = \tfrac{3}{2}\alpha_4 + \tfrac{1}{2}(\alpha_1 + \alpha_2 + \alpha_3 + 2\alpha_6) \tag{B.11a}$$

$$\eta^{o}_{z\theta,uni,disks} = \tfrac{3}{2}\alpha_4 \tag{B.11b}$$

Comparing equations (B.10a,b and B.11a,b) we have:

$$\eta^{r}_{zr,uni,disks} = \eta^{o}_{z\theta,uni,disks} \tag{B.12}$$

$$\eta^{r}_{z\theta,uni,disks} = \eta^{o}_{zr,uni,disks} \tag{B.13}$$

For discotic nematics (McHugh, 1994; Volovik, 1980), $\alpha_2 > 0$, $\alpha_3 > 0$ (Volovik, 1980), $\alpha_4 > 0$, $\alpha_5 < 0$, $\alpha_6 > 0$ (McHugh, 1994). Also from the value of α_1 approximated in (McHugh, 1994) we have:

$$\alpha_1 + \alpha_2 + \alpha_3 + 2\alpha_6 > 0 \tag{B.14}$$

Hence we obtain the following ordering among the uniaxial extensional viscosities for discotic nematics:

$$\eta^{r}_{zr,uni,disks} < \eta^{r}_{z\theta,uni,disks} \tag{B.15}$$

$$\eta^{o}_{zr,uni,disks} > \eta^{o}_{z\theta,uni,disks} \tag{B.16}$$

Bibliography

F.M. Leslie, *Theory of flow phenomena in liquid crystals*, in *Advances in Liquid Crystals*, (Academic Press), New York, USA, (1979).

J.J. McHugh, "The development of orientation in mesophase pitch during fiber formation" Ph.D. Dissertation, Clemson University, Clemson, SC, USA (1994).

A.P. Singh and A.D. Rey, "Extension dynamics of discotic nematics of variable order: geodesic flow and viscoelastic relaxation", *Journal de Physique II France* **4**, 645 (1994).

A.P. Singh and A.D. Rey, "Theory and simulation of extensional flow-induced biaxiality in discotic mesophases", *Journal de Physique II France* **5**, 1321 (1995a).

A.P. Singh and A.D. Rey, "Computer simulation of dynamics and microstructure of discotic mesophases in extensional flows", *Liquid Crystals* **18**(2), 230 (1995b).

G.E. Volovik, "Relationship between molecule shape and hydrodynamics in a nematic substance" *JETP Lett.*, **31**, 273 (1980).